

A STUDY OF EXCLUSIVE SEMILEPTONIC D DECAYS
TO PSEUDOSCALAR PION AND KAON FINAL
STATES WITH THE CLEO-C DETECTOR.

A Dissertation

Presented to the Faculty of the Graduate School

of Cornell University

in Partial Fulfillment of the Requirements for the Degree of

Doctor of Philosophy

by

Nadia Erin Adam

January 2007

© 2007 Nadia Erin Adam
ALL RIGHTS RESERVED

A STUDY OF EXCLUSIVE SEMILEPTONIC D DECAYS TO
PSEUDOSCALAR PION AND KAON FINAL STATES WITH THE CLEO-C
DETECTOR.

Nadia Erin Adam, Ph.D.

Cornell University 2007

Using a sample of 1.85 million $D\bar{D}$ mesons collected at the $\Psi(3770)$ with the CLEO-c detector, and a reconstruction method based on the full event hermeticity, we measure branching fractions and branching fraction ratios for the four exclusive semileptonic decay modes $D^0 \rightarrow \pi^- e^+ \nu$, $D^0 \rightarrow K^- e^+ \nu$, $D^+ \rightarrow \pi^0 e^+ \nu$ and, $D^+ \rightarrow \bar{K}^0 e^+ \nu$. For the branching fractions we find $\mathcal{B}(D^0 \rightarrow \pi^- e^+ \nu) = 0.299 \pm 0.011 \pm 0.008$ %, $\mathcal{B}(D^0 \rightarrow K^- e^+ \nu) = 3.55 \pm 0.03 \pm 0.08$ %, $\mathcal{B}(D^+ \rightarrow \pi^0 e^+ \nu) = 0.371 \pm 0.022 \pm 0.013$ % and $\mathcal{B}(D^+ \rightarrow \bar{K}^0 e^+ \nu) = 8.53 \pm 0.13 \pm 0.22$ %. The ratios are found to be $\mathcal{B}(D^0 \rightarrow \pi^- e^+ \nu)/\mathcal{B}(D^0 \rightarrow K^- e^+ \nu) = 0.084 \pm 0.003 \pm 0.001$, $\mathcal{B}(D^+ \rightarrow \pi^0 e^+ \nu)/\mathcal{B}(D^+ \rightarrow \bar{K}^0 e^+ \nu) = 0.044 \pm 0.003 \pm 0.001$, $\Gamma(D^0 \rightarrow \pi^- e^+ \nu)/\Gamma(D^+ \rightarrow \pi^0 e^+ \nu) = 2.04 \pm 0.14 \pm 0.08$ and $\Gamma(D^0 \rightarrow K^- e^+ \nu)/\Gamma(D^+ \rightarrow \bar{K}^0 e^+ \nu) = 1.06 \pm 0.02 \pm 0.03$. In addition, form factors are studied through fits to the partial branching fractions obtained in five q^2 ranges. Combining our results with recent unquenched lattice calculations we extract the CKM matrix elements $|V_{cs}|$ and $|V_{cd}|$. Averaging over isospin conjugate modes, we find $|V_{cs}| = 1.01 \pm 0.01 \pm 0.01 \pm 0.11$ and $|V_{cd}| = 0.217 \pm 0.010 \pm 0.004 \pm 0.023$.

BIOGRAPHICAL SKETCH

Nadia Erin Adam was born on the 23rd of June 1977 to parents Michael and Gillian Adam in Melbourne, Australia. From an early age she displayed an eager curiosity for the world around her (as long as it didn't involve dirt, sand or snow!) and was encouraged in her love of books and learning by both her parents and grandparents.

A deep interest and passion for physics and mathematics were developed by Nadia in high school. Although this was somewhat of a puzzlement for her two parents, both more inclined to the humanities side of things, she nevertheless found support and encouragement every step of the way. In 1994 she was accepted to the Science Scholar Program at Monash University where she majored in physics and applied mathematics. She graduated from the program in 1998 with a B.Sc(*hons*) and an honors thesis on Cosmic Strings. Her love of physics was encouraged at Monash by two professors in particular, whom she still remembers fondly, Michael Morgan and Charlie Osbourne.

In 1999 Nadia was accepted to a PhD program in the Physics Department at Cornell University in Ithaca, NY. After taking a one year leave of absence she joined the CLEO collaboration in 2001 and has never looked back. It was also in the fall of this year that she met her husband and best friend Jack Sankey, whom she married in June 2005.

After graduating from Cornell Nadia hopes to continue her career in particle physics until she is old and gray!

In Loving Memory

Duquenois Drummond Adam, 1921 - 2004

Stewart Alexander Adam, 1979 - 2004

ACKNOWLEDGEMENTS

First and foremost I would like to thank my advisor Lawrence Gibbons, without whose expertise and guidance none of this work would have been possible. I have enjoyed greatly my time working with Lawrence and have learned a great deal from him about the inner workings of experimental particle physics analysis. Moreover, I feel privileged to have learned from someone so dedicated and passionate about their subject.

Also in the line of advisor-ly help I wish to mention Ed Thorndike, Karl Ecklund and Jim Alexander, all of whom I had the opportunity to work with on various projects and all of whom had mountains of knowledge to impart.

Everyone at Wilson Lab deserves a big cheer, none more so than my fellow Cornell graduate students, Veronique, Tom, Lauren, Gregg, Jim, Mike, Laura, Peter, Steve and Richard. Thanks to you all!

To my family and friends in Australia I give my heartfelt thanks. This goes doubly so for my parents who have had to put up with their daughter moving to a country on the other side of the world and marrying an American! They have helped me more than I can say with their regular phone calls and constant support and understanding.

For some of the best times of my life and for making Ithaca a great place to be, I wish to thank my good friends here: Josh and Heidi Waterfall, Matt van Adelsberg, Dan Goldbaum and Adam and Lacy Swanson.

Last but not least, I couldn't have done this without my husband Jack. He has been there throughout this whole undertaking to give me perspective, love, support and of course to make fun of me when needed.

TABLE OF CONTENTS

1	Overview	1
1.1	Physics Goals	1
1.2	Structure	3
2	Semileptonic Charm Decays	4
2.1	The Physics of Elementary Particles	4
2.1.1	Particles and Fields	5
2.1.2	Gauge Symmetry	9
2.1.3	Spontaneous Symmetry Breaking	12
2.2	The Standard Model	16
2.3	Charm Physics and Semileptonic Decays	22
2.4	Form Factors	26
2.4.1	Lattice QCD	27
2.4.2	Functional Forms	35
3	The CLEO-c Detector	42
3.1	Detector Overview	42
3.2	Inner Stereo Drift Chamber (ZD)	42
3.3	Drift Chamber (DR)	43
3.4	RICH	44
3.5	Crystal Calorimeter	46
3.6	Muon Detector	47
4	Analysis Method	48
4.1	Analysis Method Overview	48
4.2	Data and MC Samples	50
4.3	Event Reconstruction	51
4.3.1	Neutrino Reconstruction	51
4.3.2	The D Meson	56
5	Event Selection	65
5.1	Particle Identification	65
5.1.1	Electron Identification	65
5.1.2	Signal π^\pm Identification	66
5.1.3	Signal K^\pm Identification	68
5.1.4	Signal π^0 Identification	69
5.1.5	Signal $K_S(\pi^+\pi^-)$ Identification	71
5.2	Event Cuts	71

6	Fitting for Yields	82
6.1	The Fit	82
6.1.1	Fit Details	84
6.2	MC Corrections	87
6.3	Fit Results	91
6.4	Testing the Fit	92
7	Systematic Uncertainties	110
7.1	Hadronic Shower Addition	110
7.2	Shower Smearing	117
7.3	Splitoff Smearing	118
7.4	K_L Energy Deposition	120
7.5	K_L Re-weight	122
7.6	Pion Momentum Spectra Re-weight	123
7.7	Kaons Faking Pions	127
7.8	Track Finding	129
7.9	Track Smearing	133
7.10	Trkman Fakes	134
7.11	π^0 Finding	138
7.12	K_S Finding	148
7.13	PID for Neutrino Reconstruction	148
7.14	Charged Kaon Signal PID	150
7.15	Charged Pion Signal PID	165
7.16	Electron ID and Fakes	183
7.17	Multiple Electron Veto	183
7.18	M_{bc} Smearing	184
7.19	Final State Radiation	186
7.20	Form Factor Dependence	187
7.21	Systematic Uncertainty Results	192
8	Results and Conclusions	197
8.1	Branching Fraction Results	197
8.2	Form Factors	202
8.3	CKM Matrix Elements: V_{cs} and V_{cd}	219
8.4	Conclusion	220
	Bibliography	222

LIST OF TABLES

2.1	Experimental measurements of the $D \rightarrow K$ form factor shape parameters. Here α is the shape parameter for the modified pole model (Eq. 2.72) and m_{pole} is the pole mass of the simple pole model (Eq. 2.71). The first errors are statistical and the second systematic.	37
2.2	Experimental measurements of the $D \rightarrow \pi$ form factor shape parameters. Here α is the shape parameter for the modified pole model (Eq. 2.72) and m_{pole} is the pole mass of the simple pole model (Eq. 2.71). The first errors are statistical and the second systematic.	38
5.1	Cut history in terms of reconstruction efficiency in signal $D^0 \rightarrow \pi^- e^+ \nu$ MC. We start with no requirements but the particle identification criteria for the electron and pion and the low beam constrained mass cut off $M_{bc} > 1.794$ GeV. To avoid efficiencies of over 100% we never count more than one candidate per event. (The effect of the multiple candidate veto therefore, is to exclude events where a better $D^0 \rightarrow K^- e^+ \nu$ candidate was found.) The given q^2 intervals are those used in the fit, see Chapter 6.	79
5.2	Full efficiency matrix - in the signal M_{bc} region - resulting from application of all event selection criteria for the reconstructed D^0 signal modes. For each type of signal MC, we give the D^0 signal mode reconstruction efficiencies (%) in each of the five reconstructed and five true q^2 ranges. The five q^2 ranges are those used in the analysis fit (detailed in Chapter 6), and are represented by the q_i , with $i = 1, \dots, 5$	80
5.3	Full efficiency matrix - in the signal M_{bc} region - resulting from application of all event selection criteria for the reconstructed D^+ signal modes. For each type of signal MC, we give the D^+ signal mode reconstruction efficiencies (%) in each of the five reconstructed and five true q^2 ranges. The five q^2 ranges are those used in the analysis fit (detailed in Chapter 6), and are represented by the q_i , with $i = 1, \dots, 5$	81
6.1	Results of fit to generic $D\bar{D}$ MC sample with statistics of $40 \times \mathcal{L}_{data}$. We define Y_{input} = input yield, Y_{fit} = efficiency corrected yield from the fit and $\sigma_{Y_{fit}}$ = one sigma error on the efficiency corrected fit yield. The q^2 bins are as given in the text.	109
7.1	Final smear bias values for the Splitoff neural net systematic uncertainty.	121
7.2	Rates of K^\pm faking π^\pm in data and MC, where f gives the fake rate and p_K is the kaon momentum.	128

7.3	Tracking efficiencies for Trkman approved tracks in data and MC. Errors are statistical only.	131
7.4	Number of extra Trkman approved tracks per event in data (281 pb^{-1}) and MC ($40 \times \mathcal{L}$). The MC is normalized to have the same number of double tag events as the data for each double tag mode.	136
7.5	Weights applied to MC in the nominal fit to correct the efficiency of selecting net charge zero events.	138
7.6	π^0 finding efficiencies for signal π^0 's in data and MC.	141
7.7	Signal K_S finding efficiencies in data and MC.	149
7.8	Mode dependent ΔE requirements for K^\pm and π^\pm signal PID fits. .	151
7.9	Signal K^\pm PID efficiencies in data and MC.	152
7.10	Signal π^\pm PID efficiencies in data and MC.	166
7.11	Number of electrons per event in data and MC for $D^0 \bar{D}^0$ and $D^+ D^-$ events. MC is normalized absolutely and then semileptonic events are scaled so that the number of MC events equals the number of data events. The abbreviations used in the MC break down are: PC - photon conversion, SL - semileptonic and FK - fake.	185
7.12	Predicted fraction of radiative events (with photon energies greater than $\sim 0.9 \text{ MeV}$) for each signal mode in PHOTOS and KLOR. . .	187
7.13	Summary of full and partial branching fraction (\mathcal{B}) systematic errors (%) for the $D^0 \rightarrow \pi^- e^+ \nu$ signal decay mode.	193
7.14	Summary of full and partial branching fraction (\mathcal{B}) systematic errors (%) for the $D^0 \rightarrow K^- e^+ \nu$ signal decay mode.	194
7.15	Summary of full and partial branching fraction (\mathcal{B}) systematic errors (%) for the $D^+ \rightarrow \pi^0 e^+ \nu$ signal decay mode.	195
7.16	Summary of full and partial branching fraction (\mathcal{B}) systematic errors (%) for the $D^+ \rightarrow \bar{K}^0 e^+ \nu$ signal decay mode.	196
8.1	Efficiencies (ε), yields and branching fractions (\mathcal{B}) for all q^2 bins and all modes. We note that for the neutral kaon mode, $D^+ \rightarrow \bar{K}^0 e^+ \nu$, the efficiencies and yields are for the reconstructed sub-mode $D^+ \rightarrow K_S(\pi^+ \pi^-) e^+ \nu$, whilst the branching fraction results are for the full mode.	199
8.2	Branching fraction and partial width ratios for all q^2 bins. To calculate the partial width ratios we use the D lifetimes $\tau_{D^0} = (410.3 \pm 1.5) \times 10^{-15} \text{ s}$ and $\tau_{D^+} = (1040 \pm 7) \times 10^{-15} \text{ s}$ [2]. R gives the appropriate ratio in each case.	201
8.3	Experimental measurements of the branching fraction ratios R_0 and R_+ . In the case where the PDG result is derived from several different measurements, we quote their fit value rather than the average. The CLEO-c No Tag 2006 results are from this analysis. .	202

8.4	Form factor parameters resulting from two parameter fits to the measured branching fractions, for the three models outlined in the text. In addition, for each set of fit parameters we give the correlation coefficient ρ and the $\chi^2/d.o.f.$ of the fit.	204
8.5	Three parameter series expansion fit results, where ρ_{ij} is the correlation coefficient for a_i and a_j	205
8.6	Experimental measurements of the $D \rightarrow K$ form factor shape parameters. Here α is the shape parameter for the modified pole model (Eq. 2.72) and m_{pole} is the pole mass of the simple pole model (Eq. 2.71). The first errors are statistical and the second systematic. If only one error is given, it is the combined statistical and systematic error. The CLEO-c tag results are preliminary numbers and the CLEO-c No Tag 2006 results are the ones from this analysis.	212
8.7	Experimental measurements of the $D \rightarrow \pi$ form factor shape parameters. Here α is the shape parameter for the modified pole model (Eq. 2.72) and m_{pole} is the pole mass of the simple pole model (Eq. 2.71). The first errors are statistical and the second systematic. If only one error is given, it is the combined statistical and systematic error. The CLEO-c tag results are preliminary numbers and the CLEO-c No Tag 2006 results are the ones from this analysis.	213
8.8	$D \rightarrow K$ form factor shape parameters from four different theoretical predictions. Here α is the shape parameter for the modified pole model (Eq. 2.72) and m_{pole} is the pole mass of the simple pole model (Eq. 2.71). For the LQCD results we have combined the statistical and systematic uncertainties.	214
8.9	$D \rightarrow \pi$ form factor shape parameters from four different theoretical predictions. Here α is the shape parameter for the modified pole model (Eq. 2.72) and m_{pole} is the pole mass of the simple pole model (Eq. 2.71). For the LQCD results we have combined the statistical and systematic uncertainties.	214

LIST OF FIGURES

2.1	Unitarity Triangle.	21
2.2	The latest experimental constraints on the unitarity triangle.	22
2.3	Example of a semi-leptonic D meson decay, $D^0 \rightarrow \pi^- e^+ \nu_e$	23
2.4	Example of a semi-leptonic D meson decay, $D^0 \rightarrow \pi^- e^+ \nu_e$. The QCD corrections are illustrated by the gluons being exchanged between the initial and final state hadrons. The leptonic vertex is easily calculated, whilst the hadronic vertex requires non-perturbative methods.	28
2.5	The discretization of space-time points in lattice QCD. The lattice spacing is given by a and the size of the lattice is given by L	31
2.6	Lattice QCD calculations of the form factor as a function of q^2 for $D^0 \rightarrow \pi^- e^+ \nu$ (top) and $D^0 \rightarrow K^- e^+ \nu$ (bottom) decays. A B-K parameterization is used for the functional form [29].	40
3.1	The CLEO-c Detector.	43
3.2	The CLEO-c RICH Detector schematic.	45
4.1	Charged pion and kaon abundances from $D\bar{D}$ MC. The left hand plot shows the overall charged hadron momentum spectrum (black line) as well as the charged kaon momentum spectrum (open triangles). On the right is shown the fraction of charged hadrons composed of kaons as a function of momentum. The black line in this plot shows the fit function used for the kaon probability weighting.	54
4.2	Neutrino resolution in signal $D^0 \rightarrow \pi^- e^+ \nu$ MC for events with zero net charge.	56
4.3	Neutrino resolution in signal $D^0 \rightarrow K^- e^+ \nu$ MC for events with zero net charge.	57
4.4	Neutrino resolution in signal $D^+ \rightarrow \pi^0 e^+ \nu$ MC for events with zero net charge.	57
4.5	Neutrino resolution in signal $D^+ \rightarrow K_S(\pi^+ \pi^-) e^+ \nu$ MC for events with zero net charge.	58
4.6	Resolution of $q_{\text{recon}}^2 - q_{\text{true}}^2$ from signal $D^0 \rightarrow \pi^- e^+ \nu$ MC.	60
4.7	Resolution of $q_{\text{recon}}^2 - q_{\text{true}}^2$ from signal $D^0 \rightarrow K^- e^+ \nu$ MC.	61
4.8	Resolution of $q_{\text{recon}}^2 - q_{\text{true}}^2$ from signal $D^+ \rightarrow \pi^0 e^+ \nu$ MC.	62
4.9	Resolution of $q_{\text{recon}}^2 - q_{\text{true}}^2$ from signal $D^+ \rightarrow K_S(\pi^+ \pi^-) e^+ \nu$ MC.	63
5.1	Electron likelihood F , distributions for electron (black line), pion, kaon and muon (gray line) tracks passing the electron candidate quality criteria. For convenience the distribution of non-electron tracks is scaled to have the same maximum as the electron distribution.	67

5.2	Signal charged pion and kaon efficiencies and fake rates from $D\bar{D}$ MC. The left hand plot shows the overall signal pion efficiency (black circles) as well as the fraction of signal pions that are faked by charged kaons (open triangles). The right hand plot shows the overall signal kaon efficiency (black circles) as well as the fraction of signal kaons that are faked by charged pions (open triangles). All quantities are shown as a function of track momentum p	70
5.3	Vee cut in MC for the $D^0 \rightarrow \pi^- e^+ \nu$ signal mode. Filled boxes show signal events, open boxes show background and the normalization is absolute. The events shown pass zero net charge, one electron veto, QCD event classification, and the multiple candidate veto. The solid lines show the signal region (and fit region) Vee cut $ M_{\text{miss}}^2 / 2p_{\text{miss}} < 0.2$	74
5.4	$D^+ \rightarrow \pi^0 e^+ \nu_e$ FOM tuning for the low (a) and high (b) side ΔE_{OS} cuts in the range $q^2 > 1.6\text{GeV}^2$. The arrows show where we place the cuts.	77
6.1	Fit M_{bc} distributions for $D^0 \rightarrow \pi^- e^+ \nu$. Points represent data (281 pb ⁻¹) and stacked histograms are: Clear - Signal MC, Gray - Summed Background MC, Black - Fakes from Data.	93
6.2	Fit M_{bc} distributions for $D^0 \rightarrow K^- e^+ \nu$. Points represent data (281 pb ⁻¹) and stacked histograms are: Clear - Signal MC, Gray - Summed Background MC, Black - Fakes from Data.	94
6.3	Fit M_{bc} distributions for $D^+ \rightarrow \pi^0 e^+ \nu$. Points represent data (281 pb ⁻¹) and stacked histograms are: Clear - Signal MC, Gray - Summed Background MC, Black - Fakes from Data.	95
6.4	Fit M_{bc} distributions for $D^+ \rightarrow K_S(\pi^+ \pi^-) e^+ \nu$. Points represent data (281 pb ⁻¹) and stacked histograms are: Clear - Signal MC, Gray - Summed Background MC, Black - Fakes from Data.	96
6.5	Fit scaled ΔE distributions for $D^0 \rightarrow \pi^- e^+ \nu$. Points represent data (281 pb ⁻¹) and stacked histograms are: Clear - Signal MC, Gray - Summed Background MC, Black - Fakes from Data.	97
6.6	Fit scaled ΔE distributions for $D^0 \rightarrow K^- e^+ \nu$. Points represent data (281 pb ⁻¹) and stacked histograms are: Clear - Signal MC, Gray - Summed Background MC, Black - Fakes from Data.	98
6.7	Fit scaled ΔE distributions for $D^+ \rightarrow \pi^0 e^+ \nu$. Points represent data (281 pb ⁻¹) and stacked histograms are: Clear - Signal MC, Gray - Summed Background MC, Black - Fakes from Data.	99
6.8	Fit scaled ΔE distributions for $D^+ \rightarrow K_S(\pi^+ \pi^-) e^+ \nu$. Points represent data (281 pb ⁻¹) and stacked histograms are: Clear - Signal MC, Gray - Summed Background MC, Black - Fakes from Data.	100
6.9	Fit scaled $\cos \theta_{W_e}$ distributions for $D^0 \rightarrow \pi^- e^+ \nu$. Points represent data (281 pb ⁻¹) and stacked histograms are: Clear - Signal MC, Gray - Summed Background MC, Black - Fakes from Data.	101

6.10	Fit scaled $\cos\theta_{W_e}$ distributions for $D^0 \rightarrow K^- e^+ \nu$. Points represent data (281 pb ⁻¹) and stacked histograms are: Clear - Signal MC, Gray - Summed Background MC, Black - Fakes from Data.	102
6.11	Fit scaled $\cos\theta_{W_e}$ distributions for $D^+ \rightarrow \pi^0 e^+ \nu$. Points represent data (281 pb ⁻¹) and stacked histograms are: Clear - Signal MC, Gray - Summed Background MC, Black - Fakes from Data.	103
6.12	Fit scaled $\cos\theta_{W_e}$ distributions for $D^+ \rightarrow K_S(\pi^+\pi^-)e^+\nu$. Points represent data (281 pb ⁻¹) and stacked histograms are: Clear - Signal MC, Gray - Summed Background MC, Black - Fakes from Data.	104
6.13	Fit scaled p_e (electron momentum) distributions for $D^0 \rightarrow \pi^- e^+ \nu$. Points represent data (281 pb ⁻¹) and stacked histograms are: Clear - Signal MC, Gray - Summed Background MC, Black - Fakes from Data.	105
6.14	Fit scaled p_e (electron momentum) distributions for $D^0 \rightarrow K^- e^+ \nu$. Points represent data (281 pb ⁻¹) and stacked histograms are: Clear - Signal MC, Gray - Summed Background MC, Black - Fakes from Data.	106
6.15	Fit scaled p_e (electron momentum) distributions for $D^+ \rightarrow \pi^0 e^+ \nu$. Points represent data (281 pb ⁻¹) and stacked histograms are: Clear - Signal MC, Gray - Summed Background MC, Black - Fakes from Data.	107
6.16	Fit scaled p_e (electron momentum) distributions for $D^+ \rightarrow K_S(\pi^+\pi^-)e^+\nu$. Points represent data (281 pb ⁻¹) and stacked histograms are: Clear - Signal MC, Gray - Summed Background MC, Black - Fakes from Data.	108
7.1	Distance to the nearest track (measured from track projection into the crystal calorimeter) for (a) Extra Hadronic Showers and (b) Photon from π^0 Showers. Points show data and the open histogram shows $D^0\bar{D}^0$ MC normalized to the number of selected data double tag events. In this case the extra hadronic showers are all extra showers in the event with energy greater than 25 MeV, i.e., we have not required that the showers be Splitoff approved.	112
7.2	The difference in the number of extra showers per track between data and MC is plotted against the number of hadrons (charged + neutral) per event (different for each of the five double tag modes). The line shows the linear best fit to the data and clearly demonstrates the dependence of the difference on the number of hadrons.	113
7.3	The difference in the number of extra showers per track between data and MC is plotted against the momentum of the closest track. The curve shows the best exponential fit to the data and clearly demonstrates the dependence of the difference on the track momentum.	114

7.4	The difference in the number of extra showers per track between data and MC versus the number of tracks per event. The lines (solid and dashed) show a piece-wise linear fit to the data.	116
7.5	Splitoff Neural Net output distributions for (a) Extra Hadronic Showers and (b) Photon from π^0 Showers. Points show data and the open histogram shows $D^0\bar{D}^0$ MC normalized to the number of data entries.	119
7.6	X_E distribution for events with missing energy consistent with a K_L (see [35] for details). Points show data and stacked histograms show Monte Carlo samples normalized by luminosity (background) and number of decays (signal). The colors represent: Clear - Signal, Grey - $D\bar{D}$ background and Black - Continuum.	122
7.7	K_S momentum distributions for (a) $D^0\bar{D}^0$ events and (b) D^+D^- events. Points show data and the stacked histograms show MC. The colors represent: Clear - True K_S , Dark Gray - Background from $D^0\bar{D}^0$ MC, Light Gray - Background from D^+D^- and Black - Background from continuum MC. The normalization is absolute.	124
7.8	Signal π^0 momentum distributions for (a) $D^0\bar{D}^0$ events and (b) D^+D^- events. Points show data and the stacked histograms show MC. The colors represent: Clear - True π^0 , Dark Gray - Background from $D^0\bar{D}^0$ MC, Light Gray - Background from D^+D^- and Black - Background from continuum MC. The normalization is absolute.	125
7.9	Signal π^\pm momentum distributions for (a) $D^0\bar{D}^0$ events and (b) D^+D^- events. Points show data and the stacked histograms show MC. The colors represent: Clear - True π^\pm , Dark Gray - Background from $D^0\bar{D}^0$ MC, Light Gray - Background from D^+D^- and Black - Background from continuum MC. The normalization is absolute.	126
7.10	Fits to MC M_{miss}^2 distributions for $p_{\text{miss}} < 0.1$ GeV/ c . Points show MC histograms, solid lines show double Gaussian signal fits and dashed line shows exponential background fit.	131
7.11	Fits to Data M_{miss}^2 distributions for $p_{\text{miss}} < 0.1$ GeV/ c . Points show Data histograms, solid lines show double Gaussian signal fits and dashed line shows exponential background fit.	132
7.12	Fits to MC M_{miss}^2 distributions for $p_{\text{miss}} \geq 0.1$ GeV/ c . Points show MC histograms, solid lines show double Gaussian signal fits and dashed line shows exponential background fit.	132
7.13	Fits to Data M_{miss}^2 distributions for $p_{\text{miss}} \geq 0.1$ GeV/ c . Points show Data histograms, solid lines show double Gaussian signal fits and dashed line shows exponential background fit.	133
7.14	Fraction of events containing one or more extra tracks as a function of the number of particles per event. Filled circles show data values and open triangles show MC.	137

7.15	Signal π^0 finding: fits to M_{miss}^2 distributions for $p_{\text{miss}} < 0.2$ GeV/ c . In (a) and (b) filled circles show the total MC histograms while open triangles represent background MC histograms. In (c) and (d) filled circles show data histograms. In all cases solid lines show fit results.	142
7.16	Signal π^0 finding: fits to M_{miss}^2 distributions for $0.2 \leq p_{\text{miss}} < 0.4$ GeV/ c . In (a) and (b) filled circles show the total MC histograms while open triangles represent background MC histograms. In (c) and (d) filled circles show data histograms. In all cases solid lines show fit results.	143
7.17	Signal π^0 finding: fits to M_{miss}^2 distributions for $0.4 \leq p_{\text{miss}} < 0.6$ GeV/ c . In (a) and (b) filled circles show the total MC histograms while open triangles represent background MC histograms. In (c) and (d) filled circles show data histograms. In all cases solid lines show fit results.	144
7.18	Signal π^0 finding: fits to M_{miss}^2 distributions for $0.6 \leq p_{\text{miss}} < 0.8$ GeV/ c . In (a) and (b) filled circles show the total MC histograms while open triangles represent background MC histograms. In (c) and (d) filled circles show data histograms. In all cases solid lines show fit results.	145
7.19	Signal π^0 finding: fits to M_{miss}^2 distributions for $p_{\text{miss}} \geq 0.8$ GeV/ c . In (a) and (b) filled circles show the total MC histograms while open triangles represent background MC histograms. In (c) and (d) filled circles show data histograms. In all cases solid lines show fit results.	146
7.20	The MC π^0 efficiency corrections as determined using the methods described in the text. The solid line shows the best linear fit to the data, it is taken as the nominal correction. The dashed and dash-dot lines show the extreme variations of the fit from the four points on the semi-major and semi-minor axes of the error ellipse.	147
7.21	The MC K_S finding efficiency corrections. The solid line shows the best linear fit to the data, it is taken as the nominal correction. The dashed and dash-dot lines show the extreme variations of the fit from the four points on the semi-major and semi-minor axes of the error ellipse.	149
7.22	The MC K^\pm PID efficiency corrections as determined using the methods described in the text. The solid line shows the best linear fit to the data, it is taken as the nominal correction. The dashed and dash-dot lines show the extreme variations of the fit from the four points on the semi-major and semi-minor axes of the error ellipse.	153

7.23	Signal K^\pm PID: fits to $D^0 \rightarrow K\pi\pi^0 M_{bc}$ distributions for $0.0 \leq p_{K^\pm} < 0.3$ GeV/ c . In (a) and (b) filled circles show MC histograms and open triangles show MC background histograms. In (c) and (d) filled circles show data histograms. In all cases solid lines show CB line shape fits and dashed lines show Argus background fits.	154
7.24	Signal K^\pm PID: fits to $D^0 \rightarrow K\pi\pi^0 M_{bc}$ distributions for $0.3 \leq p_{K^\pm} < 0.5$ GeV/ c . In (a) and (b) filled circles show MC histograms and open triangles show MC background histograms. In (c) and (d) filled circles show data histograms. In all cases solid lines show CB line shape fits and dashed lines show Argus background fits.	155
7.25	Signal K^\pm PID: fits to $D^0 \rightarrow K\pi\pi^0 M_{bc}$ distributions for $0.5 \leq p_{K^\pm} < 0.6$ GeV/ c . In (a) and (b) filled circles show MC histograms and open triangles show MC background histograms. In (c) and (d) filled circles show data histograms. In all cases solid lines show CB line shape fits and dashed lines show Argus background fits.	156
7.26	Signal K^\pm PID: fits to $D^0 \rightarrow K\pi\pi^0 M_{bc}$ distributions for $0.6 \leq p_{K^\pm} < 0.7$ GeV/ c . In (a) and (b) filled circles show MC histograms and open triangles show MC background histograms. In (c) and (d) filled circles show data histograms. In all cases solid lines show CB line shape fits and dashed lines show Argus background fits.	157
7.27	Signal K^\pm PID: fits to $D^0 \rightarrow K\pi\pi^0 M_{bc}$ distributions for $p_{K^\pm} \geq 0.7$ GeV/ c . In (a) and (b) filled circles show MC histograms and open triangles show MC background histograms. In (c) and (d) filled circles show data histograms. In all cases solid lines show CB line shape fits and dashed lines show Argus background fits.	158
7.28	Signal K^\pm PID: fits to $D^0 \rightarrow K\pi M_{bc}$ distributions for $p_{K^\pm} \geq 0.7$ GeV/ c . In (a) and (b) filled circles show MC histograms and open triangles show MC background histograms. In (c) and (d) filled circles show data histograms. In all cases solid lines show CB line shape fits and dashed lines show Argus background fits.	159
7.29	Signal K^\pm PID: fits to $D^0 \rightarrow K\pi M_{bc}$ distributions for $0.0 \leq p_{K^\pm} < 0.3$ GeV/ c . In (a) and (b) filled circles show MC histograms and open triangles show MC background histograms. In (c) and (d) filled circles show data histograms. In all cases solid lines show CB line shape fits and dashed lines show Argus background fits.	160
7.30	Signal K^\pm PID: fits to $D^0 \rightarrow K\pi M_{bc}$ distributions for $0.3 \leq p_{K^\pm} < 0.5$ GeV/ c . In (a) and (b) filled circles show MC histograms and open triangles show MC background histograms. In (c) and (d) filled circles show data histograms. In all cases solid lines show CB line shape fits and dashed lines show Argus background fits.	161

7.31	Signal K^\pm PID: fits to $D^0 \rightarrow K\pi M_{bc}$ distributions for $0.5 \leq p_{K^\pm} < 0.6$ GeV/ c . In (a) and (b) filled circles show MC histograms and open triangles show MC background histograms. In (c) and (d) filled circles show data histograms. In all cases solid lines show CB line shape fits and dashed lines show Argus background fits.	162
7.32	Signal K^\pm PID: fits to $D^0 \rightarrow K\pi M_{bc}$ distributions for $0.6 \leq p_{K^\pm} < 0.7$ GeV/ c . In (a) and (b) filled circles show MC histograms and open triangles show MC background histograms. In (c) and (d) filled circles show data histograms. In all cases solid lines show CB line shape fits and dashed lines show Argus background fits.	163
7.33	Signal K^\pm PID: fits to $D^0 \rightarrow K\pi M_{bc}$ distributions for $p_{K^\pm} \geq 0.7$ GeV/ c . In (a) and (b) filled circles show MC histograms and open triangles show MC background histograms. In (c) and (d) filled circles show data histograms. In all cases solid lines show CB line shape fits and dashed lines show Argus background fits.	164
7.34	The MC π^\pm PID efficiency corrections as determined using the methods described in the text. The solid line shows the best linear fit to the data, it is taken as the nominal correction. The dashed and dash-dot lines show the extreme variations of the fit from the four points on the semi-major and semi-minor axes of the error ellipse.	167
7.35	Signal π^\pm PID: fits to $D^0 \rightarrow K\pi\pi^0 M_{bc}$ distributions for $0.0 \leq p_{\pi^\pm} < 0.5$ GeV/ c . In (a) and (b) filled circles show MC histograms and open triangles show MC background histograms. In (c) and (d) filled circles show data histograms. In all cases solid lines show CB line shape fits and dashed lines show Argus background fits.	168
7.36	Signal π^\pm PID: fits to $D^0 \rightarrow K\pi\pi^0 M_{bc}$ distributions for $0.5 \leq p_{\pi^\pm} < 0.6$ GeV/ c . In (a) and (b) filled circles show MC histograms and open triangles show MC background histograms. In (c) and (d) filled circles show data histograms. In all cases solid lines show CB line shape fits and dashed lines show Argus background fits.	169
7.37	Signal π^\pm PID: fits to $D^0 \rightarrow K\pi\pi^0 M_{bc}$ distributions for $0.6 \leq p_{\pi^\pm} < 0.7$ GeV/ c . In (a) and (b) filled circles show MC histograms and open triangles show MC background histograms. In (c) and (d) filled circles show data histograms. In all cases solid lines show CB line shape fits and dashed lines show Argus background fits.	170
7.38	Signal π^\pm PID: fits to $D^0 \rightarrow K\pi\pi^0 M_{bc}$ distributions for $0.7 \leq p_{\pi^\pm} < 0.8$ GeV/ c . In (a) and (b) filled circles show MC histograms and open triangles show MC background histograms. In (c) and (d) filled circles show data histograms. In all cases solid lines show CB line shape fits and dashed lines show Argus background fits.	171

7.39	Signal π^\pm PID: fits to $D^0 \rightarrow K\pi\pi^0 M_{bc}$ distributions for $p_{\pi^\pm} \geq 0.8$ GeV/ c . In (a) and (b) filled circles show MC histograms and open triangles show MC background histograms. In (c) and (d) filled circles show data histograms. In all cases solid lines show CB line shape fits and dashed lines show Argus background fits.	172
7.40	Signal π^\pm PID: fits to $D^0 \rightarrow K_S\pi\pi M_{bc}$ distributions for $0.0 \leq p_{\pi^\pm} < 0.5$ GeV/ c . In (a) and (b) filled circles show MC histograms and open triangles show MC background histograms. In (c) and (d) filled circles show data histograms. In all cases solid lines show CB line shape fits and dashed lines show Argus background fits.	173
7.41	Signal π^\pm PID: fits to $D^0 \rightarrow K_S\pi\pi M_{bc}$ distributions for $0.5 \leq p_{\pi^\pm} < 0.6$ GeV/ c . In (a) and (b) filled circles show MC histograms and open triangles show MC background histograms. In (c) and (d) filled circles show data histograms. In all cases solid lines show CB line shape fits and dashed lines show Argus background fits.	174
7.42	Signal π^\pm PID: fits to $D^0 \rightarrow K_S\pi\pi M_{bc}$ distributions for $0.6 \leq p_{\pi^\pm} < 0.7$ GeV/ c . In (a) and (b) filled circles show MC histograms and open triangles show MC background histograms. In (c) and (d) filled circles show data histograms. In all cases solid lines show CB line shape fits and dashed lines show Argus background fits.	175
7.43	Signal π^\pm PID: fits to $D^0 \rightarrow K_S\pi\pi M_{bc}$ distributions for $0.7 \leq p_{\pi^\pm} < 0.8$ GeV/ c . In (a) and (b) filled circles show MC histograms and open triangles show MC background histograms. In (c) and (d) filled circles show data histograms. In all cases solid lines show CB line shape fits and dashed lines show Argus background fits.	176
7.44	Signal π^\pm PID: fits to $D^0 \rightarrow K_S\pi\pi M_{bc}$ distributions for $p_{\pi^\pm} \geq 0.8$ GeV/ c . In (a) and (b) filled circles show MC histograms and open triangles show MC background histograms. In (c) and (d) filled circles show data histograms. In all cases solid lines show CB line shape fits and dashed lines show Argus background fits.	177
7.45	Signal π^\pm PID: fits to $D^\pm \rightarrow K\pi\pi M_{bc}$ distributions for $0.0 \leq p_{\pi^\pm} < 0.5$ GeV/ c . In (a) and (b) filled circles show MC histograms and open triangles show MC background histograms. In (c) and (d) filled circles show data histograms. In all cases solid lines show CB line shape fits and dashed lines show Argus background fits.	178
7.46	Signal π^\pm PID: fits to $D^\pm \rightarrow K\pi\pi M_{bc}$ distributions for $0.5 \leq p_{\pi^\pm} < 0.6$ GeV/ c . In (a) and (b) filled circles show MC histograms and open triangles show MC background histograms. In (c) and (d) filled circles show data histograms. In all cases solid lines show CB line shape fits and dashed lines show Argus background fits.	179

7.47	Signal π^\pm PID: fits to $D^\pm \rightarrow K\pi\pi M_{bc}$ distributions for $0.6 \leq p_{\pi^\pm} < 0.7$ GeV/ c . In (a) and (b) filled circles show MC histograms and open triangles show MC background histograms. In (c) and (d) filled circles show data histograms. In all cases solid lines show CB line shape fits and dashed lines show Argus background fits.	180
7.48	Signal π^\pm PID: fits to $D^\pm \rightarrow K\pi\pi M_{bc}$ distributions for $0.7 \leq p_{\pi^\pm} < 0.8$ GeV/ c . In (a) and (b) filled circles show MC histograms and open triangles show MC background histograms. In (c) and (d) filled circles show data histograms. In all cases solid lines show CB line shape fits and dashed lines show Argus background fits.	181
7.49	Signal π^\pm PID: fits to $D^\pm \rightarrow K\pi\pi M_{bc}$ distributions for $p_{\pi^\pm} \geq 0.8$ GeV/ c . In (a) and (b) filled circles show MC histograms and open triangles show MC background histograms. In (c) and (d) filled circles show data histograms. In all cases solid lines show CB line shape fits and dashed lines show Argus background fits.	182
7.50	Signal $D^0 \rightarrow \pi^- e^+ \nu$ mode comparison of PHOTOS (filled circles) and KLOR (open triangles) generated radiative photon distributions. In (a) we show the comparison for the photon angle to the electron and in (b) we show the comparison of the photon energy distributions.	188
7.51	Signal $D^0 \rightarrow K^- e^+ \nu$ mode comparison of PHOTOS (filled circles) and KLOR (open triangles) generated radiative photon distributions. In (a) we show the comparison for the photon angle to the electron and in (b) we show the comparison of the photon energy distributions.	189
7.52	Signal $D^+ \rightarrow \pi^0 e^+ \nu$ mode comparison of PHOTOS (filled circles) and KLOR (open triangles) generated radiative photon distributions. In (a) we show the comparison for the photon angle to the electron and in (b) we show the comparison of the photon energy distributions.	190
7.53	Signal $D^+ \rightarrow K_S e^+ \nu$ mode comparison of PHOTOS (filled circles) and KLOR (open triangles) generated radiative photon distributions. In (a) we show the comparison for the photon angle to the electron and in (b) we show the comparison of the photon energy distributions.	191
7.54	The q^2 spectra from $D^0 \rightarrow K^- e^+ \nu$ signal MC generated with ISGW2 form factors (open triangles) and modified pole model (BK) [29] form factors with LQCD calculated parameters [14] (filled circles).	192

8.1	Branching fraction measurements from various experiments for our four signal modes. All measurements are normalized to the updated PDG 2006 values [3]. Solid black circles show the results from this analysis (CLEO-c No Tag 2006), open circles show the preliminary 281 pb ⁻¹ results for the CLEO-c tagged analysis [61] (CLEO-c Tag 2006), solid black squares show the recent Belle results [57] (Belle 2006) and open squares show the BES results [53, 54] (BES 2004/2005).	200
8.2	Fits of the various form factor models to the measured branching fractions of $D^0 \rightarrow \pi^- e^+ \nu$ in five q^2 bins. The solid line shows the series expansion three parameter fit (Series(3)), the gray line shows the series expansion two parameter fit (Series(2)), the dashed line shows the modified pole model fit and the dash-dot line shows the simple pole model fit.	206
8.3	Fits of the various form factor models to the measured branching fractions of $D^0 \rightarrow K^- e^+ \nu$ in five q^2 bins. The solid line shows the series expansion three parameter fit (Series(3)), the gray line shows the series expansion two parameter fit (Series(2)), the dashed line shows the modified pole model fit and the dash-dot line shows the simple pole model fit.	207
8.4	Fits of the various form factor models to the measured branching fractions of $D^+ \rightarrow \pi^0 e^+ \nu$ in five q^2 bins. The solid line shows the series expansion three parameter fit (Series(3)), the gray line shows the series expansion two parameter fit (Series(2)), the dashed line shows the modified pole model fit and the dash-dot line shows the simple pole model fit.	208
8.5	Fits of the various form factor models to the measured branching fractions of $D^+ \rightarrow \bar{K}^0 e^+ \nu$ in five q^2 bins. The solid line shows the series expansion three parameter fit (Series(3)), the gray line shows the series expansion two parameter fit (Series(2)), the dashed line shows the modified pole model fit and the dash-dot line shows the simple pole model fit.	209
8.6	Form factor fit comparison for all modes. All data and fits are normalized to the relevant three parameter series fit result. The solid line shows the series expansion three parameter fit (Series(3)), the gray line shows the series expansion two parameter fit (Series(2)), the dashed line shows the modified pole model fit and the dash-dot line shows the simple pole model fit.	210
8.7	Fraction of events in each q^2 bin for the decay mode $D^0 \rightarrow \pi^- e^+ \nu$. The event fraction in the highest q^2 bin is scaled to the same q^2 range (0.4 GeV ²) as the other four bins. We compare our data results with four theoretical predictions: LQCD [14], LCSR [17], CQM [19] and the simple pole model. The data errors represent combined statistical and systematic uncertainties.	215

8.8	Fraction of events in each q^2 bin for the decay mode $D^0 \rightarrow K^- e^+ \nu$. The event fraction in the highest q^2 bin is scaled to the same q^2 range (0.4 GeV^2) as the other four bins. We compare our data results with four theoretical predictions: LQCD [14], LCSR [17], CQM [19] and the simple pole model. The data errors represent combined statistical and systematic uncertainties.	216
8.9	Fraction of events in each q^2 bin for the decay mode $D^+ \rightarrow \pi^0 e^+ \nu$. The event fraction in the highest q^2 bin is scaled to the same q^2 range (0.4 GeV^2) as the other four bins. We compare our data results with four theoretical predictions: LQCD [14], LCSR [17], CQM [19] and the simple pole model. The data errors represent combined statistical and systematic uncertainties.	217
8.10	Fraction of events in each q^2 bin for the decay mode $D^+ \rightarrow \bar{K}^0 e^+ \nu$. The event fraction in the highest q^2 bin is scaled to the same q^2 range (0.4 GeV^2) as the other four bins. We compare our data results with four theoretical predictions: LQCD [14], LCSR [17], CQM [19] and the simple pole model. The data errors represent combined statistical and systematic uncertainties.	218

Chapter 1

Overview

This chapter orients the reader as to the goals of this analysis. We examine the measurements to be presented and give a flavor of the reasons for our interest in these decays, though these will be explored more fully in the next chapter. Finally an overall outline of the thesis structure is also given.

1.1 Physics Goals

Before embarking on the details of this analysis we should first justify our interest in the exclusive semileptonic charm decays, $D^0 \rightarrow \pi^- e^+ \nu$, $D^0 \rightarrow K^- e^+ \nu$, $D^+ \rightarrow \pi^0 e^+ \nu$ and $D^+ \rightarrow \bar{K}^0 e^+ \nu$ and their charge conjugates. In other words, why study them at all? In essence the answer is that understanding the properties of these decays provides an important contribution to our knowledge of the more fundamental underlying question: What are the basic building blocks of matter? This is perhaps a seemingly simple question, yet despite its long history we still do not have a completely satisfactory answer.

The idea of fundamental particles, imperishable and indivisible elements to serve at the foundations of matter, dates back to the Greek philosopher Democritus ($\sim 460\text{BC} - 370\text{BC}$), who first gave these particles the name “atomos”, or atom in English, literally meaning non-divisible. In the intervening two and a half thousand years since this first proposal of the “atom”, much has been discovered about the nature of the elementary particles, most of it within the last two centuries and a good portion of that within only the last few decades.

The particles currently believed to be the fundamental constituents of matter, as well the forces mediating their interactions, are described by the theory known as the “Standard Model”. Since its conception, the Standard Model of particle physics has had many successes, including numerous cases of astounding predictive accuracy. However, several shortcomings of the model hint at a higher level of underlying physics. But where, if anywhere, does the Standard Model fall apart and the new physics enter? To answer this question the predictions of the model must be carefully experimentally examined. There are many ways in which the model might be tested, but amongst the most important candidates are the predicted mixings of the quark mass eigenstates given by the Cabbibo Kobayashi Maskawa (CKM) matrix.

Experimentally one of the best places to examine the quark flavor changing currents is semileptonic decays. In particular, D semileptonic decays are of interest since they come from the charm sector of the CKM matrix, where the quark mixings are relatively well measured. This fact allows measurement of the strong dynamics of these decays, which are exceedingly difficult to determine theoretically. Confidence in these theoretical predictions, however, is key for precision measurements of the smallest CKM elements. These measurements in turn are essential for determining whether or not the mixing matrix of the Standard Model can be experimentally over-constrained to show unitarity. If the matrix proves not to appear unitary, then the Standard Model has broken down and new physics is required to explain the phenomenon.

In this analysis we study four charmed semileptonic decays: $D^0 \rightarrow \pi^- e^+ \nu$, $D^0 \rightarrow K^- e^+ \nu$, $D^+ \rightarrow \pi^0 e^+ \nu$ and $D^+ \rightarrow \bar{K}^0 e^+ \nu$. For each of the four decay modes we measure the branching fraction spectrum binned as a function of the electron-

neutrino invariant mass. We are then able to fit these results using various different theoretical models for the strong dynamics of the decays. The resulting parameter values of best fit for each model can be compared with their theoretical predictions as a test of the theory. Finally we can also measure the relevant elements of the CKM matrix and compare with those predicted using unitarity constraints.

1.2 Structure

The presentation of our analysis is structured as follows. To start we give a detailed introduction to the theory of the semileptonic charm decays. This is followed by an overview of the CLEO-c detector, with which our data was taken, as well as the details of the data and Monte Carlo (MC) samples used. A detailed description of our analysis method is given, along with our event selection criteria and the details of our fit. We specify each of our systematic errors and describe how the one standard deviation (σ) contribution to the overall systematic error was determined. Finally we give the results of our branching fraction measurements and the physics interpretation of these results in terms of the form factors and CKM matrix elements.

Chapter 2

Semileptonic Charm Decays

In this chapter we give an outline of the physics necessary for a comprehensive understanding of the semileptonic charm decays of interest. We start with the necessary background physics, building to the dynamics of the charmed D meson decays themselves and concluding with the physics into which these decays give us some new insight.

2.1 The Physics of Elementary Particles

The elementary particles are those constituents of matter believed to be the most fundamental; they are the underlying set of indivisible components from which everything else can be assembled. Much of the behavior and interaction of these particles is described, with a startling degree of accuracy, by a theory that has come to be known as the Standard Model. According to this model there are just three types of elementary particle necessary to the formation of all matter: the leptons, quarks and gauge bosons¹. The leptons and quarks, or fermions, provide the basic building blocks of matter whilst the gauge bosons are the “glue” that allows these particles to bind together in stable configurations. Put another way, gauge bosons mediate the forces that cause the fundamental particles to interact.

In nature we observe four fundamental forces: the electromagnetic, the weak, the strong and gravity. Of these four forces only first three can be described in the

¹A fourth type of particle is in fact required in order to endow these particles with the masses with which they are observed today: the Higgs Boson. This particle will be discussed in more detail in what follows.

Standard Model theory. The gravitational force differs from the other three in that it is “non-renormalizable” within the structure of the model, essentially the relevant equations become saturated with infinities that cannot be removed. Putting this fact together with several other observed shortcomings, we are compelled to postulate that the Standard Model is to some degree a low energy effective theory. In other words, it seems that there must exist a more fundamental description of nature.

Despite its flaws, however, in the electroweak sector and at energies lower than $\sim 1\text{TeV}$ the Standard Model has been experimentally verified to better than 1% precision: a remarkably successful theory by any standard. We begin our discussion of the physics of elementary particles therefore with a review of some of the key physical ideas giving rise to the Standard Model. In the next section we will go on to examine the model itself in more detail.

2.1.1 Particles and Fields

To capture the physics of the fundamental particles at all energy scales the machinery of quantum mechanics alone is insufficient. The problem arises when a quantum system enters the realm of special relativity, a regime wherein the equivalence of mass and energy implies that energy can be converted into matter and matter into energy. Consider the implications when we combine this equivalence with the uncertainty principle, which tells us that over a very short time period the energy of a particle can undergo significant fluctuations $\Delta E \Delta t \sim 1/2$.² We must expect that in the case of a system both quantum mechanical and relativistic in nature, the energetic fluctuations can produce new matter, or new particles. In

²Throughout this thesis we work in natural units where $\hbar = c = 1$.

other words, it should be possible for one particle to become many. Now take the Schrödinger equation describing the wave-function of a single electron. No matter how hard we look there is simply no mechanism for the electron to produce more particles, it will always be just a single electron. To solve this problem we need an object that can describe a continuum of possible particle states and their ability to be created from the vacuum, propagate, interact and annihilate. In essence what we need is a field that is quantum mechanical in nature. In fact it should not come as a complete surprise that this is the answer to the marriage of quantum mechanics and special relativity. We are used to thinking of the electromagnetic field as being made up of a series of tiny harmonic oscillators, particles we call photons. In quantum field theory we are simply formalizing this description and promoting the other fundamental particles to the same footing.

On their own fields are more or less classical in nature, but as we have already discovered, to think in terms of elementary particles they must be “quantized”. We must explicitly derive the relationship between particle and field. The most common way to proceed is via a canonical quantization. To do so we start with the Lagrangian for a scalar field

$$L = \int d^3x \left[\frac{1}{2}(\partial_\mu\phi)^2 - \frac{1}{2}m^2\phi^2 \right] = \int d^3x \mathcal{L} \left(\phi(\mathbf{x}, t), \dot{\phi}(\mathbf{x}, t) \right). \quad (2.1)$$

The momentum density conjugate to the field ϕ is defined in the usual way,

$$\pi(\mathbf{x}, t) \equiv \frac{\delta\mathcal{L}}{\delta\dot{\phi}(\mathbf{x}, t)}. \quad (2.2)$$

To quantize we promote the *fields* $\phi(\mathbf{x}, t)$ and $\pi(\mathbf{x}, t)$ to the status of *operators* by imposing the equal time canonical commutation relation

$$[\pi(\mathbf{x}, t), \phi(\mathbf{x}', t)] = -i\delta^3(\mathbf{x} - \mathbf{x}') \quad (2.3)$$

and of course $[\pi(\mathbf{x}, t), \pi(\mathbf{x}', t)] = [\phi(\mathbf{x}, t), \phi(\mathbf{x}', t)] = 0$. We can now write down the Hamiltonian

$$\begin{aligned} H &= \int d^3x \left[\pi(\mathbf{x}', t) \dot{\phi}(\mathbf{x}', t) - \mathcal{L} \right] \\ &= \int d^3x \frac{1}{2} \left[\pi^2 + (\nabla\phi)^2 + m^2\phi^2 \right] \end{aligned} \quad (2.4)$$

and the implied equation of motion, which we recognize as the Klein-Gordon equation

$$(\partial^2 + m^2)\phi = 0. \quad (2.5)$$

This equation can also be viewed as the equation of motion for a harmonic oscillator with frequency $\omega_{\mathbf{p}} = \sqrt{|\mathbf{p}|^2 + m^2}$.³ In quantum mechanics the spectrum of the Harmonic oscillator can be expressed in terms of ladder, or creation and annihilation operators: operators that create and annihilate single particle states. In the case of the Klein-Gordon equation each Fourier mode (or momentum state) of the field ϕ can be treated as an independent oscillator with its own creation and annihilation operators. The field can be Fourier expanded in terms of these operators as

$$\phi(\mathbf{x}, t) = \int \frac{d^3p}{\sqrt{(2\pi)^3}} \frac{1}{\sqrt{2E_p}} \left[a_{\mathbf{p}} e^{-ip \cdot x} + a_{\mathbf{p}}^\dagger e^{ip \cdot x} \right], \quad (2.6)$$

where $p = (E_p, \mathbf{p})$ and $x = (t, \mathbf{x})$. The overall multiplicative factors give the correct normalization such that the commutation relation for $a_{\mathbf{p}}$ and $a_{\mathbf{p}}^\dagger$,

$$\left[a_{\mathbf{p}}, a_{\mathbf{p}'}^\dagger \right] = \delta^3(\mathbf{p} - \mathbf{p}'), \quad (2.7)$$

implies the commutation relation in Eq. 2.3. As expected $a_{\mathbf{p}}^\dagger$ and $a_{\mathbf{p}}$ are the creation and annihilation operators for a scalar particle with momentum \mathbf{p} . That is the vacuum, or ground state, $|0\rangle$ is defined such that $a_{\mathbf{p}} |0\rangle = 0$ and $\sqrt{2E_p} a_{\mathbf{p}}^\dagger |0\rangle = |\mathbf{p}\rangle$.

³It is particularly easy to verify this by Fourier transforming to momentum space.

This then is our quantized field: an object describing a continuum of possible particle states.

One further question of interest is how we can use our result to describe the propagation of a relativistic scalar particle. What we need to calculate is the value of the propagator $\langle 0 | \phi(\mathbf{y}, t_2) \phi(\mathbf{x}, t_1) | 0 \rangle$: a scalar particle is created at \mathbf{x} at time $t_1 = x^0$ and propagates to \mathbf{y} at time $t_2 = y^0$ before being annihilated. In fact we already have enough information to write down the answer to this question. Firstly, however, we will be careful to time order the product of the fields.⁴ We define

$$T[\phi(y)\phi(x)] = \theta(y^0 - x^0)\phi(y)\phi(x) + \theta(x^0 - y^0)\phi(x)\phi(y), \quad (2.8)$$

where θ is the usual Heaviside function. Then using Eq. 2.6 together with Eq. 2.7 we find

$$\langle 0 | T[\phi(y)\phi(x)] | 0 \rangle = \int \frac{d^3p}{(2\pi)^3} \frac{1}{2E_p} \left[\theta(y^0 - x^0) e^{-ip \cdot (x-y)} + \theta(x^0 - y^0) e^{ip \cdot (x-y)} \right]. \quad (2.9)$$

It can furthermore be shown that this expression for the propagator is equal to the so called Green's function $D(x - y)$ where

$$(\partial^2 + m^2)D(x - y) = -i\delta^4(x - y), \quad (2.10)$$

so that in momentum space

$$\tilde{D}(p) = \frac{i}{p^2 - m^2}. \quad (2.11)$$

With the two point propagator in hand it is possible to calculate any property of our free relativistic scalar field.

⁴Time ordering simply ensures that if $t_2 > t_1$ we propagate from \mathbf{x} to \mathbf{y} whilst if $t_1 > t_2$ we propagate from \mathbf{y} to \mathbf{x} . This ordering also ensures that we must always create before we annihilate, a form of causality.

Of course the example of a free scalar field is rather simple and in general we will be interested in the more complicated examples of interacting spin-1 vector fields or spin- $\frac{1}{2}$ Dirac fields. The quantization for these fields can be carried out in a manner analogous to our scalar field example, although there will arise some important differences. For example, in the case of a fermionic Dirac field we must account for the anti-symmetric nature of the spin- $\frac{1}{2}$ particles by imposing anti-commutation, rather than commutation, relations. Nevertheless, we have taken the first step: we have seen how a physical description of the relativistic elementary particles can be formulated in a field theory context. The next naturally arising question is: How do these particles interact? Interestingly enough, the answer to this question begins with symmetry.

2.1.2 Gauge Symmetry

Much of what is observed in the physical world can be explained in terms of symmetry, that is invariance under a particular set of operations. Conservation of energy and momentum are the two primary examples, being implied by the invariance of a system under time and translational changes respectively. Similarly rotational invariance, known as $SO(3)$ symmetry, gives the conservation of angular momentum. Additionally many physical systems observe discrete symmetries, such as parity ($\mathbf{x} \rightarrow -\mathbf{x}$) and charge ($q \rightarrow -q$). It should not be surprising therefore that symmetries play a key role in the physics of the elementary particles. In fact it is symmetry which leads us to the interaction of gauge bosons with the fermions.

To observe this we begin by noticing that the Dirac Lagrangian for a free fermion,

$$\mathcal{L} = \bar{\psi}(i \not{\partial} - m)\psi \tag{2.12}$$

is invariant under the *global* $U(1)$ transformation

$$\psi \rightarrow \psi' \equiv e^{iq\alpha}\psi, \quad (2.13)$$

where $q\alpha$ is an arbitrary real constant. The same is not true, however, for a *local* $U(1)$ transformation

$$\psi(x) \rightarrow \psi'(x) \equiv e^{iq\alpha(x)}\psi(x), \quad (2.14)$$

where the transformed Lagrangian, \mathcal{L}' , contains an extra term,

$$\mathcal{L}' = \mathcal{L} - q\bar{\psi}\gamma^\mu\psi\partial_\mu\alpha \quad (2.15)$$

The implication is that once a given phase convention has been adopted at some reference point, x_0 , the same convention must be used at all points, x . This seems highly unnatural: what happens at one point affects all the other points in the universe. The solution is to invoke the ‘‘Gauge Principal’’, requiring invariance under *local* $U(1)$ phase changes. This can only be achieved via the addition of a new Lagrangian term that transforms in such a way as to cancel the extra $\partial_\mu\alpha$ term. The form of the new term is completely fixed by 2.14 and may be written as

$$\mathcal{L}_{gauge} = eqA_\mu\bar{\psi}\gamma^\mu\psi, \quad (2.16)$$

where the spin-1 gauge field, A_μ , transforms as

$$A_\mu \rightarrow A'_\mu \equiv A_\mu + \frac{1}{e}\partial_\mu\alpha. \quad (2.17)$$

Local gauge invariance has produced a new interaction between the Dirac spinor and the spin-1 ‘‘gauge field’’ A_μ . But A_μ is already familiar to us - it is nothing more than the electromagnetic field. Hence the photon is the ‘‘gauge boson’’ that

carries the electromagnetic interaction and we may finally write down the gauge-invariant Dirac Lagrangian

$$\mathcal{L} = \bar{\psi}(i\not{D} - m)\psi - \frac{1}{4}F_{\mu\nu}F^{\mu\nu}, \quad (2.18)$$

where the new gauge term has been incorporated into the covariant derivative,

$$D_{\mu} \equiv \partial_{\mu} - ieqA_{\mu}, \quad (2.19)$$

and a kinematic term has been added for the electromagnetic field, in which we find familiar field strength tensor $F_{\mu\nu} = \partial_{\mu}A_{\nu} - \partial_{\nu}A_{\mu}$. We should also note that a mass term for the photon, $m^2A_{\mu}A^{\mu}$, is ruled out as it would not be gauge invariant; the symmetry tells us that the photon is massless.

The requirement of a local $U(1)$ symmetry has given us the electromagnetic interaction. The two remaining forces described in the standard model also result from symmetries, with one important difference: the symmetries associated with the weak and strong forces, $SU(2)$ and $SU(3)$, are non-Abelian. Just as in the simple $U(1)$ case of the photon, however, mass terms for the gauge bosons arising from non-Abelian symmetries are ruled out by gauge invariance. This now poses a problem because the weak force is observed to be extremely short ranged, a property that would seem to imply the need for massive force carriers. Indeed it is now well known that the vector bosons of the weak gauge fields, the familiar W^{\pm} and Z^0 are massive. So how can we solve this problem? Where do the masses of these particles come from? Indeed, where do the fermion masses come from? To answer these questions we need to add another field to our repertoire of elementary particles, a scalar field whose properties will allow us to endow the gauge bosons and fermions with their observed masses.

2.1.3 Spontaneous Symmetry Breaking

As we have already suggested, the Standard Model contains one further particle in addition to the leptons, quarks and gauge bosons, namely the Higgs boson. Though the existence of such a particle has never been confirmed experimentally, the Higgs field is required in the Standard Model to explain the masses of the other particles. To understand how the Higgs scalar field results in massive fermions and gauge bosons we must first understand a little about the ideas of hidden symmetries and spontaneous symmetry breaking.

A hidden symmetry occurs when the Lagrangian itself is invariant under some exact symmetry whilst its dynamics result in a set of degenerate vacuum states that do not obey this symmetry. The original symmetry is then said to be hidden because some degeneracy, for example a set of particles with identical masses, is broken. The simplest example of spontaneous symmetry breaking resulting in a hidden symmetry is that of a scalar field ϕ with Lagrangian

$$\mathcal{L} = \frac{1}{2}(\partial_\mu\phi)(\partial^\mu\phi) + V(\phi), \quad (2.20)$$

where the scalar potential, $V(\phi)$, is given by

$$V(\phi) = \frac{1}{2}\mu^2\phi^2 + \frac{1}{4}|\lambda|\phi^4. \quad (2.21)$$

The Lagrangian respects the discrete symmetry of parity invariance, $\phi \rightarrow -\phi$. If $\mu^2 > 0$ the scalar potential will have only one vacuum state at the minimum of the potential, $\langle\phi\rangle_0 = 0$ and thus will also be invariant under parity changes. If $\mu^2 < 0$, however, there are two degenerate vacua at $\langle\phi\rangle_0 = \pm\sqrt{-\mu^2/|\lambda|} = \pm v$. Choosing one of the degenerate vacua at random, $\langle\phi\rangle_0 = +v$, and defining the shifted field $\phi' = \phi - v$, it can be seen that the Lagrangian,

$$\mathcal{L} = \frac{1}{2}(\partial_\mu\phi')(\partial^\mu\phi') - |\mu|^2 \left(\frac{\phi'^4}{4v^2} + \frac{\phi'^3}{v} + \phi'^2 - \frac{v^2}{4} \right), \quad (2.22)$$

no longer obeys the original symmetry. Effectively, because of the two possible minima, the parity invariance of the Lagrangian is broken in the physical vacuum. In addition, if we take the limit of small oscillations about the minimum the Lagrangian becomes

$$\mathcal{L} = \frac{1}{2}(\partial_\mu\phi')(\partial^\mu\phi') - |\mu|^2\phi'^2, \quad (2.23)$$

and it is readily apparent that we are describing the oscillations of a spin-zero particle with mass $2|\mu|^2$.

This idea readily generalizes to more complicated cases of continuous, non-Abelian symmetry breaking. In the case of a spontaneously broken continuous symmetry it can be shown that in addition to the appearance of the massive scalar boson from Eq. 2.23 there will appear one additional massless spin-zero particle for each broken generator of the original symmetry group. This phenomenon is known as Goldstone's theorem and the massless particles are referred to as the Goldstone bosons. This is all well and good, but we have still managed to generate only *massless* bosons, making it difficult to see how the this symmetry breaking mechanism can help us in our quest to fix the problem of our massless vector gauge bosons. For this we need to examine specifically the case of a spontaneously broken *gauge* symmetry.

Rather than explain the breaking of a gauge symmetry in general terms we will jump directly to the example of interest: the electroweak symmetry breaking. We introduce the four massless vector gauge bosons, b_μ^1 , b_μ^2 , b_μ^3 and b_μ^0 that arise from the $SU(2)_L \times U(1)_Y$ symmetry of the Lagrangian. The b_μ^i , where $i = 1, 2, 3$, are associated with the $SU(2)_L$ symmetry while b_μ^0 is associated with $U(1)_Y$. An electroweak Lagrangian is constructed from these gauge fields and the fermions in the usual way, we modify the theory, however, by adding a complex doublet of

scalar fields,

$$\phi = \begin{pmatrix} \phi^+ \\ \phi^0 \end{pmatrix}. \quad (2.24)$$

The Lagrangian for this scalar field is given by

$$\mathcal{L}_{scalar} = (D^\mu \phi)^\dagger (D_\mu \phi) + V(\phi^\dagger \phi), \quad (2.25)$$

where the covariant derivative is

$$D_\mu = \partial_\mu + \frac{ig'}{2} b_\mu^0 + \frac{ig}{2} \boldsymbol{\tau} \cdot \mathbf{b}_\mu, \quad (2.26)$$

with g and g' the coupling constants of weak-isospin $SU(2)_L$ and hypercharge $U(1)_Y$ respectively and $\boldsymbol{\tau}$ the vector of Pauli matrices. The scalar potential takes the familiar form

$$V(\phi^\dagger \phi) = \mu^2 (\phi^\dagger \phi) + |\lambda| (\phi^\dagger \phi)^2. \quad (2.27)$$

We may now assume a spontaneously broken symmetry, by setting $\mu^2 < 0$, and see what happens.

To begin we choose a vacuum expectation value for the scalar field

$$\langle \phi \rangle_0 = \begin{pmatrix} 0 \\ v/\sqrt{2} \end{pmatrix}, \quad (2.28)$$

with $v = \sqrt{-\mu^2/|\lambda|}$ as before. The physics of our broken symmetry will be contained in the expansion of the Lagrangian about the minimum of the scalar potential. To do this we define a shifted field, $\phi' = \phi - \langle \phi \rangle_0$ and parameterize ϕ as

$$\phi = \exp\left(\frac{i\boldsymbol{\eta} \cdot \boldsymbol{\tau}}{2v}\right) \begin{pmatrix} 0 \\ (v + H)/\sqrt{2} \end{pmatrix}, \quad (2.29)$$

where H and $\boldsymbol{\eta}$ are small perturbations. Since we are free to choose any gauge it is also more convenient to gauge away the non-physical Goldstone bosons (η_1, η_2

and η_3) by setting

$$\phi \rightarrow \exp\left(\frac{-i\boldsymbol{\eta} \cdot \boldsymbol{\tau}}{2v}\right)\phi \quad (2.30)$$

and assuming the corresponding changes for the gauge fields. Then in terms of the shifted field:

$$\phi' = \begin{pmatrix} 0 \\ H/\sqrt{2} \end{pmatrix} \quad (2.31)$$

the scalar field Lagrangian becomes

$$\mathcal{L}_{scalar} = \frac{1}{2}(\partial^\mu H)(\partial_\mu H) - \mu^2 H^2 + \frac{v^2}{8} [g^2 |b_\mu^1 - ib_\mu^2|^2 + (g'b_\mu^0 - gb_\mu^3)^2] + \dots \quad (2.32)$$

where we have neglected to write down the interaction terms. It is immediately apparent that the H field has acquired a mass, $M_H^2 = -2\mu^2 > 0$, indeed this particle is none other than the physical Higgs boson. To make sense of the remainder we define the charged gauge fields

$$W_\mu^\pm = \frac{b_\mu^1 \mp ib_\mu^2}{\sqrt{2}} \quad (2.33)$$

as well as the orthogonal combinations

$$Z_\mu = \frac{-g'b_\mu^0 + gb_\mu^3}{\sqrt{g^2 + g'^2}} \quad (2.34)$$

and

$$A_\mu = \frac{gb_\mu^0 + g'b_\mu^3}{\sqrt{g^2 + g'^2}}. \quad (2.35)$$

In terms of these fields it is easy to show that we have three massive vector bosons, W_μ^\pm with $M_{W^\pm} = gv/2$ and Z_μ with $M_Z = \sqrt{g^2 + g'^2}v/2$, and one massless vector boson A_μ that preserves the $U(1)_{EM}$ symmetry. Via the Higgs mechanism we have achieved exactly our observed electroweak sector.

Finally it should be noted that we are also free to add interaction terms between the Higgs field and the fermions. These Yukawa couplings will result in mass terms

for the fermions when the symmetry is spontaneously broken and the Higgs field falls to its vacuum expectation value. We thus appear to have solved all of our original problems: the Higgs field endows both the fermions and gauge bosons with mass. However, this is not quite the end of the story. We must remember that whilst the Higgs mechanism seems plausible, and even beautiful, the Higgs boson has yet to be observed in nature. In fact, with masses less than ~ 114 GeV already ruled out by current data [1], it appears we must wait for the next generation of energy frontier experiments to see if the Higgs particle really exists. If this turns out not to be the case, an alternate explanation for the particle masses must be found. In the absence of any evidence to the contrary, however, we will assume that the Higgs mechanism is valid and using the ideas we have developed, go on to describe the Standard Model in some more technical detail.

2.2 The Standard Model

In the previous section we described three key results, which taken together form the basis of modern particle physics. Namely, we saw that elementary particles can be described as relativistic quantum fields whose interactions are mediated by gauge bosons and whose masses derive from the broken symmetry of the scalar Higgs field. To proceed to the Standard Model we must piece together, in a physical manner, the fields of all the observed elementary particles. This superposition of the various particles and their interactions can be summarized in the resulting Lagrangian expression for the fields:

$$\mathcal{L}_{SM} = \mathcal{L}_G + \mathcal{L}_F + \mathcal{L}_H + \mathcal{L}_M + \mathcal{L}_{GF} + \mathcal{L}_{FP}, \quad (2.36)$$

where \mathcal{L}_{SM} is the total Standard Model Lagrangian, \mathcal{L}_G is the Yang-Mills, or gauge field, Lagrangian without matter fields, \mathcal{L}_F is the coupling of the fermionic matter fields with the gauge fields, \mathcal{L}_H is the Higgs field Lagrangian, \mathcal{L}_M contains the fermion mass terms, \mathcal{L}_{GF} contains gauge-fixing terms and \mathcal{L}_{FP} describes the Fadeev Popov ghosts. This Lagrangian contains three generations of leptons and quarks composed of left-handed doublets and right-handed singlets,

$$e_R^-, \begin{pmatrix} \nu_e \\ e^- \end{pmatrix}_L, \quad \mu_R^-, \begin{pmatrix} \nu_\mu \\ \mu^- \end{pmatrix}_L, \quad \tau_R^-, \begin{pmatrix} \nu_\tau \\ \tau^- \end{pmatrix}_L$$

and

$$u_R, \quad d_R, \begin{pmatrix} u \\ d \end{pmatrix}_L, \quad c_R, \quad s_R, \begin{pmatrix} c \\ s \end{pmatrix}_L, \quad t_R, \quad b_R, \begin{pmatrix} t \\ b \end{pmatrix}_L.$$

It should be noted here that already our description has become somewhat inaccurate. The fact that the leptonic generations contain only left-handed neutrinos (right-handed anti-neutrinos) implies massless neutrinos, whereas neutrino mixing is now an experimentally confirmed phenomenon [2][4]. This fix can be incorporated into the Standard Model, however, for the present purposes it is not necessary.

The two most useful parts of the Standard Model Lagrangian for the present purpose, that is the study of D semileptonic decays, are \mathcal{L}_F and \mathcal{L}_M , which (for one lepton generation) may be expanded fully as

$$\begin{aligned} \mathcal{L}_F + \mathcal{L}_M &= i\bar{e}\not{\partial}e + i\bar{\nu}_L\not{\partial}\nu_L + i\sum_n\bar{q}_n\not{\partial}q_n \\ &+ \frac{e}{\sqrt{2}\sin\theta_W}\left(\bar{\nu}_L W^+ e_L + \bar{e}_L W^- \nu_L\right) + \frac{e}{\sin 2\theta_W}\bar{\nu}_L\not{Z}\nu_L \\ &+ \frac{e}{\sin 2\theta_W}\left(\bar{e}\not{Z}\left(2\sin^2\theta_W - \frac{1-\gamma_5}{2}\right)e\right) - e\bar{e}\not{A}e \\ &+ \frac{e}{\sqrt{2}\sin\theta_W}\sum_{I,i}\left(\bar{q}_I W^+ q_{iL}\left(V^\dagger\right)_{Ii} + \bar{q}_i W^- q_{iL}V_{iI}\right) \end{aligned}$$

$$\begin{aligned}
& + \frac{e}{\sin 2\theta_W} \sum_I \left(\bar{q}_I \not{Z} \left(\frac{1 - \gamma_5}{2} - 2Q_I \sin^2 \theta_W \right) q_I \right) \\
& + \frac{e}{\sin 2\theta_W} \sum_I \left(\bar{q}_i \not{Z} \left(\frac{-1 + \gamma_5}{2} - 2Q_i \sin^2 \theta_W \right) q_i \right) \\
& + e \sum_n Q_n \bar{q}_n \not{A} q_n + g_s \sum_n \bar{q}_n G^a_{\mu} \gamma^{\mu} t^a q_n \\
& - \frac{em_e}{M_Z \sin 2\theta_W} H \bar{e} e - \frac{e}{M_Z \sin 2\theta_W} \sum_n m_n H \bar{q}_n q_n \\
& + \frac{ie\sqrt{2}m_e}{M_Z \sin 2\theta_W} (\omega^- \bar{e} \nu_L - \omega^+ \bar{\nu}_L e) + \frac{iem_e}{M_Z \sin 2\theta_W} z \bar{e} \gamma_5 e \\
& + \frac{ie}{\sqrt{2}M_Z \sin 2\theta_W} \omega^+ \sum_{I,i} (V^\dagger)_{I,i} \bar{q}_I (m_I - m_i - (m_I + m_i) \gamma_5) q_i \\
& + \frac{ie}{\sqrt{2}M_Z \sin 2\theta_W} \omega^- \sum_{I,i} (V)_{i,I} \bar{q}_i (m_i - m_I - (m_I + m_i) \gamma_5) q_I \\
& - \frac{ie}{M_Z \sin 2\theta_W} \left(\sum_I m_I \bar{q}_I \gamma_5 q_I + \sum_i m_i \bar{q}_i \gamma_5 q_i \right), \tag{2.37}
\end{aligned}$$

where we follow the notation used in [5]. The $I(i) = 1, 2, 3$ denote the up (down) quarks,

$$\sin \theta_W \equiv g' / \sqrt{g^2 + g'^2},$$

and the Higgs doublet ϕ is given by,

$$\phi = \begin{pmatrix} i\omega^+ \\ (v + H - iz) / \sqrt{2} \end{pmatrix}.$$

In this case ω^\pm and z are massless Goldstone bosons that may be gauged away as we saw in the previous section. In fact, it is common to think of these particles as having been “eaten” by the gauge bosons: the Goldstone bosons become the non-zero longitudinal components inherent to the massive vector bosons. The only physical field is once again H , the Higgs boson.

The Standard Model that we have just written down accurately describes many aspects of elementary particle interactions and is a useful effective theory. However, as we have already noted at the beginning of this chapter, there are still some fundamental aspects of particle physics that it fails to address.

One concern is that the theory contains many free parameters, such as the particle masses, which can be determined only by experimental measurement. There is also the so called “hierarchy problem” [6], in which the Higgs scalar field must have a mass many orders of magnitude smaller than the scale of the highest order symmetry breaking (e.g. when gravity unites with the other forces at roughly the Planck scale) in order to endow the W and Z bosons from (2.37) with their observed masses at the electroweak symmetry breaking. This requires some extraordinary cancellations, or fine tuning, in the mass-squared term of the Higgs field during renormalization. Additionally the Standard Model has no explanation for gravity or how this fourth force might be united with the other three. Such questions must be answered by physics “beyond the Standard Model”, which is to say, there must be a more fundamental underlying theory that encompasses the physics of the Standard Model to some degree. In order to grasp this new physics it is first necessary to fully test the Standard Model experimentally. Only by measuring and over-constraining the free parameters of the theory can it be seen if, and where, the Standard Model will break down to reveal the physics that lies beyond it.

One of the key places to test the physics of the Standard Model is the Cabibbo Kobayashi Maskawa (CKM) matrix. This matrix has in fact already been introduced in (2.37), where it is denoted as V_{iI} and is clearly seen to transform the quark fields from their mass eigenstate basis. By convention this matrix is defined to operate on the down, or $Q = -e/3$, quark mass eigenstates and is usually written as,

$$\begin{pmatrix} d' \\ s' \\ b' \end{pmatrix} = \begin{pmatrix} V_{ud} & V_{us} & V_{ub} \\ V_{cd} & V_{cs} & V_{cb} \\ V_{td} & V_{ts} & V_{tb} \end{pmatrix} \begin{pmatrix} d \\ s \\ b \end{pmatrix}.$$

Within the framework of the standard model the mixing matrix is derived as a product of two unitary matrices, and is therefore unitary by construction [6]. Using this unitarity constraint and removing unphysical quark phases it can be shown that the three generation CKM matrix contains just four independent, real parameters [9]. A standard parameterization is [2],

$$V = \begin{pmatrix} c_{12}c_{13} & s_{12}c_{13} & s_{13}e^{-i\delta_{13}} \\ -s_{12}c_{23} - c_{12}s_{23}s_{13}e^{-i\delta_{13}} & c_{12}c_{23} - s_{12}s_{23}s_{13}e^{-i\delta_{13}} & s_{23}c_{13} \\ s_{12}s_{23} - c_{12}c_{23}s_{13}e^{-i\delta_{13}} & -c_{12}s_{23} - s_{12}c_{23}s_{13}e^{-i\delta_{13}} & c_{23}c_{13} \end{pmatrix}, \quad (2.38)$$

where $c_{ij} = \cos \theta_{ij}$ and $s_{ij} = \sin \theta_{ij}$. The angles θ_{12} , θ_{23} and θ_{13} specify the rotation whilst δ_{13} is a complex phase that results from the presence of three quark and lepton generations.⁵ CP violation is an important, and observable, consequence of the complex phase. Another expansion of the CKM matrix is motivated by the fact that, as well as being unitary, the matrix is also close to unity. This parameterization, due to Wolfenstein [10], is an expansion of the matrix in the small parameter $\lambda = \sin \theta_C \approx 0.22$ where θ_C is the Cabibbo angle (see for example [6]), and is given by

$$\begin{pmatrix} 1 - \frac{\lambda^2}{2} & \lambda & A\lambda^3(\rho - i\eta) \\ -\lambda & 1 - \frac{\lambda^2}{2} & A\lambda^2 \\ A\lambda^3(1 - \rho - i\eta) & -A\lambda^2 & 1 \end{pmatrix} + \mathcal{O}(\lambda^4). \quad (2.39)$$

It should also be noted that all the parameters in this expansion apart from λ , i.e., A , ρ and η , are of order unity. Combining this parameterization with the unitarity constraint,

$$V_{ub}^*V_{ud} + V_{cb}^*V_{cd} + V_{tb}^*V_{td} = 0. \quad (2.40)$$

⁵We note than in general, for n generations, there are $n(n-1)/2$ angles and $(n-1)(n-2)/2$ phases [11].

allows the CKM parameters to be represented as a triangle in the complex $(\bar{\rho}, \bar{\eta})$ plane, shown in Fig. 2.1, where $\bar{\rho} = \rho(1 - \lambda^2/2)$ and $\bar{\eta} = \eta(1 - \lambda^2/2)$. The side lengths of the triangle CA and BA are given by R_b and R_t respectively where,

$$R_b \equiv \frac{|V_{ud}V_{ub}^*|}{|V_{cd}V_{cb}^*|} = \sqrt{\bar{\rho}^2 + \bar{\eta}^2} = \left(1 - \frac{\lambda^2}{2}\right) \frac{1}{\lambda} \left| \frac{V_{ub}}{V_{cb}} \right| \quad (2.41)$$

and

$$R_t \equiv \frac{|V_{td}V_{tb}^*|}{|V_{cd}V_{cb}^*|} = \sqrt{(1 - \bar{\rho})^2 + \bar{\eta}^2} = \frac{1}{\lambda} \left| \frac{V_{td}}{V_{cb}} \right|. \quad (2.42)$$

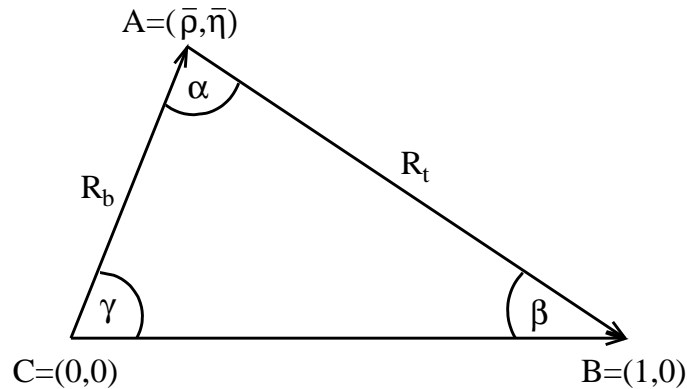


Figure 2.1: Unitarity Triangle.

Like the fermion masses, the parameters of the CKM matrix are input parameters to the standard model: they are not predicted, but must instead be measured experimentally. The CKM matrix is thus an important focus of experimental particle physics: not only must its elements be measured but it also provides a pivotal arena for testing the validity of the standard model. If the standard model is correct experimental determination of the parameters should verify unitarity, whilst deviations would indicate the presence of new physics. Unitarity may be verified by over-constraint of the unitarity triangle discussed above, the current experimental constraints are shown in Fig. 2.2 [12]. Measurement of the CKM matrix is difficult, however, precisely because it is close to unity, leaving the small off-diagonal

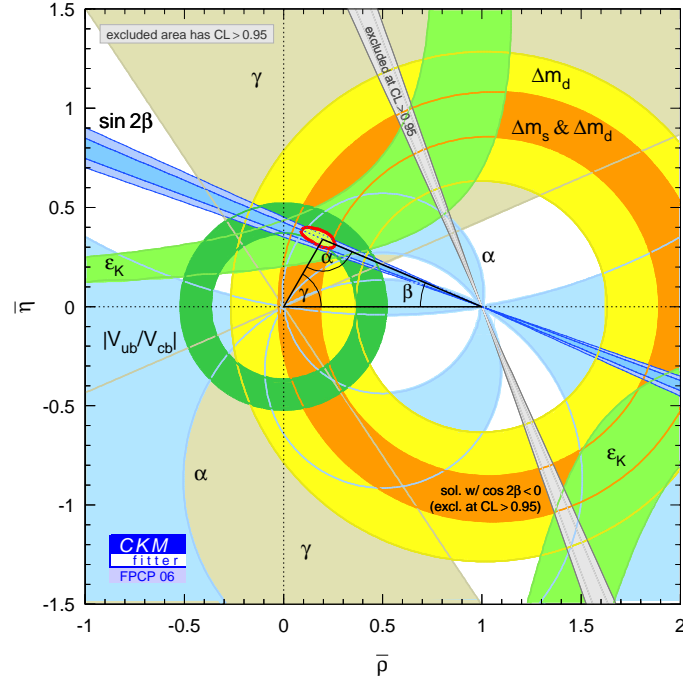


Figure 2.2: The latest experimental constraints on the unitarity triangle.

elements to be determined via decays with small branching fractions. It thus remains a continuing experimental challenge to fully test unitarity via precision measurement of the CKM matrix.

2.3 Charm Physics and Semileptonic Decays

One of the best experimental frameworks for CKM measurements is the semileptonic decays of B and D mesons, see Fig 2.3. From a theoretical viewpoint semileptonic decays are relatively simple when compared to mesons decaying via fully hadronic final states. This simplicity is due to the fact that the semileptonic decays may be factored into the product of the well understood leptonic current and the more complicated hadronic current, allowing the complexity of the strong interactions to be isolated. In addition, the strong final state interactions

present in hadronic decays are removed. Experimentally semileptonic decays are also tractable and are preferred over purely leptonic decays because of their much larger branching fractions.

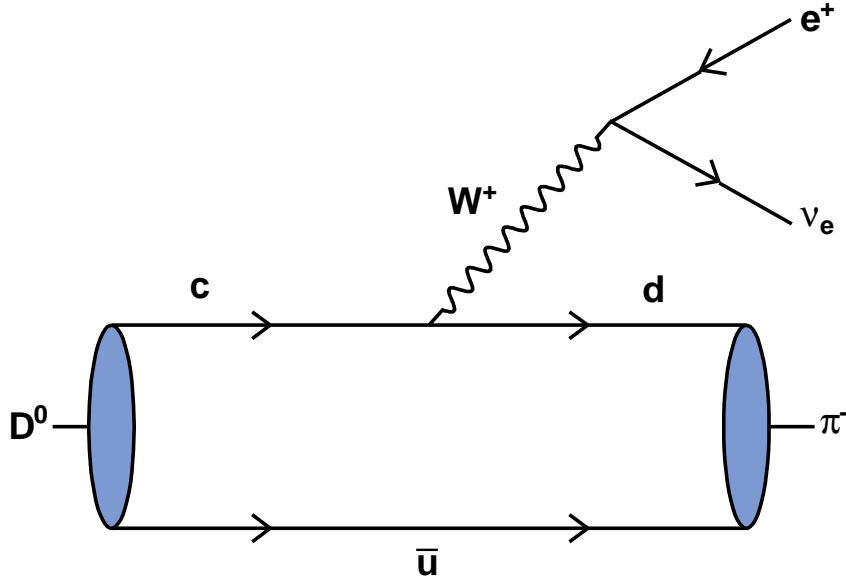


Figure 2.3: Example of a semi-leptonic D meson decay, $D^0 \rightarrow \pi^- e^+ \nu_e$

CLEO-c has obtained a very large, clean sample of D semileptonic decays at the $\psi(3770)$ charm resonance. For such decays, where the charmed D meson, $D_{c\bar{q}'}$, with $\bar{q}' = \bar{u}$ or \bar{d} , decays to some pseudoscalar meson, $P_{q\bar{q}'}$, the amplitude is of the form [13]

$$\mathcal{M}(D_{c\bar{q}'} \rightarrow P_{q\bar{q}'} e^+ \nu_e) = -i \frac{G_F}{\sqrt{2}} V_{cq} L^\mu H_\mu, \quad (2.43)$$

where G_F is the Fermi constant, V_{cq} the appropriate CKM matrix element and L^μ and H_μ are the leptonic and hadronic currents. The leptonic current can be written in terms of the electron and neutrino Dirac spinors, u_e and v_ν ,

$$L^\mu = \bar{u}_e \gamma^\mu (1 - \gamma_5) v_\nu. \quad (2.44)$$

In general the hadronic current is a matrix element given by,

$$H_\mu = \langle P | \bar{q} \gamma_\mu (1 - \gamma_5) c | D \rangle. \quad (2.45)$$

However, in the case of pseudoscalar decays, there is no axial-vector contribution and this simplifies to,

$$H_\mu = \langle P | \bar{q} \gamma_\mu c | D \rangle. \quad (2.46)$$

In either case it is no simple matter to calculate this matrix element. It is possible to simplify the situation, however, by noting that in the pseudoscalar decay there are only two independent four vectors, usually taken to be $p' + p$ and $q \equiv p' - p$ where p' and p are the four vectors of the parent D meson and the daughter P meson respectively. We recognize q as the four vector of the virtual W boson (see Fig. 2.3). The hadronic current can be written in terms of these two four vectors as

$$\langle P | \bar{q} \gamma^\mu c | D \rangle = f_+(q^2)(p' + p)^\mu + f_-(q^2)(p' - p)^\mu, \quad (2.47)$$

where f_+ and f_- are the form factors of the decay and depend only on q^2 . The current is also commonly expressed in terms of the alternate form factors F_1 and F_0 ,

$$\langle P | \bar{q} \gamma^\mu c | D \rangle = F_1(q^2) \left((p' + p)^\mu - \frac{M_D^2 - m_P^2}{q^2} q^\mu \right) + F_0(q^2) \frac{M_D^2 - m_P^2}{q^2} q^\mu, \quad (2.48)$$

where $F_1(q^2) = f_+(q^2)$ and

$$F_0(q^2) = f_+(q^2) + \frac{q^2}{M_D^2 - m_P^2} f_-(q^2). \quad (2.49)$$

Nominally we shall use the f_+ and f_- form factor notation, however, in practice the expression for the matrix element can be simplified to contain just the f_+ form factor, which is exactly the same in either case. This simplification arises due to

the small mass of the electron.⁶ In the limit $m_e \rightarrow 0$, we have $q^\mu L_\mu = 0$, so that, to a very good approximation⁷ the decays may be described by a single form factor,

$$\langle P|\bar{q}\gamma^\mu c|D\rangle = f_+(q^2)(p' + p)^\mu. \quad (2.50)$$

Substituting this form of the hadronic current into Eq. 2.43, the partial decay width becomes

$$\frac{d\Gamma(D \rightarrow Pe\nu)}{dq^2} = \frac{G_F^2 |V_{cq}|^2}{24\pi^3} p^3 |f_+(q^2)|^2. \quad (2.51)$$

It is now possible to understand why study of the D semileptonic decays is important. In the first place, from the measured branching fractions it is possible to extract values for $|V_{cs}|$ and $|V_{cd}|$, providing direct constraints on the CKM matrix. Moreover, the size and quality of the CLEO-c data sample (1.8 million $D\bar{D}$ pairs) allows for these measurements to be made with unprecedented experimental precision - at the few percent level or less. In addition, precision measurement of the branching fractions in multiple q^2 ranges enables extraction of precise results for the form factor shapes and CKM adjusted normalizations (i.e. $|V_{cq}|f_+(0)$), in both $D \rightarrow K$ and $D \rightarrow \pi$ decays. By allowing confirmation of high precision theoretical calculations of the form factors these results make an indirect, yet highly important, contribution to improvement of the experimental constraints on the unitarity of the CKM matrix. This contribution is possible, and indeed necessary, due to the fact that many of the current constraints on unitarity (shown in Fig. 2.2), and thus on physics beyond the Standard Model, are dominated by the presence of large theoretical errors. In particular, our results will contribute to the study of B semileptonic decays, which can be related to the D decays via

⁶We note that we are only concerned with the electron decays here because muons cannot be distinguished from pions in CLEO-c

⁷The exact suppression of the second form factor is given by $(m_e/M_D)^2$.

the use of heavy quark symmetry (HQET). Importantly, this can give increased accuracy for the extraction of the small CKM matrix element $|V_{ub}|$. The precise measurement of form factors in charm semileptonic decays therefore, will make significant contributions toward understanding the validity of the Standard Model.

With this motivation in view, we turn now to a more detailed description of the form factors themselves.

2.4 Form Factors

The form of the semileptonic partial decay width reveals the fundamental nature of the connection between the CKM matrix elements and the hadronic form factors: to measure one we must know the other. This tells us that for any experimental determination of the CKM matrix elements via semileptonic decays, some theoretical estimation of the form factor is necessary. Such calculations therefore have become a considerable industry in recent times, with a variety of techniques being employed.

Prominent amongst these techniques have been quark model calculations, such as the ISGW2 model [30], the use of QCD sum rules and their more advanced counterpart light-cone sum rules (LCSR) as well as lattice QCD (LQCD) methods. Quark models have long been disfavored due to a somewhat “ad hoc” construction of the quark behavior that makes it hard to quantify their accuracy. For some years the LCSR technique and LQCD, both based on the true dynamics of QCD, competed in accuracy, with errors at the 20 – 30% level. More recently, however, advances in both computing power and calculational techniques have allowed LQCD to progress significantly, to the point where it will soon be the most precise

theoretical method.⁸ Semileptonic form factors (for both B and D decays) have been calculated in LQCD with errors at the 10% level [14] and these are predicted to shrink still further, to the few percent level or less, in the near future. The implication is that lattice calculations of the form factors have come to be extremely important in the extraction of CKM elements from experimental measurements. Since the CKM measurements of this analysis will also utilize such calculations, it is worthwhile to give a brief overview of LQCD and how lattice techniques can be used to calculate form factors. This will be followed with a discussion of the some of the relevant parameterizations chosen for the form factors.

2.4.1 Lattice QCD

The necessity of tools such as lattice QCD is brought about by the nature of the running of the strong coupling constant. In low energy regimes ($E \sim 1$ GeV or less) the running leads to a strong coupling of order unity and perturbative methods fail. Thus for a broad spectrum hadronic physics, and in particular the heavy to light quark decays we are interested in, Fig 2.4, many of the fundamental quantities must be calculated non-perturbatively. Lattice QCD provides a method for such calculations.

To evaluate any quantity in quantum field theory it is common to formulate the relevant equations using a path integral approach. For our present purpose it will be useful to remind ourselves of how path integrals are formulated in quantum mechanics. We start with the amplitude for a particle to propagate from point x_I

⁸For $B \rightarrow \pi/K\ell\nu$ decays LCSR methods have also been used to predict form factors with errors as low as $\sim 10\%$ [15]. Very recent LCSR results for $D \rightarrow \pi/K\ell\nu$ decays also have errors at this level [16], whilst older published results have errors as large as $\sim 20\%$ or higher [17] [18].

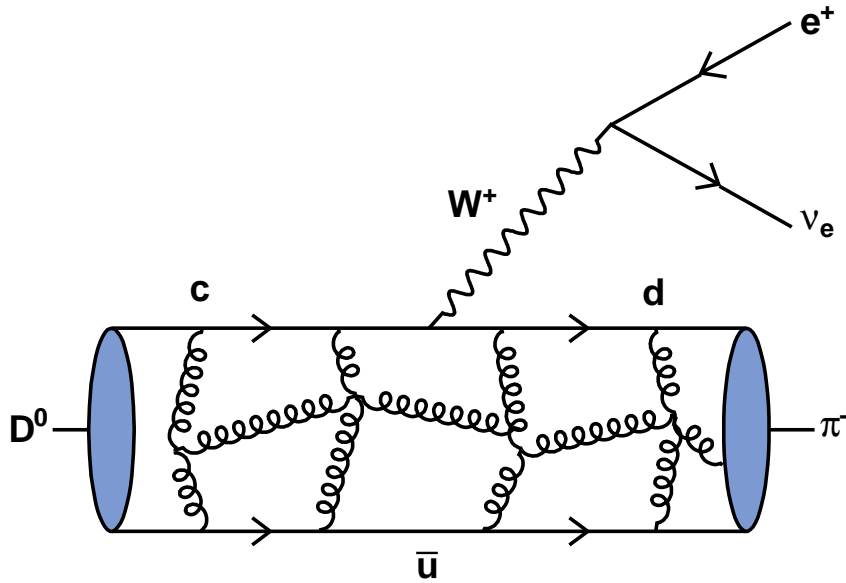


Figure 2.4: Example of a semi-leptonic D meson decay, $D^0 \rightarrow \pi^- e^+ \nu_e$. The QCD corrections are illustrated by the gluons being exchanged between the initial and final state hadrons. The leptonic vertex is easily calculated, whilst the hadronic vertex requires non-perturbative methods.

to point x_F in time T , given by

$$\langle x_F | e^{-iHT} | x_I \rangle, \quad (2.52)$$

where H is the Hamiltonian. Breaking this expression into N equal time segments δt , and using the fact that $|x\rangle$ forms a complete set of states we can write this as

$$\langle x_F | e^{-iHT} | x_I \rangle = \int dx_1 \dots dx_{N-1} \langle x_F | e^{iH\delta t} | x_{N-1} \rangle \dots \langle x_1 | e^{iH\delta t} | x_I \rangle. \quad (2.53)$$

Now consider the individual element $\langle x_{k+1} | e^{-iH\delta t} | x_k \rangle$. Each such element can be easily evaluated by Fourier transforming to momentum space. This procedure

leads to the expression

$$\langle x_{k+1} | e^{-i\delta t(\hat{p}^2/2m+V(\hat{x}))} | x_k \rangle = \left(\frac{-2\pi im}{\delta t} \right)^{\frac{1}{2}} e^{i\delta t[(m/2)((x_{k+1}-x_k)/\delta t)^2 - V(x_k)]}, \quad (2.54)$$

where we have used the standard Hamiltonian, $H = \hat{p}^2/2m + V(\hat{x})$, with potential $V(x)$ and momentum and position operators \hat{p} and \hat{x} respectively. Inserting this expression into Eq. 2.53 and taking the continuum limit $\delta t \rightarrow 0$ gives

$$\langle x_F | e^{-iHT} | x_I \rangle = \int Dx(t) e^{i\int_0^T dt [\frac{1}{2}m\dot{x}^2 - V(x)]} = \int Dx(t) e^{iS[x]}, \quad (2.55)$$

where $S[x]$ is the classical action and we have defined

$$\int Dx(t) = \lim_{N \rightarrow \infty} \left(\frac{-2\pi im}{\delta t} \right)^{\frac{N}{2}} \int dx_1 \dots dx_{N-1}. \quad (2.56)$$

This tells us something deep: the quantum mechanical amplitude, Eq. 2.52, is a sum over all possible particle paths or trajectories, $x(t)$. Moreover, this sum is weighted by the classical action so that the contributions from most paths will be largely canceled; only those paths near the extremum of the action where $\delta S = 0$, will contribute significantly. The difficulty, however, lies in the calculation of such expressions. How do we really take a sum over all possible paths?

Let us go back one step from Eq. 2.55, undoing just the fact that we have taken a continuum limit. The result is

$$\langle x_F | e^{-iHT} | x_I \rangle = C \prod_{k=1}^{N-1} \int dx_k e^{i\delta t \sum_{k=0}^{N-1} [(m/2)((x_{k+1}-x_k)/\delta t)^2 - V(x_k)]}, \quad (2.57)$$

where C is a constant. In this case we have an expression for the amplitude that is discretized in time. Importantly however, because the time steps are now discrete, the equation in this form may be solved numerically. In fact this is the key idea behind lattice QCD: to solve the exact equations of QCD numerically by discretizing the path integrals.

For the general case, where the evaluation of some excited state is required, our path integral is given by,

$$\langle 0 | \Gamma[x] | 0 \rangle = \frac{\int Dx(t) \Gamma[x] e^{-S[x]}}{\int Dx(t) e^{-S[x]}}, \quad (2.58)$$

where we have changed to a Euclidean metric, taking $t \rightarrow it$ in order that the oscillations be removed from our integrals. To calculate such an expression we first discretize as above giving,

$$\langle 0 | \Gamma[x] | 0 \rangle = \frac{\prod_k \int dx_k \Gamma[x] e^{-S_{lat}[x_k]}}{\prod_k \int dx_k e^{-S[x]}}, \quad (2.59)$$

where the paths are now given by a discrete set of points, sometimes known as a “configuration”,

$$x = \{x(t_0), x(t_1), \dots, x(t_N)\}, \quad (2.60)$$

and $S_{lat}[x_k] = \sum_{k=0}^{N-1} [(m/2)((x_{k+1} - x_k)/\delta t)^2 - V(x_k)]$ is the discrete action. The numerical evaluation proceeds by generating a large number of paths, N_p , in such a way that the probability for obtaining a particular path, $x^{(\alpha)}$ with $\alpha = 1, \dots, N_p$, is proportional to its weight,

$$P(x^{(\alpha)}) \propto e^{-S[x^{(\alpha)}]}. \quad (2.61)$$

The unweighted average of $\Gamma[x]$ over this set of paths then approximates the weighted average over the set of uniformly distributed paths. Further details on the generation of lattice paths can be found in [20].

In order to discuss the calculation of QCD quantities we must translate our simple quantum mechanical expressions into field theoretical ones. The most intuitive approach is simply to make a direct substitution, taking $x(t) \rightarrow \phi(x)$, where ϕ is the field of some given particle type and $x = (t, \vec{x})$ is now a four dimensional

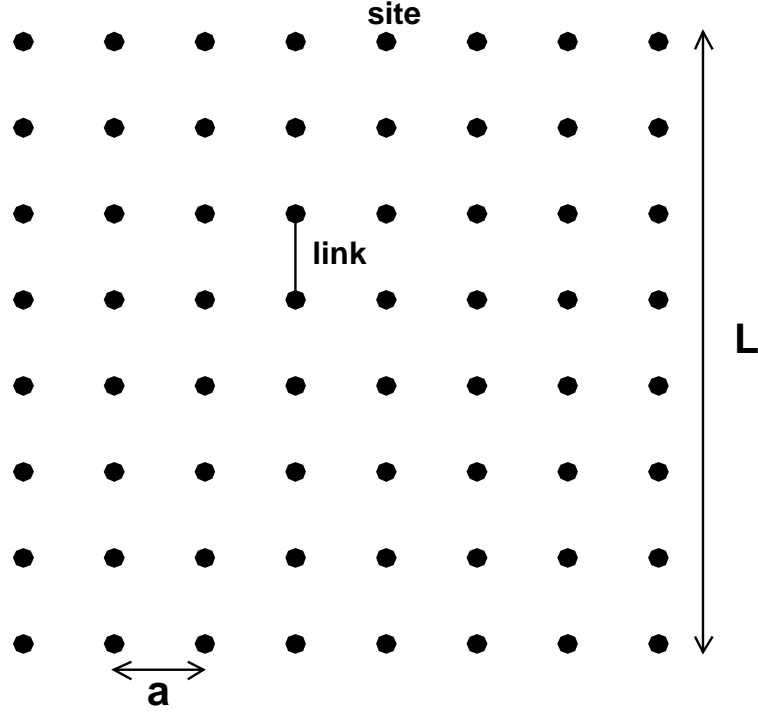


Figure 2.5: The discretization of space-time points in lattice QCD. The lattice spacing is given by a and the size of the lattice is given by L .

space-time point. The path integral in field theory is then given by

$$\langle 0 | \Gamma[\phi] | 0 \rangle = \frac{1}{Z} \int D\phi \Gamma[\phi] e^{iS[\phi]}, \quad (2.62)$$

where

$$Z = \int D\phi e^{iS[\phi]}. \quad (2.63)$$

To discretize, it is now the space-time points that become a grid, with values of the fields given at the grid points, Fig 2.5. Evaluated on the grid, the path integral

expression becomes,

$$\langle 0 | \Gamma[\phi] | 0 \rangle = \frac{1}{Z} \prod_{x_k \in \text{grid}} \int d\phi(x_k) \Gamma[\phi] e^{iS[\phi]}, \quad (2.64)$$

where the action now contains the appropriately discretized forms of the field ϕ .⁹ For example the second derivative of ϕ must be replaced by an expression wherein ϕ is evaluated only at the lattice points. For a coarse grid it is usual to make the approximation as accurate as possible. Thus a second derivative in the field, for example, would become

$$\frac{\partial^2 \phi(x_k)}{\partial x^2} = \Delta_x^{(2)} \phi(x_k) - \frac{a^2}{12} (\Delta_x^{(2)})^2 \phi(x_k) + O(a^4), \quad (2.65)$$

where

$$\Delta_x^{(2)} \equiv \frac{\phi(x+a) - 2\phi(x) + \phi(x-a)}{a^2}, \quad (2.66)$$

and a gives the lattice spacing. In general we will also need to worry about such things as putting fermions on the lattice and ensuring that gauge invariance is maintained in our discretized regime. For example, to in order to maintain gauge invariance it is necessary to express the gauge boson fields, $A_\mu(x)$, in terms of “link variables”, $U_\mu(x)$. The link variables are defined as the path integral of $A_\mu(x)$ along a “link” joining points x and $x + a\hat{\mu}$ (see Fig 2.5),

$$U_\mu(x) \equiv \mathcal{P} e^{-i \int_x^{x+a\hat{\mu}} gA \cdot dy}, \quad (2.67)$$

where \mathcal{P} is a path-ordering operator. Several nice reviews are available that cover such topics (see for example [20][21][22]), here a more general understanding is sufficient. Instead what we must now worry about is how the final results of lattice calculations will be affected by the discretization. Two factors are of vital

⁹For the calculation of semileptonic form factors $\Gamma[\phi(x)]$ will in general be the two-point and three-point correlation functions. An explanation of these functionals can be found in [23].

importance in this determination: the lattice spacing, a , and the overall size of the lattice L . We discuss each in turn.

The size of a is important in two ways. In the first place the accuracy of our derivative approximations will go as the fourth power of a . This gives accuracies of a few percent even for objects four or five lattice spacings across, so that we would expect lattice spacing about one quarter the diameter of a hadron, $\sim 0.4\text{fm}$, to suffice. However, there is another consequence of the size of a that turns out to be more limiting. In effect, because we are considering quantum mechanical objects, the lattice imposes an ultraviolet cutoff, thus gluons and quarks with wavelengths smaller than twice the lattice spacing are excluded from the theory by the lattice. To solve this problem it is usual to require that a be small enough such that for the range of momenta excluded by the cutoff perturbative techniques are valid. The effect of these states can then be mimicked with addition of some extra localized interactions and a renormalization of the discretized parameters. With sufficiently small a the required renormalization can be calculated using perturbation theory. For these calculations to be valid it has been found that lattice spacings must be less than $0.1 - 0.5\text{fm}$.¹⁰

The finite spatial extent of the entire lattice is also important. If we wish our results to be independent of this quantity we must avoid particles for which the correlation lengths are of order the size of the lattice, i.e., $1/m \sim O(L)$, where m is the particle mass. However, the lattice sizes that can be afforded are bound by the computational cost, where

$$\text{cost} \approx \left(\frac{L}{a}\right)^4 \frac{1}{m_\pi^2 a^2}. \quad (2.68)$$

¹⁰Most current calculations use a “coarse” lattice spacing of about 0.12fm , see for example [14][24].

In practice $L = 2 - 3\text{fm}$ and the light quarks u and d cannot be directly calculated with their true masses. Instead these quarks are simulated with heavier masses (as light as $m_s/8$, with m_s the mass of the strange quark, for recent calculations [14]) and the final answer is extracted using a “chiral extrapolation”. This extrapolation procedure, which uses an expansion in the quark masses from chiral perturbation theory, used to be one of the largest sources of error in the calculation of heavy to light form factors, on the order of 10 – 20%. However, one of the most significant improvements to lattice QCD in recent times, the introduction of the Kogut-Susskind or “staggered fermion” action [25][26] has dramatically reduced this error.

Staggered fermions have their spinor components split onto different lattice spacings, a technique designed to eliminate a lattice artifact known as fermion “doublers”. The doubling problem is an effect of the naive discretization of the Dirac action: for every space-time dimension on the lattice the number of fermions is doubled. Thus where we wish to simulate a single fermion 2^d fermions will appear on a lattice with d dimensions, leaving us with fifteen extra fermions in four dimensions. Staggering the fermion action reduces the doublers by a factor of four, leaving four fermion “tastes” of which three are unphysical particles. This is somewhat of a drawback for the staggered technique since the extra particles are usually removed by taking the fourth root of the four-taste fermion determinant - a technique that seems intuitive but has never been properly validated. Nevertheless, one of the great advantages of staggered fermions is that computation of the propagator is fast, greatly speeding up lattice calculations and enabling the use of much lighter u and d quark masses. Reduction in the masses of the light quarks is crucial for reducing uncertainties associated with chiral extrapolation.

The staggered fermion technique has also enabled the use of “unquenched” lattice calculations. Quenching refers to the process of ignoring the vacuum polarization contributions of the light quark loops. This approximation was commonly used because calculation of the quark loops was so computationally expensive. However, the associated errors were hard to estimate, resulting in a significant improvement in systematic errors with the use of unquenched calculations.

The overall result of these improvements is that the accuracy of lattice QCD calculations has been able to extend down to the few percent level. In several “Golden modes” agreement with experiment has also been shown at this level [27]. These calculations should therefore also be reliable for calculation of semileptonic form factors and we can test this assumption with our own results. To do so, however, we need a parameterization of the form factors to fit to our branching fractions. In fact even lattice calculations often use a specific parameterization of the form factor in order to extrapolate their measurements to the appropriate energies (see for example [14]). With this in mind we now explore some possible form factor parameterizations.

2.4.2 Functional Forms

The goal of any particular parameterization of the semileptonic form factors is to provide an accurate, and physically meaningful, expression of the strong dynamics in the decays. One possible way to achieve this goal is to express the form factors in terms of a dispersion relation. In fact this approach, the use of dispersion relations and dispersive bounds in the description of form factors, has been well established in the literature (see for example [43] and references therein). In general the dispersive representation is derived from evaluation of the two point function [43][44]

and may be written as

$$f_+(q^2) = \frac{f_+(0)}{1-\alpha} \frac{1}{1-\frac{q^2}{m_{\text{pole}}^2}} + \frac{1}{\pi} \int_{(M_D+m_P)^2}^{\infty} dt \frac{\text{Im}f_+(t)}{t-q^2}, \quad (2.69)$$

where M_D and m_P are the masses of the D meson and pseudoscalar meson respectively, while m_{pole} is the mass of the lowest lying $c\bar{q}$ vector meson, with $c \rightarrow q$ the quark transition of the semileptonic decay.¹¹ The parameter α expresses the size of the vector meson pole contribution at $f_+(0)$.

It is common to write the contribution from the continuum integral in Eq. 2.69 as a sum of effective poles:

$$f_+(q^2) = \frac{f_+(0)}{1-\alpha} \frac{1}{1-\frac{q^2}{m_{\text{pole}}^2}} + \sum_{k=1}^N \frac{\rho_k}{1-\frac{1}{\gamma_k} \frac{q^2}{m_{\text{pole}}^2}}, \quad (2.70)$$

where ρ_k and γ_k are expansion parameters. The true form factor can then be approximated to any desired degree of accuracy by keeping a given numbers of terms, or effective poles, in the expansion. A commonly conceived drawback of such an approach, however, is that the decay dynamics are not explicitly predicted. Additionally, experimental data has suggested the need for only two parameters in the description of the form factor shape. It is natural therefore, to seek simplifications of this parameterization that can still capture all the necessary physics.

One way to simplify is to remove the contribution of the effective poles entirely, keeping only the explicit vector meson pole. This scheme is referred to as “nearest pole dominance” or “vector-meson dominance” and the resulting parameterization of the form factor, known as the simple pole model, is given by

$$f^+(q^2) = \frac{f^+(0)}{\left(1-\frac{q^2}{m_{\text{pole}}^2}\right)}. \quad (2.71)$$

¹¹For the charm semileptonic decays we have $m_{\text{pole}} = M_{D^*}$ for $D \rightarrow \pi e \nu$ decays and $m_{\text{pole}} = M_{D_s^*}$ for $D \rightarrow K e \nu$ decays.

Experimental data, however, appear to disagree with the physical basis for this approximation, since measurements of the parameter m_{pole} that fit the data do not agree with the true vector meson masses, see [47] and Tables 2.1 and 2.2. Effectively, at low or medium values of q^2 the spectrum is distorted compared to the simple pole model, receiving contributions from the continuum of effective poles above the lowest lying pole mass.

Table 2.1: Experimental measurements of the $D \rightarrow K$ form factor shape parameters. Here α is the shape parameter for the modified pole model (Eq. 2.72) and m_{pole} is the pole mass of the simple pole model (Eq. 2.71). The first errors are statistical and the second systematic.

<i>Measurement</i>	<i>Shape Parameter</i>	
	α	m_{pole} GeV
E691 1989 [48]	-	$2.1_{-0.2}^{+0.4} \pm 0.2$
CLEO 1991 [49]	-	$2.0_{-0.2-0.2}^{+0.4+0.3}$
MarkIII 1991 [50]	-	$1.8_{-0.2-0.2}^{+0.5+0.3}$
CLEOII 1993 [51]	-	$2.00 \pm 0.12 \pm 0.18$
E687 1995 [52]	-	$1.87_{-0.08-0.06}^{+0.11+0.07}$
CLEOIII 2005 [55]	$0.36 \pm 0.10_{-0.07}^{+0.03}$	$1.89 \pm 0.05_{-0.02}^{+0.04}$
FOCUS 2005 [56]	$0.28 \pm 0.08 \pm 0.07$	$1.93 \pm 0.05 \pm 0.03$
Belle 2006 [57]	$0.40 \pm 0.12 \pm 0.09$	-
Babar 2006 [58]	$0.43 \pm 0.03 \pm 0.04$	$1.854 \pm 0.016 \pm 0.020$

The modified pole model, or Becirevic-Kaidelov (BK) parameterization [29], is proposed to take care of this problem. The idea is to add the first term in the effective pole expansion, while making simplifications such that the form factor can

Table 2.2: Experimental measurements of the $D \rightarrow \pi$ form factor shape parameters. Here α is the shape parameter for the modified pole model (Eq. 2.72) and m_{pole} is the pole mass of the simple pole model (Eq. 2.71). The first errors are statistical and the second systematic.

<i>Measurement</i>	<i>Shape Parameter</i>	
	α	m_{pole} GeV
CLEOIII 2005 [55]	$0.37^{+0.20}_{-0.31} \pm 0.15$	$1.86^{+0.10+0.07}_{-0.06-0.03}$
FOCUS 2005 [56]	-	$1.91^{+0.30}_{-0.15} \pm 0.07$
Belle 2006 [57]	$0.03 \pm 0.27 \pm 0.13$	-

be determined with only two parameters: the intercept $f_+(0)$ and an additional shape parameter.¹² The simplified one term expansion is usually written in the form

$$f^+(q^2) = \frac{f^+(0)}{\left(1 - \frac{q^2}{m_{pole}^2}\right)\left(1 - \alpha \frac{q^2}{m_{pole}^2}\right)}. \quad (2.72)$$

This model has been widely used in the extraction of semileptonic form factors from experimental measurements. In addition, some recent lattice QCD calculations of the form factor as a function of q^2 have relied on this model for extrapolation and interpolation purposes [14] and the results, which give the shape of the predicted spectrum, are shown in Fig 2.6. To realize such a scheme, however, it is necessary to make some physical assumptions in order that the multiple parameters initially present (Eq. 2.70) be reduced to one. In the BK ansatz it is assumed that spectator quark interactions (δ) are close to zero while scaling violations (β) are close to one,

¹²There will be three parameters if $f_-(q^2)$ or $F_0(q^2)$ is also taken into account.

a motivation that may be succinctly expressed as

$$1 + 1/\beta - \delta \equiv \frac{(M_D^2 - m_P^2)}{f_+(0)} \left. \frac{df_+}{dq^2} \right|_{q^2=0} \sim 2. \quad (2.73)$$

Once again, however, the experimental data do not bear out these assumptions, see [47] and Tables 2.1 and 2.2. We should observe $\alpha \sim 1.75$ in order to obtain $1 + 1/\beta - \delta = 2$, whereas the observed data are removed from such values by many standard deviations (σ).

It is thus apparent that while both the simple and modified pole functional forms are able to provide adequate parameterizations of the data, this can only happen if their parameters are allowed to be non-physical. Without a physical underpinning for the parameterization, however, agreement between parameters obtained by different experiments, or by theory and experiment, may not agree if the form factor sensitivity differs as a function of q^2 .

To avoid the problem of non-physical parameterizations therefore, we utilize a series expansion around $q^2 = t_0$ that has been advocated by several groups for a physical description of heavy meson form factors [43, 44, 45, 46]. The series expansion is commensurate with the dispersion relations, being guaranteed to contain the true form factor, yet still rich enough to describe all variations that affect the physical observables. Naive expansions in q^2 have problems with convergence due to the nearby poles, however, this series expansion allows convergence over the entire q^2 region. Convergence is obtained via a change in the expansion variable from q^2 to z such that the form factor is given by

$$f_+(q^2) = \frac{1}{P(q^2)\phi(q^2, t_0)} \sum_{k=0}^{\infty} a_k(t_0) [z(q^2, t_0)]^k, \quad (2.74)$$

with

$$z(q^2, t_0) = \frac{\sqrt{t_+ - q^2} - \sqrt{t_+ - t_0}}{\sqrt{t_+ - q^2} + \sqrt{t_+ - t_0}}, \quad t_{\pm} \equiv (M_D \pm m_P)^2, \quad (2.75)$$

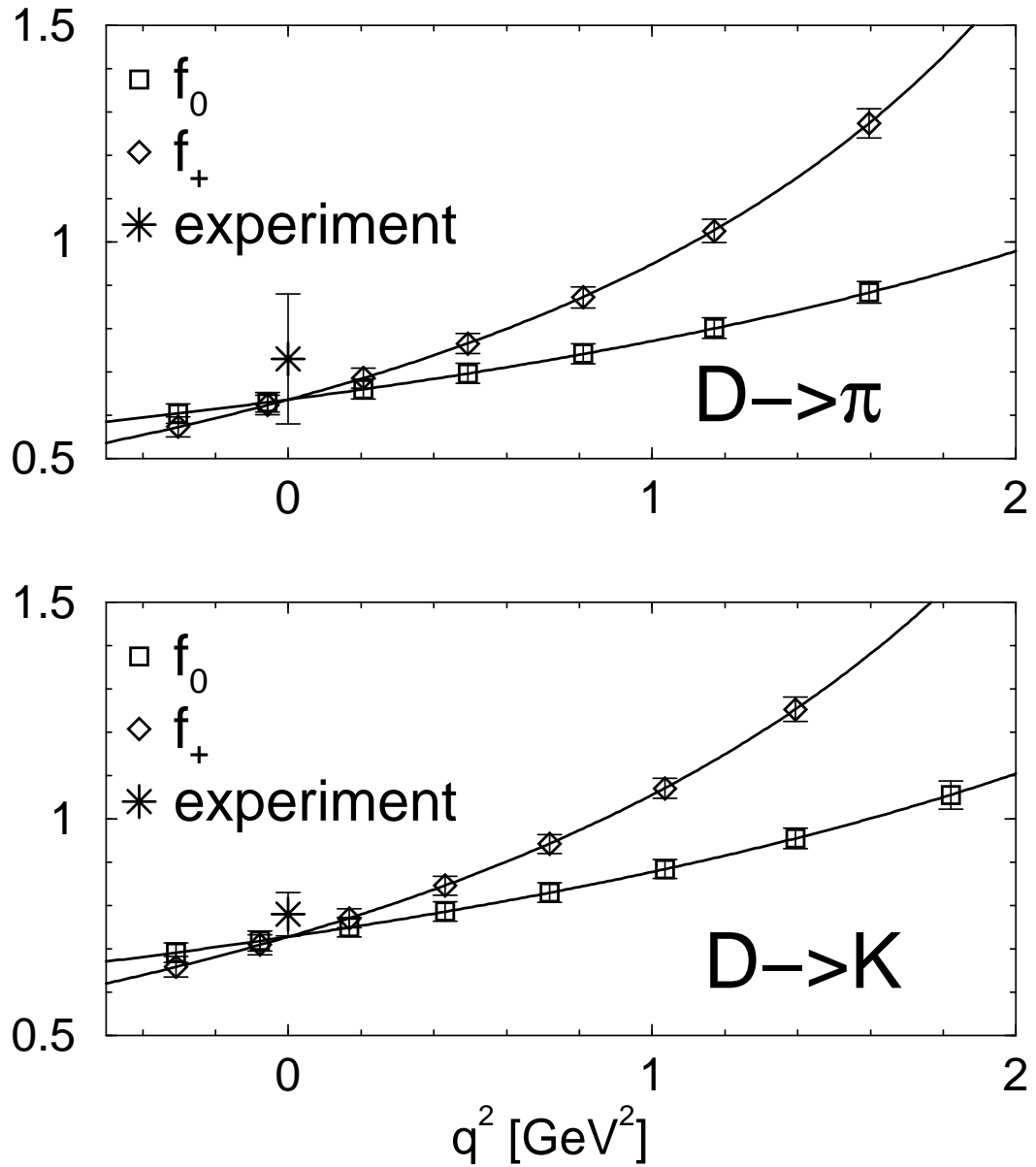


Figure 2.6: Lattice QCD calculations of the form factor as a function of q^2 for $D^0 \rightarrow \pi^- e^+ \nu$ (top) and $D^0 \rightarrow K^- e^+ \nu$ (bottom) decays. A B-K parameterization is used for the functional form [29].

and

$$P(q^2) \equiv \begin{cases} 1, & D \rightarrow \pi \\ z(q^2, M_{D_s^*}^2), & D \rightarrow K \end{cases}. \quad (2.76)$$

The physical observables do not depend on the choice of ϕ or t_0 . We choose ϕ as given in [46] and take $t_0 = 0$. Using this parameterization it is possible to obtain an unbiased comparison between lattice QCD results for the form factors and experimental results. There is also the potential to assess how many terms in the series we are sensitive to. If the series converges quickly it is likely that only the first two or three terms will be observable in the data.

In our analysis of the D semileptonic decays we examine all three of the models just described and their ability to describe our experimental results for the branching fractions. We take as our primary result the fits to the functional form described by the series expansion, which is able to give a more physically meaningful description. The simple and modified pole models are useful for comparative purposes since they have been more widely used to extract form factor results, both theoretically and experimentally. We fit our results with these models therefore, purely in order to have an easy basis for the comparison of our measurements with other experimental measurements, as well as the numbers predicted using various theoretical calculations. Before we can proceed to such exploration of the physical results of our analysis, however, we must first give a detailed description of the experimental procedure.

Chapter 3

The CLEO-c Detector

In this chapter we give an overview of the CLEO-c detector and its components.

3.1 Detector Overview

The CLEO-c detector is a multi-component device designed to detect the particles resulting from collisions of electrons and positrons in the Cornell Electron Storage Ring (CESR) at beam energies ranging from 1 – 3 GeV. The results of this analysis are based on 281 pb^{-1} of data collected at the Ψ'' resonance, $E_{beam} \sim 1.885 \text{ GeV}$. The detector is mostly cylindrical and nearly hermetic, with some sub-components having up to 93% coverage of the solid angle. A 3D cut away view of the detector and its sub-components is shown in Fig. 3.1.

3.2 Inner Stereo Drift Chamber (ZD)

The innermost section of the CLEO-c detector is the ZD, a small, six layer drift chamber (with an outer radius of less than 15 cm) that surrounds the beam pipe. All six layers of the ZD are wired with a stereo angle between 10.3° and 15.4° , so that it provides both z and $r - \phi$ information for charged particles close to the beam pipe. The ZD works in a similar manner to the stereo sections of its outer neighbor, the DR, whose function is described in detail in the next section.

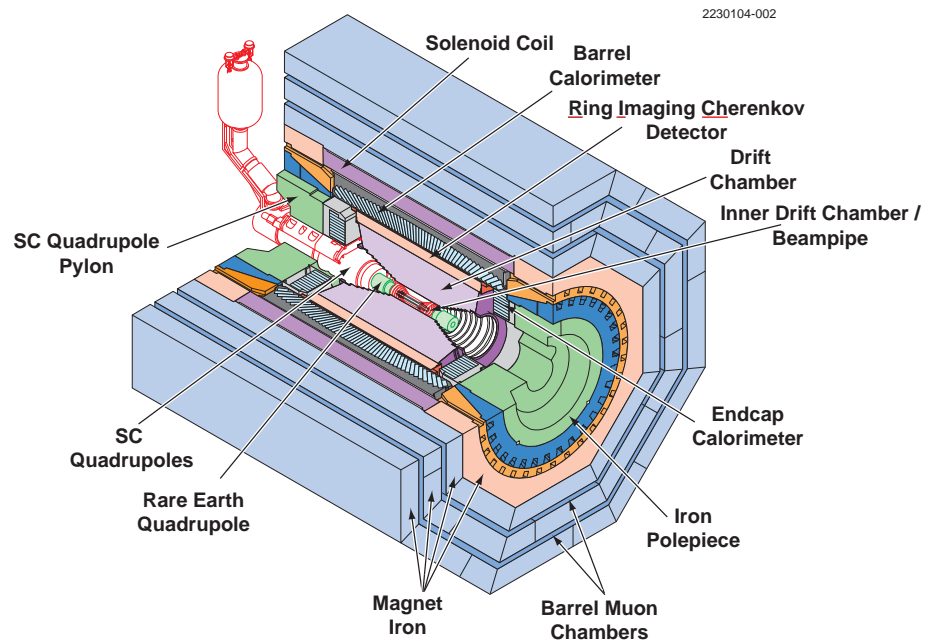


Figure 3.1: The CLEO-c Detector.

3.3 Drift Chamber (DR)

The main drift chamber surrounds the beam pipe and the ZD. It consists of forty-seven layers of cells, where a cell is a sense wire surrounded by field wires. The sense wires are held at a large positive voltage relative to the field wires and the DR is filled with a helium-propane gas mixture which is ionized by charged particles as they travel through it. The electric field resulting from the potential difference between the voltage and sense wires attracts electrons from the ionized atoms. As the electrons near the sense wires the electric field gets very large and supplies them with enough energy to ionize more atoms. The electrons from these atoms ionize further atoms and particles avalanche towards the sense wire.

When the avalanche of electrons arrives at the sense wire it is detected as a

pulse. From the arrival time of the pulse the distance of closest approach of the charged particle to the wire can be calculated. This is achieved by determining the speed with which the electrons drift through the different regions of the DR cell (sometimes called a drift cell) and combining this information with the precisely known timing of the bunch trains through the storage ring. As the particle passes through the many layers of the DR its distance of closest approach in each cell that it “hits” gives information about its $r - \phi$ trajectory. To contribute information about the z trajectory of the particle, thirty-one of the forty-seven DR layers are arranged in groups of four layers with alternating negative and positive stereo angles. The stereo angle is created by giving the wires in these layers a “twist”: unlike the wires in the axial layers, they are not strung parallel to the beam axis, but instead have different ϕ coordinates at either end. Additional z information is provided by cathode strips surrounding the drift chamber.

The DR provides the information about the trajectory of a charged particle, its momentum and the energy it loses per meter, its dE/dx , which can help identify the particle type. The track momentum resolution at CLEO-c is 0.6% at 800 MeV.

3.4 RICH

Outside the DR is a Rich Imaging Cherenkov (RICH) detector that provides additional particle species identification. When particles travel faster than the speed of light in a medium they create a cone of coherent light called Cherenkov radiation. The half angle between the cone and the particle’s trajectory, θ_C , is given by the expression,

$$\cos \theta_C = \frac{1}{n\beta}, \quad (3.1)$$

where n is the refractive index of the medium and $\beta = v/c$ is the velocity of the particle as a fraction of the speed of light. Measuring this angle gives the velocity of the particle. If its momentum is also known (i.e., from DR measurement) then the mass of the particle and hence the type of particle can be determined.

The CLEO-c RICH is made up of a plane of LiF radiators at a radius of 82 cm, surrounded by a nitrogen expansion volume to let the Cherenkov photons spread out. The ring of photons is detected using a triethylamine gas (TEA), which is photosensitive. The geometry of a RICH cell is depicted in Fig.3.2. For

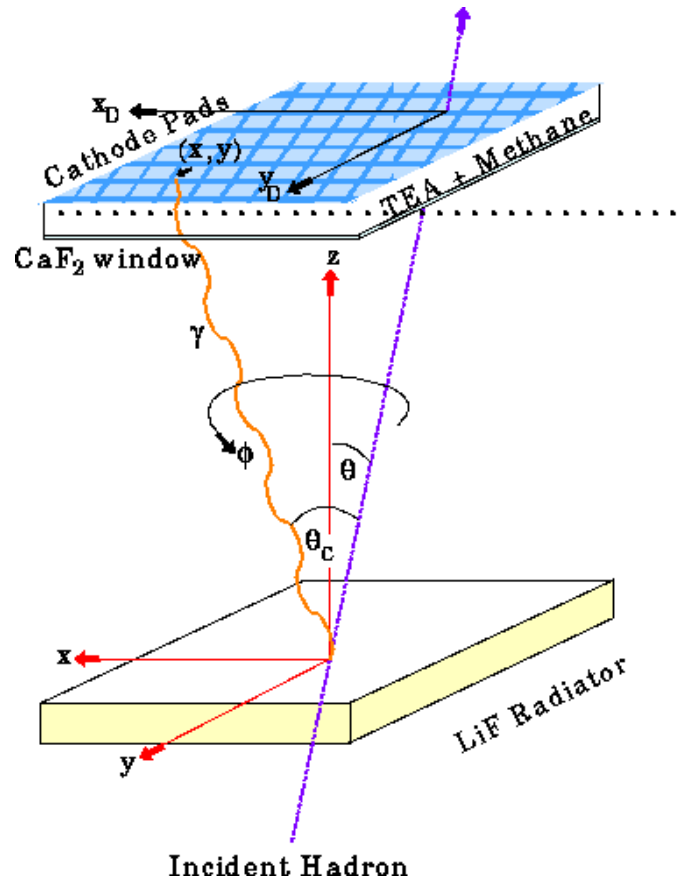


Figure 3.2: The CLEO-c RICH Detector schematic.

each charged particle found in the DR, the trajectory is projected out to the LiF

radiators and an expected Cherenkov angle calculated for each particle hypothesis (e.g., π , K , etc ...). All photons within $\pm 5\sigma$ of the expected angle are used to calculate a likelihood for the hypothesis. The likelihood depends upon the angles of the photons and the total photon yield. For CLEO-c analyses, likelihood differences are used to indicate the best particle hypothesis for a track.

3.5 Crystal Calorimeter

Outside of the RICH is the crystal calorimeter (CC) configured with a barrel section that surrounds the entire drift chamber and two end caps at either end of the detector. The CC consists of 7784 CsI crystals doped with thallium. Each crystal is 30 cm long and 5 cm \times 5 cm on a face. At the end caps, the crystals are parallel to the beam pipe whilst outside the RICH they are shaped to point at the interaction region, with some small adjustments to minimize photon loss through gaps.

Particles passing through the crystals interact in the material and lose energy, which is released in a shower of daughter particles. These daughters excite the atoms in the crystal, which release photons as they de-excite. The photons are detected at the back of the crystal where they are collected in photodiodes. Particles will typically deposit energy in more than one crystal and these energies are added together to give the total energy of the particle. Neutral particles are distinguished from charged particles by the fact that they are not matched to tracks coming from the DR. Additionally photon showers may be distinguished from other particles by the shape of the shower. The typical π^0 resolution achieved with the CC is about 6 MeV.

3.6 Muon Detector

The Muon detector is the last element in the CLEO-c detector. This detector is situated outside of the solenoidal coils that provide the magnetic field for the DR. Particle detectors are interspersed between the layers of iron that serve as the flux return for the magnet. Muons are the only particles that can penetrate deeply into the layers of iron and thus may be identified according to the depth that is penetrated by a detected particle.

Chapter 4

Analysis Method

In this chapter the data and monte carlo samples used for the analysis are detailed.

In addition, we describe the method used to reconstruct the neutrino and the signal D decay candidates.

4.1 Analysis Method Overview

To reconstruct the semileptonic decay modes of interest for this analysis namely, $D^0 \rightarrow \pi^- e^+ \nu$, $D^0 \rightarrow K^- e^+ \nu$, $D^+ \rightarrow \pi^0 e^+ \nu$ and, $D^+ \rightarrow \bar{K}^0 e^+ \nu$, it is first necessary to have some means of reconstructing the four-momentum of the neutrino. Neutrinos, neutral particles that are almost massless, long lived and only weakly interacting, are notoriously difficult to reconstruct due to the fact that they do not interact in the detector. As a result their presence can only be inferred by the occurrence of events with missing energy and momentum corresponding to a massless particle. At CLEO-c there are two main approaches to obtaining the neutrino four-momentum and reconstructing semileptonic decays.

In the first method, a hadronically decaying D is reconstructed on one side of the event and the semileptonic decay is reconstructed opposite this D “tag”. The known momentum of the tagging D can be used to estimate the momentum of the semileptonic D , which is not measured due to the undetected neutrino. The remaining tracks and showers in the event (e.g. from K^- and e^+ or π^- and e^+ , etc.) can be then used to reconstruct the semileptonic decay. This method has been used to measure semileptonic branching fractions with the first 56 pb^{-1} of

CLEO-c data [59, 60], and preliminary results are available for an updated analysis with 281 pb^{-1} of data [61].

At CLEO-c however, the excellent hermeticity and resolution of the detector allow us to use an alternate “neutrino reconstruction” approach, wherein the neutrino is associated with the missing energy and momentum of the entire event. In the neutrino reconstruction approach, which we use for this analysis, there is no need for a D tag: the total reconstructed charged and neutral energies are summed and used in combination with the known beam four-momentum to give the missing event four-momentum. Standard full-reconstruction techniques can then be employed to combine the missing four-momentum with other daughter candidates (e.g. K^- and e^+ or π^- and e^+) to give the reconstructed semileptonic D decay.

The advantage of this method is that we are not restricted to events in which a D tag can be reconstructed, and can thus gain higher statistics for each mode. On the other hand, there will also be more background and the resolution will be poorer in comparison to a tagged analysis. Indeed, one of the key elements in doing a precision measurement utilizing the neutrino reconstruction approach is correct modeling of the backgrounds (discussed further in Chapter 6). The dominant background contribution is from signal mode cross-feed, however, there are also important background contributions from events with fake electrons, non-charm continuum production ($e^+e^- \rightarrow q\bar{q}$, $e^+e^- \rightarrow \tau^+\tau^-$ and $e^+e^- \rightarrow \gamma\psi(2S)$), and $D\bar{D}$ processes other than signal.

In the sections below we discuss the data and Monte Carlo (MC) samples used in this analysis as well as the details of reconstructing semileptonic decays using the neutrino reconstruction method.

4.2 Data and MC Samples

The analysis presented here is based on 281 pb^{-1} of CLEO-c data taken at the $\psi(3770)$ resonance. Luminosities are calculated using the run by run luminosity with an appropriate scale factor, as given in [28].

The analysis uses ten different MC samples, four of which are signal samples and six of which are background. The four signal samples, $D^0 \rightarrow \pi^- e^+ \nu$, $D^0 \rightarrow K^- e^+ \nu$, $D^+ \rightarrow \pi^0 e^+ \nu$, $D^+ \rightarrow K_S(\pi^+ \pi^-) e^+ \nu$ and two related background samples $D^+ \rightarrow K_S(\pi^0 \pi^0) e^+ \nu$ and $D^+ \rightarrow K_L e^+ \nu$, consist of $\psi(3770) \rightarrow D\bar{D}$ events, where one D always decays in the required semileptonic mode and the other D decays generically. The semileptonic modes in these samples are decayed using a BK parameterization [29] for the form factors, with parameters provided by the latest FNAL lattice predictions for $D \rightarrow K$ and $D \rightarrow \pi$ [14]. For the generically decaying D meson, semileptonic form factors are calculated according to the ISGW2 model [30]. Each sample has statistics corresponding to approximately $20 \times \mathcal{L}_{\text{data}}$, where $\mathcal{L}_{\text{data}}$ is the data luminosity.

The four remaining background samples consist of generic (non-signal) $D\bar{D}$, continuum, radiative returns from the $\psi(2S)$ and τ pair production. The $D\bar{D}$ background MC, a sample of approximately $40 \times \mathcal{L}_{\text{data}}$, consists of generic $\psi(3770) \rightarrow D\bar{D}$ MC with events containing any of the six semileptonic modes discussed above removed. The non- $D\bar{D}$ background samples are generated to approximately $5 \times \mathcal{L}_{\text{data}}$. It should also be briefly noted that any resonant $D\bar{D}$ production is removed from the continuum MC. This is consistent with the method used to measure the $D\bar{D}$ cross section at the $\psi(3770)$ [31].

4.3 Event Reconstruction

In this section we describe the general algorithm applied to the reconstruction of exclusive semileptonic decays without the use of a D tag. As we have already stated, the most important aspect in finding the semileptonic decay is the reconstruction of the neutrino which, as it cannot be detected, appears only as missing four-momentum. The entire event must be carefully analyzed in order to find the missing particle. Below we describe this procedure, as well as the subsequent reconstruction of the semileptonic decay, in detail.

4.3.1 Neutrino Reconstruction

The missing four-momentum of an event is given by

$$P_{\text{miss}} = P_{\text{event}} - P_{\text{visible}}, \quad (4.1)$$

where P_{visible} is the total event four-momentum visible to the detector as either charged or neutral particles, i.e.,

$$P_{\text{visible}} = \sum P_{\text{charged}} + \sum P_{\text{neutral}}. \quad (4.2)$$

The event four-momentum may be written simply as a combination of the known quantities, beam energy, E_{beam} , and crossing angle, α ,

$$P_{\text{event}} = (2E_{\text{beam}}, -2E_{\text{beam}} \sin \alpha, 0, 0). \quad (4.3)$$

Calculation of the visible four-momentum, however, is not quite so simple. Naively this quantity is given by the sum of the four-momenta from tracks left by charged particles and showers left by neutral particles. The overwhelming problem we are faced with in the case of both neutral and charged particle addition, however, is that of double counting.

In the case of tracks, double counting may be caused in three main ways. In the first place, any charged particle with low enough transverse momentum can complete one or more full revolutions of its helix before exiting the drift chamber. Known as “curlers” such particles often cause more than one outgoing track to be reconstructed, whereas we require only a single four-momentum measurement (preferably the best available) for each particle in our charged four-momentum sum. Secondly, the charged particle can decay, undergo material interactions, or hard scatter inside the drift chamber, causing the initial track to terminate and one or more new tracks to begin. For calculation of the true visible energy only the initial track is needed. Finally, noise hits in the drift chamber can cause the reconstruction of spurious tracks. Thus in order to calculate the visible charged four-momentum, we must choose the correct set of tracks by removing the back halves of curlers, extra tracks from decaying particles and noise tracks. Furthermore, we must do this while retaining a high efficiency for measuring every charged particle, since loss of particles is as detrimental as double counting. A specialist software package known as Trkman [32] provides the best estimate of this correct set of tracks. In addition to the correct set of tracks for calculating the visible charged four-momentum, Trkman also provides a second set of tracks to be used for track-shower matching. This second set, which will usually differ from the first, excludes any tracks that terminate within the drift chamber and includes any decay or scatter products that may reach the calorimeter.

One final item to be considered in the charged particle four-momenta summation is the particle identification assigned to each track. The particle identification is important since the mass hypothesis of a track will change the calculated four-momentum. The energy calculation depends directly on the mass, but the momen-

tum is also affected because the energy loss corrections used in the Kalman fitting technique (see for example [33]) are mass dependent. To get the best estimate of the neutrino four-momentum therefore, it is necessary to assign each charged particle its most likely mass hypothesis.

We assign the mass hypotheses by first identifying any electrons in the event (see below) and assigning the associated tracks an electron hypothesis. The remaining tracks consist of hadrons (with the exception of muons, which cannot be distinguished from pions in CLEO-c) for which we must choose either a kaon or pion hypothesis. For every hadronic track we calculate a probability for each mass hypothesis based on the available particle identification information. If only dE/dx is available the probability for each hypothesis is simply calculated using the number of standard deviations that the track lies from the mean for that hypothesis. If both dE/dx and RICH are available pions and kaons are separated by combining χ^2 values from both sources, and probabilities are extracted from the cumulative χ^2 distribution with two degrees of freedom.

The probabilities calculated in this manner are then weighted by the relative abundances for each type of particle (as determined from generic $D\bar{D}$ MC). The importance of this weighting is demonstrated in Fig. 4.1, which shows the relative abundance of pions and kaons as a function of momentum, along with the total kaon fraction as a function of momentum. Overall about four times more pions than kaons are produced in $D\bar{D}$ events, thus even if the raw probabilities from particle identification show that a track is equally likely to be a pion or a kaon, there is still a greater probability that it is a pion. Weighting the raw probability by the species abundance as a function of momentum reflects this.¹ Finally, using the

¹The weighting is done by calculating the kaon production probability as a function of momentum. This function is found by fitting a polynomial to the

production weighted probability, each track is assigned its most likely hypothesis. With this technique we correctly identify 99.8% of pion tracks and 94.7% of kaon tracks. Incorrectly identified kaon tracks are identified as pions 97.1% of the time.

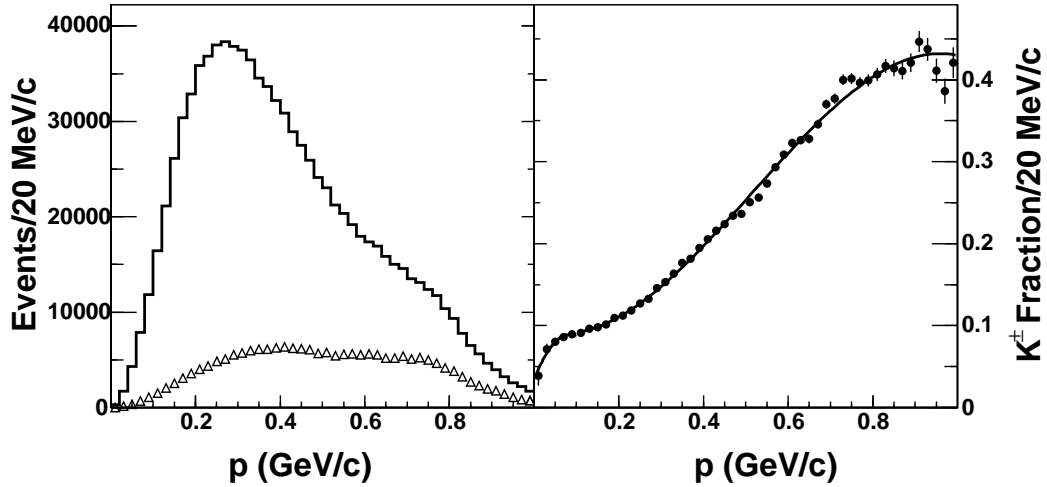


Figure 4.1: Charged pion and kaon abundances from $D\bar{D}$ MC. The left hand plot shows the overall charged hadron momentum spectrum (black line) as well as the charged kaon momentum spectrum (open triangles). On the right is shown the fraction of charged hadrons composed of kaons as a function of momentum. The black line in this plot shows the fit function used for the kaon probability weighting.

For neutral particles the visible energy can appear only as showers in the crystal calorimeter. However, of the neutral particles only photons will reliably leave an appreciable fraction of their energy in the crystal calorimeter. Other particles, such as K_L 's or neutrons, will shower only partially and only some of the time, whilst neutrinos leave no trace at all. For this reason neutral particles other than photons

fraction of charged hadrons comprised of kaons as a function of track momentum, Fig 4.1. In $D\bar{D}$ events the charged hadron spectrum is composed only of pions and kaons, the pion probability therefore is simply one minus the kaon probability.

can be problematic for neutrino reconstruction, tending to degrade association of the neutrino four-momentum with the event missing four-momentum (i.e., since these particles will also have contributed to the total missing four-momentum). A variety of cuts are implemented to try and remove such events from our samples, see Chapter 5.

The remaining problem for the neutral energy sum therefore, is to separate photon showers from those caused by charged particles. As an initial approximation this can be achieved by excluding all showers that have been proximity matched to tracks. Track shower matching is performed by projecting tracks into the calorimeter. Any showers occurring within a certain (small) distance of the projection are considered to be “matched” to the track. In addition, for neutrino reconstruction we determined the best set of tracks to be used for shower matching using Trkman information (see above). In this manner true photon showers are rarely vetoed through track matching. Of the remaining “unmatched” showers, however, a significant fraction will be caused by daughter particles produced in the hadronic showers. Such showers, known as hadronic splitoffs, need not be in close proximity to the hadronic track causing the initial shower and will thus often be unmatched. To remove as many of these showers as possible, without throwing away too many real photon showers, we use a package called Splitoff. Splitoff utilizes that fact that the energy in the 3×3 array of crystals from a hadronic splitoff will usually point back towards the parent hadronic shower (which is matched to a track), whilst photon showers have no preferred direction. A neural net that takes into account the shower’s shape, energy and proximity to any Trkman shower matching approved tracks, is used to perform this task. Only showers approved by Splitoff are used for neutrino reconstruction.

The resulting energy and momentum resolutions for neutrinos reconstructed in this manner are shown in Figs. 4.2 - 4.5. For all modes the one sigma resolution in the peak region of the missing momentum is about 10 MeV/ c , while in the missing energy it roughly twice as large, at about 20 MeV.

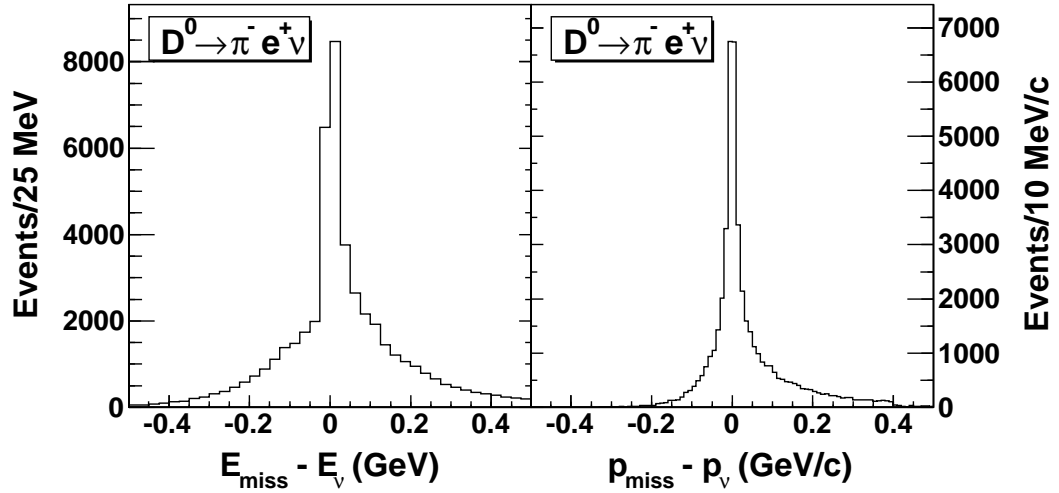


Figure 4.2: Neutrino resolution in signal $D^0 \rightarrow \pi^- e^+ \nu$ MC for events with zero net charge.

4.3.2 The D Meson

Once the missing four-momentum of the event has been found we may search for possible signal candidates. A signal candidate is formed by combining a signal electron track and signal hadron² with the missing four-momentum, or neutrino. The quality of the resulting D meson is determined based on how well the total energy and total three-momentum of the event have been reconstructed. The D energy is compared to the beam energy, and the momentum constraint is recast as a “beam-constrained” mass $M_{\text{bc}} = \sqrt{E_{\text{beam}}^2 - \vec{p}^2}$, which should reconstruct at the

²Criteria for signal electrons and hadrons will be outlined in section 5.

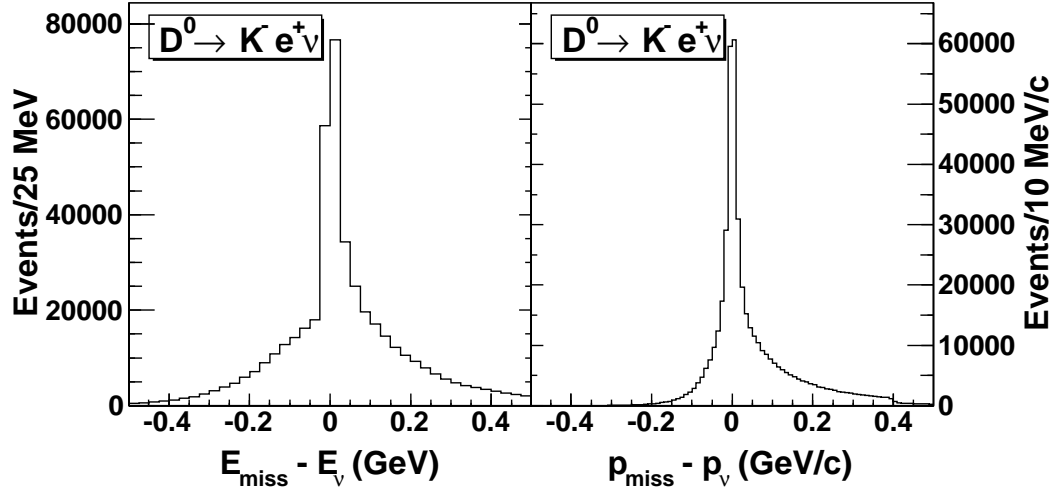


Figure 4.3: Neutrino resolution in signal $D^0 \rightarrow K^- e^+ \nu$ MC for events with zero net charge.

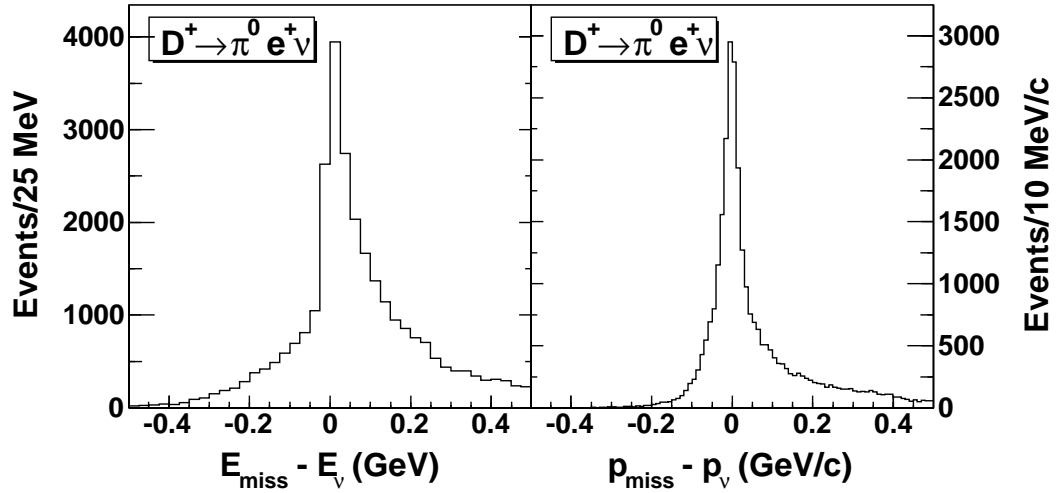


Figure 4.4: Neutrino resolution in signal $D^+ \rightarrow \pi^0 e^+ \nu$ MC for events with zero net charge.

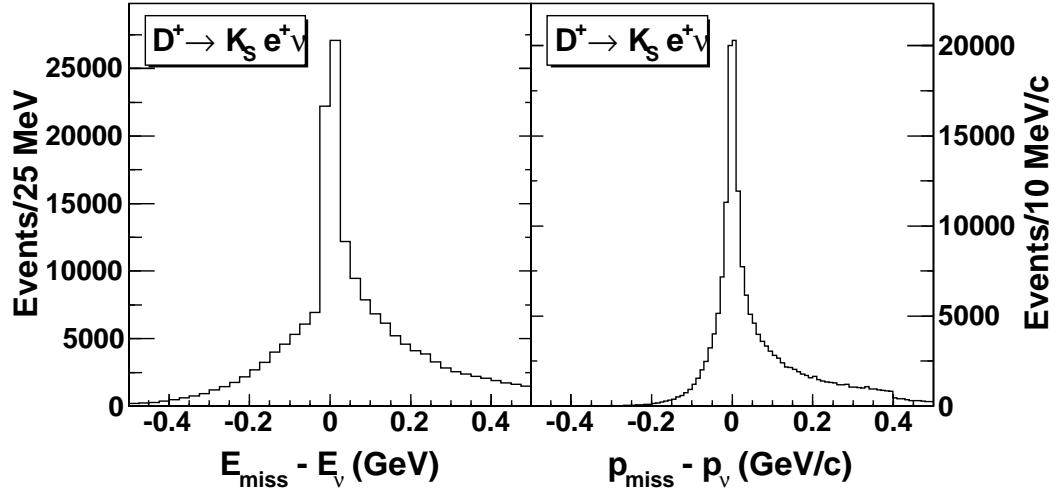


Figure 4.5: Neutrino resolution in signal $D^+ \rightarrow K_S(\pi^+\pi^-)e^+\nu$ MC for events with zero net charge.

mass M_D , of the D meson.

For D mesons produced at CLEO-c via the decay chain $e^+e^- \rightarrow \psi'' \rightarrow D\bar{D}$, the error in the measured D energy is known since the true energy is given by the beam energy, E_{beam} . We define

$$\Delta E = E_D - E_{\text{beam}}. \quad (4.4)$$

Since, as can be seen in Figs. 4.2 to 4.5, the resolution of the missing momentum is far superior to the resolution of the missing energy, we may improve the ΔE resolution by replacing the missing energy with the magnitude of the missing momentum, i.e.,

$$P_{\text{miss}} = (|\vec{p}_{\text{miss}}|, \vec{p}_{\text{miss}}), \quad (4.5)$$

so that,

$$E_D = E_e + E_{\text{hadron}} + |\vec{p}_{\text{miss}}|. \quad (4.6)$$

To calculate the best M_{bc} we use the fact that the resolution of ΔE is dominated

by the resolution of $|\vec{p}_{\text{miss}}|$; the implication being that we can further improve the missing four-momentum by scaling it such that $\Delta E = 0$. That is,

$$P_{\text{miss}} \rightarrow P'_{\text{miss}} \equiv \beta P_{\text{miss}} = \beta(|\vec{p}_{\text{miss}}|, \vec{p}_{\text{miss}}), \quad (4.7)$$

where β is given by

$$\Delta E = E_e + E_{\text{hadron}} + \beta|\vec{p}_{\text{miss}}| - E_{\text{beam}} = 0. \quad (4.8)$$

The beam constrained mass is then calculated as

$$M_{\text{bc}} = \sqrt{E_{\text{beam}}^2 - \vec{p}_{\text{D}}^2} \quad (4.9)$$

with

$$\vec{p}_{\text{D}} = \vec{p}_e + \vec{p}_{\text{hadron}} + \beta\vec{p}_{\text{miss}}. \quad (4.10)$$

It should also be noted that the beam constrained mass M_{bc} , is calculated in the center of mass rest frame in order to account for the crossing angle α , as introduced in Eq. 4.3. For CLEO-c the crossing angle is very small, $\sim 10^{-3}$ radians, so that this correction is not necessary in the calculation of ΔE , where the resolution is much poorer.

Finally for each signal decay candidate we also calculate q^2 , the invariant mass of the virtual W boson (see Fig. 2.3) given by

$$q^2 = (P_e + P'_{\text{miss}})^2. \quad (4.11)$$

In addition to scaling the neutrino momentum as described above, for calculation of q^2 the missing momentum is rotated through the smallest angle consistent with forcing $M_{\text{bc}} = M_D$. The resulting q^2 resolutions for each mode, and for each q^2 bin used in the fit, are shown in Figs. 4.6 - 4.9. The overall widths (as $\sigma =$

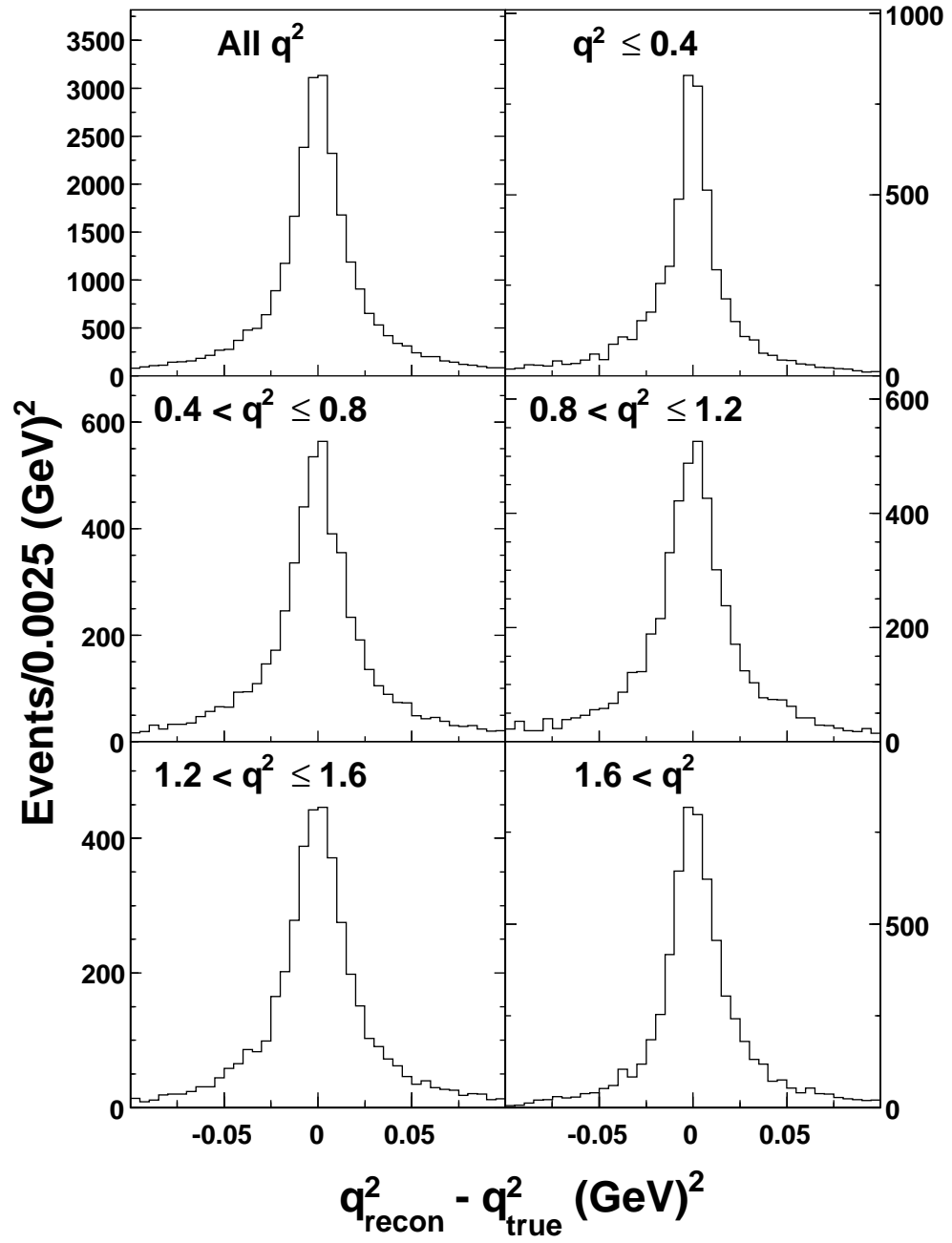


Figure 4.6: Resolution of $q^2_{\text{recon}} - q^2_{\text{true}}$ from signal $D^0 \rightarrow \pi^- e^+ \nu$ MC.

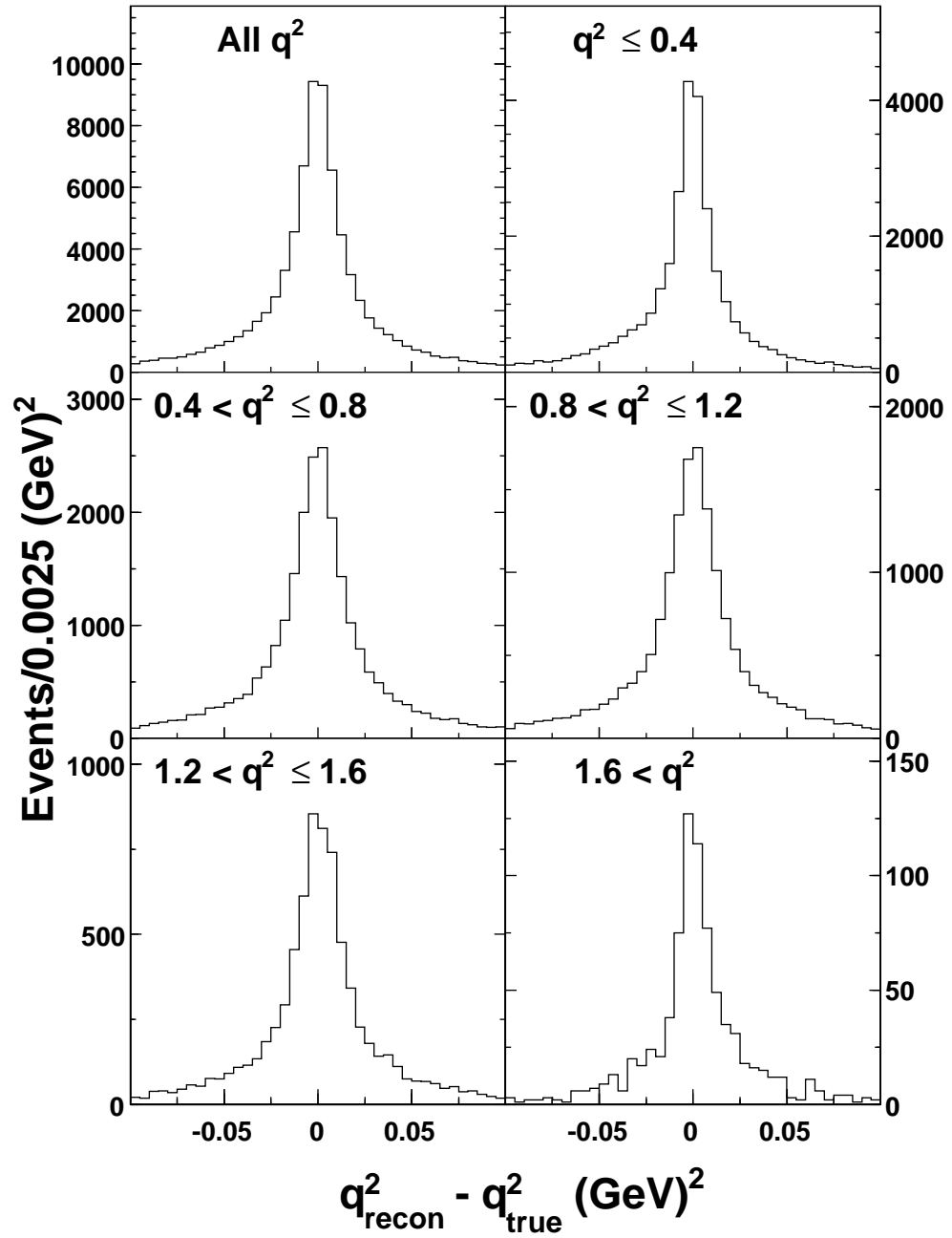


Figure 4.7: Resolution of $q^2_{\text{recon}} - q^2_{\text{true}}$ from signal $D^0 \rightarrow K^- e^+ \nu$ MC.

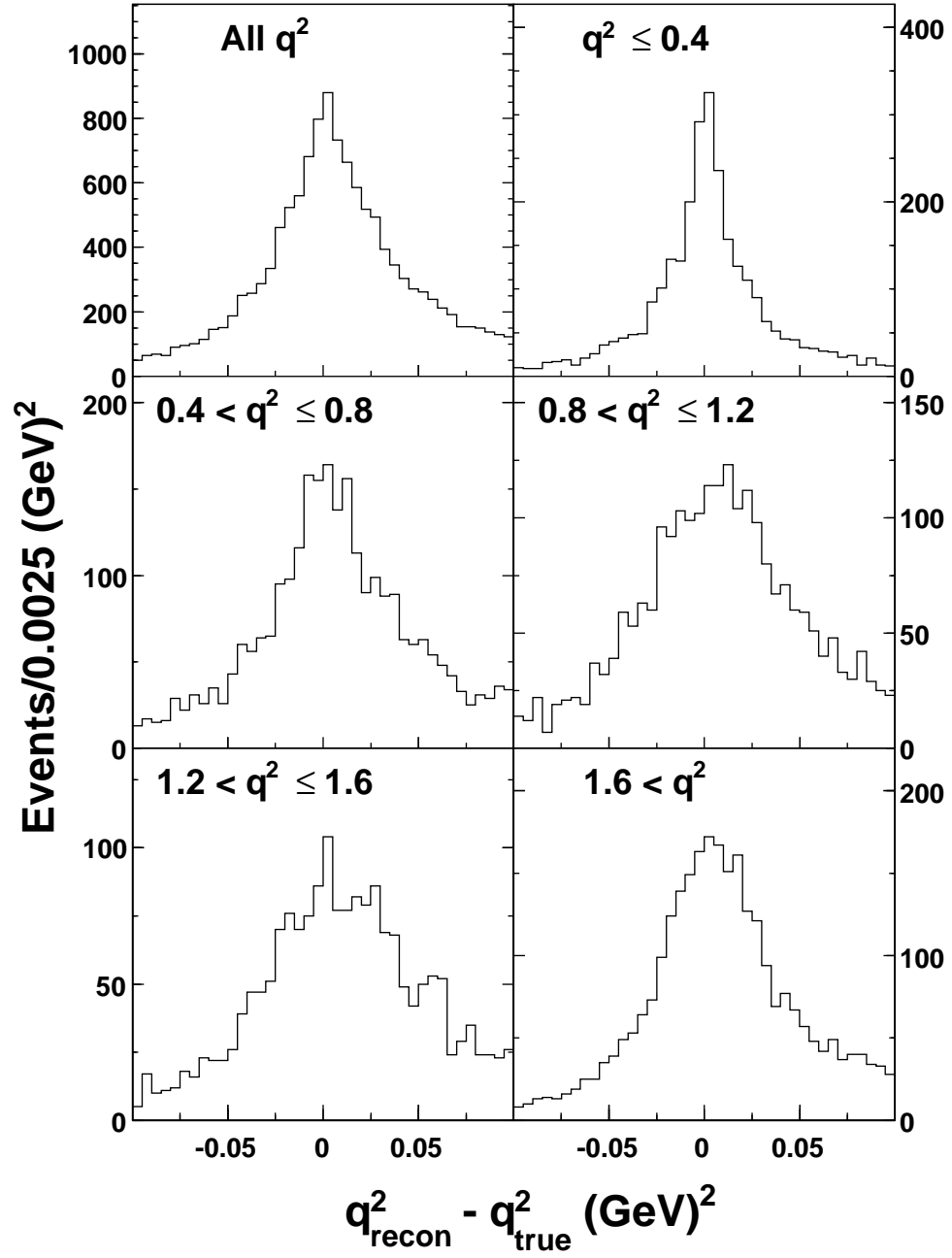


Figure 4.8: Resolution of $q^2_{\text{recon}} - q^2_{\text{true}}$ from signal $D^+ \rightarrow \pi^0 e^+ \nu$ MC.

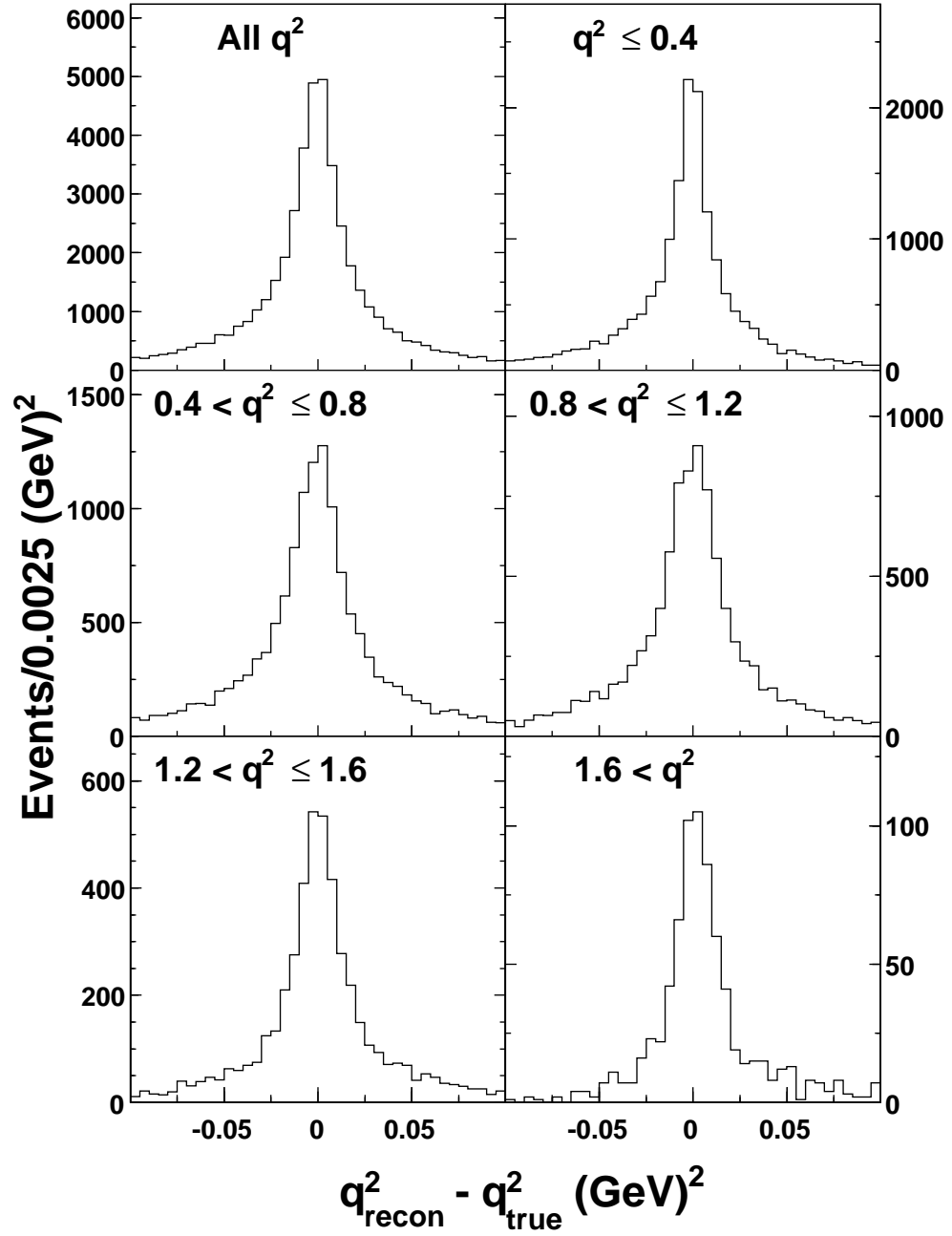


Figure 4.9: Resolution of $q^2_{\text{recon}} - q^2_{\text{true}}$ from signal $D^+ \rightarrow K_S(\pi^+\pi^-)e^+\nu$ MC.

FWHM/ $(2\sqrt{2\ln 2})$) of the q^2 resolutions for each mode are: $\sigma_{\pi^-e^+\nu_e} = 0.013 \text{ GeV}^2$, $\sigma_{K^-e^+\nu_e} = 0.008 \text{ GeV}^2$, $\sigma_{\pi^0e^+\nu_e} = 0.021 \text{ GeV}^2$ and $\sigma_{K_S^0e^+\nu_e} = 0.011 \text{ GeV}^2$.

One last important step in the reconstruction of the D semileptonic decay is the recovery of Final State Radiation (FSR). FSR can occur through either radiation of the electron, a charged hadron daughter or charged hadron parent, and results in an additional photon in the final state, e.g., $D^0 \rightarrow \pi^-e^+\nu\gamma$. The electron is the most likely particle to radiate, so we focus our efforts there. We take the Splitoff approved photons and any Bremsstrahlung candidate showers³ and from this list any showers within a $\sim 3.5^\circ$ cone around the electron track are added to the electron four-momentum. In addition, if the shower was not previously used in the calculation of the missing four-momentum it is now added. In this manner we recover approximately 53% of all reconstructed FSR showers and about 97% of those within the angular cut. Just over 86% of the showers added are from either true FSR or true Bremsstrahlung photons. FSR recovery gives a small efficiency improvement for each of the signal decays modes (order 0.5% or less) and, in reducing our sensitivity to the presence of FSR, also helps reduce the associated systematic error.

³These are defined to be all showers within 100 mrad of a track's projection into the calorimeter.

Chapter 5

Event Selection

Selecting exclusive semileptonic events requires a number of event cuts designed to remove background while retaining signal events. There is also some work in identifying the signal electron and hadrons with the same goals in mind. In this section we outline the particle identification criteria as well as the overall requirements for event selection.

5.1 Particle Identification

In this section we describe our identification criteria for signal electrons and hadrons. The goal in identifying these particles is to find the optimal balance between good efficiency and rejection of fakes. The balance that is considered “optimal” differs between the various particle types, depending on the dominant sources of fakes and whether or not they are significant.

5.1.1 Electron Identification

Electron identification occurs differently for data and MC, a procedure designed to avoid using fake electron distributions from MC. In both cases, however, electron candidate tracks are required to satisfy the following basic track quality criteria:

- Track is Trkman approved.
- Track was fit to an electron hypothesis and the fit did not abort.
- Track momentum $> 0.200 \text{ GeV}/c$.

- $|\cos\theta| < 0.9$.

In data electron tracks are identified using the Rochester Electron Identification package (REId). This package combines assorted information about the track (dE/dx , RICH, E/p , etc.) and its matched shower to form an electron likelihood, F , where $0 \leq F \leq 1$ with $F = 0$ indicating a track least likely to be an electron and $F = 1$ indicating a track most likely to be an electron. The resulting F distributions for electrons, as compared to pions, kaons and muons, are shown in Fig 5.1. Those tracks passing the above quality criteria and having $F > 0.8$ are considered to be electrons. Electron candidates are identified with momenta (p_e) above 200 MeV/ c and over 90% of the solid angle. The identification efficiency (measured in data) above $p_e = 300$ MeV/ c is greater than 90% and above $p_e = 500$ MeV/ c is greater than 96%; the probability that a hadron is misidentified as an electron is less than 0.8%. Below $p_e = 300$ MeV/ c the efficiency falls rapidly, reaching 60% in the $p_e = 200 - 250$ MeV/ c region.

In MC only true electrons are selected. We loop through the decay tree for each event and identify true electrons that are matched to tracks passing the above quality criteria. Electron candidates are selected at random from this sample, with a selection rate based on the data measured efficiencies outlined in brief above. In fact the efficiencies are measured in 50 MeV/ c momentum bins from 200 MeV/ c to 1400 MeV/ c .

5.1.2 Signal π^\pm Identification

The signal charged pion selection criteria are chosen to maximize pion efficiency whilst removing as many charged kaon and $K_S \rightarrow \pi^+\pi^-$ daughter candidates as possible. In particular, it is important to remove charged kaons that fake signal

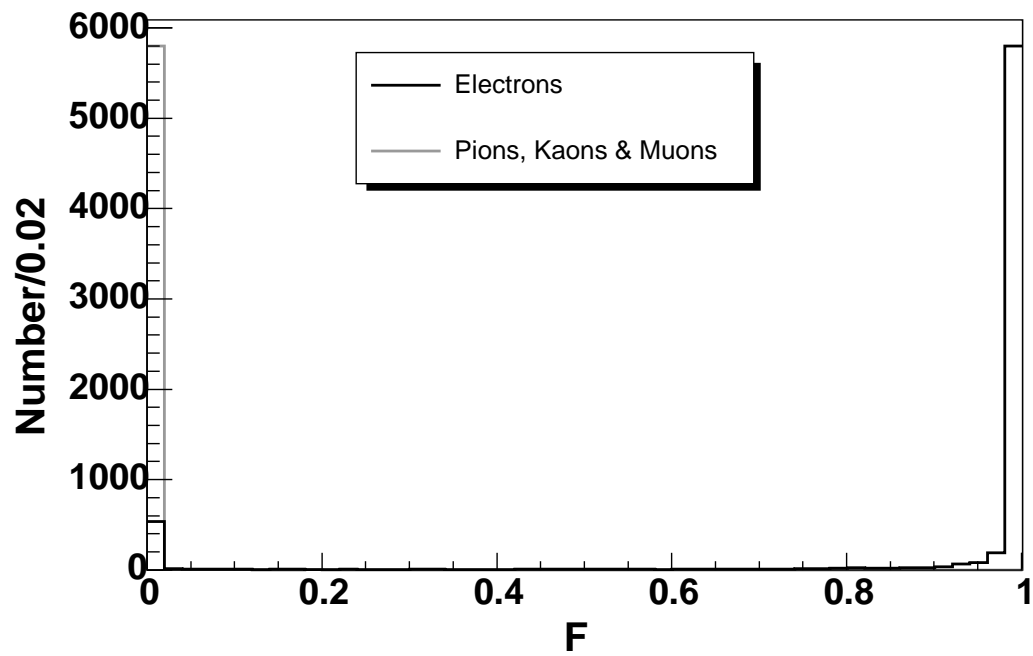


Figure 5.1: Electron likelihood F , distributions for electron (black line), pion, kaon and muon (gray line) tracks passing the electron candidate quality criteria. For convenience the distribution of non-electron tracks is scaled to have the same maximum as the electron distribution.

pions, since these will be a source of peaking background in the $D^0 \rightarrow \pi^- e^+ \nu$ mode. In accordance with these criteria, a track is considered a signal charged pion candidate if it satisfies the following momentum dependent criteria:

- Track is Trkman approved.
- Track has a pion fit.
- Track is not in a reconstructed K_S with a clean vertex and $-1.5 < \sigma_{M_{K_S}} < 2.0$.
- $p_\pi < 650 \text{ MeV}/c$:
 - $|\sigma_{dE/dx}(\pi)| < 3$.
- $650 \text{ MeV}/c \leq p_\pi < 750 \text{ MeV}/c$:
 - $|\sigma_{dE/dx}(\pi)| < 3$ and $|\sigma_{dE/dx}(\pi)| < |\sigma_{dE/dx}(K)|$.
- $p_\pi \geq 750 \text{ MeV}/c$:
 - RICH available,
 - No. of photons in π hypothesis > 3 ,
 - $\chi_{\text{RICH}}^2(K) - \chi_{\text{RICH}}^2(\pi) \geq 1.0$ and $|\sigma_{dE/dx}(\pi)| < 3$.

The resulting signal charged pion efficiency and the rate at which true kaons fake signal pions are shown in Fig 5.2.

5.1.3 Signal K^\pm Identification

For identifying signal charged kaons the most important criterion is to obtain a high efficiency. In this case, the presence of signal kaons being faked by charged

pions is not a significant source of background because the pion semileptonic rate is Cabibbo suppressed. Nevertheless we try to eliminate as many true pions from the sample as possible, while keeping the overall efficiency high. A track is thus considered to be a signal charged kaon candidate if it satisfies:

- Track is Trkman approved.
- Track has a kaon fit.
- $p_K < 500 \text{ MeV}/c$:
 - $|\sigma_{dE/dx}(K)| < 3$.
- $p_K \geq 500 \text{ MeV}/c$:
 - $|\sigma_{dE/dx}(K)| < 3$.
 - If RICH available and No. of photons in K hypothesis > 3 :
 - * $\chi_{\text{RICH}}^2(\pi) - \chi_{\text{RICH}}^2(K) \geq 1.0$.

The resulting signal charged kaon efficiency and the rate at which true pions fake signal kaons are shown in Fig 5.2.

5.1.4 Signal π^0 Identification

For signal π^0 identification the goal is to eliminate as much combinatoric background as possible, while still keeping enough candidates to produce a significant signal rate. To achieve this goal we select kinematically fit π^0 's with a mass cut corresponding to roughly 2.5 standard deviations. Signal π^0 's are thus all reconstructed $\pi^0 \rightarrow \gamma\gamma$ decays with Splitoff approved showers passing

- At least one shower in the barrel calorimeter.

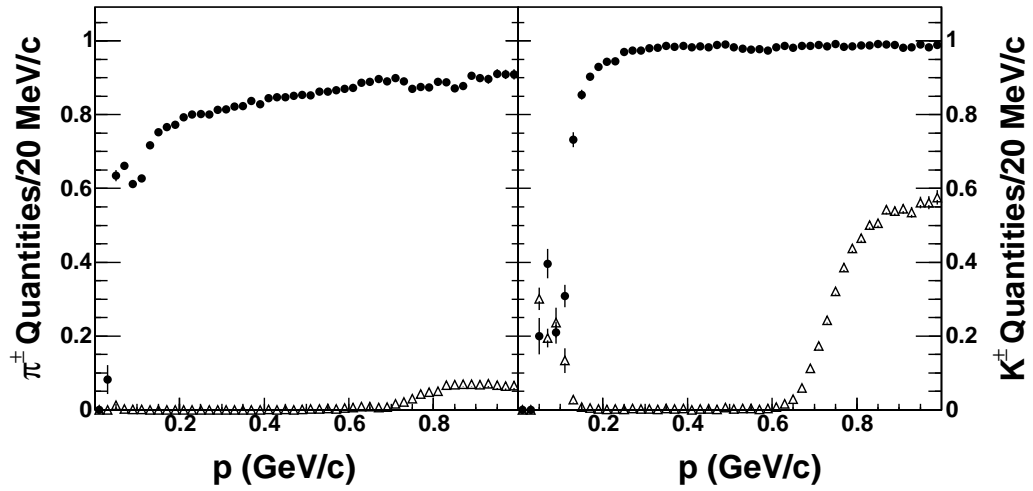


Figure 5.2: Signal charged pion and kaon efficiencies and fake rates from $D\bar{D}$ MC. The left hand plot shows the overall signal pion efficiency (black circles) as well as the fraction of signal pions that are faked by charged kaons (open triangles). The right hand plot shows the overall signal kaon efficiency (black circles) as well as the fraction of signal kaons that are faked by charged pions (open triangles). All quantities are shown as a function of track momentum p .

- Both showers pass $E9/E25$ 99% photon like, or, if shower centers are within 25 cm, both showers pass unfolded $E9/E25$ 99% photon like.
- $|m_{\pi^0} - 0.135| < 0.015$ GeV.

Requiring that the component showers be Splitoff approved has a two fold purpose. In the first place this requirement helps remove combinatoric background from non-photon showers, and secondly it ensures consistency with the reconstructed missing event four-momentum. The resulting signal π^0 efficiency as a function of momentum is discussed in detail in section 7.11.

5.1.5 Signal $K_S(\pi^+\pi^-)$ Identification

Signal K_S are reconstructed using a vertex fit to the $\pi^+\pi^-$ daughter tracks. Both pion tracks are required to be Trkman approved¹ and the mass of the $\pi^+\pi^-$ pair is required to be within 4.5 standard deviations of the K_S mass. Neither tighter mass cuts, nor clean-up cuts, were of benefit as the backgrounds for this mode were already so small. All further K_S restrictions only created efficiency loss. the resulting K_S efficiency as a function of momentum is discussed in detail in section 7.12.

5.2 Event Cuts

In this section we list the selection criteria for reconstructed signal D decays to be passed to the fit. These criteria fall into three distinct groups according to their general purpose. The focus of the first group of selection criteria is the improvement of neutrino resolution: these are cuts designed specifically to assist with the

¹Trkman tries to avoid cutting tracks from K_S candidates, so requiring Trkman approved tracks for the K_S daughters should make almost no difference

accurate reconstruction of the missing energy and momentum. In the second group we class together those cuts which aim to improve the overall quality of the signal D candidate. The final group, meanwhile, contains several miscellaneous cuts designed to remove background from sources other than those represented in our MC. It is also worthwhile to note that all selection criteria relying on specific numerical “cut” values have been tuned on an independent sample of signal $D^0 \rightarrow \pi^\pm e \nu$ MC. We tune to maximize $S^2/(S + B)$, where S is the number of signal events and B the number of background events retained after the cut.

To ensure quality neutrino candidates it is desirable to remove events where association of neutrino with the missing energy and momentum has been destroyed. For example, as we have already discussed in section 4.3.1, this association will be destroyed in events with any extra missing particles e.g., more than one neutrino, partially showering K_L 's, missing tracks, etc. To remove such events therefore we implement three event selection criteria:

- Event Net Charge = 0 (from Trkman approved tracks).
- The event contains exactly one electron.
- $|M_{\text{miss}}^2/2p_{\text{miss}}| < 0.2 \text{ GeV}/c^3$.

Of these selection criteria the net charge requirement needs the least explanation: it removes events with extra or missing charged particles. The other two cuts, however, require some additional details.

The one electron cut, or multiple electron veto, is designed to eliminate events containing more than one neutrino (which we cannot correctly reconstruct since the missing mass will always contain both particles). The veto succeeds in this goal because events containing more than one electron are likely to also contain

more than one neutrino.

The final neutrino requirement, the third listed above, ensures that the missing mass of the event is consistent with the zero mass neutrino hypothesis. It is familiarly known as the “Vee Cut”, Fig. 5.3. As we have already noted, such a requirement is important for removing events with extra missing neutral particles such as K_L ’s. The logic behind the particular form of the “Vee Cut” can be motivated by looking at the resolution of M_{miss}^2 in terms of E_{miss} and p_{miss} :

$$\sigma_{M_{\text{miss}}^2} = \sqrt{(2E_{\text{miss}})^2\sigma_{E_{\text{miss}}}^2 + (2p_{\text{miss}})^2\sigma_{p_{\text{miss}}}^2}. \quad (5.1)$$

Utilizing the fact that the contribution from the spread in missing energy will dominate this resolution, we can then make the approximation

$$\sigma_{M_{\text{miss}}^2} \sim 2E_{\text{miss}}\sigma_{E_{\text{miss}}} \sim 2p_{\text{miss}}\sigma_{E_{\text{miss}}}. \quad (5.2)$$

The “Vee Cut” therefore, is simply a zero missing mass requirement scaled to be approximately uniform in the number of $\sigma_{E_{\text{miss}}}$; it removes a large amount of background that might otherwise fall into the D candidate signal region.

To ensure a signal D candidate of decent quality we firstly require consistency with energy and momentum conservation:

- $M_{\text{bc}} > 1.794$ GeV.
- $-0.06 < \Delta E < 0.10$ GeV.

These requirements are mostly self explanatory after our discussion of ΔE and M_{bc} in Chapter 4. However, we pause to note that although all D candidates with $M_{\text{bc}} > 1.794$ GeV are passed to the fit, a very loose requirement, we still define the signal region as the subset of these decays with $|M_{\text{bc}} - M_D| < 15$ MeV. This requirement gives us signal candidates with masses consistent with that of a D

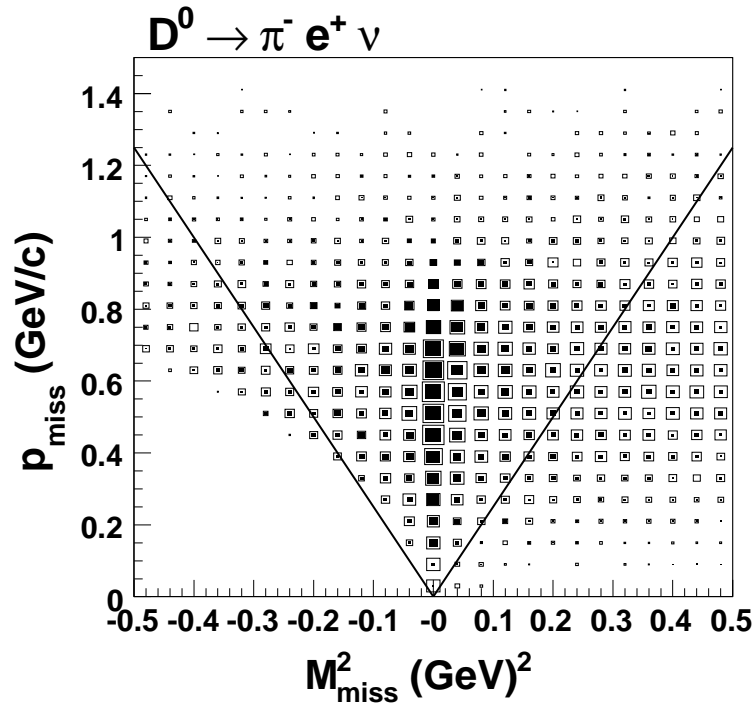


Figure 5.3: Vee cut in MC for the $D^0 \rightarrow \pi^- e^+ \nu$ signal mode. Filled boxes show signal events, open boxes show background and the normalization is absolute. The events shown pass zero net charge, one electron veto, QCD event classification, and the multiple candidate veto. The solid lines show the signal region (and fit region) Vee cut $|M_{\text{miss}}^2/2p_{\text{miss}}| < 0.2$.

meson and covers a wide range in terms of our M_{bc} resolution of ~ 4 MeV. The range of ΔE values passed to the fit covers roughly three standard deviations in terms of the resolution of ~ 50 MeV.

We next implement the following multiple candidate vetos, which simplify the statistical interpretation of our results and ensure that the best quality candidate is passed to the fit.

- A given event can contribute to at most one D^0 and one D^+ final state. From multiple candidates with $M_{bc} > 1.794$ GeV and a given parent D charge, we choose the one with the smallest $|\Delta E|$.²
- If the candidate is a $D^+ \rightarrow \pi^0 e^+ \nu$ decay the multiple candidate requirements are stricter: the candidate must have the best ΔE in the whole event and there must be *no* reconstructed $D^0 \rightarrow K^- e^+ \nu$ in the event.

For the $D^+ \rightarrow \pi^0 e^+ \nu$ mode the stricter requirements remove almost all $D^0 \rightarrow K^- e^+ \nu$ cross-feed (with very little signal efficiency loss) as well as a significant amount of other signal mode cross-feed backgrounds. This is important for the π^0 signal mode, where the cross-feed backgrounds are large, and reduction of the cross-feed rate helps reduce the associated systematic uncertainties.

The pion modes have additional requirements on the energy of the non-signal side of the event ΔE_{OS} ,³ that help reduce cross-feed background. These cuts are q^2 bin dependent and are given by:

- $D^0 \rightarrow \pi^- e^+ \nu_e$

²For example, a $D^0 \rightarrow \pi^- e^+ \nu$ candidate and a $D^0 \rightarrow K^- e^+ \nu$ cannot be found in the same event, while it is possible for the two candidate decays $D^0 \rightarrow \pi^- e^+ \nu$ and $D^+ \rightarrow \pi^0 e^+ \nu$, to have come from the same event.

³The ΔE calculated from the sum of tracks and showers on the other side of the event.

- $0.0 \leq q^2 < 0.4$: $-0.20 < \Delta E_{\text{OS}} < 0.20$
- $0.4 \leq q^2 < 0.8$: $-0.18 < \Delta E_{\text{OS}} < 0.20$
- $0.8 \leq q^2 < 1.2$: $-0.20 < \Delta E_{\text{OS}} < 0.22$
- $1.2 \leq q^2 < 1.6$: $-0.18 < \Delta E_{\text{OS}} < 0.22$
- $q^2 > 1.6$: $-0.14 < \Delta E_{\text{OS}} < 0.38$

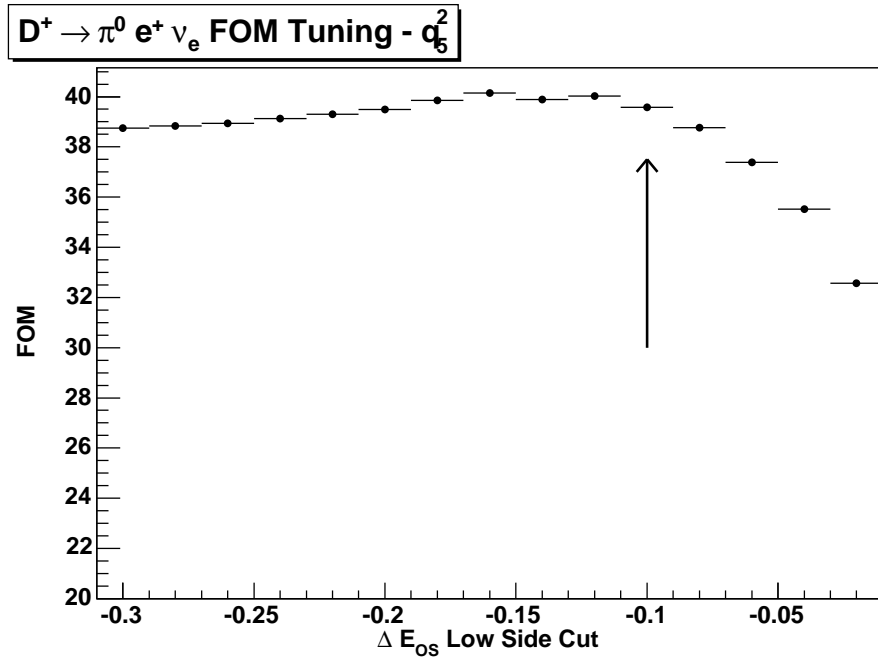
- $D^+ \rightarrow \pi^0 e^+ \nu_e$

- $0.0 \leq q^2 < 0.4$: $-0.20 < \Delta E_{\text{OS}} < 0.22$
- $0.4 \leq q^2 < 0.8$: $-0.20 < \Delta E_{\text{OS}} < 0.34$
- $0.8 \leq q^2 < 1.2$: $-0.22 < \Delta E_{\text{OS}} < 0.24$
- $1.2 \leq q^2 < 1.6$: $-0.24 < \Delta E_{\text{OS}} < 0.38$
- $q^2 > 1.6$: $-0.10 < \Delta E_{\text{OS}} < 0.16$

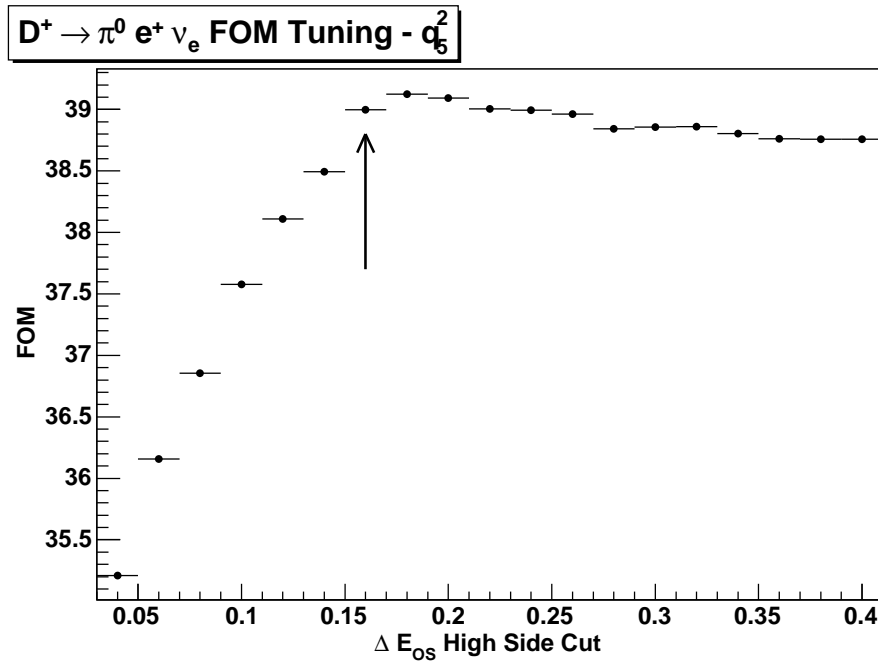
As stated above, these requirements are tuned using $S^2/(S+B)$ as a figure of merit (FOM). To give an example, we show the figure of merit plots for $D^+ \rightarrow \pi^0 e^+ \nu_e$ in the highest q^2 bin, Fig. 5.4. In this case, where there are long, relatively flat tails in the FOM we choose to place the cut at the start of the tail since this eliminates more background.

The final group of event level selection criteria removes backgrounds other than those modeled in the MC. The first of these requirements looks at the event shape and removes any events unlikely to fall into the desired categories for analysis. For example, Bhabha events and events caused by cosmic rays are removed here. Specifically we require:

- Event topology indicates that it is likely to contain QCD physics.



(a) Low Side Tail



(b) High Side Tail

Figure 5.4: $D^+ \rightarrow \pi^0 e^+ \nu_e$ FOM tuning for the low (a) and high (b) side ΔE_{OS} cuts in the range $q^2 > 1.6 \text{ GeV}^2$. The arrows show where we place the cuts.

Our final two requirements in this group are designed to remove an unexplained discrepancy between data and MC at the corners of the $q_e \cos \theta_e$ vs $q_e \cos \theta_{\text{miss}}$ distributions. Here q_e is the electron charge, $\cos \theta_e$ is the electron track $\cos \theta$ and $\cos \theta_{\text{miss}} = p_{z \text{ miss}}/p_{\text{miss}}$. The form of the discrepancy is a build up of events in the data in these regions that is not apparent in the MC. Most likely this is due to some background that has not been accounted for, such as two-photon events, for which one expects the kind of charge-angle correlations that we observe. Since these requirements remove almost no signal events, there seems to be no disadvantage in making them. We require therefore, that all events passed to the fit must satisfy:

- $!(q_e \cos \theta_e > 0.7 \text{ AND } q_e \cos \theta_{\text{miss}} > 0.9)$.
- $!(q_e \cos \theta_e > 0.7 \text{ AND } q_e \cos \theta_{\text{miss}} < -0.9)$.

We conclude this section by looking at the effects of our event selection criteria on the reconstruction efficiency. The individual selection requirements and the resultant full efficiency matrix are both examined.

To document the effect of each event selection criterion on the overall reconstruction efficiency, we look at a ‘‘cut history’’. The cut history is created via the successive addition of requirements to the list of event selection criteria. After the addition of each new requirement the signal reconstruction efficiency, as a function of q^2 , is extracted from MC. The results of this process for our signal $D^0 \rightarrow \pi^- e^+ \nu$ MC⁴ are given in Table 5.1. The final efficiencies (in the last row of the table) are the total efficiencies in the signal M_{bc} region. We note that these will differ from

⁴The effects of the each of the event selection criteria on efficiency will be similar for all of our signal modes. Each mode, however, will start with a different ‘‘no cut’’ efficiency resulting primarily from differences in the signal hadron identification efficiencies.

the fit efficiencies we quote in Chapter 8, since the latter cover the entire fit range $1.794 < M_{bc} < 1.878$ GeV (see Chapter 6 for details).

For completeness we also give the full efficiency matrix that results from application our event selection criteria in the signal M_{bc} region, Tables 5.2 and 5.3. This is the 20×20 matrix of efficiencies from our four signal modes and five fit q^2 ranges (see Chapter 6 for details). A similar efficiency matrix - with efficiencies from the fit, rather than the signal, M_{bc} region - is input to our fitter in order to extract the final yields for each mode. In fact, the details of this process will be the topic of the next chapter.

Table 5.1: Cut history in terms of reconstruction efficiency in signal $D^0 \rightarrow \pi^- e^+ \nu$ MC. We start with no requirements but the particle identification criteria for the electron and pion and the low beam constrained mass cut off $M_{bc} > 1.794$ GeV. To avoid efficiencies of over 100% we never count more than one candidate per event. (The effect of the multiple candidate veto therefore, is to exclude events where a better $D^0 \rightarrow K^- e^+ \nu$ candidate was found.) The given q^2 intervals are those used in the fit, see Chapter 6.

Cut Added	Cut History Efficiencies (%)					
	q^2 Interval (GeV) ²					
	< 0.4	0.4 – 0.8	0.8 – 1.2	1.2 – 1.6	> 1.6	All
None	60.30	65.73	68.11	70.08	78.82	68.63
Is QCD Event	60.24	65.64	68.03	69.95	78.57	68.50
Net Charge	48.18	52.25	54.68	55.28	58.69	53.73
Multiple Candidate	43.38	48.70	53.64	55.05	58.37	51.61
e^\pm Veto	43.29	48.62	53.54	55.00	58.26	51.52
“Vee Cut”	26.83	28.56	30.57	31.14	32.52	29.85
ΔE	20.75	22.01	23.59	24.00	25.29	23.08
ΔE_{OS}	19.94	21.11	22.85	23.24	23.77	22.11
“ $q \cos \theta$ ” Cuts	19.81	21.08	22.66	22.80	23.17	21.83
M_{bc}	18.81	19.99	21.25	21.31	20.96	20.27

Table 5.2: Full efficiency matrix - in the signal M_{bc} region - resulting from application of all event selection criteria for the reconstructed D^0 signal modes. For each type of signal MC, we give the D^0 signal mode reconstruction efficiencies (%) in each of the five reconstructed and five true q^2 ranges. The five q^2 ranges are those used in the analysis fit (detailed in Chapter 6), and are represented by the q_i , with $i = 1, \dots, 5$.

Signal MC Type	Reconstructed Mode										
	$D^0 \rightarrow \pi^- e^+ \nu$					$D^0 \rightarrow K^- e^+ \nu$					
	q_1	q_2	q_3	q_4	q_5	q_1	q_2	q_3	q_4	q_5	
$D^0 \rightarrow \pi^- e^+ \nu$	q_1	18.0	0.8	0.0	0.0	0.0	1.6	0.0	0.0	0.0	0.0
	q_2	0.8	18.4	0.9	0.0	0.0	0.4	0.6	0.0	0.0	0.0
	q_3	0.0	0.8	19.5	1.0	0.0	0.0	0.2	0.0	0.0	0.0
	q_4	0.0	0.0	0.8	19.8	0.5	0.0	0.0	0.0	0.0	0.0
	q_5	0.0	0.0	0.0	0.5	20.4	0.0	0.0	0.0	0.0	0.0
$D^0 \rightarrow K^- e^+ \nu$	q_1	0.2	0.0	0.0	0.0	0.1	17.7	0.8	0.0	0.0	0.0
	q_2	0.0	0.1	0.1	0.0	0.3	0.7	18.0	0.9	0.0	0.1
	q_3	0.0	0.0	0.1	0.2	0.8	0.0	0.7	17.5	0.9	0.1
	q_4	0.0	0.0	0.0	0.1	1.9	0.0	0.0	0.5	16.0	1.5
	q_5	0.0	0.0	0.0	0.0	0.7	0.0	0.0	0.0	0.3	10.9
$D^+ \rightarrow \pi^0 e^+ \nu$	q_1	0.0	0.0	0.0	0.0	0.0	0.0	0.0	0.0	0.0	0.0
	q_2	0.0	0.1	0.0	0.0	0.0	0.0	0.0	0.0	0.0	0.0
	q_3	0.0	0.0	0.2	0.0	0.0	0.0	0.0	0.0	0.0	0.0
	q_4	0.0	0.0	0.1	0.3	0.1	0.0	0.0	0.0	0.0	0.0
	q_5	0.0	0.0	0.0	0.1	1.3	0.0	0.0	0.0	0.0	0.0
$D^+ \rightarrow K_S e^+ \nu$	q_1	0.1	0.0	0.0	0.0	0.1	0.3	0.0	0.0	0.0	0.0
	q_2	0.0	0.1	0.1	0.0	0.2	0.0	0.1	0.0	0.0	0.0
	q_3	0.0	0.0	0.2	0.2	0.7	0.0	0.0	0.0	0.0	0.0
	q_4	0.0	0.0	0.0	0.3	1.4	0.0	0.0	0.0	0.1	0.2
	q_5	0.0	0.0	0.0	0.0	0.7	0.0	0.0	0.0	0.0	0.1

Chapter 6

Fitting for Yields

To determine a branching fraction for each of the signal decay modes we fit our MC samples to the data. All four signal decay modes are fit simultaneously, which allows us to correctly account for cross-feed between the modes. The fit, to be discussed in more detail below, is a binned maximum likelihood fit following the method of Barlow and Beeston [34]. It is binned in q^2 and M_{bc} and the signal MC is binned also in true q^2 to account for q^2 bin cross-feed. We will first discuss the general details of the fit method, and then the specific details of the yield fits for this analysis, including some necessary adjustments to the MC.

6.1 The Fit

To extract the branching fraction information, we perform a binned maximum likelihood fit (described below) using the reconstructed M_{bc} distributions from our four signal modes. The four modes are fit simultaneously and we extract partial branching fractions in five q^2 ranges: $0.0 - 0.4 \text{ GeV}^2$, $0.4 - 0.8 \text{ GeV}^2$, $0.8 - 1.2 \text{ GeV}^2$, $1.2 - 1.6 \text{ GeV}^2$, and $\geq 1.6 \text{ GeV}^2$. The M_{bc} distributions in each q^2 range are divided into fourteen uniform bins over the region $1.794 < M_{bc} < 1.878 \text{ GeV}$.¹ In addition, we partition each of our signal MC samples into five subsamples based on the generator level q^2 range. Each of these subsamples is then analyzed individually to obtain the 20 reconstructed M_{bc} distributions (4 modes \times 5 reconstructed q^2

¹For our fit result plots we show an additional two bins above $M_{bc} = 1.878 \text{ GeV}$. This gives us confidence that the fit results are also valid in the high M_{bc} tail.

ranges) for input to the fit. With this approach, the fit will automatically account for the cross-feed among the four modes and five reconstructed q^2 intervals that is a result of finite resolution and mis-reconstruction. In other words, as was foreshadowed in the previous chapter, we are effectively inputting a generalization of the full efficiency matrix to the fit.

In addition to the signal MC components just described, the fit also contains six background samples obtained from MC (see Section 4.2) and a sample of fake electron backgrounds obtained from data. The fake electron fit component is assembled by selecting approximately every fourth data event not containing an identified electron track. For each of these events we make a list of tracks that pass the basic electron track quality criteria (Section 5.1.1), these tracks are our fake electrons. We loop over the events choosing each fake track in turn to be our electron and reconstructing the event as usual. Any D candidates are then stored with a weight representing the probability of the fake track having been chosen as an electron. The weights come from data measured electron fake rates consistent with our electron identification scheme; they are species and momentum dependent. The fake electron component is added to the fit with a fixed scale factor calculated from the ratio of the data luminosity to the fake luminosity (a factor of only roughly four, since we actually use all non-electron events in every fourth data run).

The fit normalizations of the six background MC samples vary according to the physics they describe. The background MC samples for continuum, radiative returns from the $\psi(2S)$ and τ pair are normalized according to their measured or predicted cross sections at the $\psi(3770)$ and the total luminosity of our data. Hence, the normalizations of these samples are fixed within the fit. The normaliza-

tion for the generic $D\bar{D}$ background floats separately for each reconstructed decay mode, minimizing our sensitivity to poorly known branching fractions or missing decay modes in our D decay model. The relative distribution across reconstructed q^2 within a mode remains fixed. The normalizations of the remaining background components, $D^+ \rightarrow K_L e^+ \nu$ and $D^+ \rightarrow K_S(\pi^0 \pi^0) e^+ \nu$, are fixed by the normalization of the signal $D^+ \rightarrow K_S(\pi^+ \pi^-) e^+ \nu$ mode. These normalizations are derived by combining the fact that the K^0 is a two state quantum system - appearing in our detector 50% of the time as K_S and 50% as K_L - with the known branching fractions [2],

$$\mathcal{B}(K_S \rightarrow \pi^0 \pi^0) = 0.3105, \quad (6.1)$$

and

$$\mathcal{B}(K_S \rightarrow \pi^+ \pi^-) = 0.6895. \quad (6.2)$$

6.1.1 Fit Details

As stated above, to extract yields for our four signal modes we perform a binned maximum likelihood fit. Following the method of Barlow and Beeston [34], the likelihood fit is extended from its standard form to account for the finite statistics of the MC samples. In this section we outline the details of the fit, following closely the discussion of Barlow and Beeston.

The job of the fit is to determine the proportions of the signal decay modes in the data, i.e., the P_j , where the index j enumerates the set of m MC sources. The data is binned into a set of n bins with d_i events in bin i and the expected number of events in this bin is given by,

$$f_i = \sum_{j=1}^m p_j a_{ji}, \quad (6.3)$$

where a_{ji} is the number of events in bin i from MC source j , and $p_j = N_D P_j / N_j$, with, $N_D = \sum_i d_i$ and $N_j = \sum_i a_{ji}$. The standard approach to estimating the values of the p_j is to use a binned maximum likelihood fit, wherein a Poisson distribution is assumed for each bin and the correct p_j values are found by maximizing,

$$\ln \mathcal{L} = \sum_{i=1}^n d_i \ln f_i - f_i. \quad (6.4)$$

The problem with this method is that it fails to account for the fact that the MC samples are also of finite size and will thus contribute to the uncertainty. Ideally therefore, the quantity we maximize should allow for statistical fluctuations in the a_{ji} . To correct this omission we follow the solution of Barlow and Beeston [34]. In this case we now assume each source bin contains an unknown expected number of events A_{ji} , so that in place of Eq. 6.3, the expected number of events is now given by,

$$f_i = \sum_{j=1}^m p_j A_{ji}. \quad (6.5)$$

The A_{ji} are the generating distribution for the a_{ji} . Nominally, the a_{ij} would be distributed about the A_{ij} according to a binomial distribution, but with typical experimental acceptances we may approximate with the Poisson distribution. This procedure results in a new likelihood expression where the combined probability of the d_i and the a_{ji} is accounted for,

$$\ln \mathcal{L} = \sum_{i=1}^n d_i \ln f_i - f_i + \sum_{i=1}^n \sum_{j=1}^m a_{ji} \ln A_{ji} - A_{ji}. \quad (6.6)$$

The new expression for the likelihood is a maximization problem in $m \times (n + 1)$ unknowns. By differentiating Eq. 6.6 and setting the derivatives to zero we obtain the two sets of simultaneous equations that must be solved,

$$\sum_{i=1}^n \frac{d_i A_{ji}}{f_i} - A_{ji} = 0 \quad \forall j \quad (6.7)$$

and

$$\frac{d_i p_j}{f_i} - p_j + \frac{a_{ji}}{A_{ji}} = 0 \quad \forall i, j. \quad (6.8)$$

Fortunately this large system of equations may be greatly simplified. We start by rewriting Eq. 6.8 as,

$$1 - \frac{d_i}{f_i} = \frac{1}{p_j} \left(\frac{a_{ji}}{A_{ji} - 1} \right) \quad \forall i, j. \quad (6.9)$$

The left hand side depends only on i , let us call it t_i ,

$$t_i = 1 - \frac{d_i}{f_i}. \quad (6.10)$$

Effectively this results in the reduction of an $m \times n$ problem to an order n problem.

To see this we note that we now have

$$A_{ji} = \frac{a_{ji}}{1 + p_j t_i}, \quad (6.11)$$

so that the $m \times n$ unknowns A_{ji} depend only on the n unknowns t_i . Except in the case where $d_i = 0$, for which set $t_i = 1$, the t_i are solved for using Eq. 6.10:

$$f_i = \frac{d_i}{1 - t_i} = \sum_j p_j A_{ji} = \sum_j \frac{p_j a_{ji}}{1 + p_j t_i}, \quad (6.12)$$

a system of n equations which, if satisfied, give a complete solution to the set of simultaneous equations.

In order that the final value of the likelihood give an understandable estimate of the fit quality we choose to maximize a slight modification of Eq. 6.6. What we want to maximize is the likelihood ratio, which may be equated to the χ^2 goodness of fit test via $\chi^2 = -2 \ln \mathcal{L}$. As an example, for just the data portion the ratio is given by,

$$\mathcal{L} = \prod_{i=1}^n \frac{p(d_i, f_i)}{p(d_i, d_i)}, \quad (6.13)$$

where $p(a, b)$ is the probability the the predicted value a will fluctuate to the observed value b . This leads to the new log likelihood expression

$$\ln \mathcal{L} = \sum_{i=1}^n d_i \ln f_i - f_i - d_i \ln d_i + d_i + \sum_{i=1}^n \sum_{j=1}^m a_{ji} \ln A_{ji} - A_{ji} - a_{ji} \ln a_{ji} + a_{ji}, \quad (6.14)$$

which may be maximized exactly as described above since the newly added terms are no more than constant offsets.

6.2 MC Corrections

To obtain a reasonable fit to the data it is necessary to make several corrections to the generated MC. Below we list briefly each of the corrections along with the section where a full discussion of the correction and its associated systematic error can be found.

1. *Fake Electrons* (Section 7.16)

In the data, events can be vetoed as multiple electron events for one of two reasons: the event may contain two or more real electrons or the event may contain a real electron and a “fake” electron, a hadron incorrectly called an electron. As we have already seen, however, in the MC, there are no fake electrons, we use only real electrons.

To achieve the correct efficiency in our signal MC therefore, we must somehow account for the fact that in data the multiple electron veto will remove events with extra fake electrons as well as events with only real electrons. What we require is a method for deciding whether or not a given MC event is likely to contain a fake electron. To this end, in each event we sum the electron fake probability (as measured in data) for each track that passes the basic electron track quality criteria. This sum gives us the quantity necessary to

make the desired efficiency correction, namely the total probability that the event contains a fake. It is then simply a matter of using this probability to decide whether or not a fake electron is to be added to event for veto purposes.

2. M_{bc} Smear (Section 7.18)

In the three of the signal MC modes, $D^0 \rightarrow \pi^- e^+ \nu$, $D^0 \rightarrow K^- e^+ \nu$ and $D^+ \rightarrow \pi^0 e^+ \nu$, the M_{bc} resolution appears too small. To correct this resolution discrepancy we adjust the M_{bc} distributions of these signal samples² using a Gaussian smear to rearrange the contents of each bin. For each M_{bc} bin, i , the smeared bin contents, a'_i , are obtained from the original bin contents, a_i , via the formula,

$$a'_i = \sum_j a_j p(|i - j|), \quad (6.15)$$

where

$$p(n) = \frac{1}{2} \left(\operatorname{erf} \left(\frac{(2n+1)w}{\sqrt{2}\sigma} \right) - \operatorname{erf} \left(\frac{(2n-1)w}{\sqrt{2}\sigma} \right) \right), \quad (6.16)$$

with w giving the bin half width and σ the adjustable width of the smear Gaussian. To find the appropriate smear for each mode we allow the width of the smear σ , to float in the fit. The smear is fixed over q^2 so that there is only one new parameter for each of the three smeared modes. The resulting smears from the fit are: $\sigma_{\pi^- e^+ \nu} = 1.80 \pm 0.24$ MeV, $\sigma_{K^- e^+ \nu} = 1.54 \pm 0.07$ MeV and $\sigma_{\pi^0 e^+ \nu} = 1.86 \pm 0.38$ MeV. These may be compared with our M_{bc} resolution of 4 MeV.

3. Hadronic Shower Addition (Sections 7.1 and 7.4)

To correctly estimate our neutrino reconstruction efficiency and resolution

²Note that in each q^2 bin for each mode, we smear only the signal histogram.

it is important to accurately model the production of hadronic showers in the MC. In particular, the overall number of hadronic splitoff showers produced will strongly affect the precision of the neutral four-momentum sums (see Chapter 4). However, using double tagged events it can be shown that the number of extra showers (showers that are neither from π^0 photons or matched to tracks) in data exceeds the number of extra showers in MC. For this reason we randomly add the appropriate number of extra hadronic showers to the MC for inclusion in the calculation of the missing 4-momentum. The poor hadronic shower modeling also results in a difference between the number of K_L 's depositing energy in the calorimeter in data and MC [35]. We also correct this difference by adding K_L showers to the MC as needed.

4. K_L Reweight (Section 7.5)

In any event containing a K_L that does not fully shower in the calorimeter, the association of the missing event four-momentum with the neutrino four-momentum will be degraded and the neutrino energy and momentum distorted. The momentum spectrum of K_L 's in the MC therefore will influence the neutrino resolution. It is thus important that we ensure the MC produces the correct distribution and number of K_L 's. We use K_S 's from data and MC to determine the necessary adjustments and re-weight the MC accordingly.

5. $Pion$ Background Reweight (Section 7.6)

The primary background for the signal pion modes is cross-feed from the other signal modes. In most cases this cross-feed occurs when a pion from the generically decaying D is swapped in to replace the signal hadron on the

semileptonic side of the event. For example, we can get background from $D^0 \rightarrow K^- e^+ \nu$ events in our signal $D^0 \rightarrow \pi^- e^+ \nu$ mode if a π^- from the generically decaying D on the other side is combined with the electron and neutrino from the $K^- e^+ \nu$ decay. It is therefore necessary to model the rate and q^2 dependence of this process accurately. We use generically produced pions from data and MC to determine the necessary adjustments and re-weight the MC accordingly.

6. *Kaons Faking Pions* (Section 7.7)

Cross-feed from $D^0 \rightarrow K^- e^+ \nu_e$ into the $D^0 \rightarrow \pi^- e^+ \nu_e$ signal mode can become a peaking background if the K^\pm is mis-identified as a signal π^\pm . To ensure that the mis-identification probability is modeled correctly in the MC we use a sample of K^\pm from data to determine the true rate of π^\pm fakes. The necessary corrections are then applied to the MC in the nominal fit.

7. *Trkman Fakes* (Section 7.10)

It is important to accurately model the number of fake tracks passing the Trkman selection criteria. Any differences in this number between data and MC will result in an inaccurate efficiency estimation due to the net charge zero requirement in our event selection. We study the number of extra Trkman tracks in data and MC using the CLEO-c double tag sample and apply the required correction to the MC based on the number of tracks with $p_T < 0.15$ GeV in a given event.

8. *Signal PID Efficiency* (Sections 7.11, 7.14, 7.15 and 7.12)

The MC does not always estimate correctly the efficiencies of our signal hadrons. For each of the signal hadronic particles, π^0 , π^\pm , K^\pm and $K_S(\pi^+\pi^-)$,

we therefore study the finding efficiencies³ in data and MC and weight to make the necessary corrections to the MC.

9. *FSR Reweight* (Section 7.19)

The final adjustment to the MC for fitting is specific to the radiatively generated decays. By default these are generated by PHOTOS [41], however, the PHOTOS generator ignores leading order correction diagrams, which contain important interference terms. The modeling of the photon angular distributions in PHOTOS therefore, is expected to be inaccurate. The photon energy distributions should be reasonably accurate, but could have small deviations. For our nominal MC therefore we re-weight the photon energy and angular distributions of the final state radiation events to match those generated by the improved KLOR generator [42]. The weights include an overall factor to match the radiative branching fractions to those predicted by KLOR.

6.3 Fit Results

The results of our simultaneous fit to the twenty M_{bc} distributions are shown in Figs. 6.1 - 6.4. For this nominal fit we obtain $-2 \ln \mathcal{L} = 275.55$ for $280 - 27 = 253$ degrees of freedom. To assess the validity of our fit results outside the fit region, other important kinematic variables are also shown with MC components scaled according to the results of the nominal fit. In all cases the variables are examined in the signal M_{bc} region defined by $|M_{bc} - M_D| < 15$ MeV. The ΔE plots are shown in Figs. 6.5 - 6.8. The ΔE region included in the fit corresponds to the four bins in the range $-0.06 < \Delta E < 0.1$ GeV. Another important kinematic

³For the charged hadrons we refer here to PID finding efficiencies only, since the track finding error in the MC is accounted for separately, see Section 7.8

variable is $\cos \theta_{We}$, the cosine of the angle between the W in the D rest frame and the electron in the W rest frame, which we expect to follow a $\sin^2 \theta$ distribution (barring any adjustments for acceptance) when integrated over all q^2 , i.e.,

$$\frac{dN}{d \cos \theta_{We}} \propto \sin^2 \theta_{We}. \quad (6.17)$$

Plots of this variable for each signal decay mode in the signal region are shown in Figs. 6.9 - 6.12. Finally it is also important to see that the momentum of the signal electron, p_e , is being correctly modeled. Figs. 6.13 - 6.16 show plots of p_e in the signal region.

Summarizing these outcomes we find that our nominal fit has an excellent reduced χ^2 value of 1.01, produces results that describe the data accurately even in regions well outside of those included in the fit, and shows accurate MC modeling of several key kinematic variables. Confidence in our fit results therefore, would appear to be well justified.

6.4 Testing the Fit

To test our fitting procedure we fit a set of mock data with known input branching fractions. The mock data we use is the CLEO-c generic $D\bar{D}$ MC sample ($\sim 40 \times \mathcal{L}_{\text{data}}$). We fit this sample with our signal MC and the signal removed generic $D\bar{D}$ background MC. The results, given in Table 6.1, clearly demonstrate that our fit method is reliable and also that our branching fractions are model independent (to be explored further in Section 7.20). Model independence can be inferred from this test fit because our signal MC is generated with LQCD form factors (Section. 4.2), whilst the generic $D\bar{D}$ MC is generated using ISGW2 form factors and thus predicts a very different shape for the q^2 distributions (see Section 7.20).

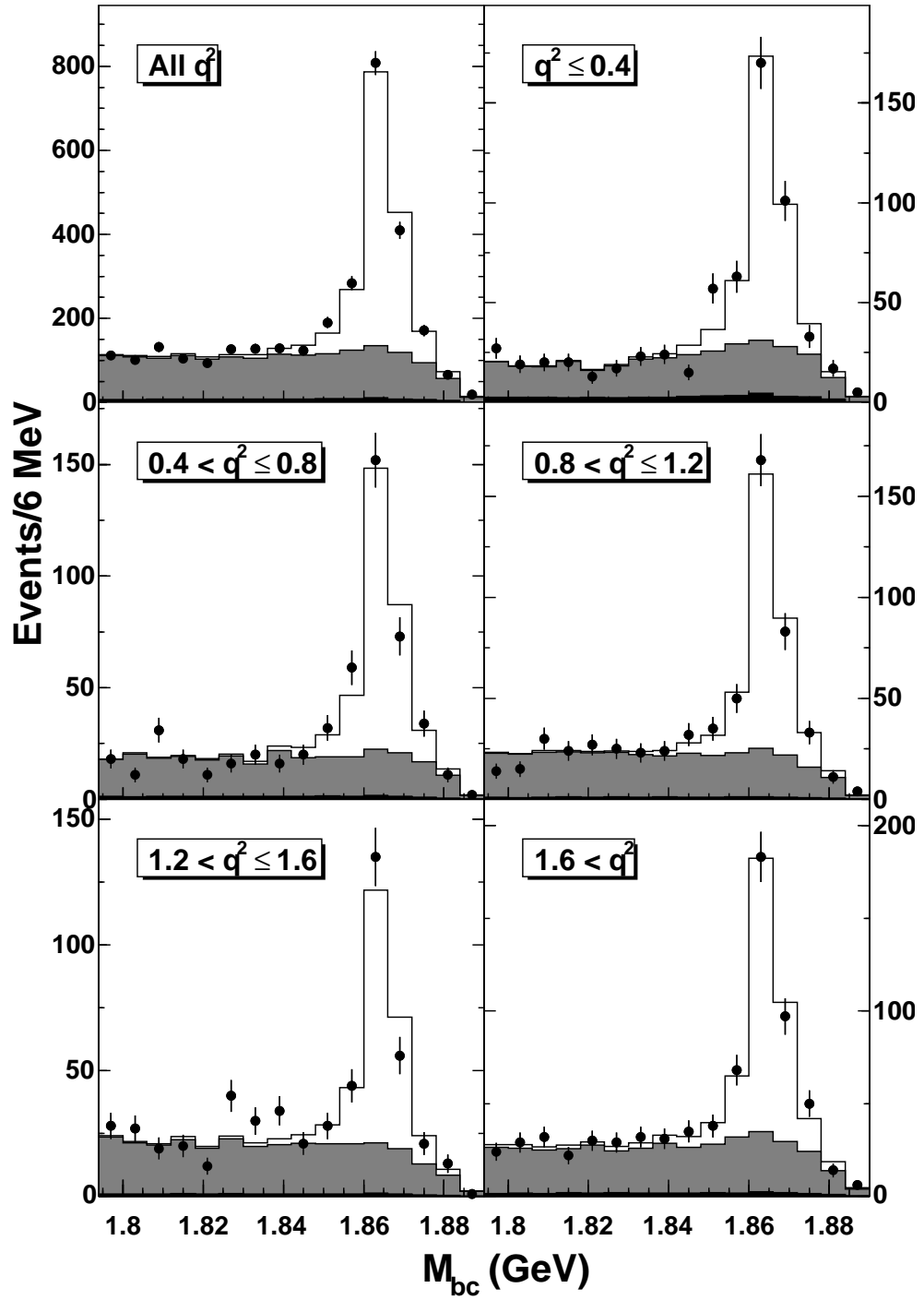


Figure 6.1: Fit M_{bc} distributions for $D^0 \rightarrow \pi^- e^+ \nu$. Points represent data (281 pb^{-1}) and stacked histograms are: Clear - Signal MC, Gray - Summed Background MC, Black - Fakes from Data.

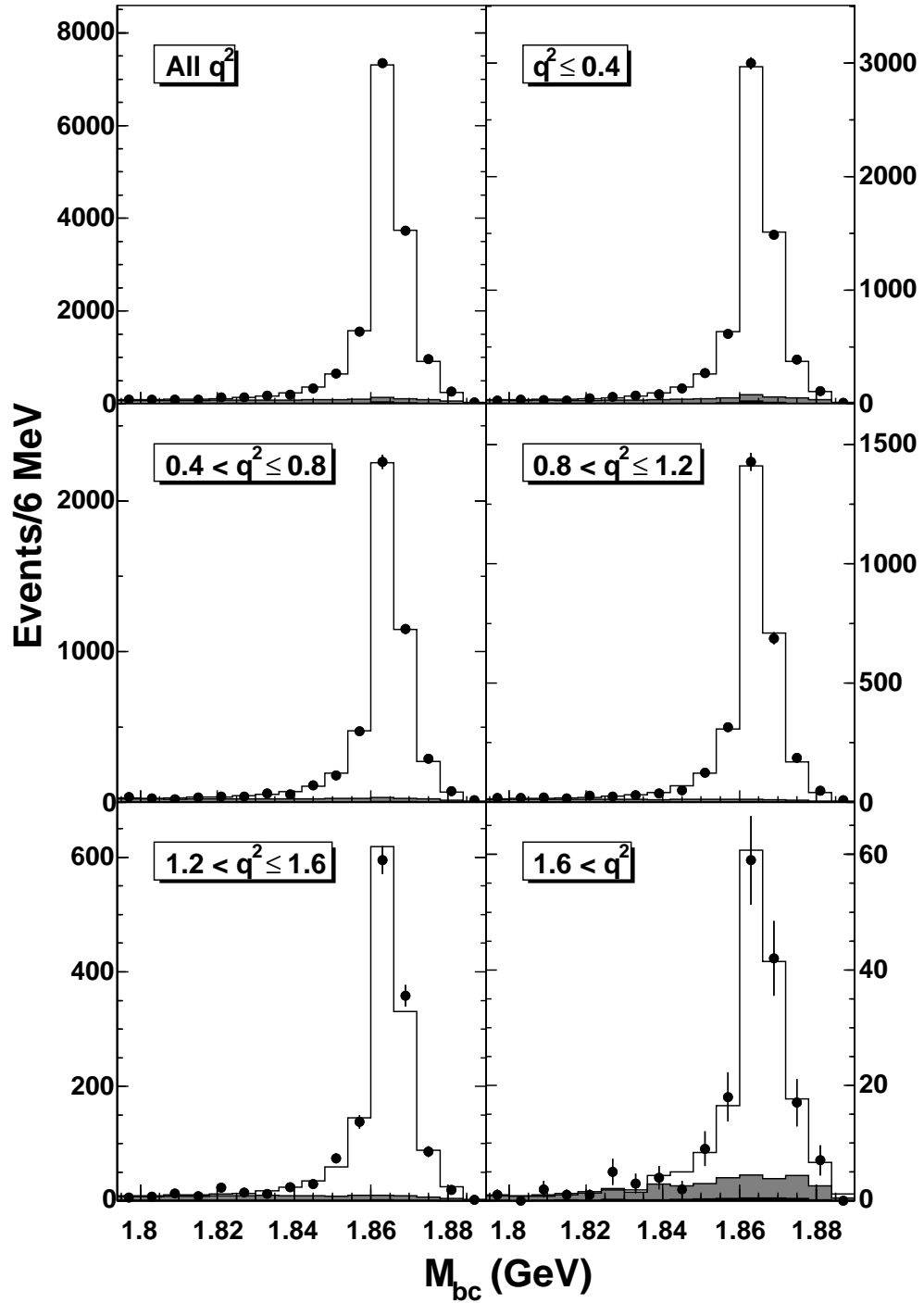


Figure 6.2: Fit M_{bc} distributions for $D^0 \rightarrow K^- e^+ \nu$. Points represent data (281 pb^{-1}) and stacked histograms are: Clear - Signal MC, Gray - Summed Background MC, Black - Fakes from Data.

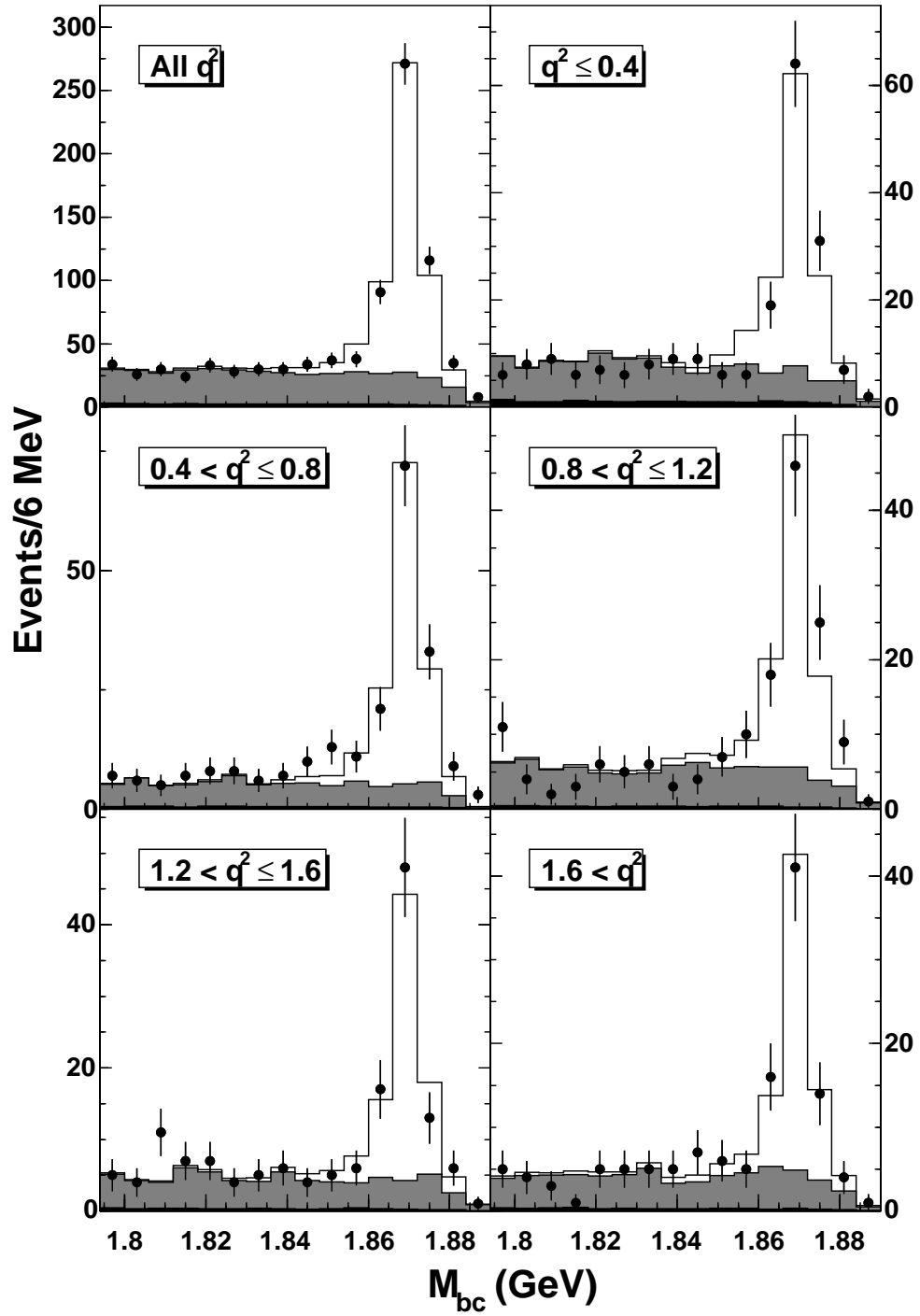


Figure 6.3: Fit M_{bc} distributions for $D^+ \rightarrow \pi^0 e^+ \nu$. Points represent data (281 pb^{-1}) and stacked histograms are: Clear - Signal MC, Gray - Summed Background MC, Black - Fakes from Data.

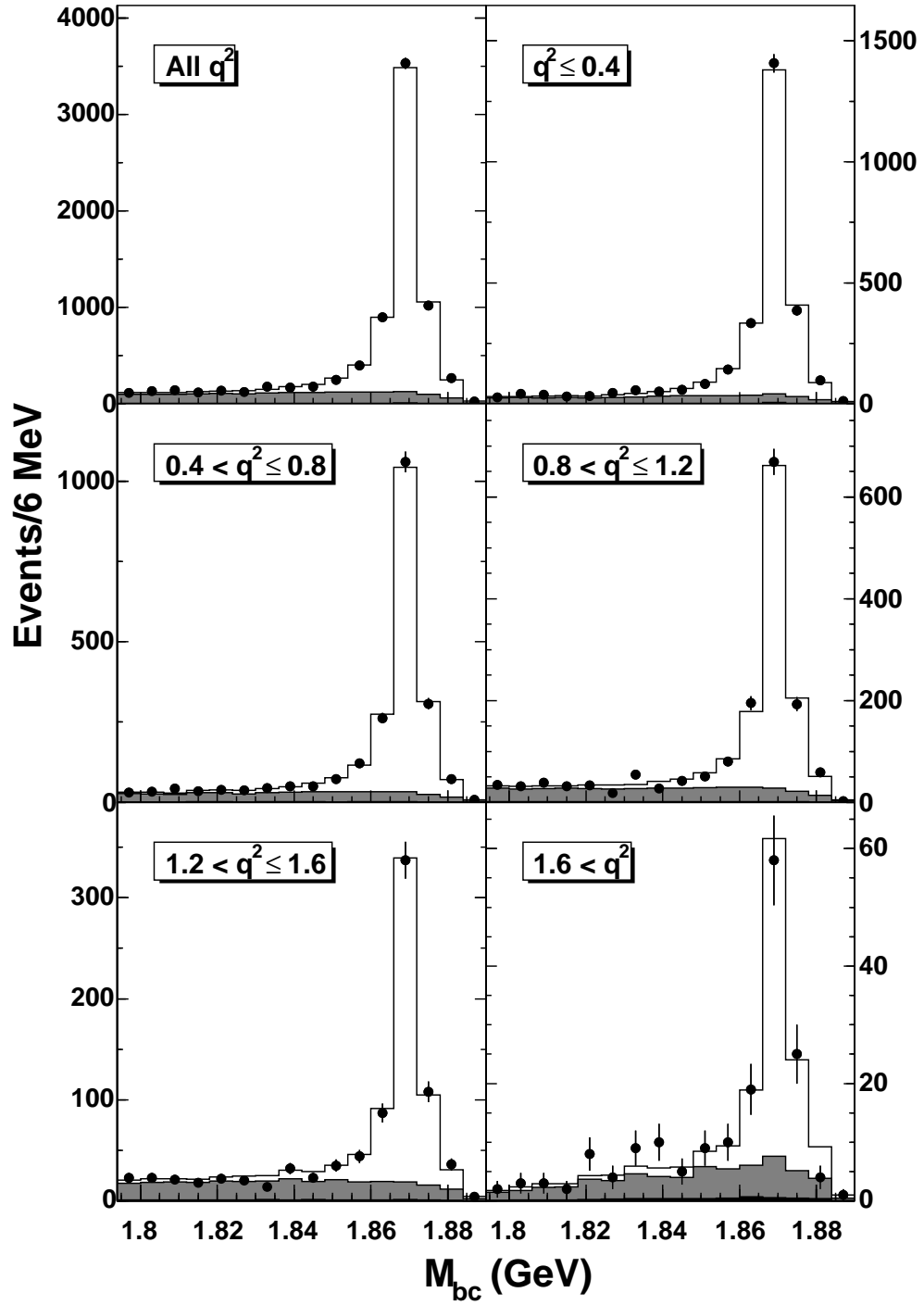


Figure 6.4: Fit M_{bc} distributions for $D^+ \rightarrow K_S(\pi^+\pi^-)e^+\nu$. Points represent data (281 pb^{-1}) and stacked histograms are: Clear - Signal MC, Gray - Summed Background MC, Black - Fakes from Data.

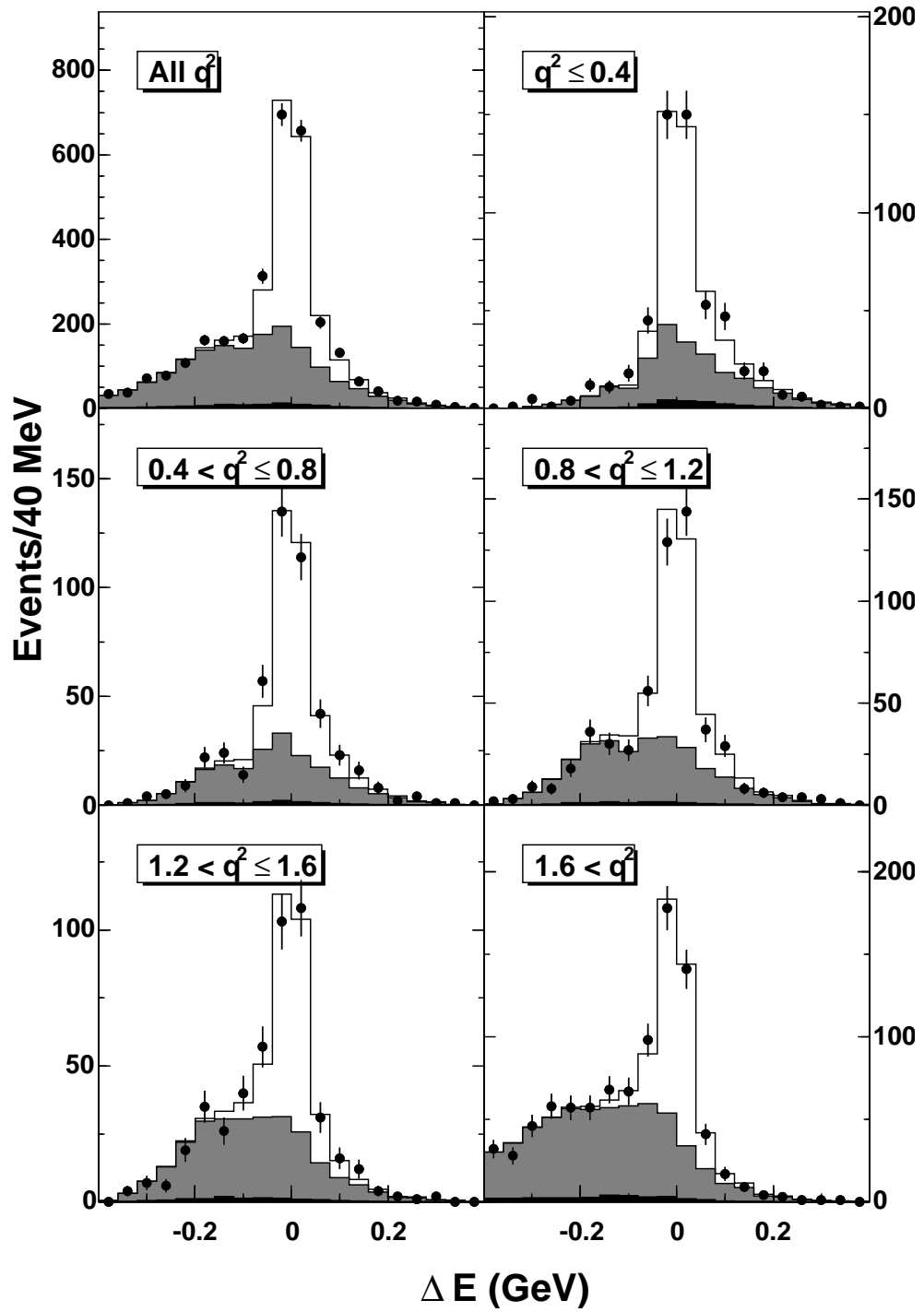


Figure 6.5: Fit scaled ΔE distributions for $D^0 \rightarrow \pi^- e^+ \nu$. Points represent data (281 pb⁻¹) and stacked histograms are: Clear - Signal MC, Gray - Summed Background MC, Black - Fakes from Data.

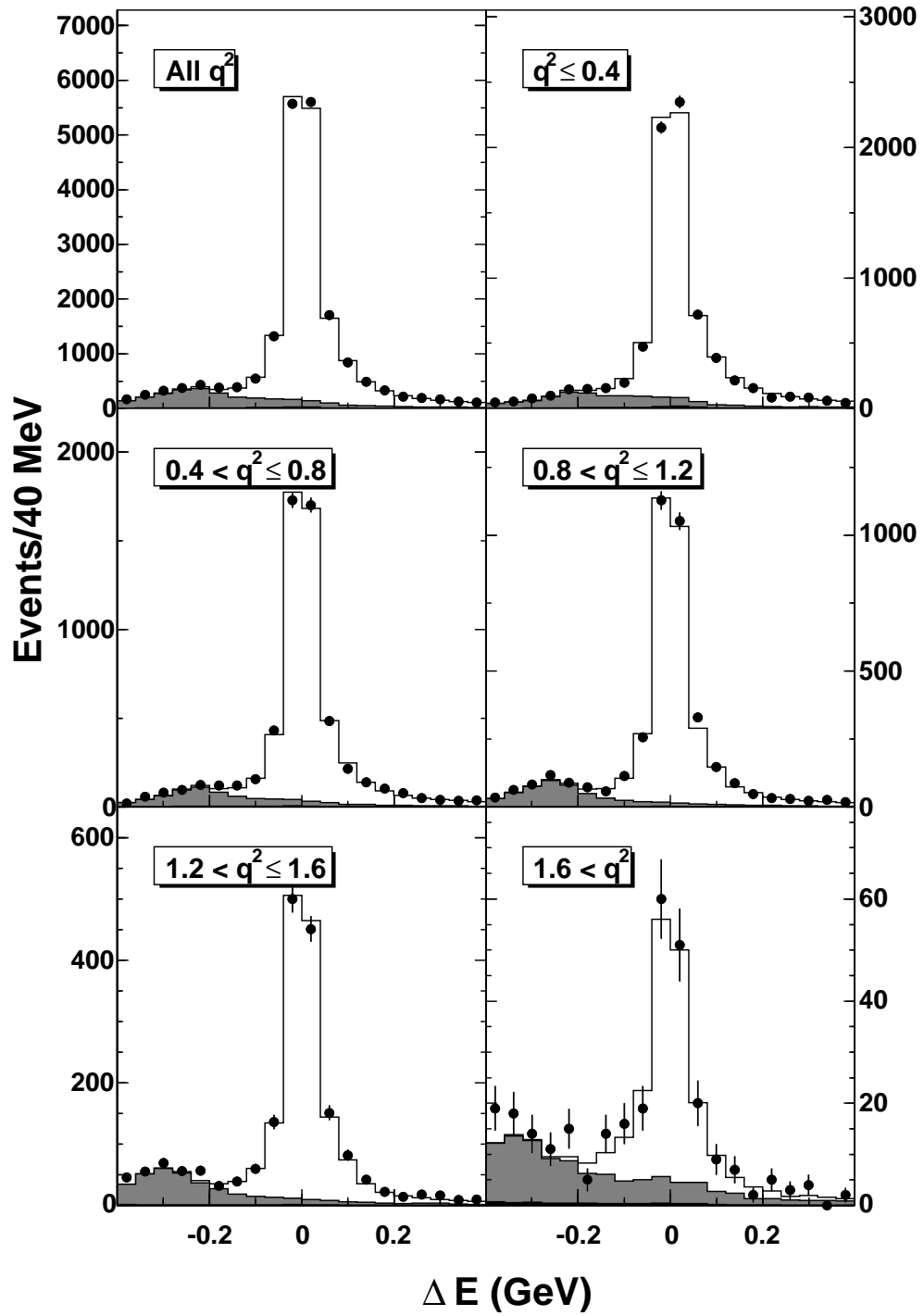


Figure 6.6: Fit scaled ΔE distributions for $D^0 \rightarrow K^- e^+ \nu$. Points represent data (281 pb⁻¹) and stacked histograms are: Clear - Signal MC, Gray - Summed Background MC, Black - Fakes from Data.

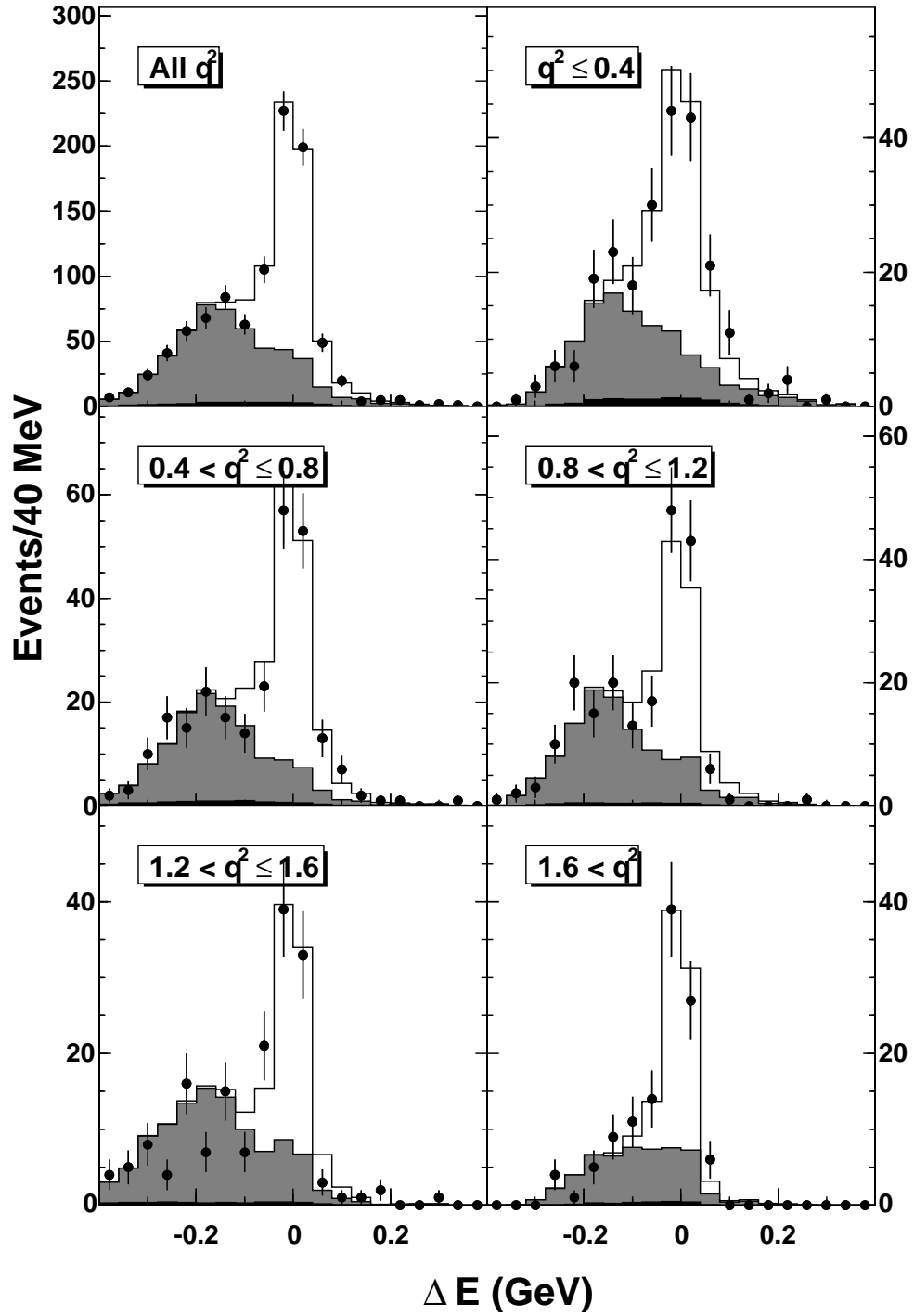


Figure 6.7: Fit scaled ΔE distributions for $D^+ \rightarrow \pi^0 e^+ \nu$. Points represent data (281 pb⁻¹) and stacked histograms are: Clear - Signal MC, Gray - Summed Background MC, Black - Fakes from Data.

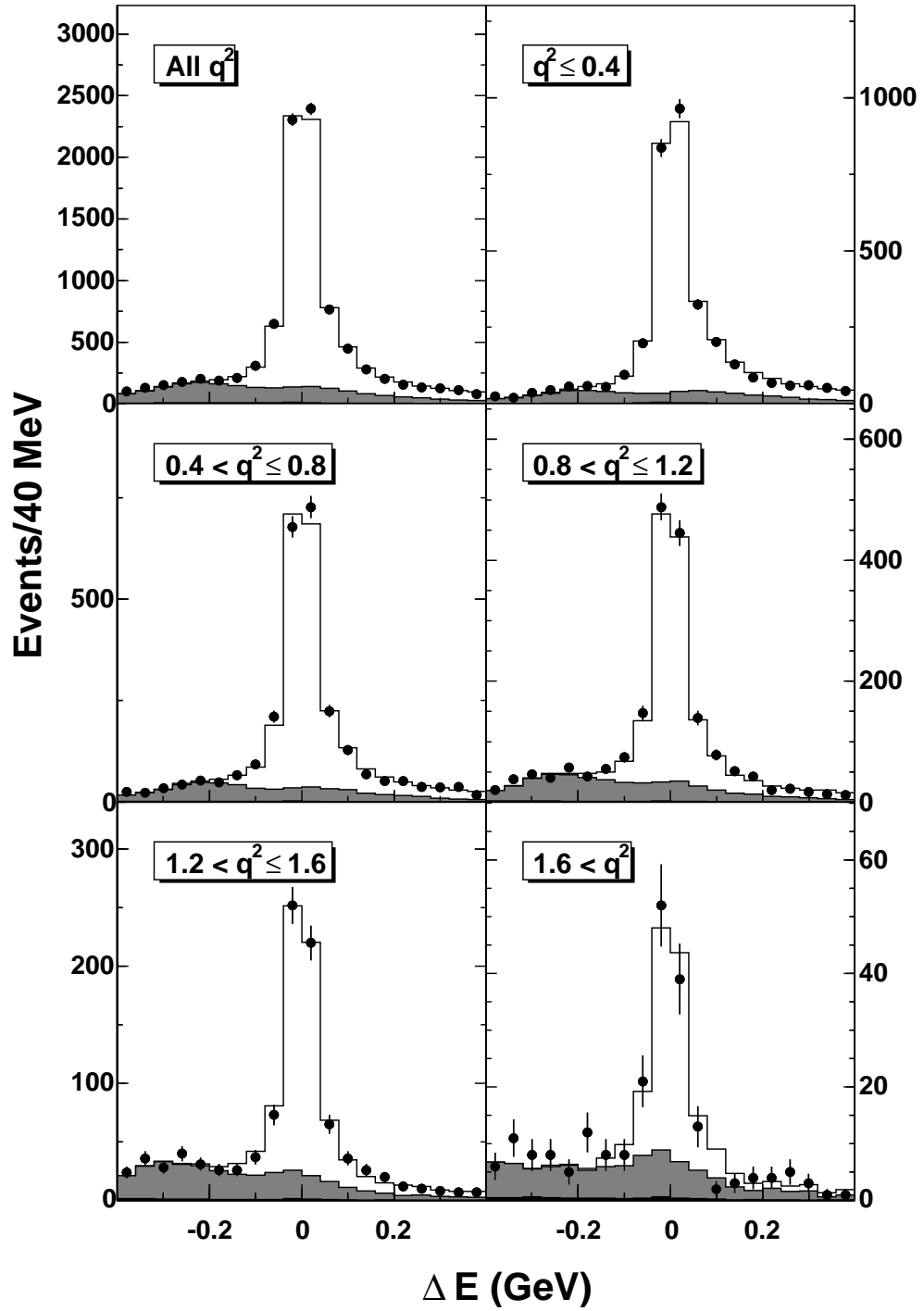


Figure 6.8: Fit scaled ΔE distributions for $D^+ \rightarrow K_S(\pi^+\pi^-)e^+\nu$. Points represent data (281 pb^{-1}) and stacked histograms are: Clear - Signal MC, Gray - Summed Background MC, Black - Fakes from Data.

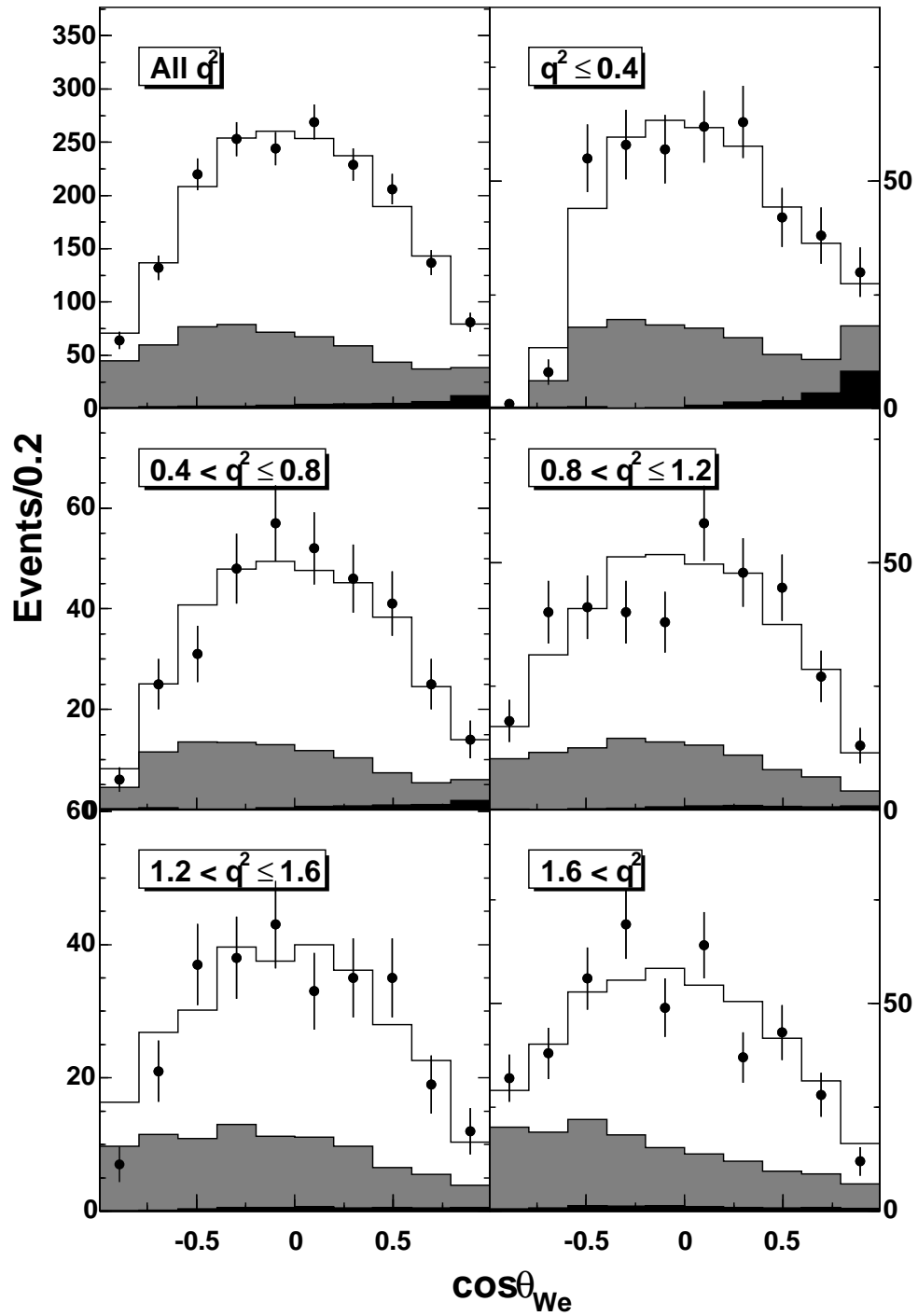


Figure 6.9: Fit scaled $\cos\theta_{We}$ distributions for $D^0 \rightarrow \pi^- e^+ \nu$. Points represent data (281 pb^{-1}) and stacked histograms are: Clear - Signal MC, Gray - Summed Background MC, Black - Fakes from Data.

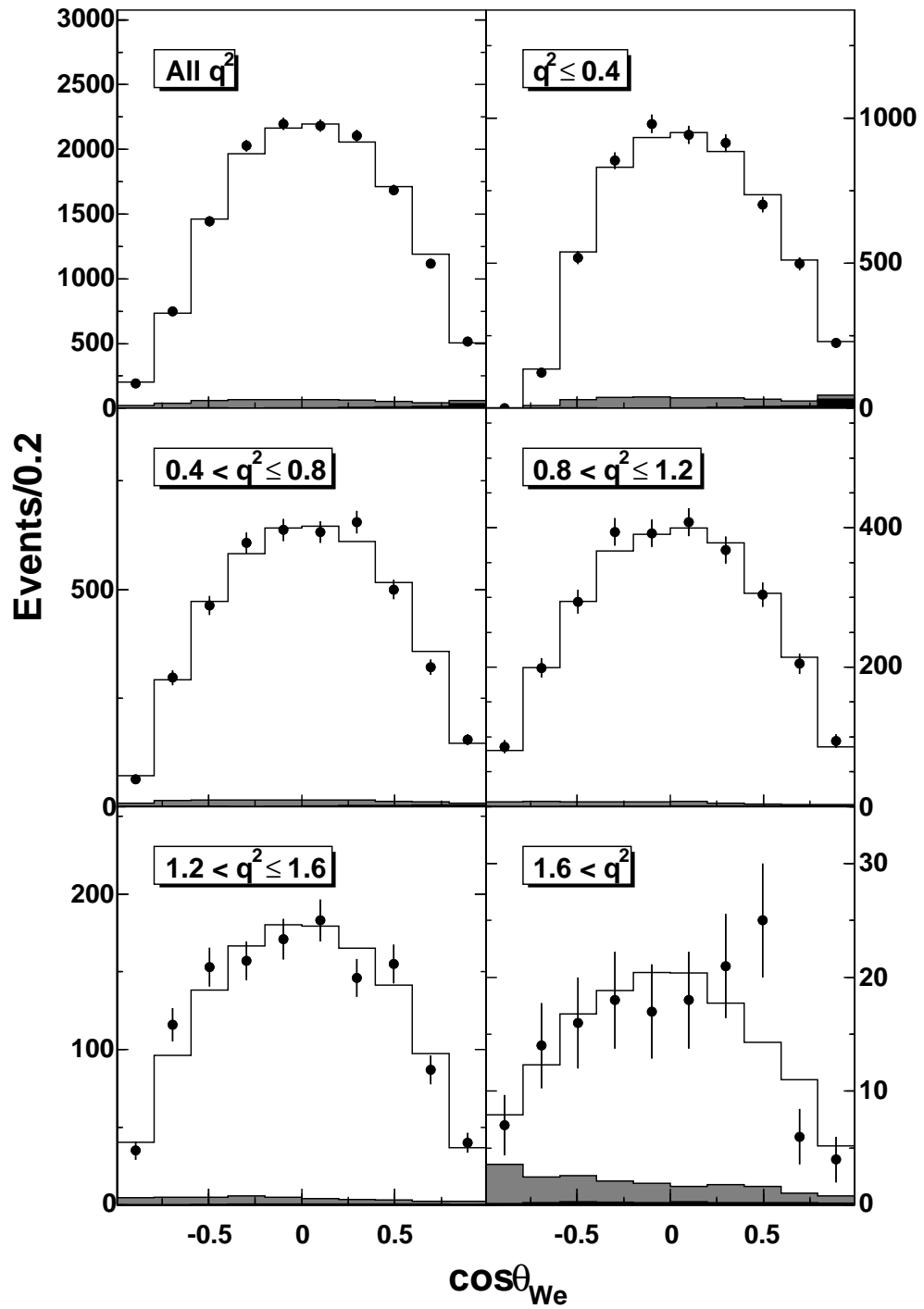


Figure 6.10: Fit scaled $\cos\theta_{We}$ distributions for $D^0 \rightarrow K^- e^+ \nu$. Points represent data (281 pb^{-1}) and stacked histograms are: Clear - Signal MC, Gray - Summed Background MC, Black - Fakes from Data.

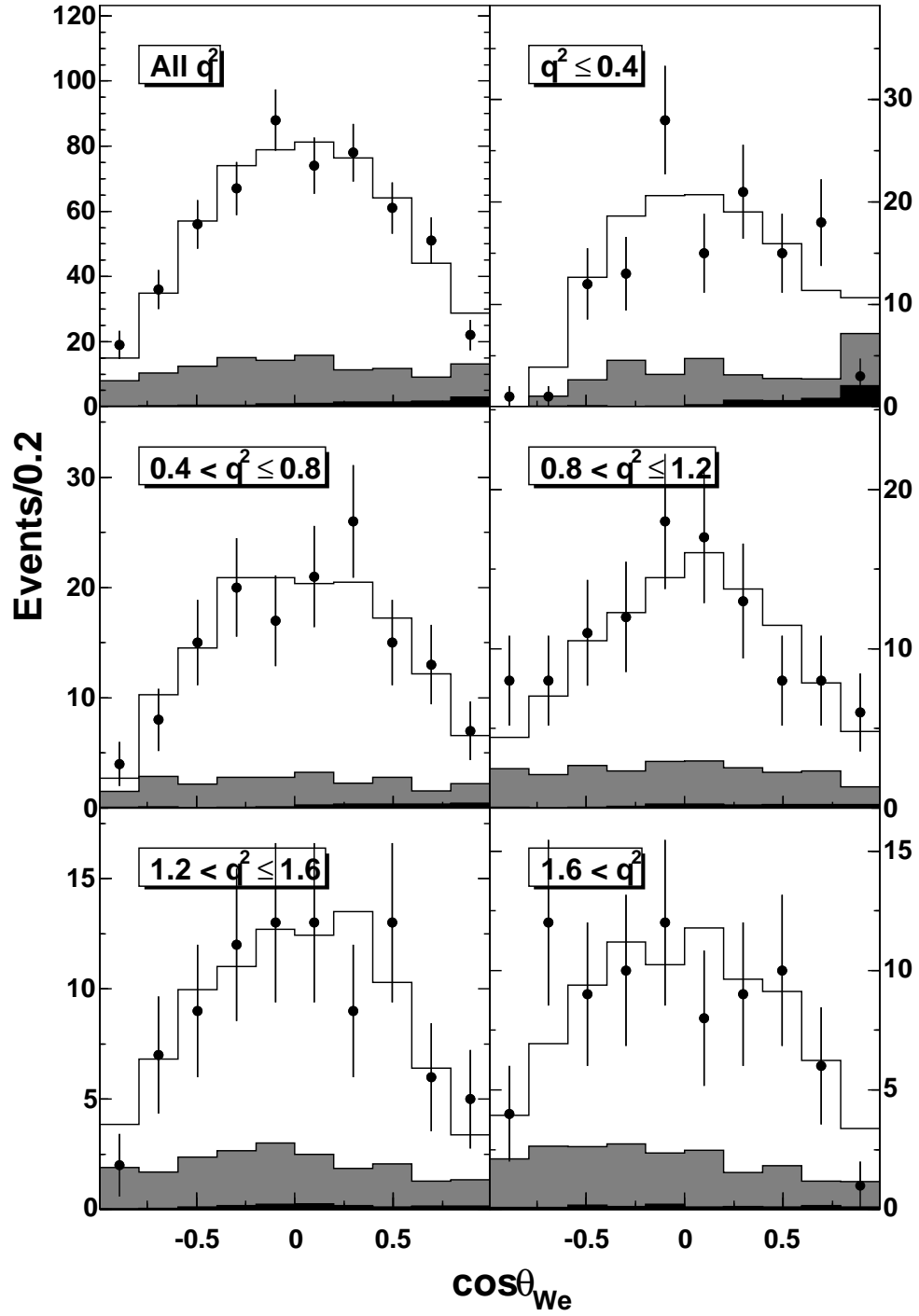


Figure 6.11: Fit scaled $\cos\theta_{We}$ distributions for $D^+ \rightarrow \pi^0 e^+ \nu$. Points represent data (281 pb^{-1}) and stacked histograms are: Clear - Signal MC, Gray - Summed Background MC, Black - Fakes from Data.

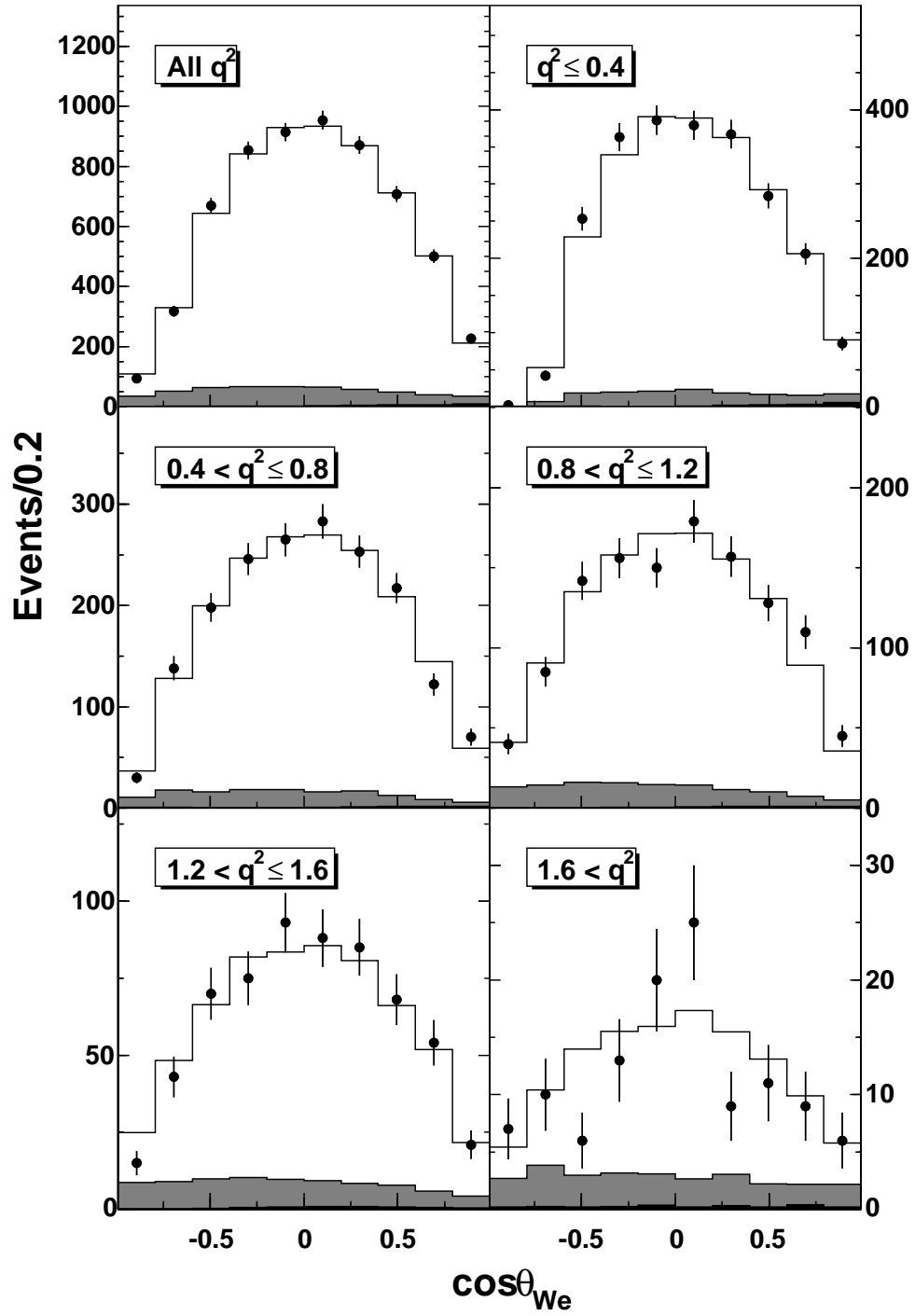


Figure 6.12: Fit scaled $\cos\theta_{We}$ distributions for $D^+ \rightarrow K_S(\pi^+\pi^-)e^+\nu$. Points represent data (281 pb^{-1}) and stacked histograms are: Clear - Signal MC, Gray - Summed Background MC, Black - Fakes from Data.

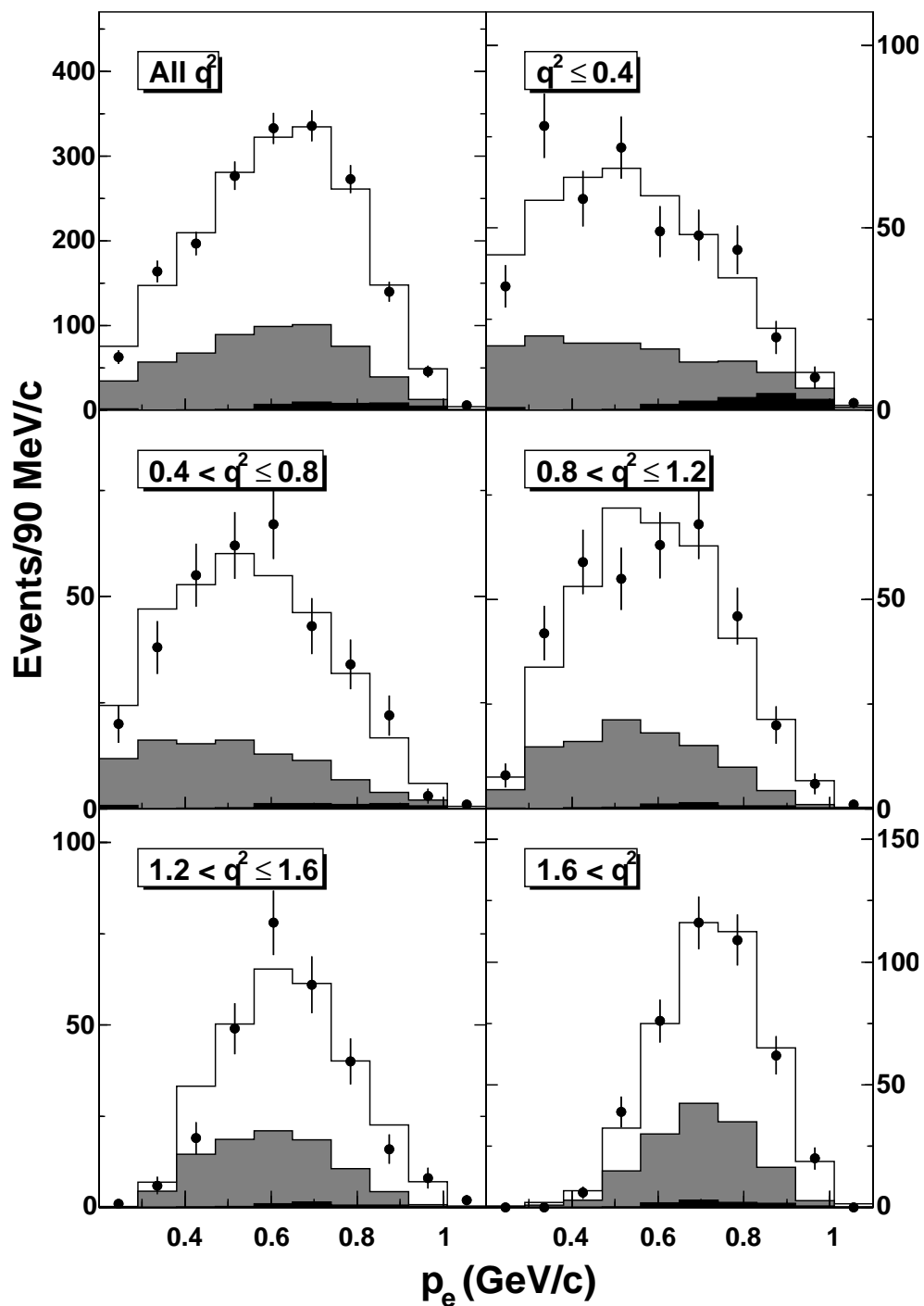


Figure 6.13: Fit scaled p_e (electron momentum) distributions for $D^0 \rightarrow \pi^- e^+ \nu$. Points represent data (281 pb^{-1}) and stacked histograms are: Clear - Signal MC, Gray - Summed Background MC, Black - Fakes from Data.

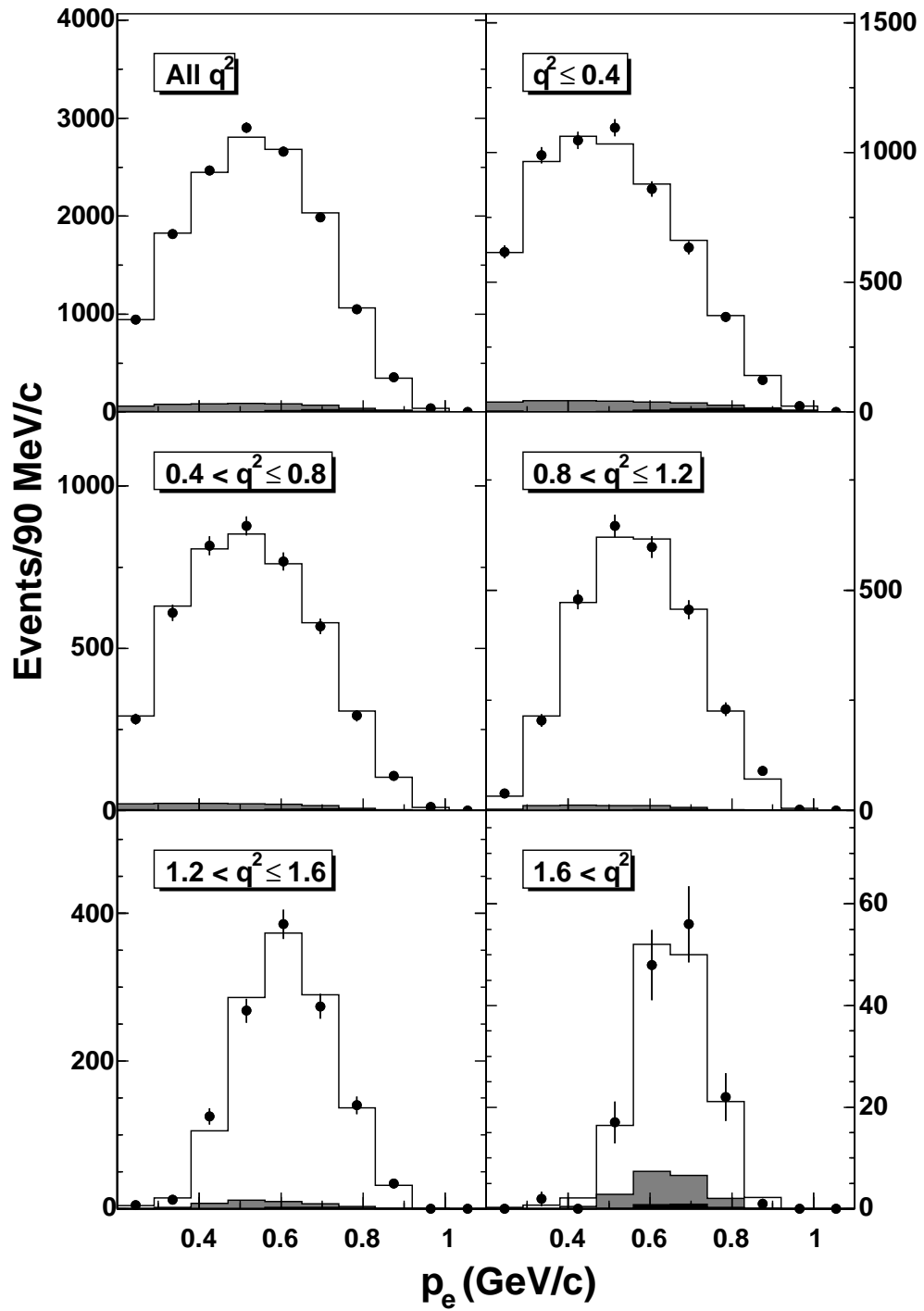


Figure 6.14: Fit scaled p_e (electron momentum) distributions for $D^0 \rightarrow K^- e^+ \nu$. Points represent data (281 pb^{-1}) and stacked histograms are: Clear - Signal MC, Gray - Summed Background MC, Black - Fakes from Data.

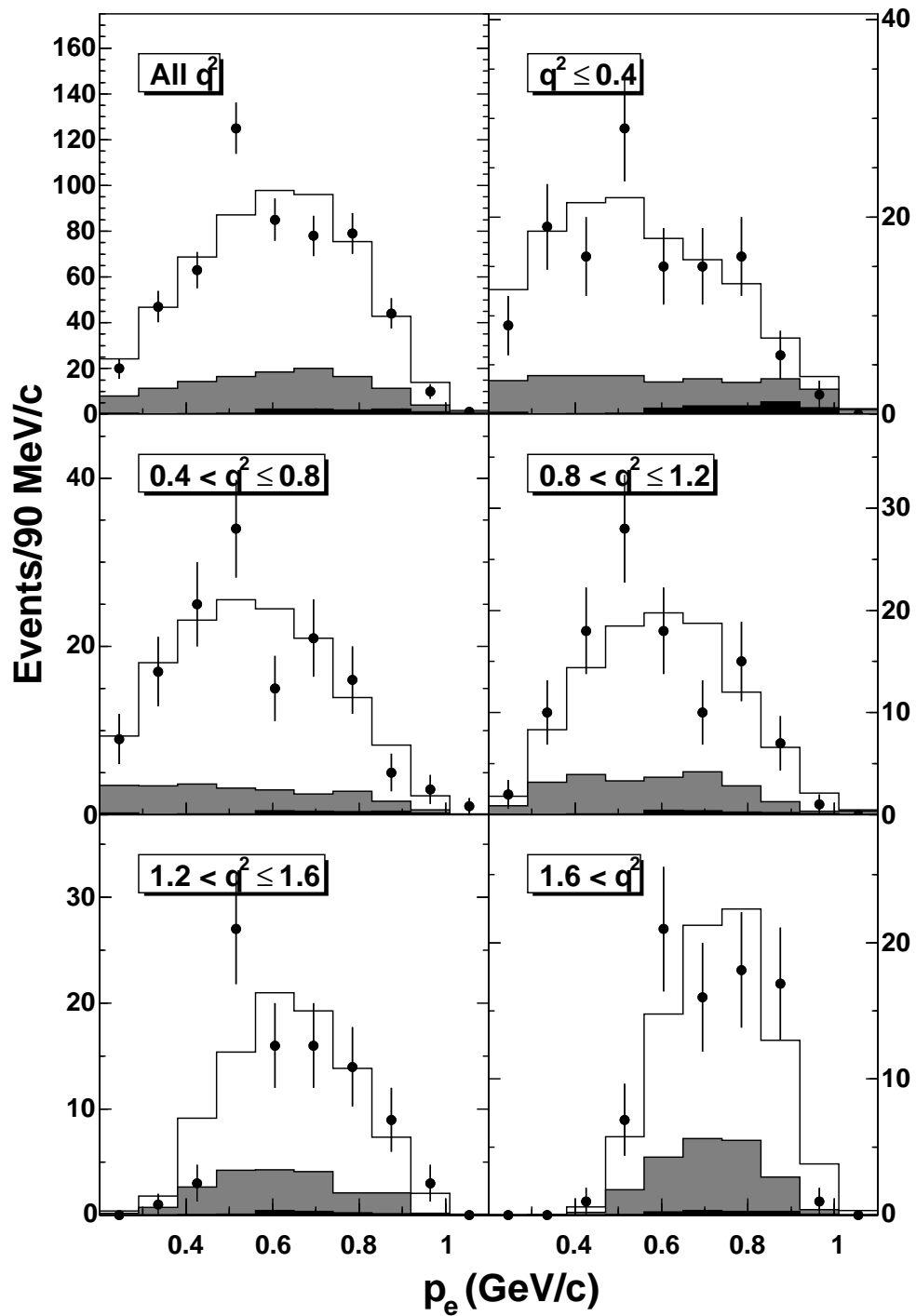


Figure 6.15: Fit scaled p_e (electron momentum) distributions for $D^+ \rightarrow \pi^0 e^+ \nu$. Points represent data (281 pb^{-1}) and stacked histograms are: Clear - Signal MC, Gray - Summed Background MC, Black - Fakes from Data.

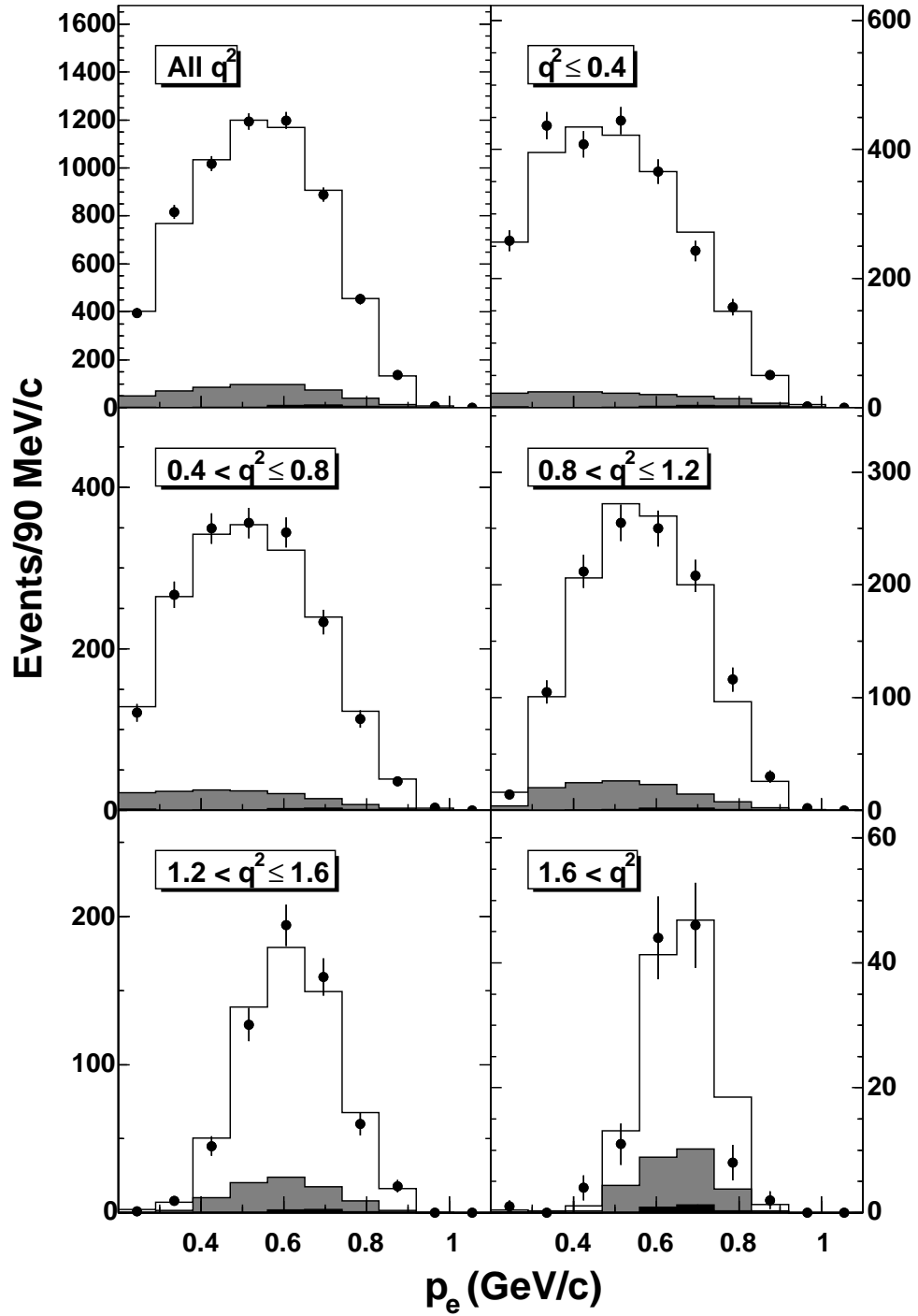


Figure 6.16: Fit scaled p_e (electron momentum) distributions for $D^+ \rightarrow K_S(\pi^+\pi^-)e^+\nu$. Points represent data (281 pb^{-1}) and stacked histograms are: Clear - Signal MC, Gray - Summed Background MC, Black - Fakes from Data.

Table 6.1: Results of fit to generic $D\bar{D}$ MC sample with statistics of $40 \times \mathcal{L}_{\text{data}}$. We define $Y_{\text{input}} =$ input yield, $Y_{\text{fit}} =$ efficiency corrected yield from the fit and $\sigma_{Y_{\text{fit}}} =$ one sigma error on the efficiency corrected fit yield. The q^2 bins are as given in the text.

<i>Decay Mode</i>	$(Y_{\text{input}} - Y_{\text{fit}})/\sigma_{Y_{\text{fit}}}$					<i>All q^2</i>
	< 0.4	$0.4 - 0.8$	$0.8 - 1.2$	$1.2 - 1.6$	≥ 1.6	
$D^0 \rightarrow \pi^- e^+ \nu$	0.55	-0.92	0.98	-0.33	1.16	0.51
$D^0 \rightarrow K^- e^+ \nu$	-2.34	1.27	1.54	0.18	0.99	-0.14
$D^+ \rightarrow \pi^0 e^+ \nu$	-1.57	0.37	-0.55	0.85	0.98	-0.95
$D^+ \rightarrow K_S e^+ \nu$	-0.29	-0.49	1.77	1.14	0.54	0.76

Chapter 7

Systematic Uncertainties

To evaluate the systematic uncertainties for this analysis we take each source of systematic error in turn and re-run the analysis with the error source modified by approximately one standard deviation. The resulting central values are then subtracted from the nominal central values to give the systematic errors. In this chapter we examine each source of systematic uncertainty in turn and derive its appropriate one standard deviation modification.

7.1 Hadronic Shower Addition

It is known that the modeling of hadronic showers in the MC is not always accurate in every regard. For neutrino reconstruction we can be strongly affected by such a discrepancy due to the fact that these showers are important in the reconstruction of the missing four-momentum. In particular, we would like to know if the MC has the correct number of hadronic splitoff showers (as described earlier), a factor that affects the neutrino resolution.

To examine the hadronic showers we use the CLEO-c sample of D double tags, that is events containing two hadronically decaying D mesons. The double tagged modes used are: $D^0 \rightarrow K\pi$ vs $D^0 \rightarrow K\pi$, $D^0 \rightarrow K\pi$ vs $D^0 \rightarrow K\pi\pi^0$, $D^0 \rightarrow K\pi\pi^0$ vs $D^0 \rightarrow K\pi\pi^0$, $D^0 \rightarrow K\pi$ vs $D^0 \rightarrow K\pi\pi\pi$, $D^0 \rightarrow K\pi\pi^0$ vs $D^0 \rightarrow K\pi\pi\pi$ and $D^0 \rightarrow K\pi\pi\pi$ vs $D^0 \rightarrow K\pi\pi\pi$. Events containing these selected modes are required to satisfy the following criteria:

- The reconstructed D tags do not overlap (i.e. no overlapping tracks or show-

ers)

- Both tags satisfy $|\Delta E| < 0.02$ GeV
- Both tags satisfy $|M_{bc} - M_D| < 0.01$ GeV.

With the double tag sample we may count the number of extra showers in each event. In general a shower is considered to be an “extra” shower if it is not proximity matched to any track and does not belong to any of the signal π^0 's. In this case we also require that the shower be Splitoff approved, since for this systematic uncertainty we are concerned only with the extra showers that will add to the missing four-momentum. Using this counting method we then compare the number of extra showers per track in data and MC. Of course, in looking at the number of extra showers *per track* we are assuming that the extra showers in an event are in some way caused by charged hadrons. This idea is motivated by the fact that the extra showers are most likely hadronic splitoffs: secondary showers caused by energetic particles generated in charged-hadron showers. To demonstrate that this is a valid assumption we study the distance from each shower to the nearest track, as measured from the shower center to the projection of the track into the calorimeter. The correlation between extra showers and tracks is tested by comparing the distribution of these distances for extra showers with the same distribution for showers from π^0 's. The resulting spectra, given in Fig. 7.1, clearly demonstrate that extra showers are associated with tracks.

Using the double tag method to count the extra showers, we find that overall the data contains more extra showers per track than the MC. On average $11.28 \pm 0.21\%$ of data tracks are associated with an extra shower, while in MC the number is significantly lower at $9.02 \pm 0.03\%$, a difference of $2.26 \pm 0.21\%$. In addition, it is

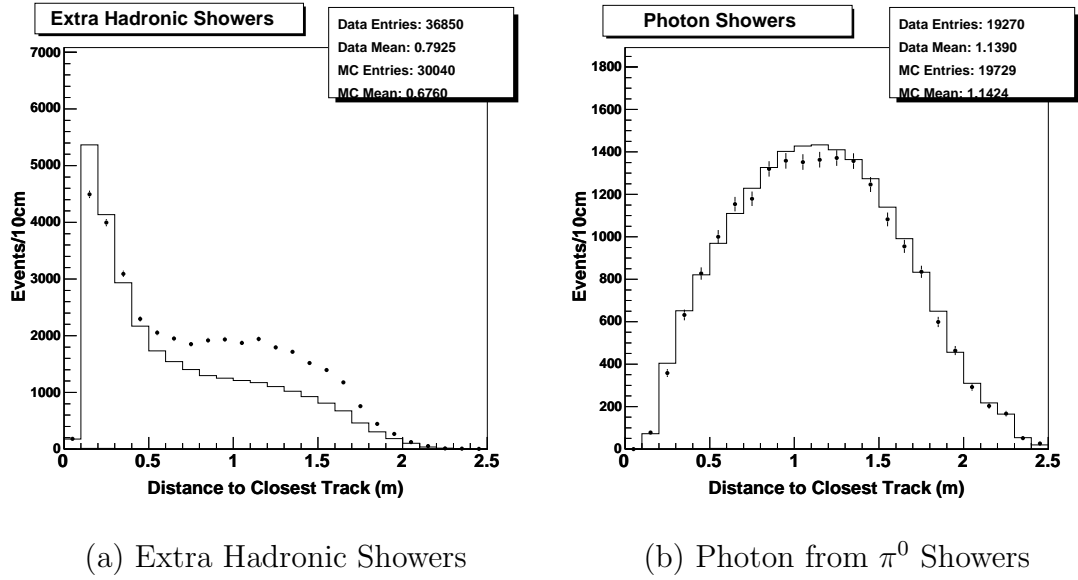


Figure 7.1: Distance to the nearest track (measured from track projection into the crystal calorimeter) for (a) Extra Hadronic Showers and (b) Photon from π^0 Showers. Points show data and the open histogram shows $D^0\bar{D}^0$ MC normalized to the number of selected data double tag events. In this case the extra hadronic showers are all extra showers in the event with energy greater than 25 MeV, i.e., we have not required that the showers be Splitoff approved.

evident that the data MC discrepancy is not flat across the double tag modes, but rather shows a clear dependence on the number of hadrons (charged and neutral) per event, see Fig 7.2. The most obvious source of such a dependence is if the data

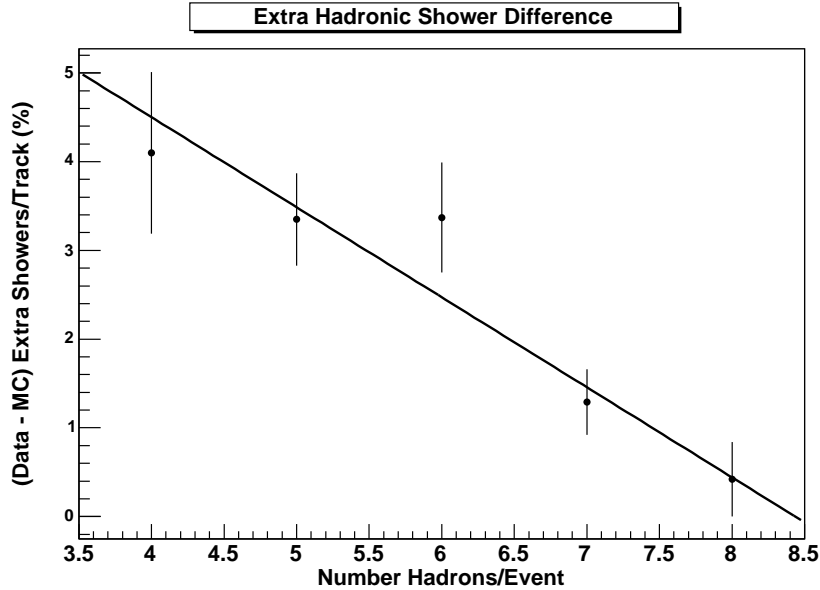


Figure 7.2: The difference in the number of extra showers per track between data and MC is plotted against the number of hadrons (charged + neutral) per event (different for each of the five double tag modes). The line shows the linear best fit to the data and clearly demonstrates the dependence of the difference on the number of hadrons.

MC extra shower discrepancy were somehow dependent on the track momentum. The difference as a function of track momentum is shown in Fig. 7.3. The resulting distribution can be modeled with an exponential function, also shown in the figure.

We correct the MC by adding showers according to the measured discrepancy between MC and data. Specifically, we loop over hadronic tracks and for each

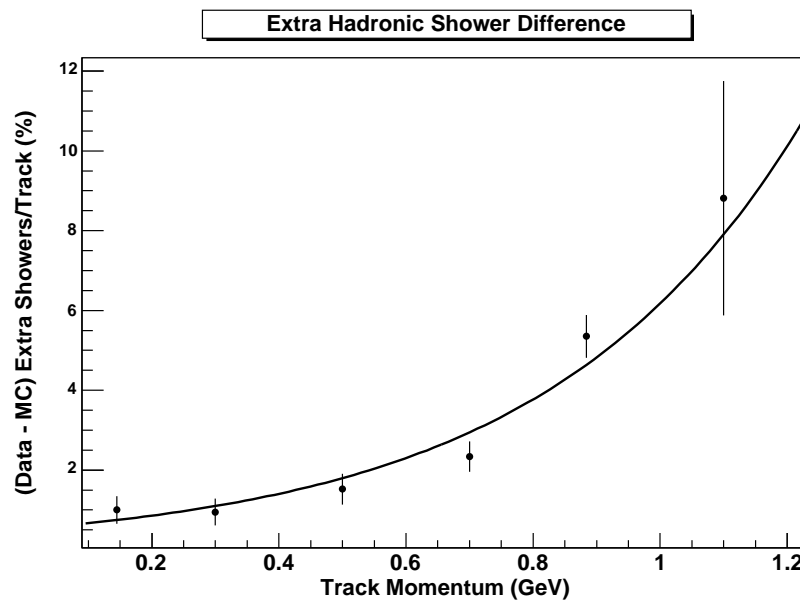


Figure 7.3: The difference in the number of extra showers per track between data and MC is plotted against the momentum of the closest track. The curve shows the best exponential fit to the data and clearly demonstrates the dependence of the difference on the track momentum.

one we compare a random number with that track's probability of requiring an associated extra shower. If a shower is added, we choose an energy and a distance from the parent track at random from the MC distribution of these values, which studies show to be reliable.¹ Finally, the shower is appended to the total list of showers and forced onto the list of showers to be used for neutrino reconstruction.

Our main concern in this endeavor therefore, is to define the probability with which we should add the additional MC showers. In fact, from the preceding discussion it can be seen that there are two possible ways to calculate this quantity. The probability for a MC generated charged hadron to acquire an extra shower can be extracted from either the momentum of the associated track and the exponential distribution in Fig. 7.3, or from the total number of charged and neutral hadrons in the event, Fig 7.2.

If we choose the second method, based on the total number of hadrons in the event, there is one draw back: at the time of shower addition we don't actually know the number of neutral hadrons (essentially π^0 's) in the event, only the number of hadronic tracks. This is a result of a technical difficulty in analyzing the data: we must add the extra MC showers *before* the total list of showers is used in π^0 reconstruction. Thus, rather than using Fig. 7.2, we are reduced to looking at the dependence on the number of tracks per event (i.e, we can use only the charged hadrons), as shown in Fig. 7.4. In this case we extract the probability of an extra shower using a piece-wise linear fit to the three points in Fig 7.4. There is a danger, however, that in events with few tracks this method will badly overestimate the probability of adding a shower (i.e., because the total number of

¹If the energy and distance fall into a category that would be excluded by Splitoff we do not add this shower. To maintain the correct overall probability we must correct our input probability for these dropped showers.

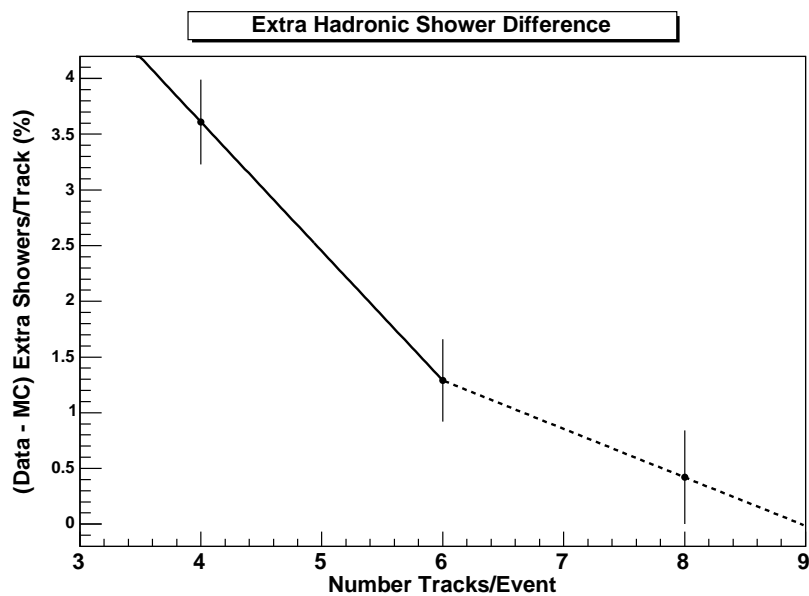


Figure 7.4: The difference in the number of extra showers per track between data and MC versus the number of tracks per event. The lines (solid and dashed) show a piece-wise linear fit to the data.

hadrons in the event could still be large). For this reason we prefer to take the track momentum method as our nominal MC fix: using the exponential fit to the data (Fig. 7.3) to calculate the rates with which extra hadronic showers should be added. To calculate the one standard deviation systematic uncertainty on the hadronic shower discrepancy, we compare the results of our nominal method to those obtained using the linear method (or number of tracks per event method). Since the results from the linear method are known to be an overestimate, this difference gives us a good estimate of the uncertainty on our MC hadronic shower correction.

7.2 Shower Smearing

There is a systematic uncertainty associated with the resolution of showers in the CLEO-c crystal calorimeter. This uncertainty will once again affect the modeling of neutrino resolution via the neutral four-momentum sum. The calorimeter resolution has been measured for single photon MC [36], along with the required correction to this nominal resolution in order to match the data [39]. It is found that in general the MC underestimates the shower resolution, requiring a relative correction of $6 \pm 3\%$. In other words, the MC resolution should be increased by a factor of 1.06 to match the resolution found in data. Summing the central value and error in quadrature we find an upper limit on the MC correction of $\sim 7\%$. We therefore choose this as our “smear” value to obtain the associated systematic uncertainty for our analysis.

Specifically, to estimate the systematic uncertainty we smear the momentum of all MC showers tagged to true photons (i.e., degrade their resolution) using the

formula

$$\vec{p}' = \vec{p} + s(\vec{p} - \vec{p}_\gamma). \quad (7.1)$$

Here \vec{p} is the original shower momentum, \vec{p}' is the smeared shower momentum, \vec{p}_γ is the generated momentum of the photon causing the shower, and s is the chosen smear value or fractional resolution adjustment (in our case $s = 0.07$). The smeared shower energy is just the magnitude of the momentum, $E' = |\vec{p}'|$.

7.3 Splitoff Smearing

As we described earlier, during the process of approving showers for neutrino reconstruction the showers are passed through a neural net.² The neural net selection criteria depend on a shower's energy, position in the detector and proximity to tracks. If the neural net distributions differ in MC and data this will be another source of systematic uncertainty affecting the neutrino resolution. To obtain a quantitative estimate regarding the effect of this uncertainty on the analysis, we need a way of examining the Splitoff neural net distributions for true photons and hadronic splitoffs in both MC and data. Once again we turn to the CLEO-c D double tags.

Using double tags, we follow the same procedure as for the hadronic shower addition systematic (see Section 7.1) to find extra showers and true photon showers. The resulting distributions of Splitoff neural net value for the two types of shower are shown in Fig. 7.5. Since the neural net selection criteria are binned in shower energy, we also compare the data and MC neural net distributions separately for each energy bin. The eight energy bins, given in GeV are: < 0.05 , $0.05 - 0.075$,

²In fact, each shower is passed to one member of a set of neural nets, with each neural net applying to a specific range of shower energies, track types, etc.

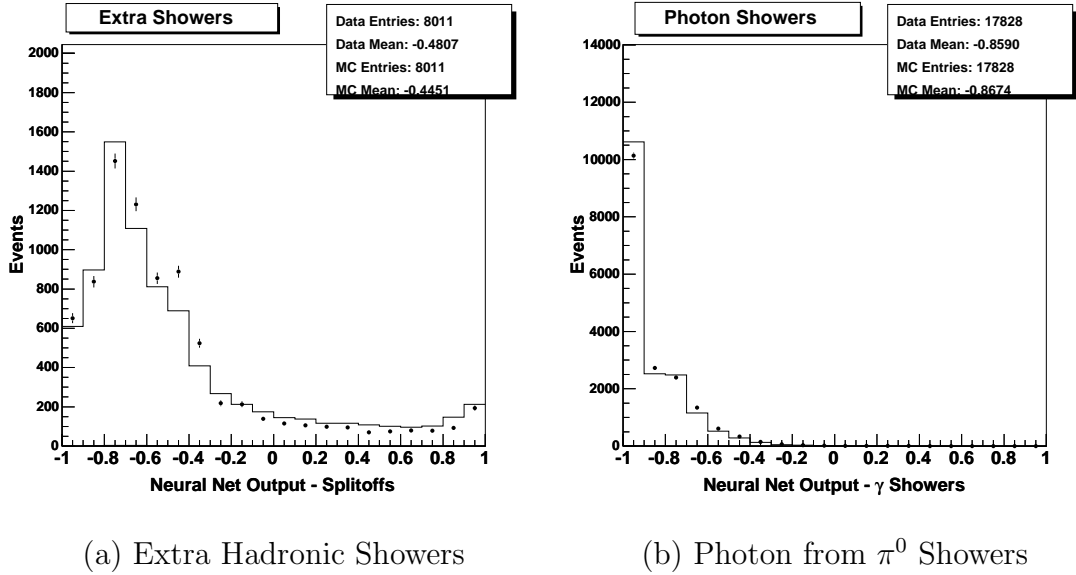


Figure 7.5: Splitoff Neural Net output distributions for (a) Extra Hadronic Showers and (b) Photon from π^0 Showers. Points show data and the open histogram shows $D^0\bar{D}^0$ MC normalized to the number of data entries.

0.075 – 0.1, 0.1 – 0.2, 0.2 – 0.3, 0.3 – 0.4, 0.4 – 0.6 and ≥ 0.6 . We choose a χ^2 comparison test to determine the difference between the data and MC distributions. The comparison test is performed on MC normalized to the number of data entries so as to obtain the best shape comparison and exclude the effects of such things as missing hadronic showers in the MC.

To evaluate the systematic uncertainty we use these χ^2 differences to determine a 1σ smear for the Splitoff neural net distributions in MC. As we do not have access to the total neural net distributions when the MC is being analyzed, however, we must adjust the neural net value of each shower individually in such a way as to produce the desired final result. This is achieved by selecting the neural net adjustment for each shower at random from a Gaussian distribution, the characteristics of which depend on the type of shower and its deviation from

the expected value. For true photon showers we wish to smear the neural net value toward the hadronic shower end of the spectrum (i.e., toward +1), and we thus *add* an adjustment chosen at random from the Gaussian distribution characterized by $\mu = 0$ and $\sigma = b|N + 1|$, where N is the original neural net value and b is the bias controlling the amount of smearing. Similarly for extra showers, or splitoffs, we wish to smear in the opposite direction (i.e., toward -1), so we adjust the neural net value by *subtracting* a random value chosen from the Gaussian distribution given by $\mu = 0$ and $\sigma = b|N - 1|$.

It is the value of the bias, b , giving the 1σ smear that needs to be determined for the systematic uncertainty. In each energy bin and for the two distributions, we choose this value to be that of the bias which gives a χ^2 difference between the data and MC distributions of ~ 1 from the minimum.³ The resulting bias values used to estimate the systematic error are given in Table 7.1.

7.4 K_L Energy Deposition

To correctly model the process of neutrino reconstruction in the MC it is important that the properties of K_L 's are also modeled accurately. Any mismatches between data and MC regarding K_L 's will be a source of systematic uncertainty, affecting the efficiency and resolution of neutrino reconstruction as discussed earlier. The two most important K_L properties to examine are energy deposition in the crystal calorimeter and the momentum spectrum (in terms of both rate and shape), which we will talk about in the next section. The first systematic uncertainty we focus on is that relating to the showering properties of K_L 's. These properties have been

³We note that the minimum is not necessarily the nominal value of the χ^2 difference, as sometimes the initial smearing actually improves the agreement. For the systematic error we go beyond this minimum to the next $\Delta\chi^2 = 1$ bias value.

Table 7.1: Final smear bias values for the Splitoff neural net systematic uncertainty.

<i>Energy Bin</i>	<i>True Photon Bias</i>	<i>Extra Shower Bias</i>
$0.000 < E \leq 0.050$	0.01	0.2
$0.050 < E \leq 0.075$	0.02	0.1
$0.075 < E \leq 0.100$	0.02	0.075
$0.100 < E \leq 0.200$	0.02	0.1
$0.200 < E \leq 0.300$	0.02	0.2
$0.300 < E \leq 0.400$	0.03	0.15
$0.400 < E \leq 0.600$	0.03	0.3
$E > 0.600$	0.15	0.2

studied extensively in CLEO-c [35] and it is found that the data and MC differ significantly in both the fraction of K_L 's that deposit energy in the calorimeter and in the distribution of the energy deposited. In data K_L 's shower $52.2 \pm 1.3\%$ of the time, whilst in MC they shower only $46.7 \pm 0.3\%$ of the time. The difference in the X_E distributions, where X_E is the fraction of the K_L energy deposited as showers, is shown in Fig. 7.6.

To fix this problem in our analysis we add K_L showers to the MC in approximately 10% of cases where the K_L did not shower. We distribute the energy of these showers in order to fill the gap in the MC X_E distribution as compared to data. We take the fixed case as our nominal value and use the original MC to estimate the systematic error.

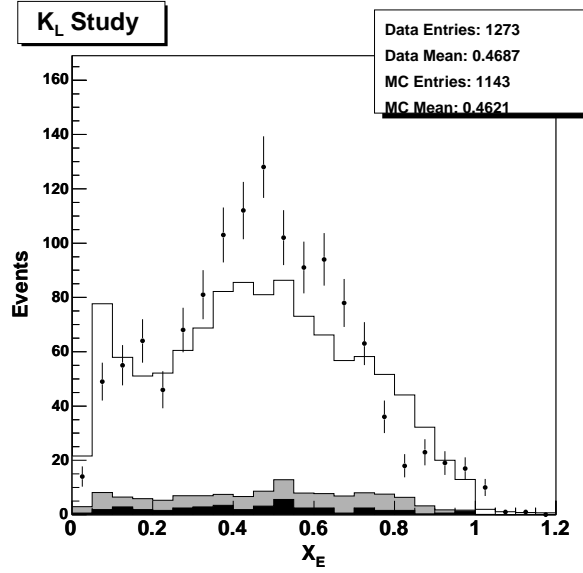


Figure 7.6: X_E distribution for events with missing energy consistent with a K_L (see [35] for details). Points show data and stacked histograms show Monte Carlo samples normalized by luminosity (background) and number of decays (signal). The colors represent: Clear - Signal, Grey - $D\bar{D}$ background and Black - Continuum.

7.5 K_L Re-weight

As we mentioned above, the K_L momentum spectrum can also affect neutrino reconstruction. To find the systematic uncertainty associated with the modeling of this spectrum in MC, we look at the K_S momentum spectrum in both data and MC. The K_S sample is obtained from events containing a tagged D meson. We look separately for D^+D^- events and $D^0\bar{D}^0$ events using all available tag modes⁴. In addition, since we are interested in the momentum spectra of K_S 's coming from generically decaying D 's, events containing electrons are vetoed to remove as

⁴The quality of the K_S sample did not seem to be affected by the choice of tag, so we use the largest sample possible.

many K_S 's from non-hadronic decays as possible. The tagged D is then required to satisfy:

- $|\Delta E| < 0.02 \text{ GeV}$
- $|M_{bc} - M_D| < 0.01 \text{ GeV}$.

We take any K_S from the other side of the event (i.e., not part of the tagged D) that satisfies:

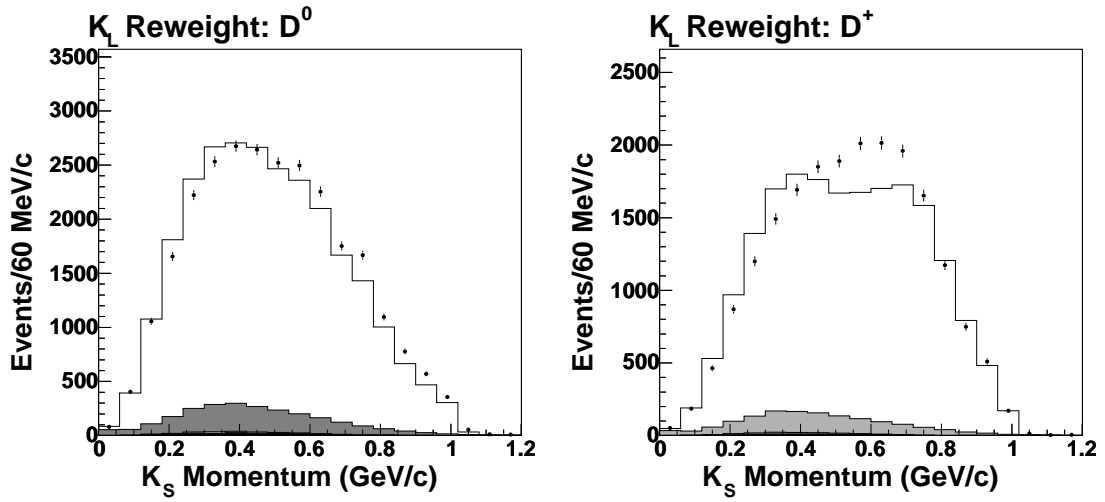
- $0.491 < M_{K_S} < 0.503 \text{ GeV}$
- K_S passes clean vertex (vertex fit succeeded and flight significance ≥ 3).

The resulting momentum spectra for these K_S 's are shown in Fig. 7.7.

These spectra show some differences in shape between data and MC, and also some difference in the overall number of K_S 's. We correct these differences by re-weighting MC events containing a K_L in order to match the data. The re-weighting uses the momentum binning shown in Fig. 7.7. It is the re-weighted MC that we use in our nominal fit. To estimate the systematic error associated with the K_L production spectra, we modify the weights by their one standard deviation errors and then re-fit the data with these distorted spectra.

7.6 Pion Momentum Spectra Re-weight

The backgrounds in the two pion signal modes receive their major contributions from cross-feed of the other signal modes. The cross-feed background is most commonly caused by selecting, as the signal hadron, a pion from the generically decaying side of the event. For this reason it is important that the charged and neutral pion momentum spectra in these generic decays be corrected to the observed



(a) $D^0\bar{D}^0$ K_S Momentum Spectrum (b) D^+D^- K_S Momentum Spectrum

Figure 7.7: K_S momentum distributions for (a) $D^0\bar{D}^0$ events and (b) D^+D^- events. Points show data and the stacked histograms show MC. The colors represent: Clear - True K_S , Dark Gray - Background from $D^0\bar{D}^0$ MC, Light Gray - Background from D^+D^- and Black - Background from continuum MC. The normalization is absolute.

data values when considering cross-feed backgrounds to the pion signal modes. To make these corrections we follow the same D tagging procedure as outlined above for the K_S momentum spectra. The resulting momentum spectra in data and MC for π^0 's and π^\pm 's are shown in Figs 7.8 and 7.9 respectively.

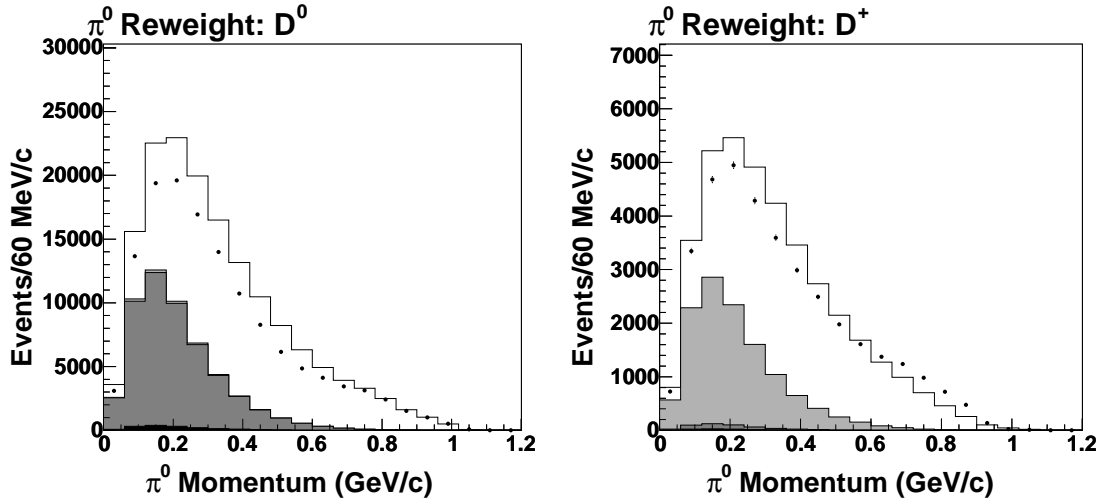
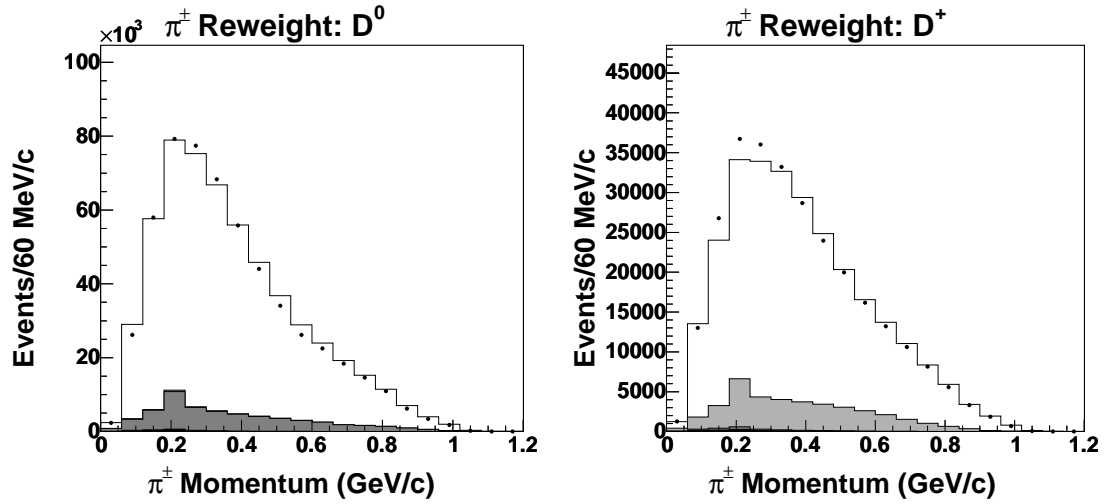
(a) $D^0\bar{D}^0$ π^0 Momentum Spectrum(b) D^+D^- π^0 Momentum Spectrum

Figure 7.8: Signal π^0 momentum distributions for (a) $D^0\bar{D}^0$ events and (b) D^+D^- events. Points show data and the stacked histograms show MC. The colors represent: Clear - True π^0 , Dark Gray - Background from $D^0\bar{D}^0$ MC, Light Gray - Background from D^+D^- and Black - Background from continuum MC. The normalization is absolute.

We correct the differences in shape and normalization by re-weighting MC background events in $D^0 \rightarrow \pi^- e^+ \nu$ or $D^+ \rightarrow \pi^0 e^+ \nu$ according to the momentum of the falsely chosen signal pion. The re-weighting uses the momentum binning shown in Figs. 7.8 and 7.9. In the charged pion case we re-weight only in the event of a true pion to prevent the incorrect weighting of backgrounds from fakes, which are dealt with separately. In both cases the nominal fit has the re-weight applied



(a) $D^0\bar{D}^0$ π^\pm Momentum Spectrum (b) D^+D^- π^\pm Momentum Spectrum

Figure 7.9: Signal π^\pm momentum distributions for (a) $D^0\bar{D}^0$ events and (b) D^+D^- events. Points show data and the stacked histograms show MC. The colors represent: Clear - True π^\pm , Dark Gray - Background from $D^0\bar{D}^0$ MC, Light Gray - Background from D^+D^- and Black - Background from continuum MC. The normalization is absolute.

and we take the systematic uncertainty to be the resulting difference when the re-weight is dropped.

7.7 Kaons Faking Pions

In the $D^0 \rightarrow \pi^- e^+ \nu$ signal mode there is a sizeable background contribution from $D^0 \rightarrow K^- e^+ \nu$ cross-feed. Some of this background will be caused by the kaon faking a signal pion and will be peaking in M_{bc} . It is thus important to know that the rate of kaons faking pions is correctly estimated in the MC. To measure these rates in data and MC we turn once again to the tagged sample. We take a D tag and look on the other side of the event for a $D^0 \rightarrow K\pi$ or $D^0 \rightarrow K\pi\pi^0$ decay if the tag is neutral, or a $D^+ \rightarrow K\pi\pi$ decay if the tag is charged. We use the tag modes: $D^0 \rightarrow K\pi$, $D^0 \rightarrow K\pi\pi^0$, $D^0 \rightarrow K\pi\pi^0\pi^0$, $D^0 \rightarrow K\pi\pi\pi$, $D^0 \rightarrow K\pi\pi\pi\pi^0$, $D^+ \rightarrow K\pi\pi$, $D^+ \rightarrow K\pi\pi\pi^0$, $D^+ \rightarrow K_S\pi$, $D^+ \rightarrow K_S\pi\pi^0$, $D^+ \rightarrow K_S\pi\pi\pi$ and $D^+ \rightarrow KK\pi$. The tag is required to satisfy:

- $|\Delta E| < 0.02$
- $|M_{bc} - M_D| < 0.01$

On the signal side of the event we must find the correct number of tracks and π^0 's, and the kaon track is identified using the flavor of the tagged D . The charged pions are required to pass signal pion criteria and the π^0 , if present, is required to be from the best set of non-overlapping π^0 's with a pull mass less than 2σ . In addition, to remove background, we require $|\Delta E| < 0.03$. We then fit the M_{bc} distributions in data using the MC signal and background histograms for each mode. The signal histogram is defined to be the set of events where the track identified as a kaon was a true kaon. The total number of events is constrained

so that there is just one parameter in the fit: the fraction of signal events. In each mode we fit the data histograms for both the whole sample and the subset of events in which the kaon track passed our signal pion identification criteria. The resulting fake rates in data and MC, and the required corrections to the MC, are given in Table 7.2.

Table 7.2: Rates of K^\pm faking π^\pm in data and MC, where f gives the fake rate and p_K is the kaon momentum.

<i>Method 1 - Signal Shape Fit</i>			
<i>Momentum Bin</i>	f_{MC}	f_{data}	<i>MC Correction</i>
$p_K < 0.6 \text{ GeV}/c$	0.0293 ± 0.0003	0.0578 ± 0.0035	1.9744 ± 0.1208
$0.6 \leq p_K < 0.7 \text{ GeV}/c$	0.0248 ± 0.0005	0.0538 ± 0.0034	2.1674 ± 0.1826
$0.7 \leq p_K < 0.8 \text{ GeV}/c$	0.0481 ± 0.0006	0.0619 ± 0.0039	1.2879 ± 0.0826
$p_K > 0.8 \text{ GeV}/c$	0.0764 ± 0.0009	0.0788 ± 0.0050	1.0306 ± 0.0661

We also consider the issue of kaons that decay in flight, $K^\pm \rightarrow \mu^\pm \nu_\mu$. At low momentum ($p_K < 0.6 \text{ GeV}/c$) these events comprise the totality of the $D^0 \rightarrow K^- e^+ \nu$ contribution to the $D^0 \rightarrow \pi^- e^+ \nu$ background and it is the muon, rather than the kaon, that fakes the signal pion. We do not re-weight these events since in our study they are flatly distributed in M_{bc} , whereas the fakes discrepancy between data and MC clearly occurs as a peak in M_{bc} around the D mass. In other words, the tails of the M_{bc} distribution from events where a kaon (or its muon daughter) faked a pion are well matched between data and MC, and it is only the peaking contribution that appears to be incorrectly modeled. Since the fake pion contribution from muon daughters (i.e., $K^\pm \rightarrow \mu^\pm \nu_\mu$) does not peak in

M_{bc} , the excess may therefore be assumed to be from real kaons faking pions, and we may leave the decays in flight unaltered in the MC. This also means that we will not be affected by fluctuations of the fake rate discrepancy within our broad lowest momentum bin, $p_K < 0.6$ GeV/ c .

Therefore, to correct the MC we apply the measured corrections to $D^0 \rightarrow \pi^- e^+ \nu$ background events from $D^0 \rightarrow K^- e^+ \nu$ cross-feed if the reconstructed signal π^\pm is MC truth matched to a generated K^\pm . We use this correction for the nominal fit and take the difference between corrected and uncorrected MC as the systematic error.

7.8 Track Finding

For the track finding systematic we need to know how well the MC estimates the track finding efficiency since this will affect the neutrino resolution through our charged four-momentum sums. For this purpose we use $\psi(2S) \rightarrow J/\psi \pi^+ \pi^-$ events to study the charged pion track finding efficiency. To reconstruct these events we look for a good $J/\psi \rightarrow e^+ e^-$ or $J/\psi \rightarrow \mu^+ \mu^-$ and one good pion track. Together these particles form the recoil combination, R , with four-momentum,

$$P_R = P_{J/\psi} + P_{\pi^\pm}. \quad (7.2)$$

The recoil combination must satisfy,

- Both J/ψ tracks (j^+ and j^- where $j = e$ or $j = \mu$) pass simple electron id or both have depth $\mu > 3.0$.
- $|M_{j^+ j^-} - M_{J/\psi}| < 0.05$ GeV
- Recoil pion track is Trkman approved.

We then search the remaining Trkman approved tracks in the event for a second pion track that would yield a fully reconstructed $\psi(2S)$ candidate, i.e. $\psi(2S) \rightarrow R\pi^\mp$, via the criterion

$$|(M_{R\pi} - M_{j^+j^-}) - (M_{\psi(2S)} - M_{J/\psi})| < 0.05 \text{ GeV}. \quad (7.3)$$

The tracking efficiency is determined by looking at the two possible outcomes,

1. $\psi(2S)$ is found (pion track found)
2. $\psi(2S)$ not found (pion track not found).

The tracking efficiency for Trkman approved tracks is then

$$\varepsilon = \frac{N_{\text{found}}}{N_{\text{found}} + N_{\text{miss}}}, \quad (7.4)$$

where N_{found} is the number of events with a found $\psi(2S)$ candidate and N_{miss} is the number of events with a missing $\psi(2S)$ candidate and thus a missing charged pion track. The number of events in each category is determined by fitting the missing mass squared, M_{miss}^2 , distributions, where the missing four-momentum is given by,

$$P_{\text{miss}} = P_{\text{lab}} - P_R, \quad (7.5)$$

and

$$M_{\text{miss}}^2 = P_{\text{miss}}^2. \quad (7.6)$$

In the case where the pion track is found, we fit the M_{miss}^2 distribution with a double Gaussian peak. If the pion track is not found we fit with a double Gaussian peak plus an exponential background. We follow this procedure separately for both data and MC and compare the resulting efficiencies. The fits are performed in two momentum bins, $p_{\text{miss}} < 0.1 \text{ GeV}/c$ and $p_{\text{miss}} \geq 0.1 \text{ GeV}/c$, since we want

to be sure that the low momentum tracks, which may not exit the drift chamber, are also well modeled. The fit results are shown in Figs. 7.10 - 7.13.

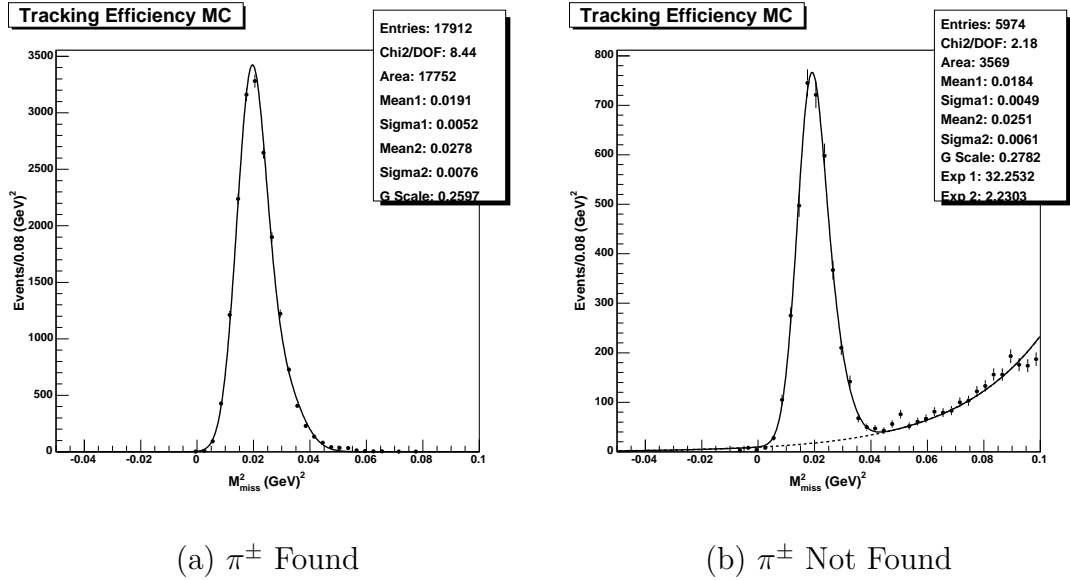


Figure 7.10: Fits to MC M^2_{miss} distributions for $p_{\text{miss}} < 0.1$ GeV/c. Points show MC histograms, solid lines show double Gaussian signal fits and dashed line shows exponential background fit.

The resulting efficiencies in these bins for MC and data are shown in Table 7.3.

To check the results of the fit for $p_{\text{miss}} \geq 0.1$ GeV/c we fit for efficiencies in the p_{miss}

Table 7.3: Tracking efficiencies for Trkman approved tracks in data and MC. Errors are statistical only.

<i>Momentum Bin</i>	ε_{MC}	$\varepsilon_{\text{data}}$	$\varepsilon_{\text{data}} - \varepsilon_{\text{MC}}$
$p_{\text{miss}} < 0.1$ GeV/c	0.8326 ± 0.0027	0.8416 ± 0.0086	0.0090 ± 0.0090
$p_{\text{miss}} \geq 0.1$ GeV/c	0.9734 ± 0.0003	0.9738 ± 0.0008	0.0004 ± 0.0008

bins: $0.1-0.13$ GeV/c, $0.13-0.16$ GeV/c, $0.16-0.25$ GeV/c and $0.25-p_{\text{miss}}^{\text{max}}$ GeV/c,

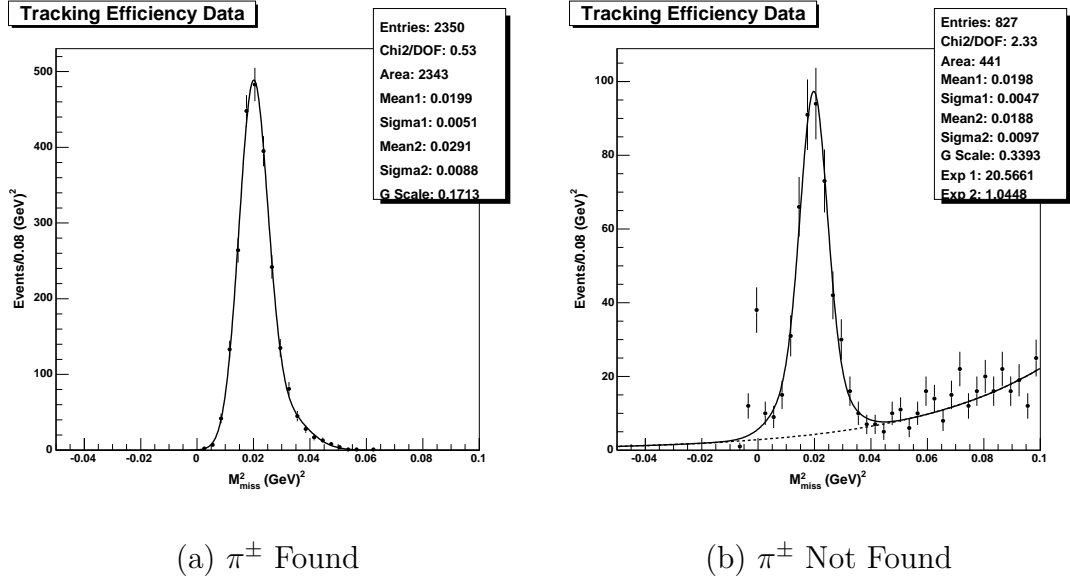


Figure 7.11: Fits to Data M_{miss}^2 distributions for $p_{\text{miss}} < 0.1$ GeV/ c . Points show Data histograms, solid lines show double Gaussian signal fits and dashed line shows exponential background fit.

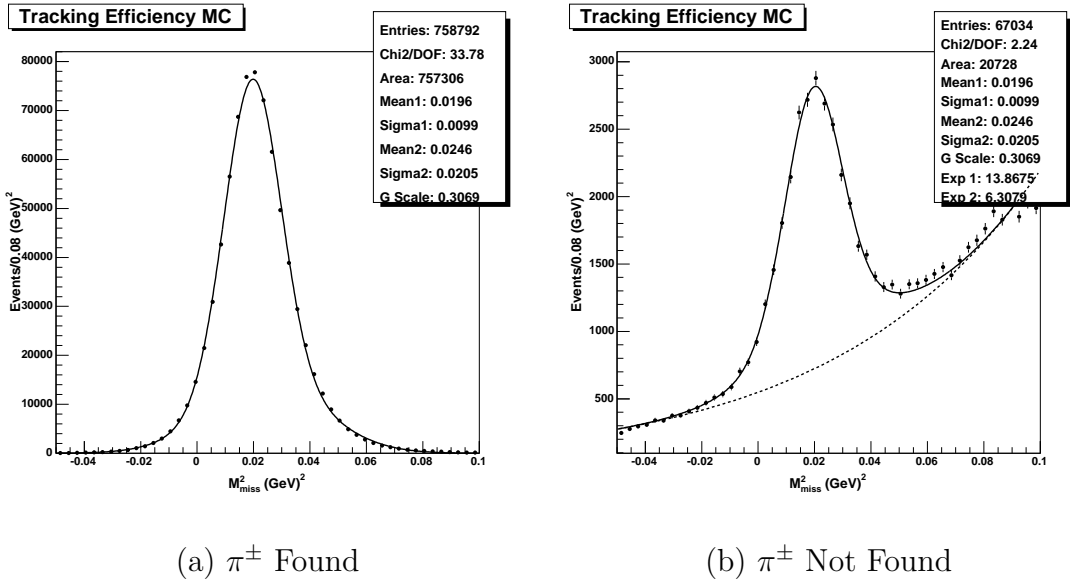


Figure 7.12: Fits to MC M_{miss}^2 distributions for $p_{\text{miss}} \geq 0.1$ GeV/ c . Points show MC histograms, solid lines show double Gaussian signal fits and dashed line shows exponential background fit.

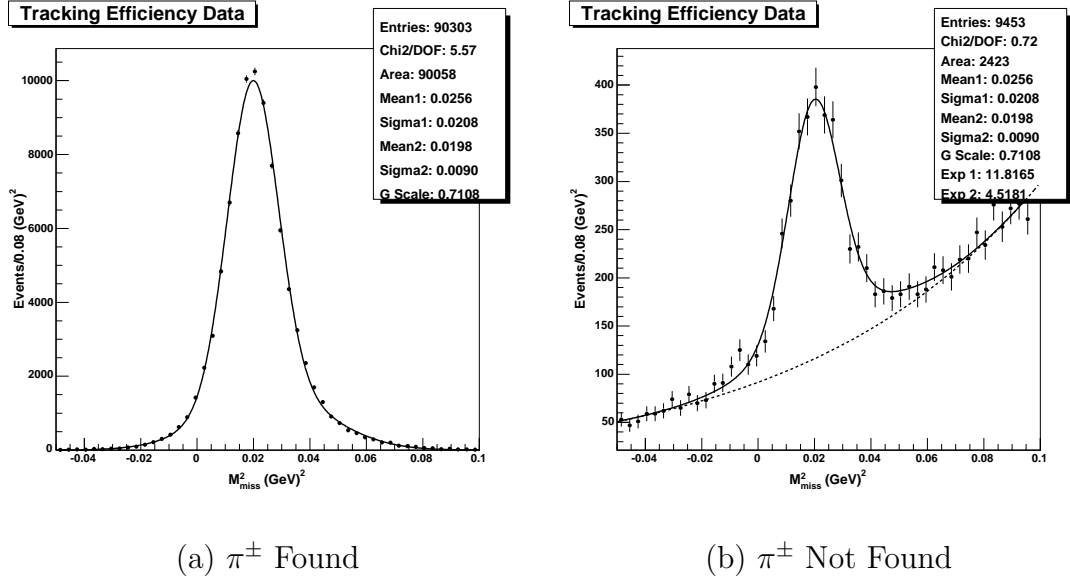


Figure 7.13: Fits to Data M_{miss}^2 distributions for $p_{\text{miss}} \geq 0.1$ GeV/ c . Points show Data histograms, solid lines show double Gaussian signal fits and dashed line shows exponential background fit.

and sum the results. Using this method the efficiency difference between data and MC is found to be 0.0000 ± 0.0008 , consistent with the result in Table 7.3. Finally, to evaluate the systematic error we drop the appropriate fraction of tracks from the MC for the two momentum bins. The fraction to drop is taken as the efficiency difference and its error summed in quadrature, thus for $p_{\text{miss}} < 0.1$ GeV/ c we drop 1.27% of MC tracks and for $p_{\text{miss}} \geq 0.1$ GeV/ c we drop 0.09% of MC tracks.

7.9 Track Smearing

Another source of tracking systematic uncertainty comes from the modeling of track momentum resolution in the MC. To evaluate the effects of mismodeling the resolution we re-run the analysis, replacing the \vec{p} of each tagged track with smeared

momentum \vec{p}' given by,

$$\vec{p}' = \vec{p} + s\Delta\vec{p}, \quad (7.7)$$

where s is the chosen fractional smearing increase (resolution adjustment) and $\Delta\vec{p} = \vec{p} - \vec{p}_{\text{true}}$. For the CLEO-c systematic error we use a track smear derived from the difference in ΔE resolutions of $D \rightarrow K\pi$ between data and MC. This value is just under 6% so we set $s = 0.06$.

7.10 Trkman Fakes

In Section 7.8 we discussed the efficiency for finding good tracks that are Trkman approved. In addition to these good tracks, however, the Trkman selection criteria will also pass a certain number of “junk” or fake tracks. For example, these could be back halves of curlers or false tracks made by connecting noise hits together with segments of real tracks. If the number of extra tracks passing the Trkman selection criteria differs between data and MC, our overall efficiency will be mis-measured due to the net charge zero requirement.

To examine this possible source of discrepancy we again use the CLEO-c sample of D double tag events. The double tagged modes used are: $D^0 \rightarrow K\pi$ vs $D^0 \rightarrow K\pi$, $D^0 \rightarrow K\pi$ vs $D^0 \rightarrow K\pi\pi^0$, $D^0 \rightarrow K\pi\pi^0$ vs $D^0 \rightarrow K\pi\pi^0$, $D^0 \rightarrow K\pi$ vs $D^0 \rightarrow K\pi\pi\pi$, $D^0 \rightarrow K\pi\pi^0$ vs $D^0 \rightarrow K\pi\pi\pi$, $D^0 \rightarrow K\pi\pi\pi$ vs $D^0 \rightarrow K\pi\pi\pi$, $D^+ \rightarrow K\pi\pi$ vs $D^+ \rightarrow K\pi\pi$, $D^+ \rightarrow K\pi\pi$ vs $D^+ \rightarrow K\pi\pi\pi^0$, $D^+ \rightarrow K\pi\pi\pi^0$ vs $D^+ \rightarrow K\pi\pi\pi^0$, $D^+ \rightarrow K\pi\pi$ vs $D^+ \rightarrow K_S\pi\pi\pi$, $D^+ \rightarrow K\pi\pi\pi^0$ vs $D^+ \rightarrow K_S\pi\pi\pi$ and $D^+ \rightarrow K_S\pi\pi\pi$ vs $D^+ \rightarrow K_S\pi\pi\pi$. Events containing these selected modes are required to satisfy the following criteria:

- The reconstructed D tags do not overlap (i.e. no overlapping tracks or show-

ers)

- Both tags satisfy $|\Delta E| < 0.02$ GeV
- Both tags satisfy $|M_{bc} - M_D| < 0.01$ GeV.

We then look in each event and count the number of Trkman approved tracks not appearing in either of the D tags. These are considered to be extra tracks. The results, summed over all double tag modes, are given in Table 7.4.

It is clear from these numbers that there are more extra tracks in the data than in the MC. We thus need to correct the efficiency for passing net charge zero events in the MC; if left uncorrected this will be overestimated by approximately 1%. To make this correction to the MC we first note that the fraction of events with extra tracks shows a clear dependence on the total number of particles in the event, Fig 7.14. With an increasing number of particles in the event the average track momentum decreases, so this dependence is most likely due to an increase in the number of low momentum tracks. To correct the MC efficiency therefore, we bin in terms of the number of tracks per event with $p_T < 0.15$ GeV/ c , where $p_T \leq 0.12$ GeV/ c is the transverse momentum required for a track to curl in the drift chamber.

The correction itself is made by weighting the MC input to our nominal fit. The input MC already has a net charge zero requirement applied, thus for each of these events we wish to apply a weight representing the true (data measured) probability that the event would not have contained a single extra track. We ignore events with two or more extra tracks, since these make up only a very small fraction of our sample, and calculate a weight for each bin. The weights are given by

$$w = 1 - \frac{(E_{data} - E_{mc})}{N_{total}}, \quad (7.8)$$

Table 7.4: Number of extra Trkman approved tracks per event in data (281 pb^{-1}) and MC ($40 \times \mathcal{L}$). The MC is normalized to have the same number of double tag events as the data for each double tag mode.

$D^0\bar{D}^0$		
<i>Extra Tracks per Event</i>	<i>Data</i>	<i>MC</i>
0	13964 ± 118	14066 ± 22
1	351 ± 19	263 ± 3
2	43 ± 7	27 ± 1
3	3 ± 2	2.0 ± 0.2
4	1 ± 1	0.33 ± 0.11
<i>Total Events</i>	14362 ± 120	14359 ± 23
<i>Total Extra</i>	398 ± 20	293 ± 3
<i>Fraction Extra</i>	$2.77 \pm 0.14\%$	$2.04 \pm 0.02\%$
D^+D^-		
<i>Extra Tracks per Event</i>	<i>Data</i>	<i>MC</i>
0	5432 ± 74	5490 ± 13
1	211 ± 15	164 ± 2
2	24 ± 5	18 ± 1
3	4 ± 2	1.21 ± 0.2
4	0 ± 0	0.18 ± 0.08
<i>Total Events</i>	5671 ± 75	5674 ± 13
<i>Total Extra</i>	239 ± 15	184 ± 2
<i>Fraction Extra</i>	$4.21 \pm 0.27\%$	$3.24 \pm 0.04\%$

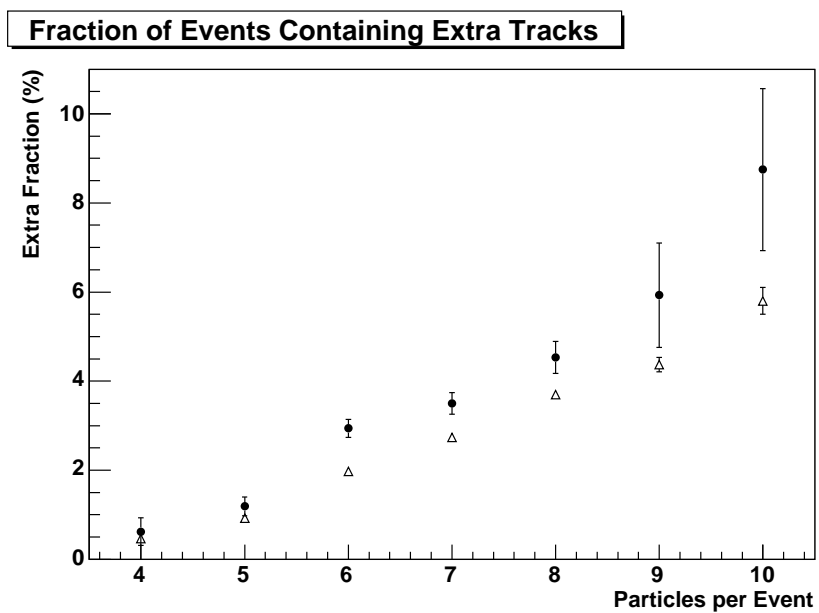


Figure 7.14: Fraction of events containing one or more extra tracks as a function of the number of particles per event. Filled circles show data values and open triangles show MC.

where E_{data} is the number of data events with one extra track, E_{mc} is the number of MC events with one extra track and N_{total} is the total number of events (normalized to be the same for data and MC). The resulting weights used in the nominal fit are given in Table 7.5. The systematic error for this correction is estimated conservatively by taking the difference between corrected and uncorrected MC.

Table 7.5: Weights applied to MC in the nominal fit to correct the efficiency of selecting net charge zero events.

Num Tracks: $p_T < 0.15 \text{ GeV}/c$	Weight
0	0.992741
1	0.994730
2	0.988082
≥ 3	0.952252

7.11 π^0 Finding

For the signal mode $D^+ \rightarrow \pi^0 e^+ \nu$ there is a systematic uncertainty associated with the π^0 finding efficiency. To probe for any efficiency difference between data and MC we follow a procedure similar to that used in evaluation of the track-finding efficiency, Section 7.8. In this case, however, it is important to establish the efficiency difference for the entire signal π^0 momentum range. We thus use $\psi(3770)$ events rather than trying to look at $\psi(2S) \rightarrow J/\psi \pi^0 \pi^0$ decays.

To determine the π^0 finding efficiency we use events with a tagged D^0 meson on one side. The tag modes used are: $D^0 \rightarrow K\pi$, $D^0 \rightarrow K\pi\pi^0$, $D^0 \rightarrow K\pi\pi\pi$, $D^0 \rightarrow K\pi\pi\pi\pi^0$, $D^0 \rightarrow K\pi\pi^0\pi^0$ and $D^0 \rightarrow K\pi\eta$. All are required to satisfy:

- $|\Delta E| < 0.025 \text{ GeV}$
- $|M_{bc} - M_D| < 0.005 \text{ GeV}$.

On the other side of the tagged events we look for $D^0 \rightarrow K\pi\pi^0$ decays. We require there to be one good kaon track (using signal K^\pm criteria listed in Section 5.1.3) and one good, oppositely charged, pion track (signal π^\pm criteria listed in Section 5.1.2).

The missing four-momentum is calculated as,

$$P_{\text{miss}} = P_{\text{event}} - P_{\text{tag}} - P_{K^\pm} - P_{\pi^\mp}, \quad (7.9)$$

where P_{event} is the event four-momentum from Eq. 4.3, P_{tag} is the tagged D four-momentum, P_{K^\pm} is the charged kaon four-momentum and P_{π^\mp} is the charged pion four-momentum. We now have two cases,

1. Signal π^0 found
2. Signal π^0 not found,

where the signal π^0 criteria are as defined in Section 5.1.4 and we also require no overlap with the tagged D particles. Once again the efficiency, ε , is then given by Eq. 7.4.

For the π^0 efficiencies we use five momentum (p_{miss}) bins: $< 0.2 \text{ GeV}/c$, $0.2-0.4 \text{ GeV}/c$, $0.4-0.6 \text{ GeV}/c$, $0.6-0.8 \text{ GeV}/c$ and $\geq 0.8 \text{ GeV}/c$. In each of the bins there is a large background consisting almost purely of $D^0 \rightarrow K^\pm\mu\nu$ events. To eliminate this background as much as possible we make the following requirements:

- There must be at least one Splitoff-approved shower, not in the tag and with energy $> 30 \text{ MeV}$
- $0 \leq p_{\text{miss}} < 0.2 \text{ GeV}/c$

- Maximum shower energy > 0.05 GeV
- $0.2 \leq p_{\text{miss}} < 0.4$ GeV/ c
 - Maximum shower energy > 0.15 GeV
 - $|\text{MAX}(\cos \theta_{\pi^0\pi^\pm}, \cos \theta_{\pi^0K^\pm})| < 0.92$
- $0.4 \leq p_{\text{miss}} < 0.6$ GeV/ c
 - Maximum shower energy > 0.35 GeV
 - $|\text{MAX}(\cos \theta_{\pi^0\pi^\pm}, \cos \theta_{\pi^0K^\pm})| < 0.92$
- $0.6 \leq p_{\text{miss}} < 0.8$ GeV/ c
 - Maximum shower energy > 0.275 GeV
- $p_{\text{miss}} \geq 0.8$ GeV/ c
 - Maximum shower energy > 0.25 GeV.

The $D^0 \rightarrow K^- \mu^+ \nu$ background also makes the M_{miss}^2 distributions difficult to fit. We accommodate this error by finding the efficiencies for data and MC in two different ways and averaging the resulting MC corrections assuming fully correlated errors. In the first method we fit for the yields of π^0 found and π^0 not found events using the smoothed MC $D^0 \rightarrow K^- \mu^+ \nu$ histogram for the background and a double Gaussian shape for the signal peak. The results of these fits for data and MC are shown in Figs. 7.15 - 7.19. For the second method we calculate the data efficiencies using a simple “cut and count” system. Here the data signal yields are determined by subtracting the absolutely normalized MC background from the total number of data entries in both the found and not found π^0 cases.

The $D^0 \rightarrow K^- \mu^+ \nu$ branching fraction is measured to 5% accuracy, so we add a conservative 10% systematic uncertainty to the background subtraction.

Table 7.6: π^0 finding efficiencies for signal π^0 's in data and MC.

<i>Method 1 - Signal Shape Fit</i>			
<i>Momentum Bin</i>	ε_{MC}	$\varepsilon_{\text{data}}$	<i>MC Correction</i>
$p_{\text{miss}} < 0.2 \text{ GeV}/c$	0.3814 ± 0.0020	0.3894 ± 0.0136	1.0209 ± 0.0360
$0.2 \leq p_{\text{miss}} < 0.4 \text{ GeV}/c$	0.4457 ± 0.0016	0.4289 ± 0.0099	0.9623 ± 0.0224
$0.4 \leq p_{\text{miss}} < 0.6 \text{ GeV}/c$	0.4932 ± 0.0029	0.4768 ± 0.0173	0.9668 ± 0.0356
$0.6 \leq p_{\text{miss}} < 0.8 \text{ GeV}/c$	0.6040 ± 0.0012	0.5810 ± 0.0070	0.9619 ± 0.0117
$p_{\text{miss}} \geq 0.8 \text{ GeV}/c$	0.6632 ± 0.0019	0.6324 ± 0.0115	0.9535 ± 0.0175
<i>Method 2 - Cut and Count</i>			
<i>Momentum Bin</i>	ε_{MC}	$\varepsilon_{\text{data}}$	<i>MC Correction</i>
$p_{\text{miss}} < 0.2 \text{ GeV}/c$	0.3815 ± 0.0019	0.3928 ± 0.0133	1.0298 ± 0.0352
$0.2 \leq p_{\text{miss}} < 0.4 \text{ GeV}/c$	0.4456 ± 0.0015	0.4350 ± 0.0101	0.9763 ± 0.0228
$0.4 \leq p_{\text{miss}} < 0.6 \text{ GeV}/c$	0.4938 ± 0.0024	0.4812 ± 0.0170	0.9744 ± 0.0348
$0.6 \leq p_{\text{miss}} < 0.8 \text{ GeV}/c$	0.6040 ± 0.0011	0.5820 ± 0.0073	0.9636 ± 0.0122
$p_{\text{miss}} \geq 0.8 \text{ GeV}/c$	0.6641 ± 0.0018	0.6297 ± 0.0113	0.9483 ± 0.0171

The resulting efficiencies and MC correction factors for each method are given in Table 7.6. The average corrections are plotted in Fig. 7.20 along with the linear best fit. We use this fit to correct the MC π^0 efficiencies in the nominal branching fraction fit. The corrections are calculated from the signal π^0 momentum as,

$$w = -0.0586p_{\pi^0} + 1.003, \quad (7.10)$$

where w is the correcting weight given to signal $D^+ \rightarrow \pi^0 e^+ \nu$ MC events containing

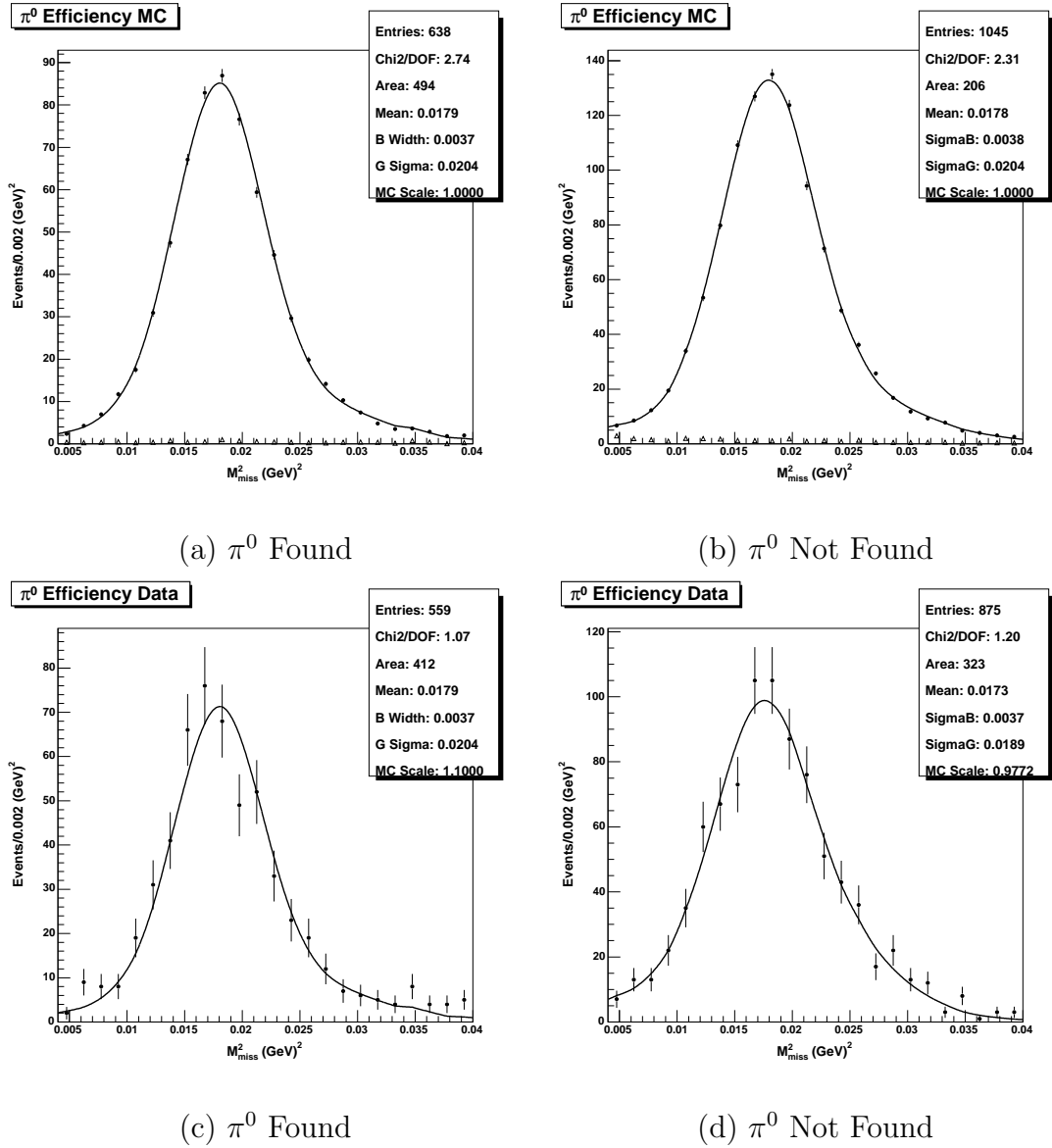


Figure 7.15: Signal π^0 finding: fits to M_{miss}^2 distributions for $p_{\text{miss}} < 0.2 \text{ GeV}/c$. In (a) and (b) filled circles show the total MC histograms while open triangles represent background MC histograms. In (c) and (d) filled circles show data histograms. In all cases solid lines show fit results.

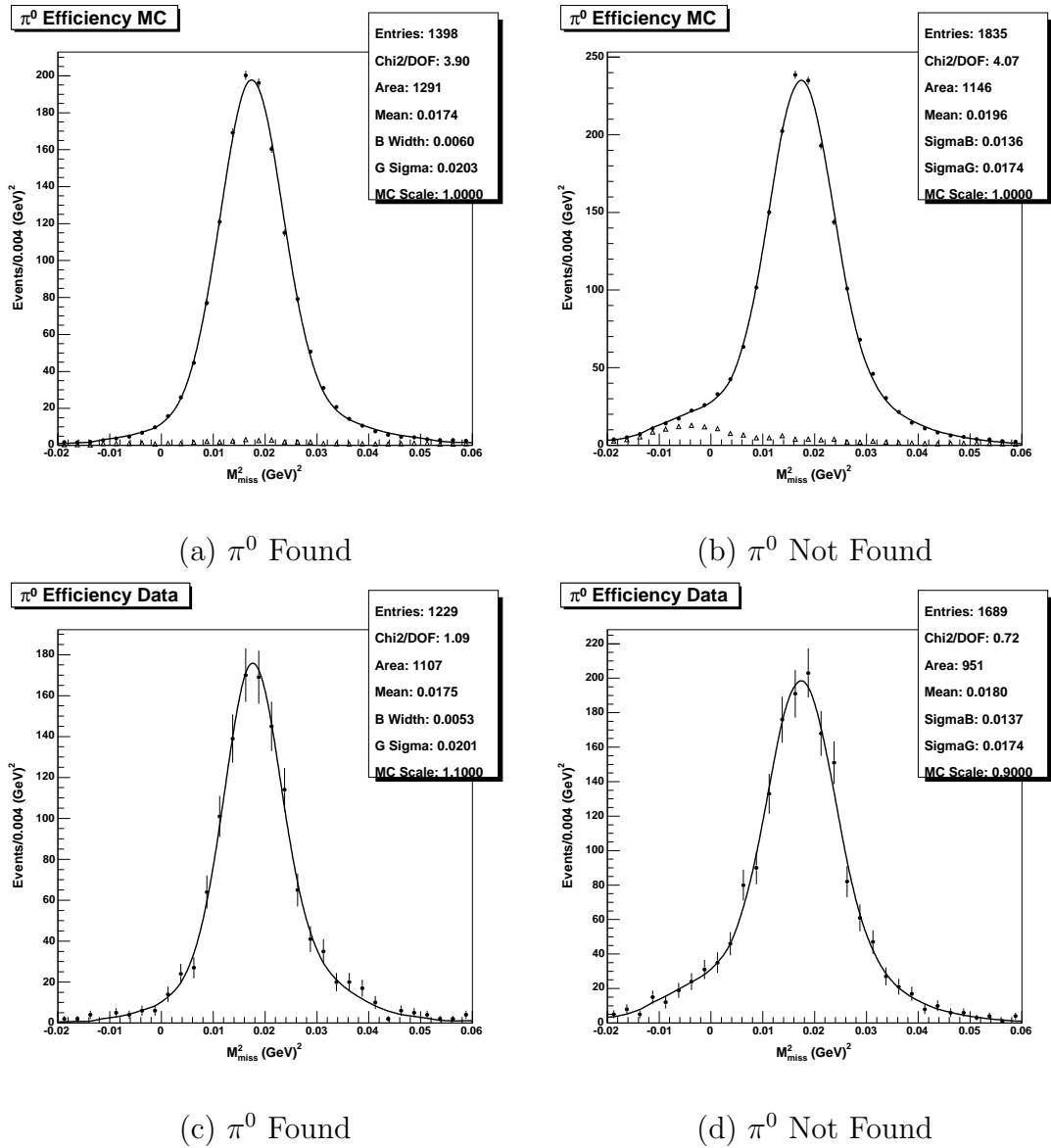


Figure 7.16: Signal π^0 finding: fits to M_{miss}^2 distributions for $0.2 \leq p_{\text{miss}} < 0.4$ GeV/c. In (a) and (b) filled circles show the total MC histograms while open triangles represent background MC histograms. In (c) and (d) filled circles show data histograms. In all cases solid lines show fit results.

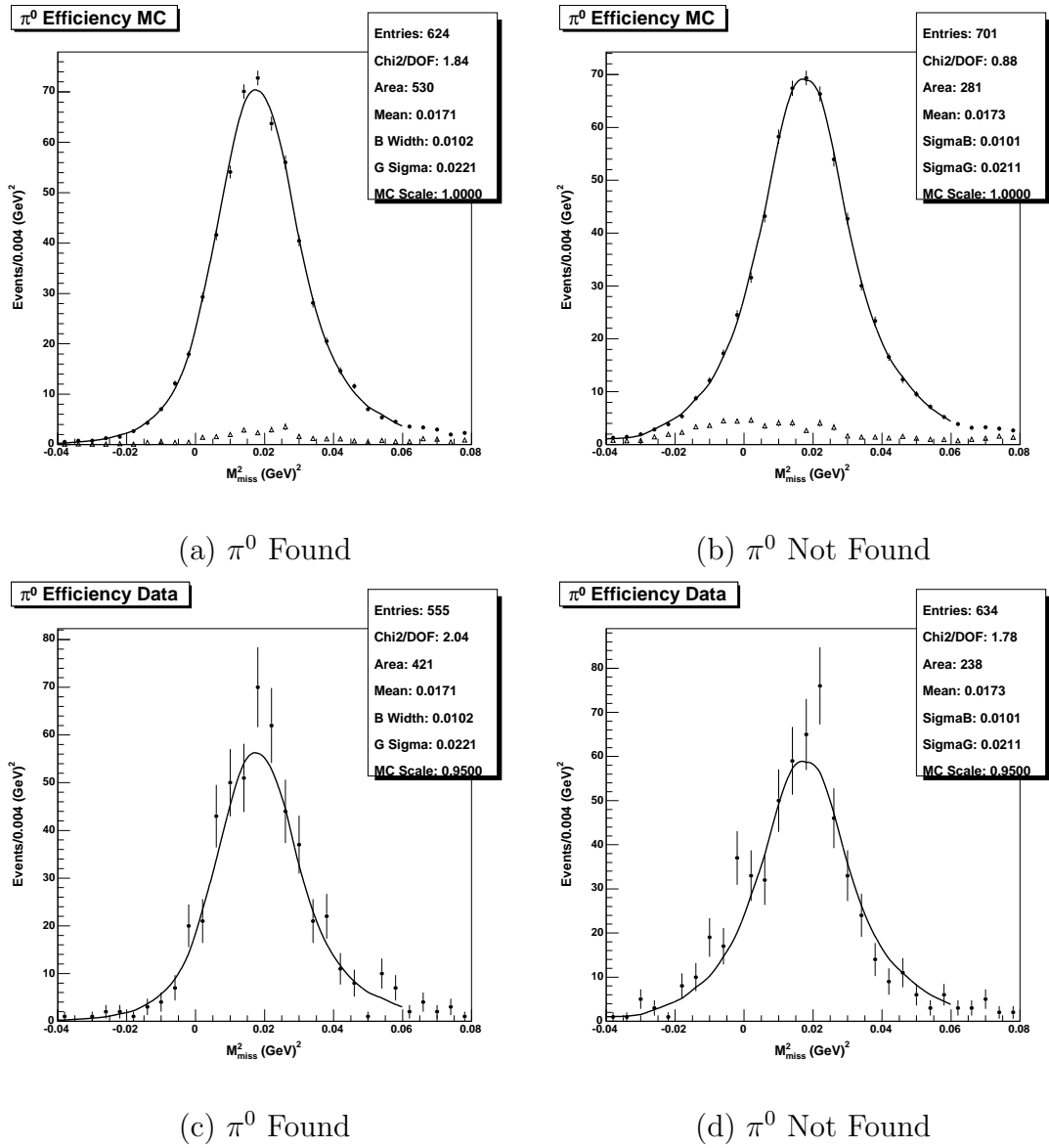


Figure 7.17: Signal π^0 finding: fits to M_{miss}^2 distributions for $0.4 \leq p_{\text{miss}} < 0.6$ GeV/c. In (a) and (b) filled circles show the total MC histograms while open triangles represent background MC histograms. In (c) and (d) filled circles show data histograms. In all cases solid lines show fit results.

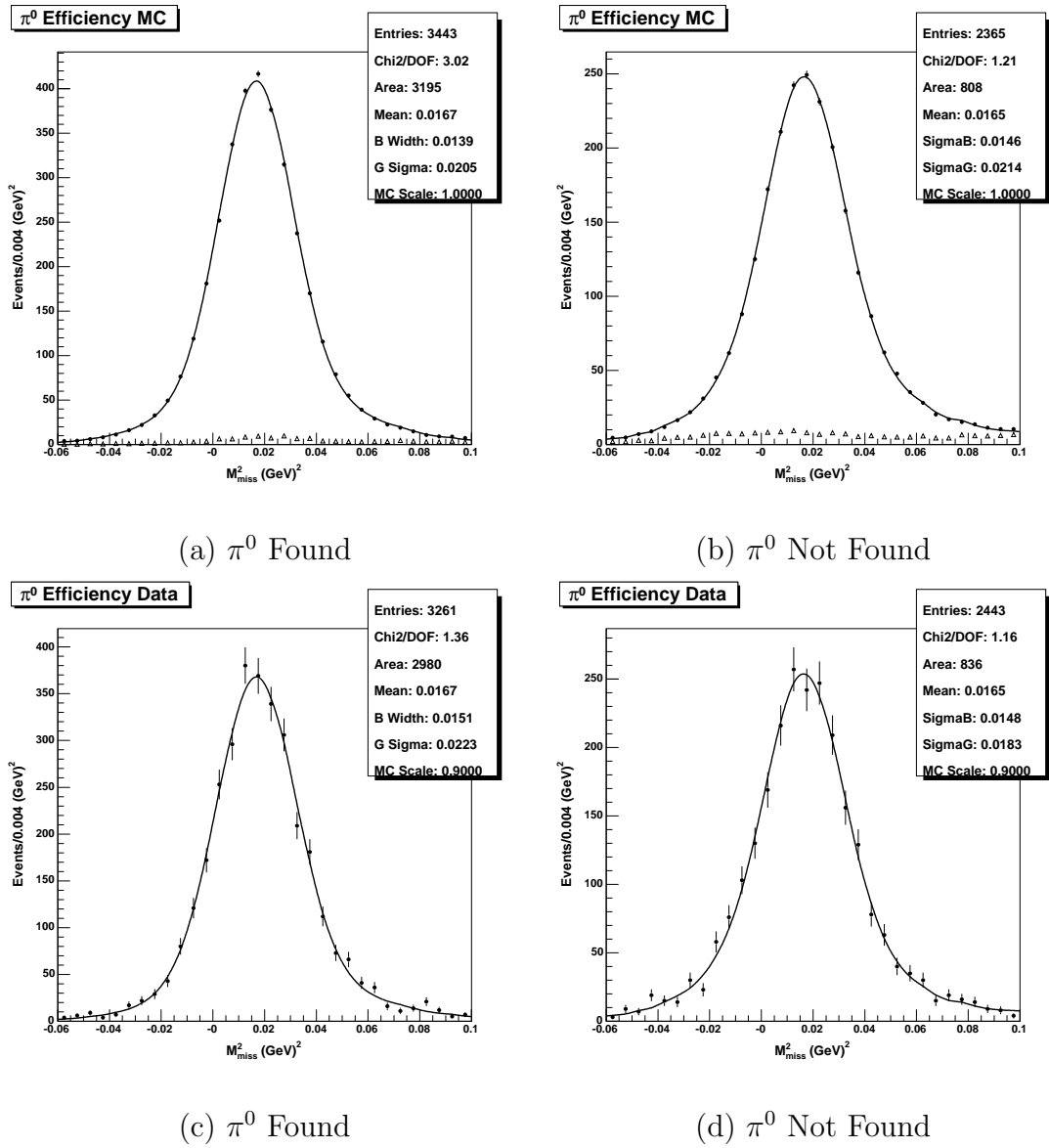


Figure 7.18: Signal π^0 finding: fits to M_{miss}^2 distributions for $0.6 \leq p_{\text{miss}} < 0.8$ GeV/c. In (a) and (b) filled circles show the total MC histograms while open triangles represent background MC histograms. In (c) and (d) filled circles show data histograms. In all cases solid lines show fit results.

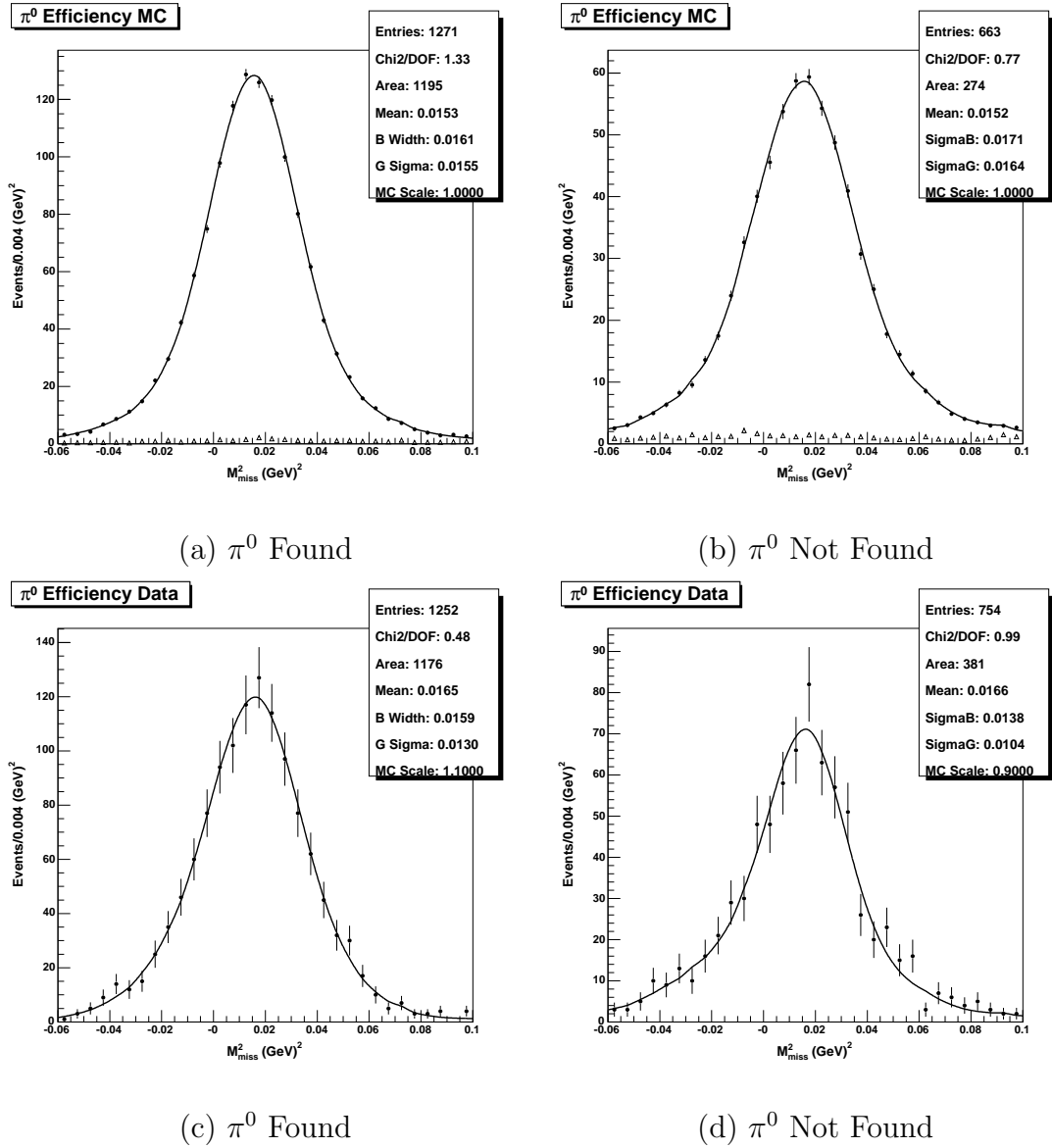


Figure 7.19: Signal π^0 finding: fits to M_{miss}^2 distributions for $p_{\text{miss}} \geq 0.8 \text{ GeV}/c$. In (a) and (b) filled circles show the total MC histograms while open triangles represent background MC histograms. In (c) and (d) filled circles show data histograms. In all cases solid lines show fit results.

a π^0 of momentum p_{π^0} GeV/ c . To determine the systematic error we move around the error ellipse of the linear fit in χ^2 space. We look at the four fits that correspond to the points on the semi-major and semi-minor axes of the ellipse, as shown in Fig. 7.20. For branching fraction evaluation, the systematic error is taken to be the fit that gives the largest correction to the signal $D^+ \rightarrow \pi^0 e^+ \nu$ yield (dashed lines), while for form factor evaluation the systematic error is taken to be the fit that gives the largest correction to the shape of the q^2 distribution (dash-dot lines).

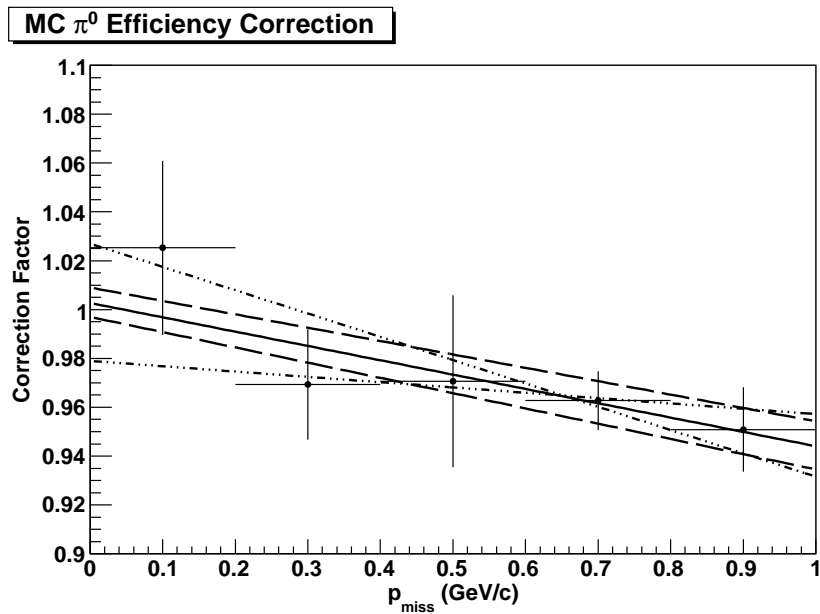


Figure 7.20: The MC π^0 efficiency corrections as determined using the methods described in the text. The solid line shows the best linear fit to the data, it is taken as the nominal correction. The dashed and dash-dot lines show the extreme variations of the fit from the four points on the semi-major and semi-minor axes of the error ellipse.

7.12 K_S Finding

To correct the $K_S \rightarrow \pi^+\pi^-$ finding efficiency in the MC we use the results of an external study [40]. The resulting efficiencies for finding K_S 's in data and MC, broken down into our signal momentum bins, are given in Table 7.7. An artifact of the procedure used to calculate these efficiencies is that they can achieve values greater than 100%. In these cases we set the efficiency to exactly 100% and leave the error as it is. To get the MC correction and systematic errors from these results we follow the procedures familiarized in Sections 7.11, 7.14 and 7.15.

An overall MC correction is obtained via a linear fit to the momentum dependent corrections, Fig 7.21. The correction, w , obtained in this fashion and given by,

$$w = 0.0302p_{K_S} + 1.001 \quad (7.11)$$

is used to weight each MC event where a signal $D^+ \rightarrow K_S e^+ \nu$ decay is found and the K_S is tagged to a true K_S . Once again for the systematic error we walk around the one standard deviation error ellipse to the four points on the semi-major and semi-minor axes, shown by the dash and dash-dot lines in Fig. 7.21. The points giving the largest $D^+ \rightarrow K_S e^+ \nu$ yield deviations (dashed lines) are used to obtain the branching fraction systematic errors, while the points giving the largest deviation in the shape of the q^2 distributions (dash-dot lines) are used to obtain the form factor systematic errors.

7.13 PID for Neutrino Reconstruction

For neutrino reconstruction we assign each charged hadron in the event a particle identification based on the associated track's RICH and dE/dx measurements. To

Table 7.7: Signal K_S finding efficiencies in data and MC.

<i>Momentum Bin</i>	ε_{MC}	$\varepsilon_{\text{data}}$	<i>MC Correction</i>
$p_{K_S} < 0.3 \text{ GeV}/c$	0.9335 ± 0.0042	0.9335 ± 0.0121	1.0000 ± 0.0137
$0.3 \leq p_{K_S} < 0.5 \text{ GeV}/c$	0.9707 ± 0.006	0.9714 ± 0.0163	1.0007 ± 0.0179
$0.5 \leq p_{K_S} < 0.6 \text{ GeV}/c$	0.9861 ± 0.0109	0.9766 ± 0.0324	0.9904 ± 0.0346
$0.6 \leq p_{K_S} < 0.7 \text{ GeV}/c$	0.9821 ± 0.0094	1.0000 ± 0.0383	1.0182 ± 0.0402
$p_{K_S} \geq 0.7 \text{ GeV}/c$	1.0000 ± 0.0078	1.0000 ± 0.0228	1.0000 ± 0.0241

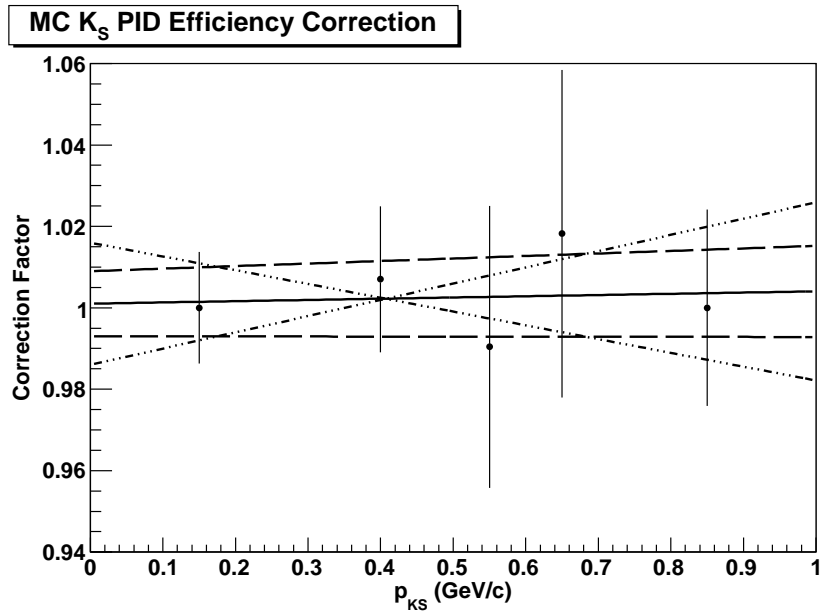


Figure 7.21: The MC K_S finding efficiency corrections. The solid line shows the best linear fit to the data, it is taken as the nominal correction. The dashed and dash-dot lines show the extreme variations of the fit from the four points on the semi-major and semi-minor axes of the error ellipse.

determine the systematic error associated with these assignments we degrade the RICH and dE/dx measurements by 30% of itself (i.e., a factor of 1.3). This number is determined from the D meson mass resolution in CLEOIII data. For CLEO-c we expect a better resolution, however, we retain the CLEOIII value as this is a small systematic uncertainty.

7.14 Charged Kaon Signal PID

Identification of charged kaons for the signal decay mode $D^0 \rightarrow K^- e^+ \nu$ relies on dE/dx and RICH measurements as outlined in Section 5.1.3. If these measurements are imperfectly modeled in the MC there will be an associated systematic uncertainty affecting the finding efficiency of the signal kaons and thus the overall reconstruction efficiency of the signal decay mode. It is necessary therefore to determine the K^\pm signal PID efficiency in both the data and MC and correct any discrepancies. To determine these differences, if any, between K^\pm PID in the MC and the data we once again use the CLEO-c tagged D meson sample.

We follow loosely the methods used to determine PID efficiencies for tagged D particles, see [37] and [38]. Each of the tag modes used, namely $D^0 \rightarrow K\pi$, $D^0 \rightarrow K\pi\pi^0$ and $D^+ \rightarrow K\pi\pi$, is reconstructed with no particle identification criteria applied to the kaons, although these tracks are still required to be Trkman approved. For the π^\pm and π^0 's the standard D tag identification criteria is retained [31]. To find the K^\pm PID efficiency we fit M_{bc} distributions both for the totality of found D tags and for the subset where the K^\pm passes signal PID criteria. The efficiency is then given by

$$\varepsilon_{PID} = \frac{Y_{\text{signal}}}{Y_{\text{all}}}, \quad (7.12)$$

where Y_{signal} is the yield of tags containing kaons that pass signal PID criteria and Y_{all} is the total number of tags.

To fit the M_{bc} distributions we apply the mode dependent ΔE requirements as determined in [31]. For the selected modes these are given in Table. 7.8. The fit range, divided into 28 bins of width 1.5 MeV, is given by $1.845 < M_{\text{bc}} < 1.887$. An inverted Crystal-Ball line shape is used for the signal while the background is modeled by an Argus function.

Table 7.8: Mode dependent ΔE requirements for K^\pm and π^\pm signal PID fits.

<i>Tag Mode</i>	<i>ΔE Range (GeV)</i>
$D^0 \rightarrow K\pi$	$ \Delta E < 0.0294$
$D^0 \rightarrow K\pi\pi^0$	$-0.0583 < \Delta E < 0.035$
$D^0 \rightarrow K_S\pi\pi$	$ \Delta E < 0.0265$
$D^\pm \rightarrow K\pi\pi$	$ \Delta E < 0.0218$

For our purposes it is also important to determine any momentum dependence associated with the data-MC PID difference. Specifically we would like to determine the dependence for each of our signal q^2 bins, since this will affect the shape of the $d\Gamma/dq^2$ distributions. We therefore fit for yields and obtain efficiencies in the five K^\pm signal momentum bins: < 0.3 GeV/ c , $0.3 - 0.5$ GeV/ c , $0.5 - 0.6$ GeV/ c , $0.6 - 0.7$ GeV/ c and ≥ 0.7 GeV/ c . The data and MC fits for the five momentum bins in the tag mode $D^0 \rightarrow K\pi\pi^0$ are given in Figs 7.23 - 7.27. Fits for the tag mode $D^0 \rightarrow K\pi$, which contributes only in the highest momentum bin, are shown in Fig. 7.28 and fits for the tag mode $D^+ \rightarrow K\pi\pi$ are shown in Figs. 7.29 - 7.33. The resulting combined efficiencies and MC corrections are given in Table 7.9.

Table 7.9: Signal K^\pm PID efficiencies in data and MC.

<i>Momentum Bin</i>	ε_{MC}	$\varepsilon_{\text{data}}$	<i>MC Correction</i>
$p_{K^\pm} < 0.3 \text{ GeV}/c$	0.7854 ± 0.0035	0.7707 ± 0.0078	0.9814 ± 0.0108
$0.3 \leq p_{K^\pm} < 0.5 \text{ GeV}/c$	0.9307 ± 0.0034	0.9204 ± 0.0073	0.9890 ± 0.0086
$0.5 \leq p_{K^\pm} < 0.6 \text{ GeV}/c$	0.9387 ± 0.0029	0.9208 ± 0.0079	0.9809 ± 0.0090
$0.6 \leq p_{K^\pm} < 0.7 \text{ GeV}/c$	0.9534 ± 0.0022	0.9392 ± 0.0063	0.9851 ± 0.0070
$p_{K^\pm} \geq 0.7 \text{ GeV}/c$	0.9820 ± 0.0014	0.9690 ± 0.0038	0.9868 ± 0.0041

An overall signal K^\pm PID correction for the MC is obtained by making a linear fit to the correction in each momentum bin, Fig 7.22. The correction, w , obtained in this fashion and given by

$$w = 0.0048p_{K^\pm} + 0.982, \quad (7.13)$$

is used to weight each MC event where a signal $D^0 \rightarrow K^- e^+ \nu$ decay is found and the K^- is a true kaon. For the systematic error we walk around the one standard deviation error ellipse of the linear fit parameters to the four points on the semi-major and semi-minor axes, shown by the dash and dash-dot lines in Fig. 7.22. The points giving the largest yield deviations (dashed lines) are used to obtain the branching fraction systematic errors, while the points giving the largest deviation in the shape of the q^2 distributions (dash-dot lines) are used to obtain the form factor systematic errors.

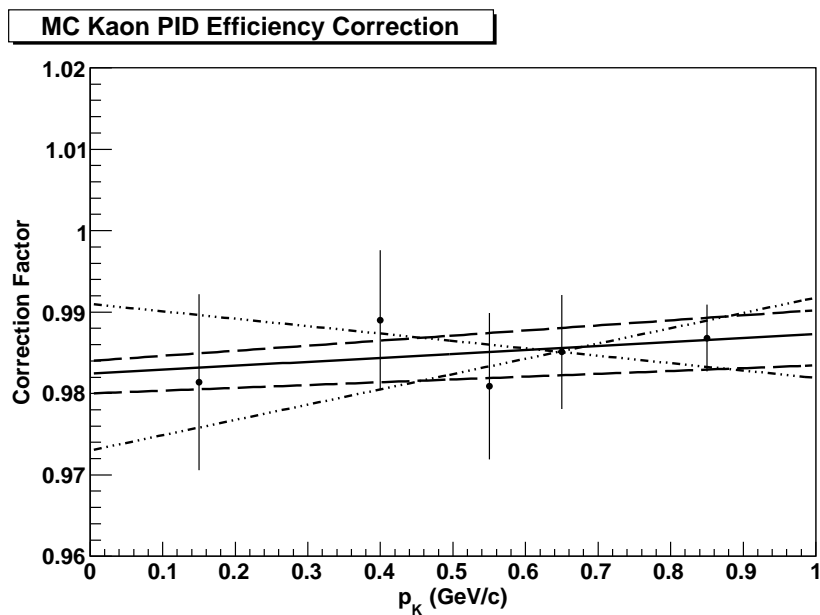


Figure 7.22: The MC K^\pm PID efficiency corrections as determined using the methods described in the text. The solid line shows the best linear fit to the data, it is taken as the nominal correction. The dashed and dash-dot lines show the extreme variations of the fit from the four points on the semi-major and semi-minor axes of the error ellipse.

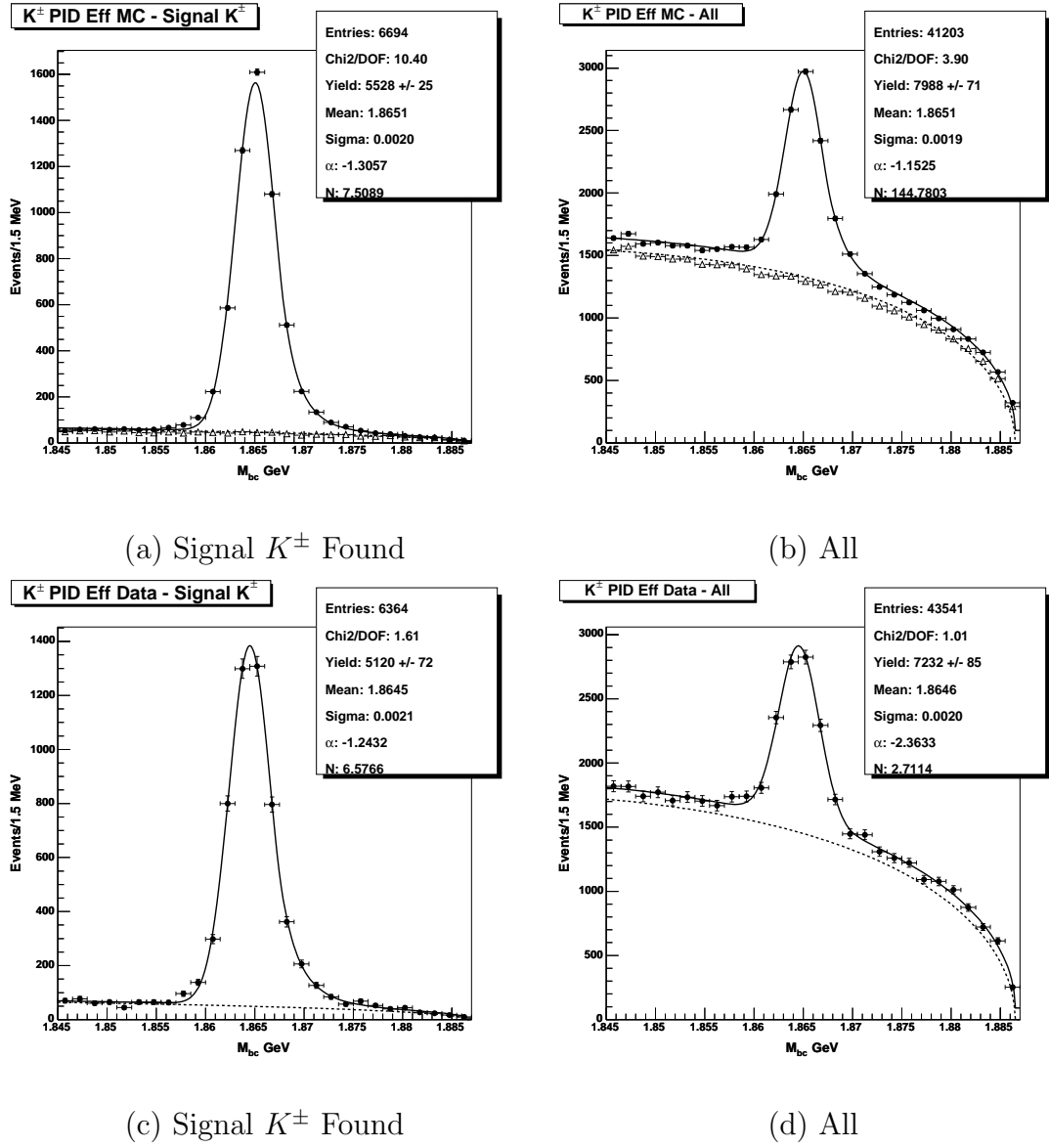


Figure 7.23: Signal K^\pm PID: fits to $D^0 \rightarrow K\pi\pi^0 M_{bc}$ distributions for $0.0 \leq p_{K^\pm} < 0.3$ GeV/ c . In (a) and (b) filled circles show MC histograms and open triangles show MC background histograms. In (c) and (d) filled circles show data histograms. In all cases solid lines show CB line shape fits and dashed lines show Argus background fits.

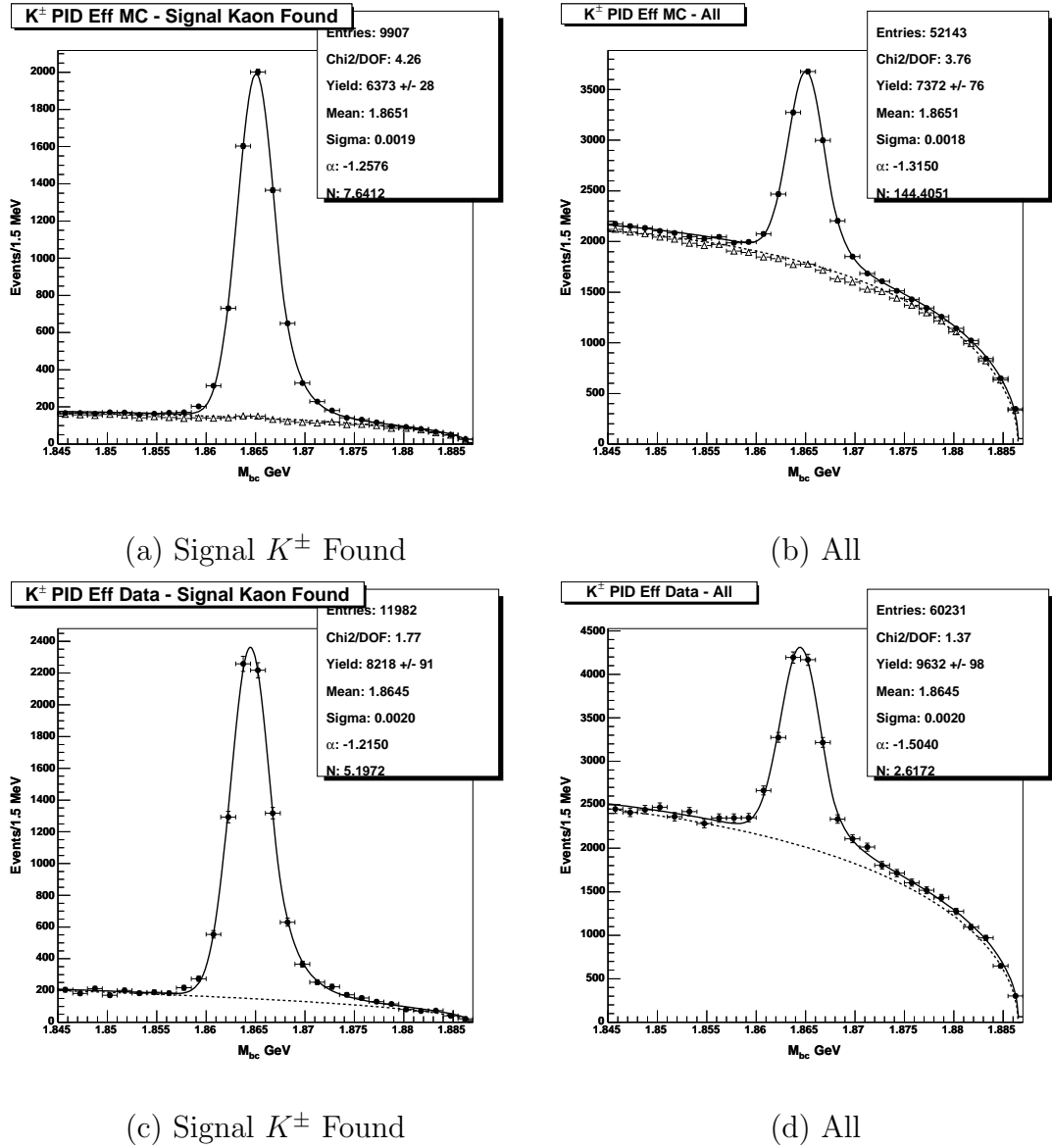


Figure 7.24: Signal K^\pm PID: fits to $D^0 \rightarrow K\pi\pi^0 M_{bc}$ distributions for $0.3 \leq p_{K^\pm} < 0.5$ GeV/c. In (a) and (b) filled circles show MC histograms and open triangles show MC background histograms. In (c) and (d) filled circles show data histograms. In all cases solid lines show CB line shape fits and dashed lines show Argus background fits.

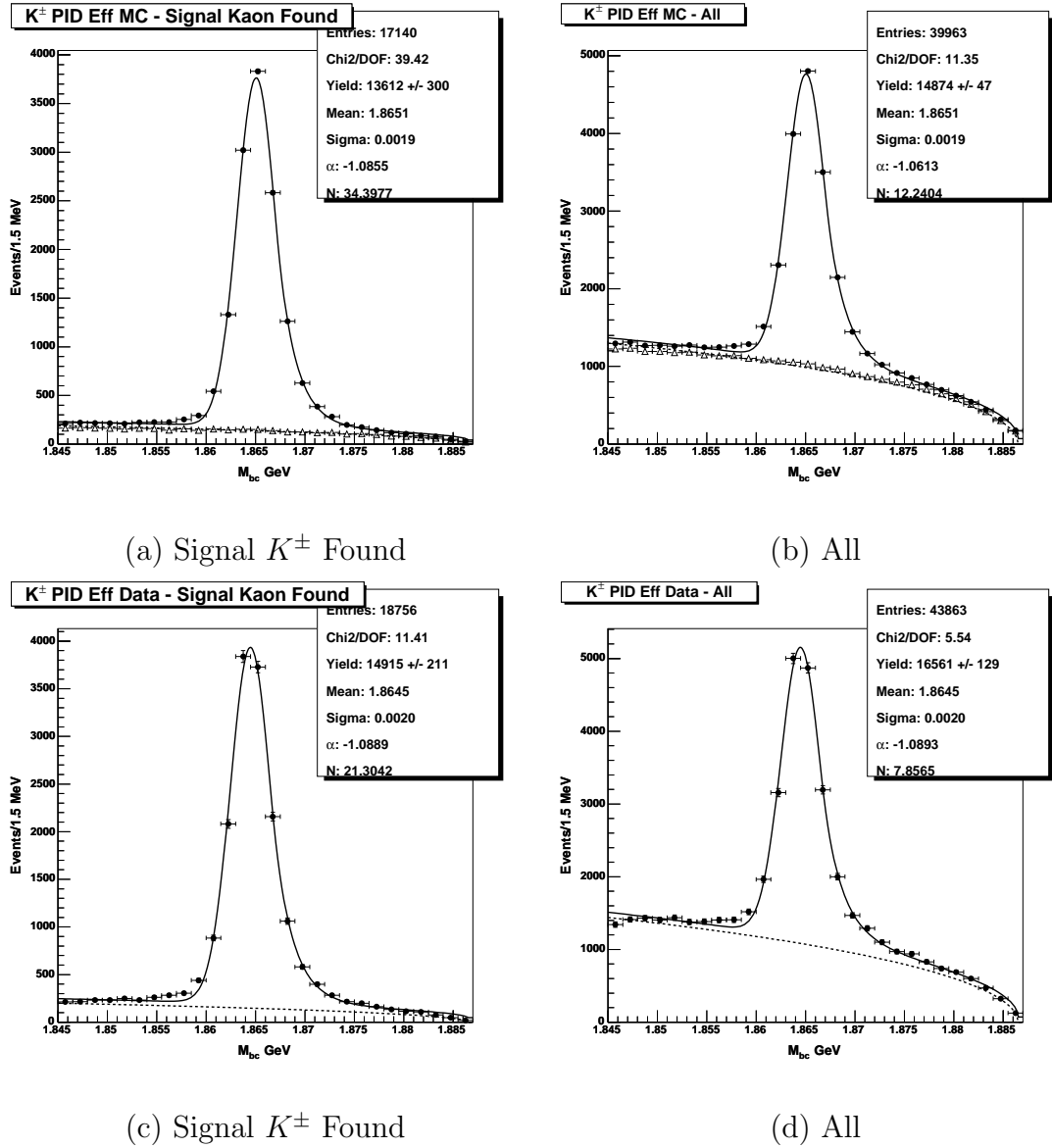


Figure 7.25: Signal K^\pm PID: fits to $D^0 \rightarrow K\pi\pi^0 M_{bc}$ distributions for $0.5 \leq p_{K^\pm} < 0.6$ GeV/c. In (a) and (b) filled circles show MC histograms and open triangles show MC background histograms. In (c) and (d) filled circles show data histograms. In all cases solid lines show CB line shape fits and dashed lines show Argus background fits.

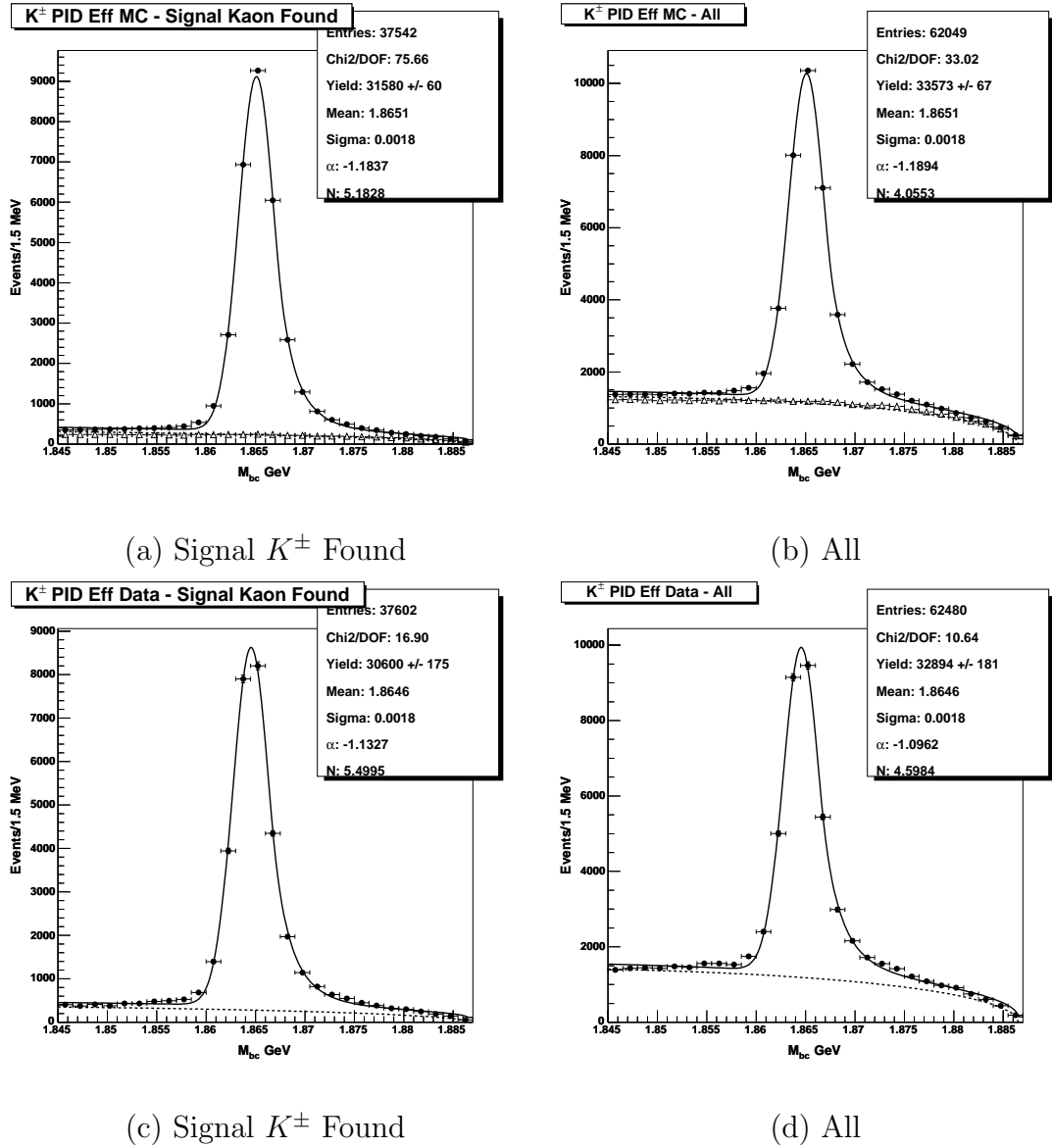


Figure 7.26: Signal K^\pm PID: fits to $D^0 \rightarrow K\pi\pi^0 M_{bc}$ distributions for $0.6 \leq p_{K^\pm} < 0.7$ GeV/c. In (a) and (b) filled circles show MC histograms and open triangles show MC background histograms. In (c) and (d) filled circles show data histograms. In all cases solid lines show CB line shape fits and dashed lines show Argus background fits.

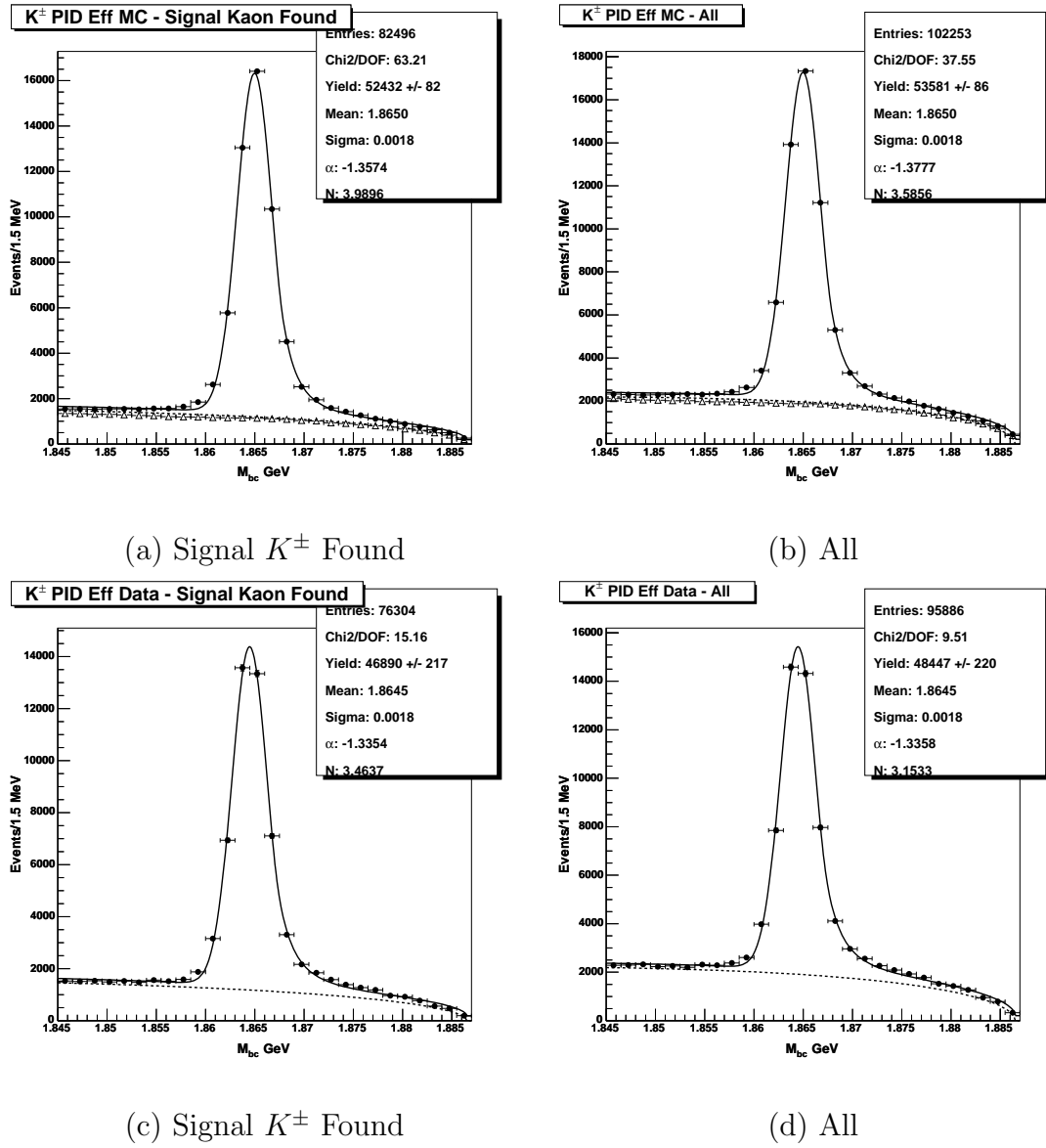
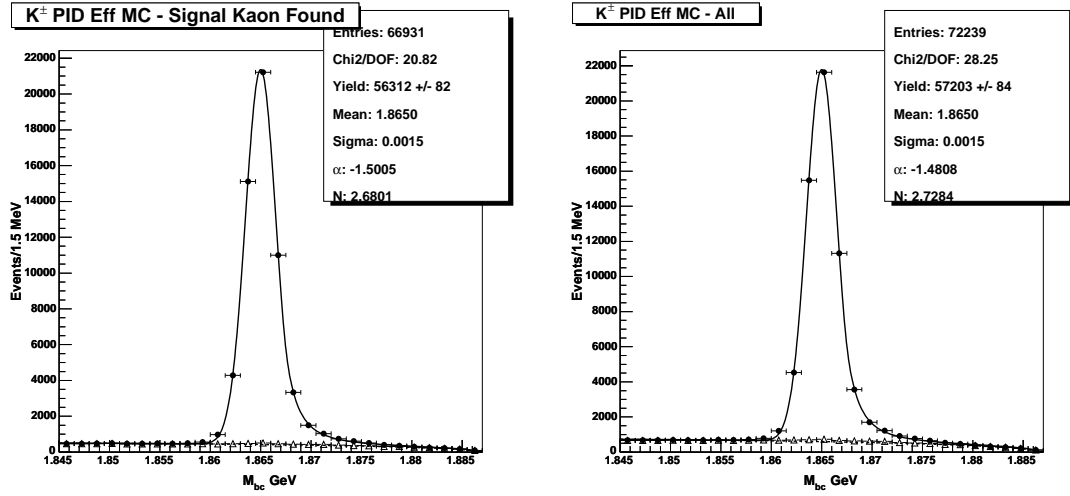
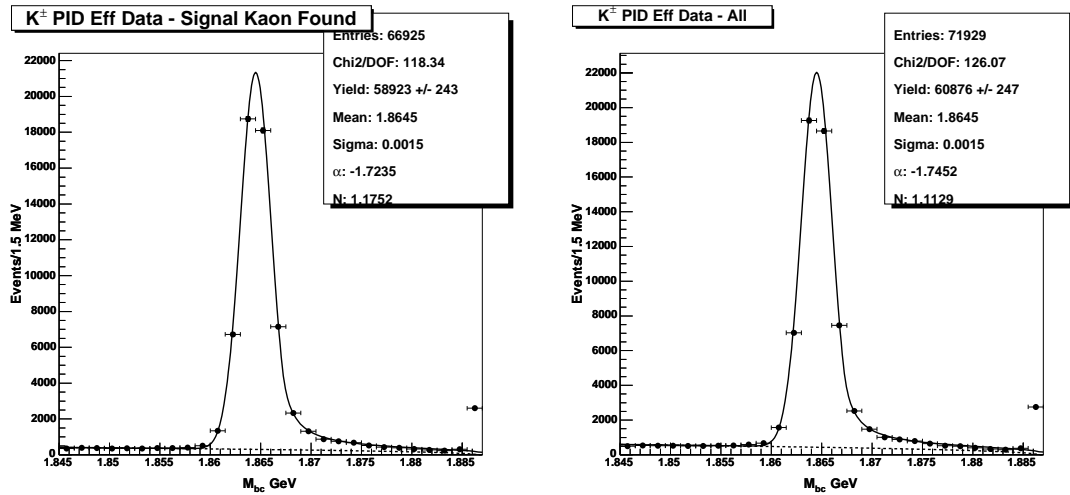


Figure 7.27: Signal K^\pm PID: fits to $D^0 \rightarrow K\pi\pi^0 M_{bc}$ distributions for $p_{K^\pm} \geq 0.7$ GeV/c. In (a) and (b) filled circles show MC histograms and open triangles show MC background histograms. In (c) and (d) filled circles show data histograms. In all cases solid lines show CB line shape fits and dashed lines show Argus background fits.

(a) Signal K^\pm Found

(b) All

(c) Signal K^\pm Found

(d) All

Figure 7.28: Signal K^\pm PID: fits to $D^0 \rightarrow K\pi$ M_{bc} distributions for $p_{K^\pm} \geq 0.7$ GeV/c. In (a) and (b) filled circles show MC histograms and open triangles show MC background histograms. In (c) and (d) filled circles show data histograms. In all cases solid lines show CB line shape fits and dashed lines show Argus background fits.

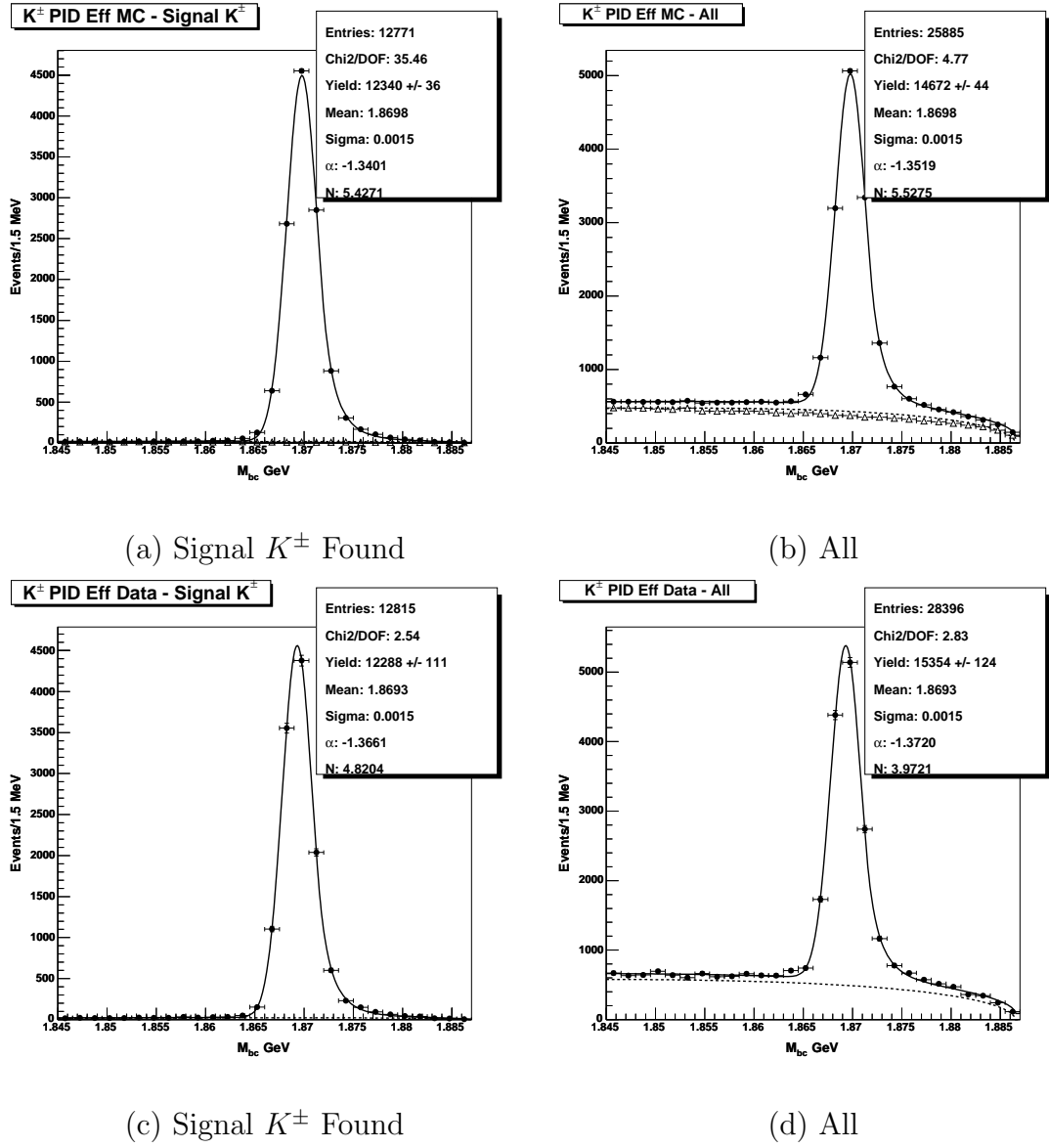


Figure 7.29: Signal K^\pm PID: fits to $D^0 \rightarrow K\pi$ M_{bc} distributions for $0.0 \leq p_{K^\pm} < 0.3$ GeV/ c . In (a) and (b) filled circles show MC histograms and open triangles show MC background histograms. In (c) and (d) filled circles show data histograms. In all cases solid lines show CB line shape fits and dashed lines show Argus background fits.

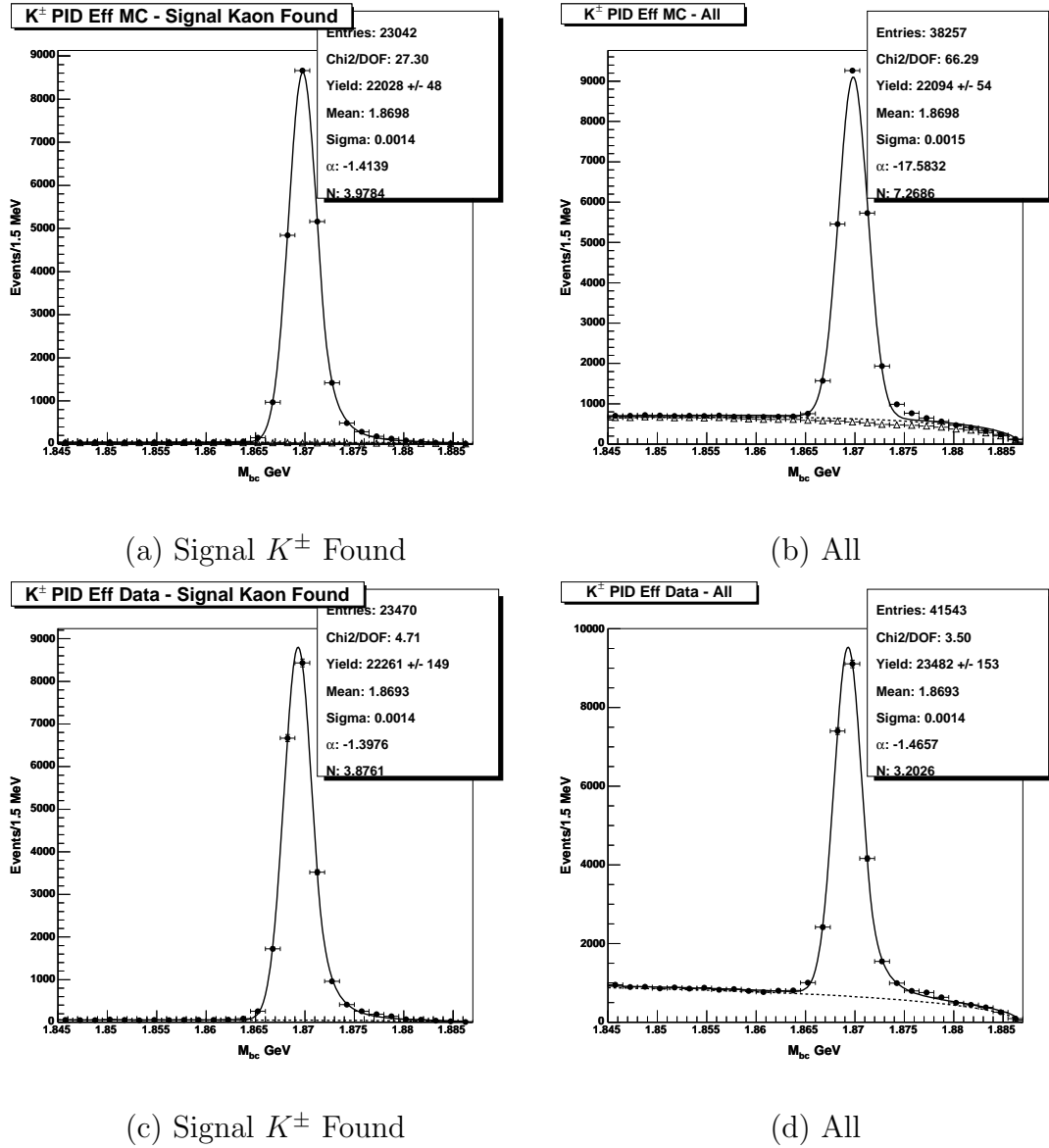


Figure 7.30: Signal K^\pm PID: fits to $D^0 \rightarrow K\pi$ M_{bc} distributions for $0.3 \leq p_{K^\pm} < 0.5$ GeV/c. In (a) and (b) filled circles show MC histograms and open triangles show MC background histograms. In (c) and (d) filled circles show data histograms. In all cases solid lines show CB line shape fits and dashed lines show Argus background fits.

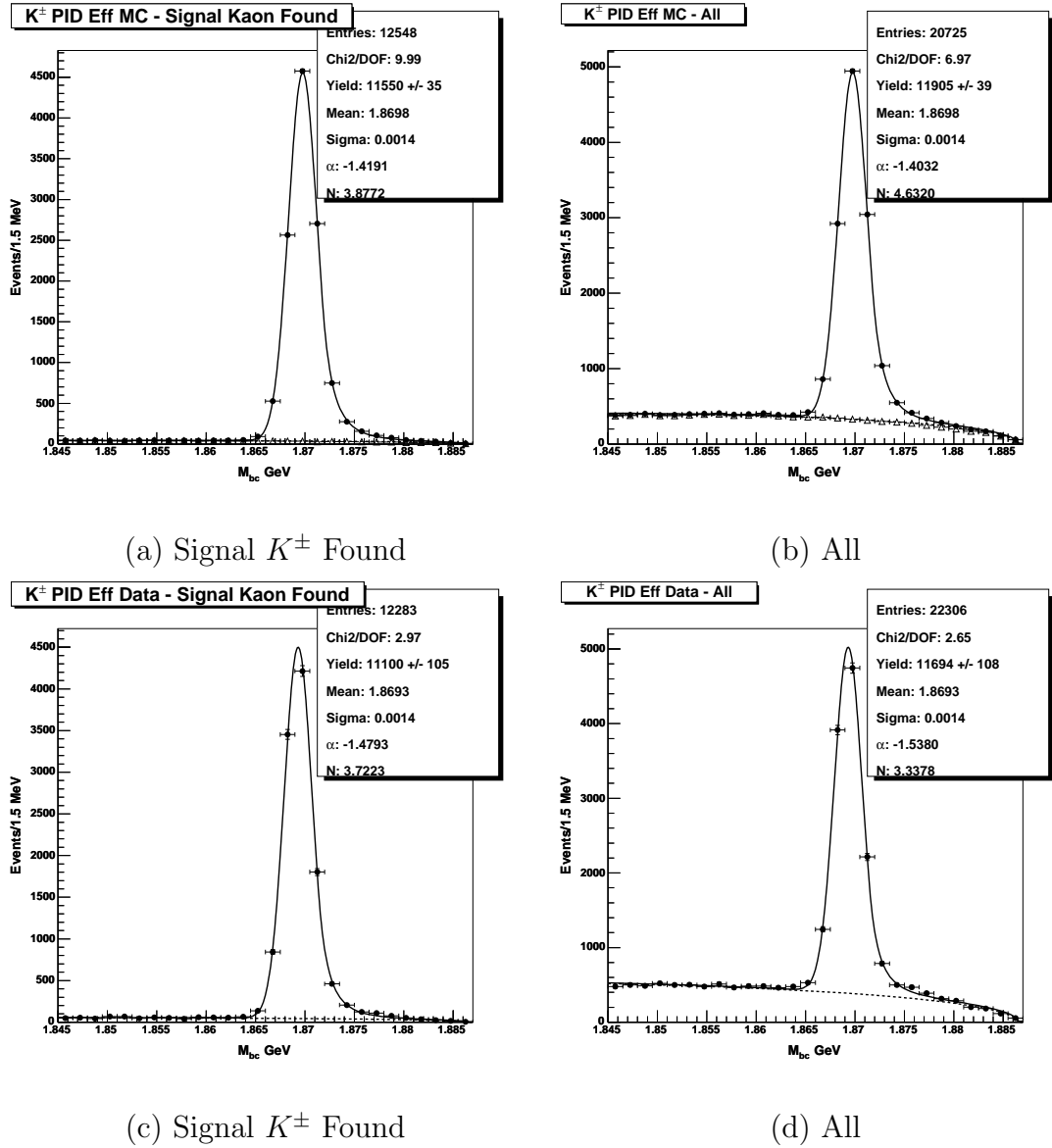


Figure 7.31: Signal K^\pm PID: fits to $D^0 \rightarrow K\pi$ M_{bc} distributions for $0.5 \leq p_{K^\pm} < 0.6$ GeV/c. In (a) and (b) filled circles show MC histograms and open triangles show MC background histograms. In (c) and (d) filled circles show data histograms. In all cases solid lines show CB line shape fits and dashed lines show Argus background fits.

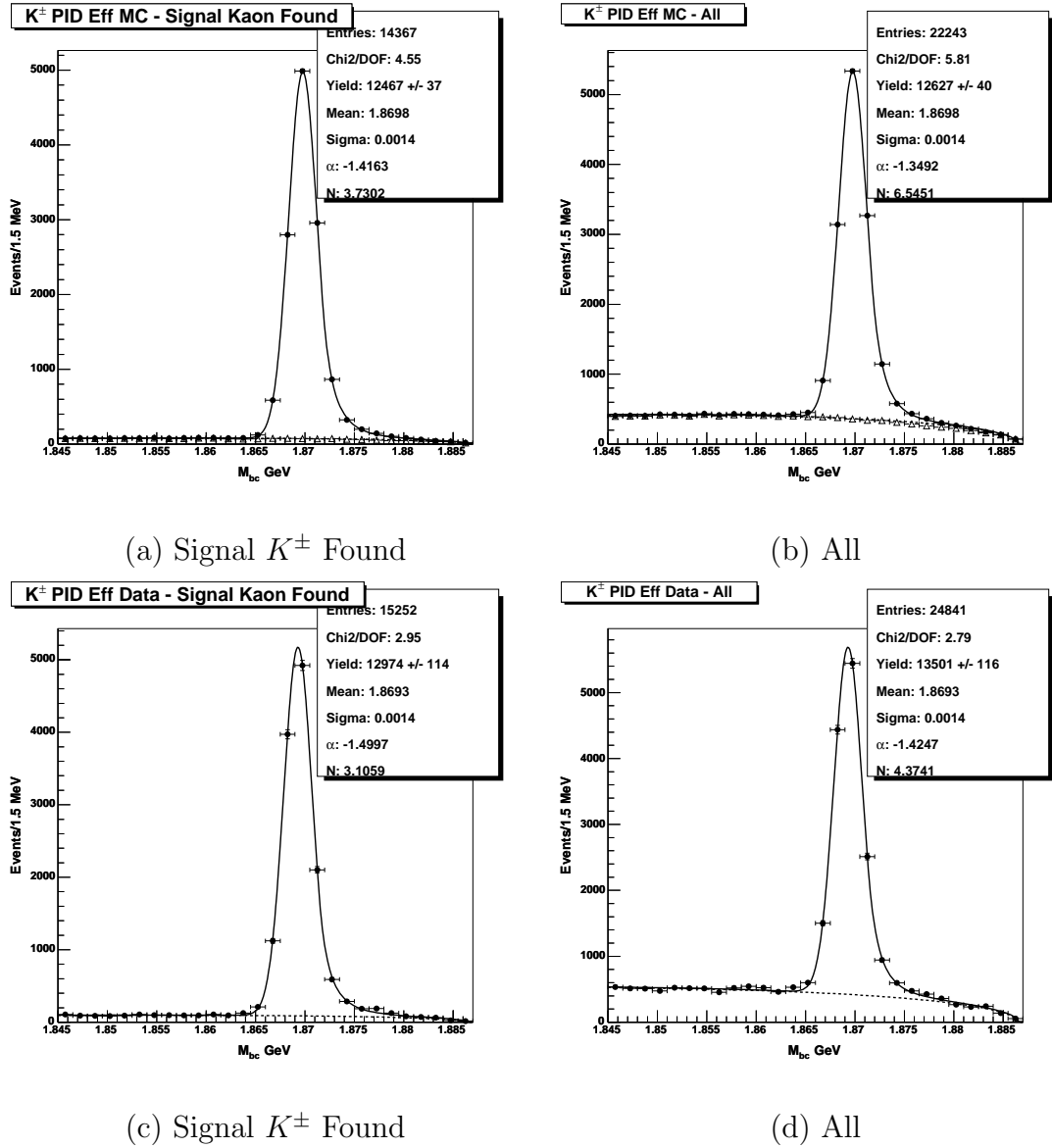


Figure 7.32: Signal K^\pm PID: fits to $D^0 \rightarrow K\pi$ M_{bc} distributions for $0.6 \leq p_{K^\pm} < 0.7$ GeV/c. In (a) and (b) filled circles show MC histograms and open triangles show MC background histograms. In (c) and (d) filled circles show data histograms. In all cases solid lines show CB line shape fits and dashed lines show Argus background fits.

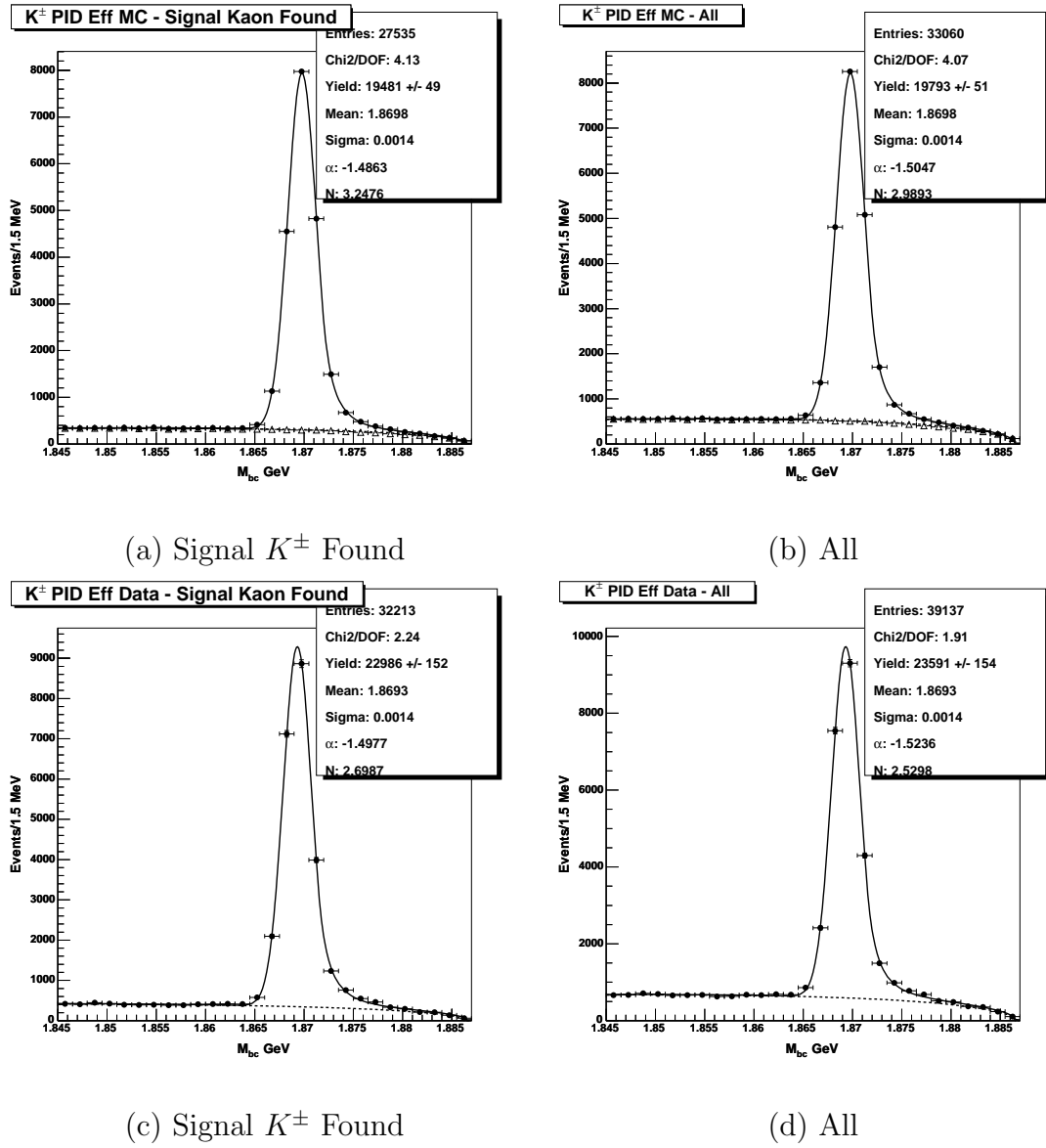


Figure 7.33: Signal K^\pm PID: fits to $D^0 \rightarrow K\pi$ M_{bc} distributions for $p_{K^\pm} \geq 0.7$ GeV/c. In (a) and (b) filled circles show MC histograms and open triangles show MC background histograms. In (c) and (d) filled circles show data histograms. In all cases solid lines show CB line shape fits and dashed lines show Argus background fits.

7.15 Charged Pion Signal PID

Just as for the signal K^\pm particles in the previous section, there is also a systematic uncertainty associated with the signal π^\pm PID efficiency. To determine any data-MC discrepancies for π^\pm PID we follow a similar procedure to that outlined above. There are two main differences in the case of charged pion PID. In the first case, we use the tag mode $D^0 \rightarrow K_S \pi \pi$ in place of $D^0 \rightarrow K \pi$. Secondly, we must also account for the fact that it is now possible for a tag mode to contain two signal π^\pm particles. Since we are only interested in the efficiency of detecting one of these particles, we require in these cases that one of the pions in the tag satisfy the usual D tag particle identification. The other pion, treated as our signal pion, has no PID applied to it, but just as for the K^\pm case, is required to be Trkman approved.

Fits are performed exactly as previously using a Crystal Ball line shape and an Argus background, with the mode dependent ΔE requirements given once again in Table 7.8. The signal momentum bins for the π^\pm (as corresponding to the signal q^2 bins) are: < 0.5 GeV/ c , $0.5 - 0.6$ GeV/ c , $0.6 - 0.7$ GeV/ c , $0.7 - 0.8$ GeV/ c and ≥ 0.8 GeV/ c . The fits for each tag mode and each momentum bin are shown in Figs. 7.35 to 7.49. The resulting efficiencies and MC corrections are given in Table. 7.10.

Once again the the overall PID efficiency correction to the MC is obtained via a linear fit to the momentum dependent corrections, Fig 7.34. The correction, w , obtained in this fashion and given by,

$$w = 0.0198 p_{\pi^\pm} + 0.979, \quad (7.14)$$

is used to weight each MC event where a signal $D^0 \rightarrow \pi^- e^+ \nu$ decay is found and the π^- is a true pion. For the systematic error we again walk around the one sigma

Table 7.10: Signal π^\pm PID efficiencies in data and MC.

<i>Momentum Bin</i>	ε_{MC}	$\varepsilon_{\text{data}}$	<i>MC Correction</i>
$p_{\pi^\pm} < 0.5 \text{ GeV}/c$	0.9627 ± 0.0017	0.9460 ± 0.0047	0.9826 ± 0.0052
$0.5 \leq p_{\pi^\pm} < 0.6 \text{ GeV}/c$	0.9793 ± 0.0028	0.9781 ± 0.0082	0.9988 ± 0.0089
$0.6 \leq p_{\pi^\pm} < 0.7 \text{ GeV}/c$	0.9780 ± 0.0023	0.9689 ± 0.0067	0.9907 ± 0.0072
$0.7 \leq p_{\pi^\pm} < 0.8 \text{ GeV}/c$	0.9310 ± 0.0024	0.9253 ± 0.0069	0.9938 ± 0.0078
$p_{\pi^\pm} \geq 0.8 \text{ GeV}/c$	0.9210 ± 0.0033	0.9140 ± 0.0096	0.9925 ± 0.0110

error ellipse to the four points on the semi-major and semi-minor axes, shown by the dash and dash-dot lines in Fig. 7.34. Once again, the points giving the largest yield deviations are used to obtain the branching fraction systematic errors, while the points giving the largest deviation in the shape of the q^2 distributions are used to obtain the form factor systematic errors. The dashed lines give the branching fraction variations and the dash-dot lines give the form factor variations.

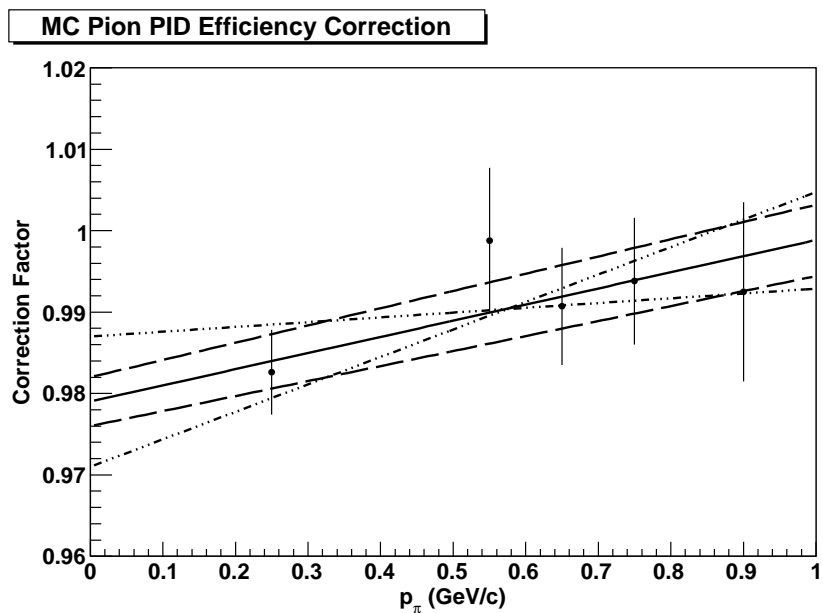


Figure 7.34: The MC π^\pm PID efficiency corrections as determined using the methods described in the text. The solid line shows the best linear fit to the data, it is taken as the nominal correction. The dashed and dash-dot lines show the extreme variations of the fit from the four points on the semi-major and semi-minor axes of the error ellipse.

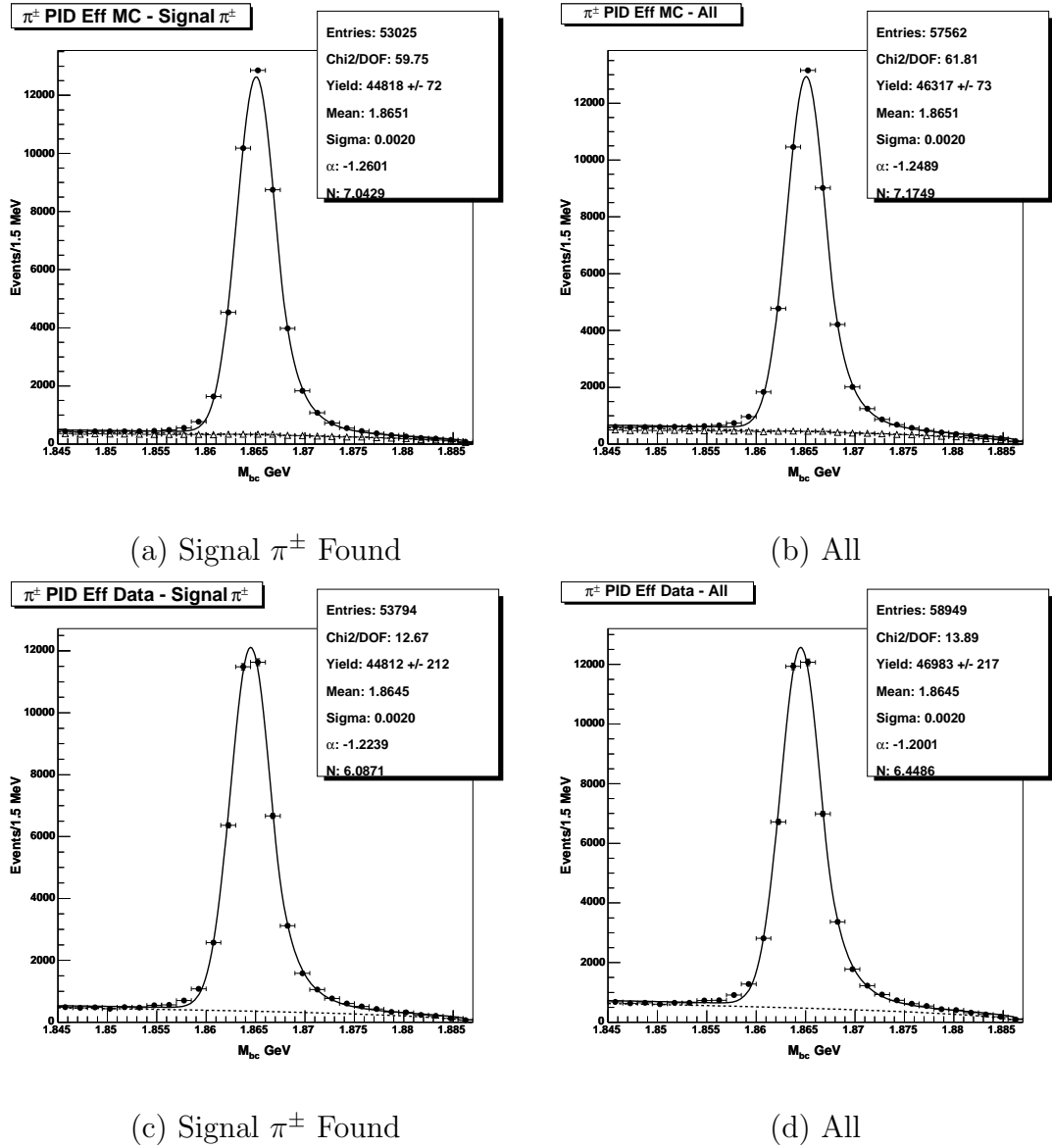


Figure 7.35: Signal π^\pm PID: fits to $D^0 \rightarrow K\pi\pi^0 M_{bc}$ distributions for $0.0 \leq p_{\pi^\pm} < 0.5$ GeV/c. In (a) and (b) filled circles show MC histograms and open triangles show MC background histograms. In (c) and (d) filled circles show data histograms. In all cases solid lines show CB line shape fits and dashed lines show Argus background fits.

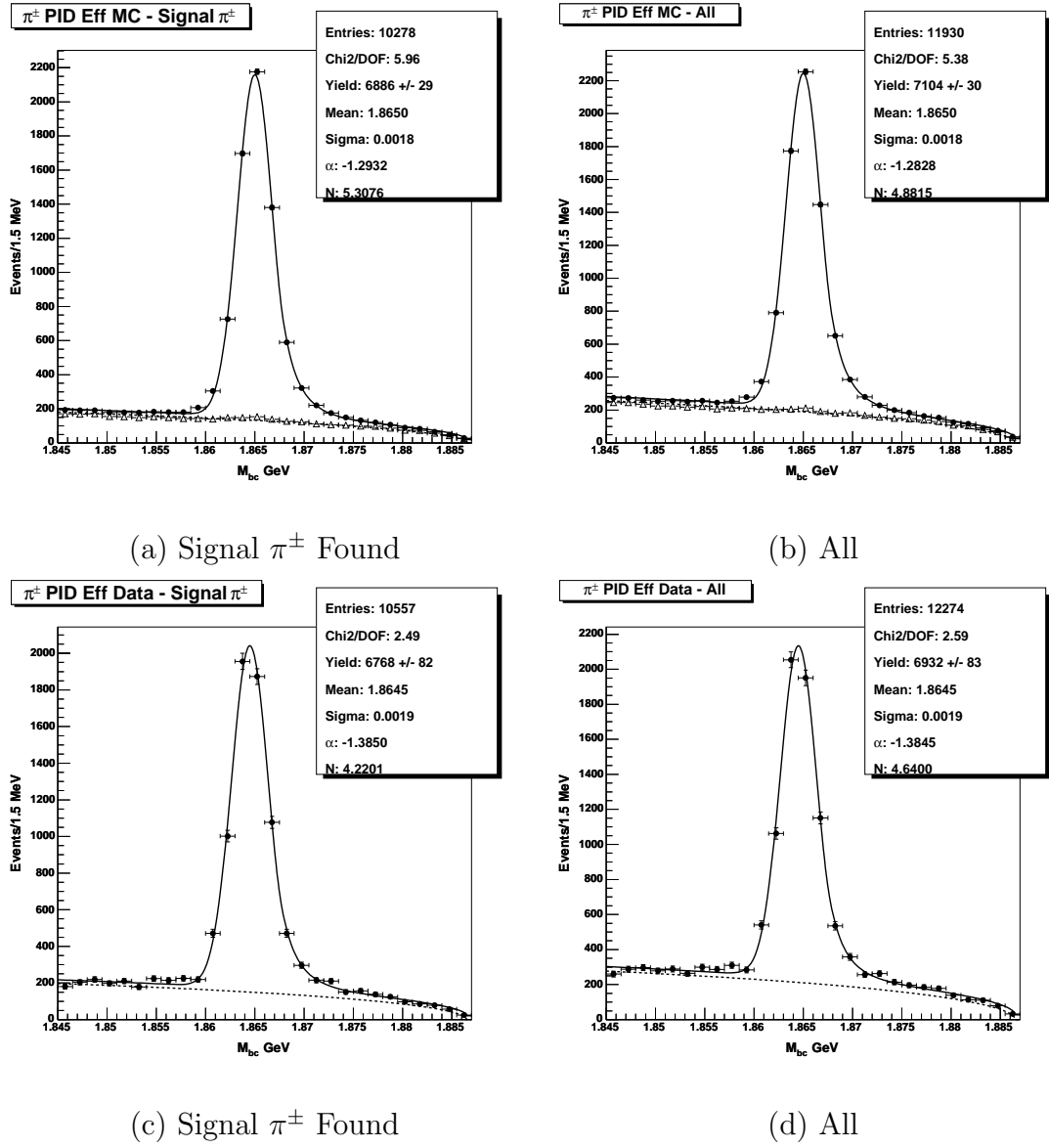


Figure 7.36: Signal π^\pm PID: fits to $D^0 \rightarrow K\pi\pi^0 M_{bc}$ distributions for $0.5 \leq p_{\pi^\pm} < 0.6$ GeV/c. In (a) and (b) filled circles show MC histograms and open triangles show MC background histograms. In (c) and (d) filled circles show data histograms. In all cases solid lines show CB line shape fits and dashed lines show Argus background fits.

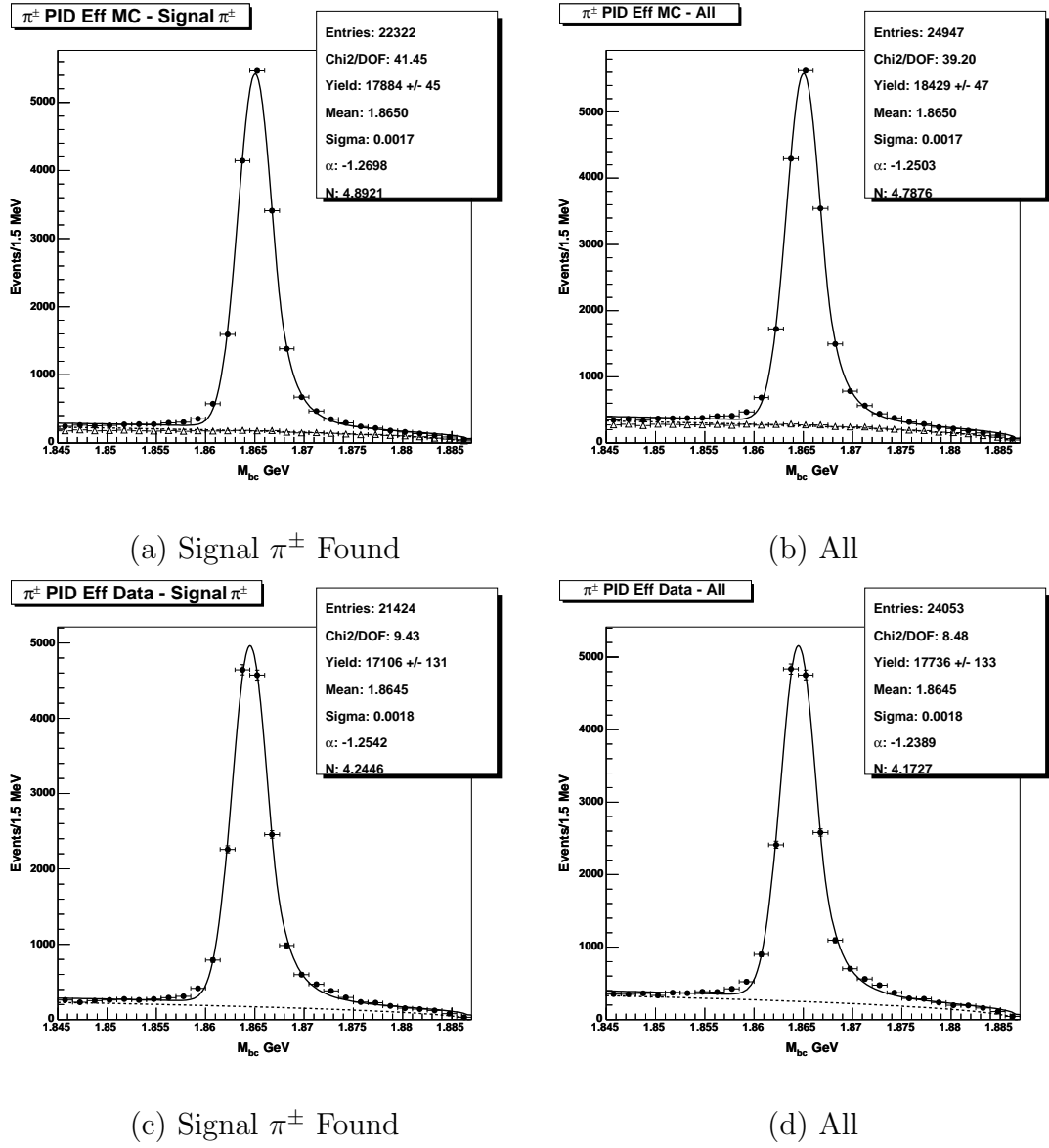


Figure 7.37: Signal π^\pm PID: fits to $D^0 \rightarrow K\pi\pi^0 M_{bc}$ distributions for $0.6 \leq p_{\pi^\pm} < 0.7$ GeV/c. In (a) and (b) filled circles show MC histograms and open triangles show MC background histograms. In (c) and (d) filled circles show data histograms. In all cases solid lines show CB line shape fits and dashed lines show Argus background fits.

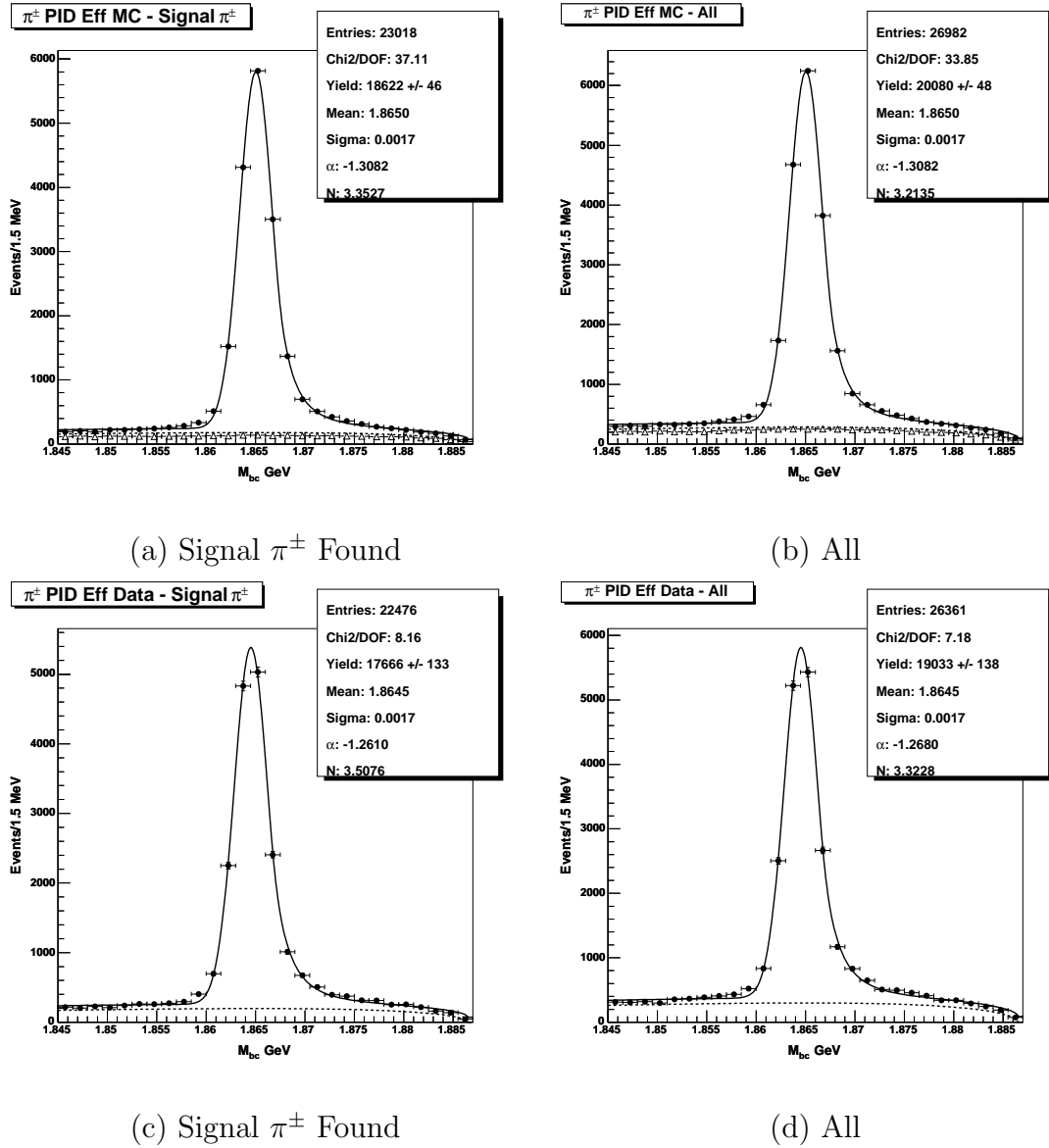


Figure 7.38: Signal π^\pm PID: fits to $D^0 \rightarrow K\pi\pi^0 M_{bc}$ distributions for $0.7 \leq p_{\pi^\pm} < 0.8$ GeV/c. In (a) and (b) filled circles show MC histograms and open triangles show MC background histograms. In (c) and (d) filled circles show data histograms. In all cases solid lines show CB line shape fits and dashed lines show Argus background fits.

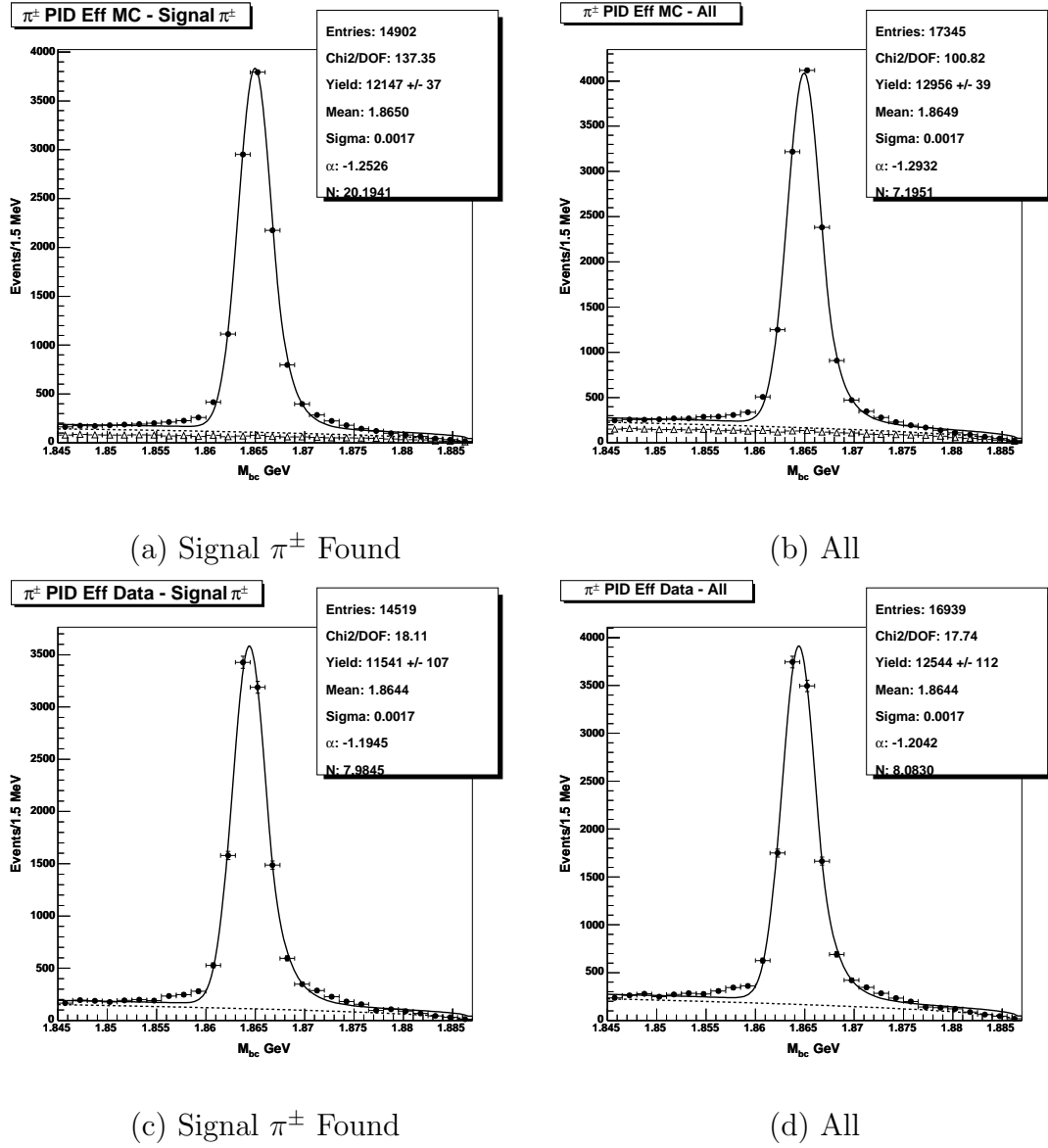


Figure 7.39: Signal π^\pm PID: fits to $D^0 \rightarrow K\pi\pi^0$ M_{bc} distributions for $p_{\pi^\pm} \geq 0.8$ GeV/c. In (a) and (b) filled circles show MC histograms and open triangles show MC background histograms. In (c) and (d) filled circles show data histograms. In all cases solid lines show CB line shape fits and dashed lines show Argus background fits.

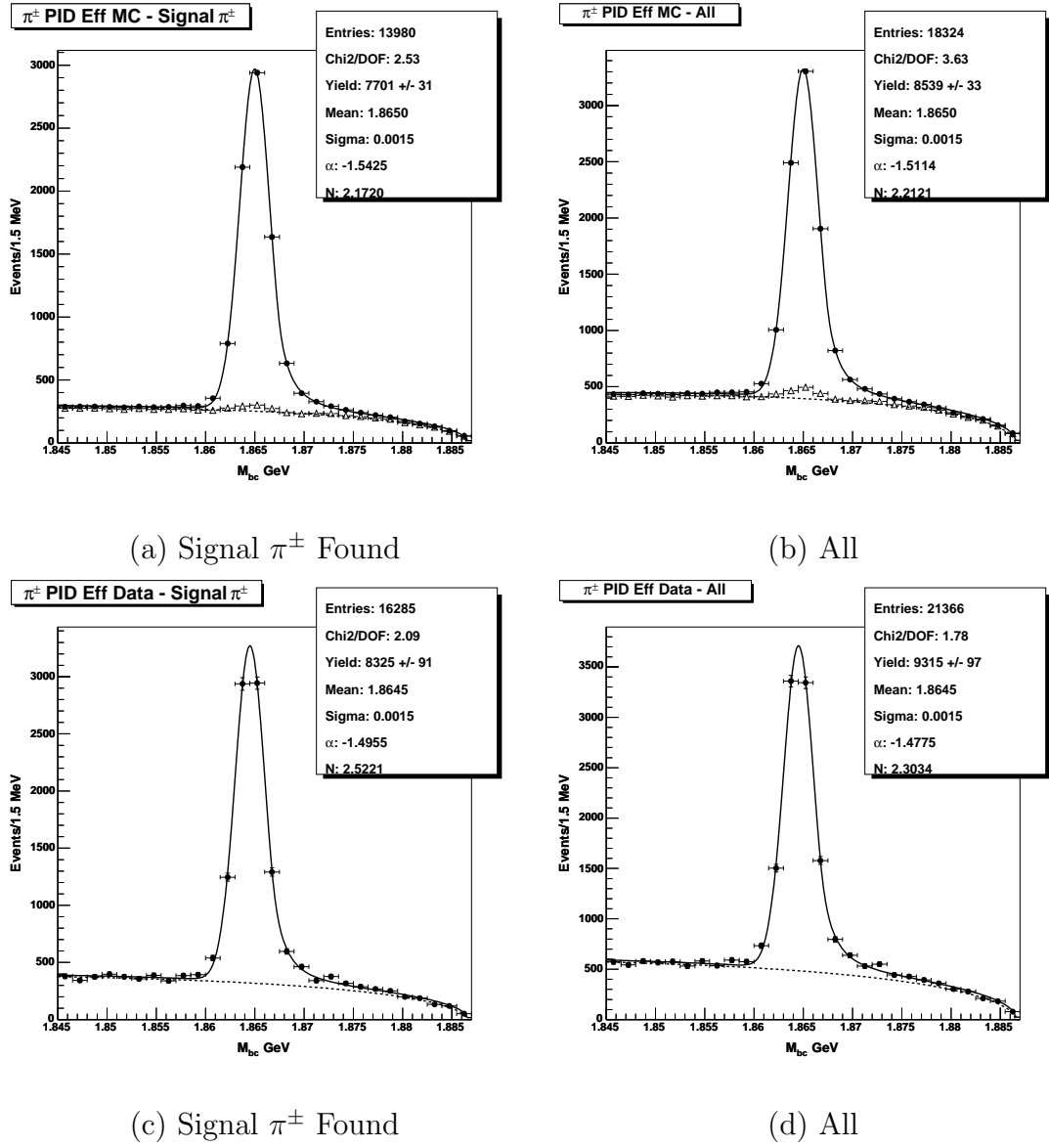


Figure 7.40: Signal π^\pm PID: fits to $D^0 \rightarrow K_S \pi \pi$ M_{bc} distributions for $0.0 \leq p_{\pi^\pm} < 0.5$ GeV/c. In (a) and (b) filled circles show MC histograms and open triangles show MC background histograms. In (c) and (d) filled circles show data histograms. In all cases solid lines show CB line shape fits and dashed lines show Argus background fits.

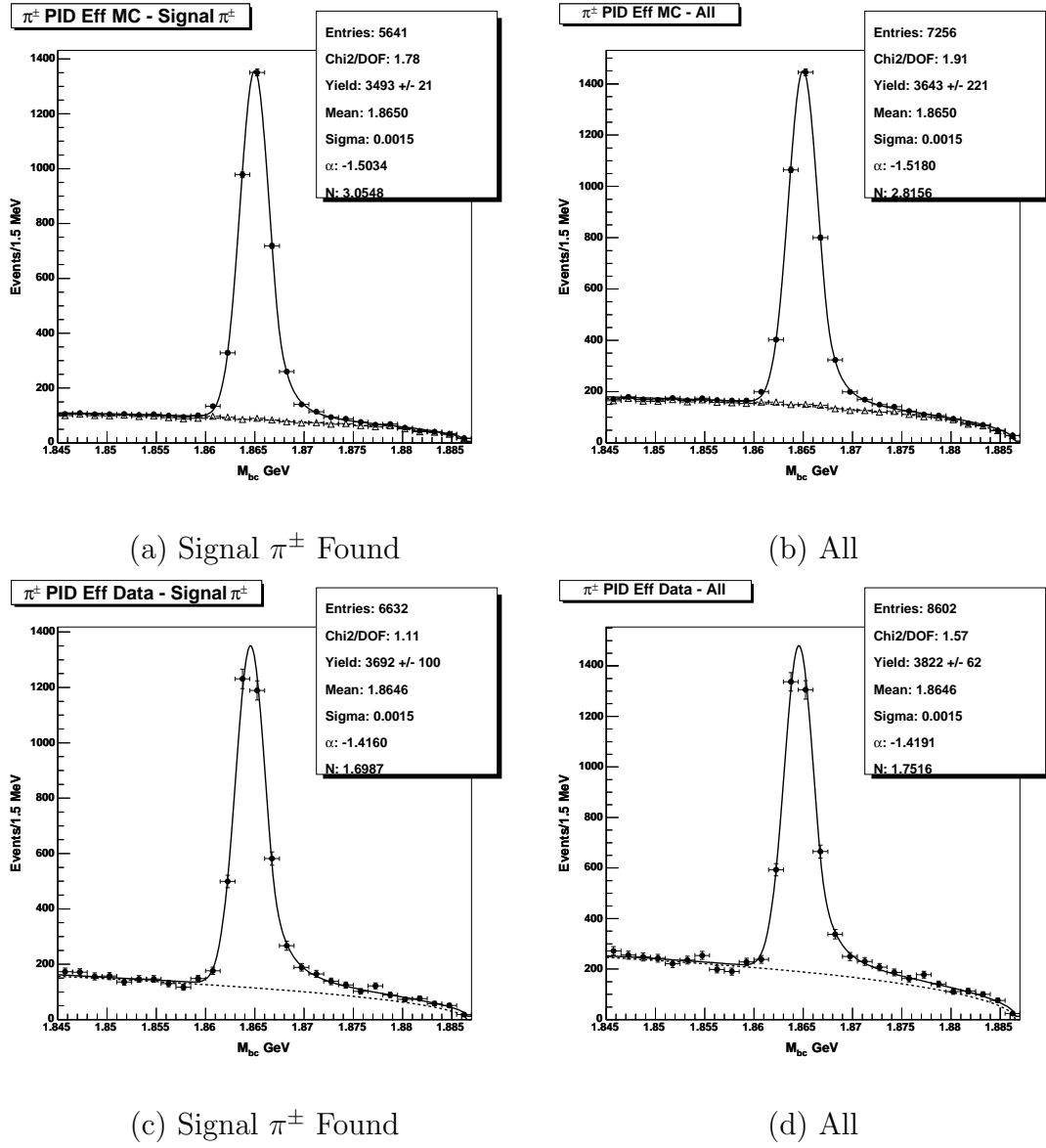


Figure 7.41: Signal π^\pm PID: fits to $D^0 \rightarrow K_S \pi \pi$ M_{bc} distributions for $0.5 \leq p_{\pi^\pm} < 0.6$ GeV/c. In (a) and (b) filled circles show MC histograms and open triangles show MC background histograms. In (c) and (d) filled circles show data histograms. In all cases solid lines show CB line shape fits and dashed lines show Argus background fits.

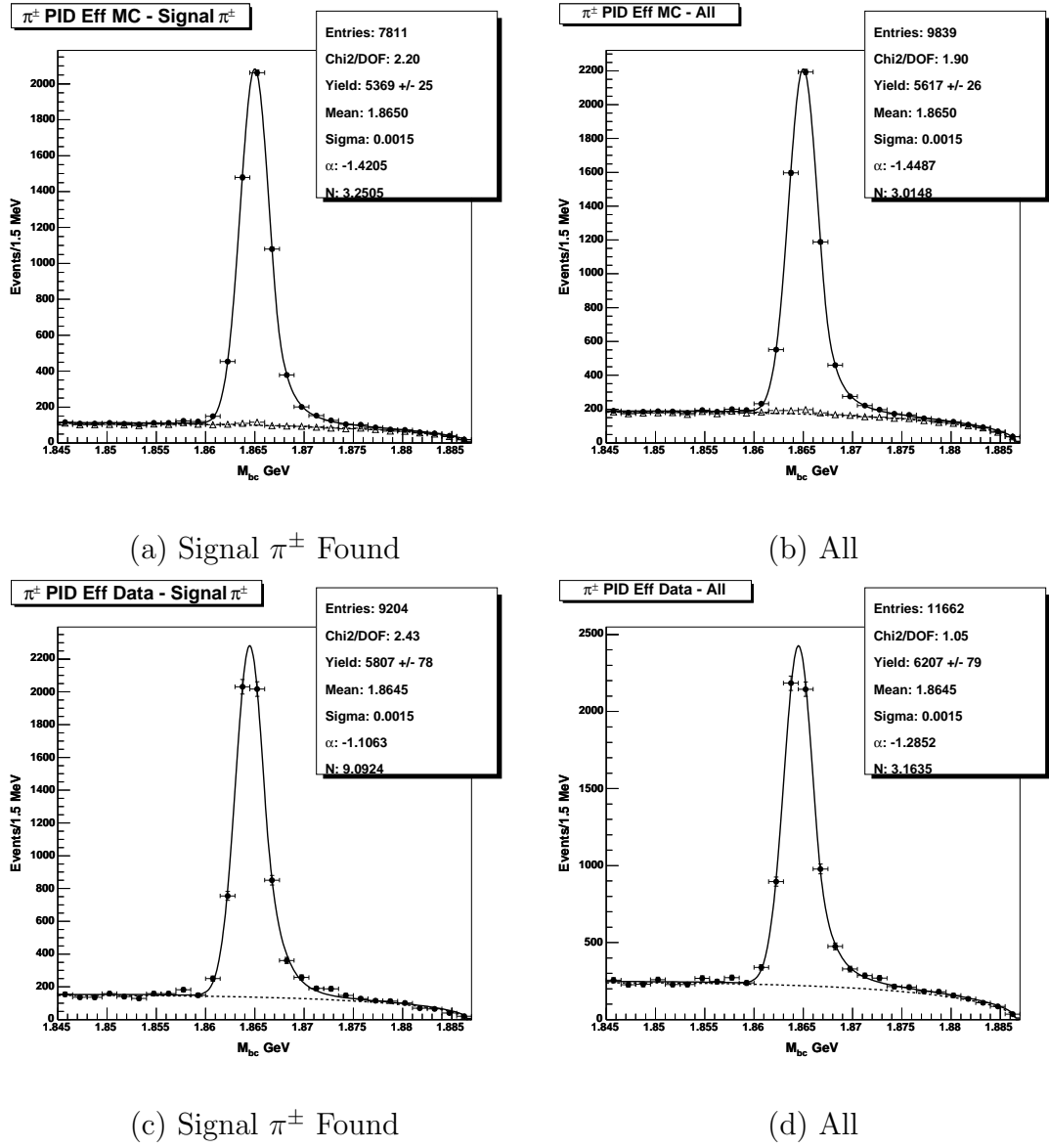


Figure 7.42: Signal π^\pm PID: fits to $D^0 \rightarrow K_S \pi \pi$ M_{bc} distributions for $0.6 \leq p_{\pi^\pm} < 0.7$ GeV/c. In (a) and (b) filled circles show MC histograms and open triangles show MC background histograms. In (c) and (d) filled circles show data histograms. In all cases solid lines show CB line shape fits and dashed lines show Argus background fits.

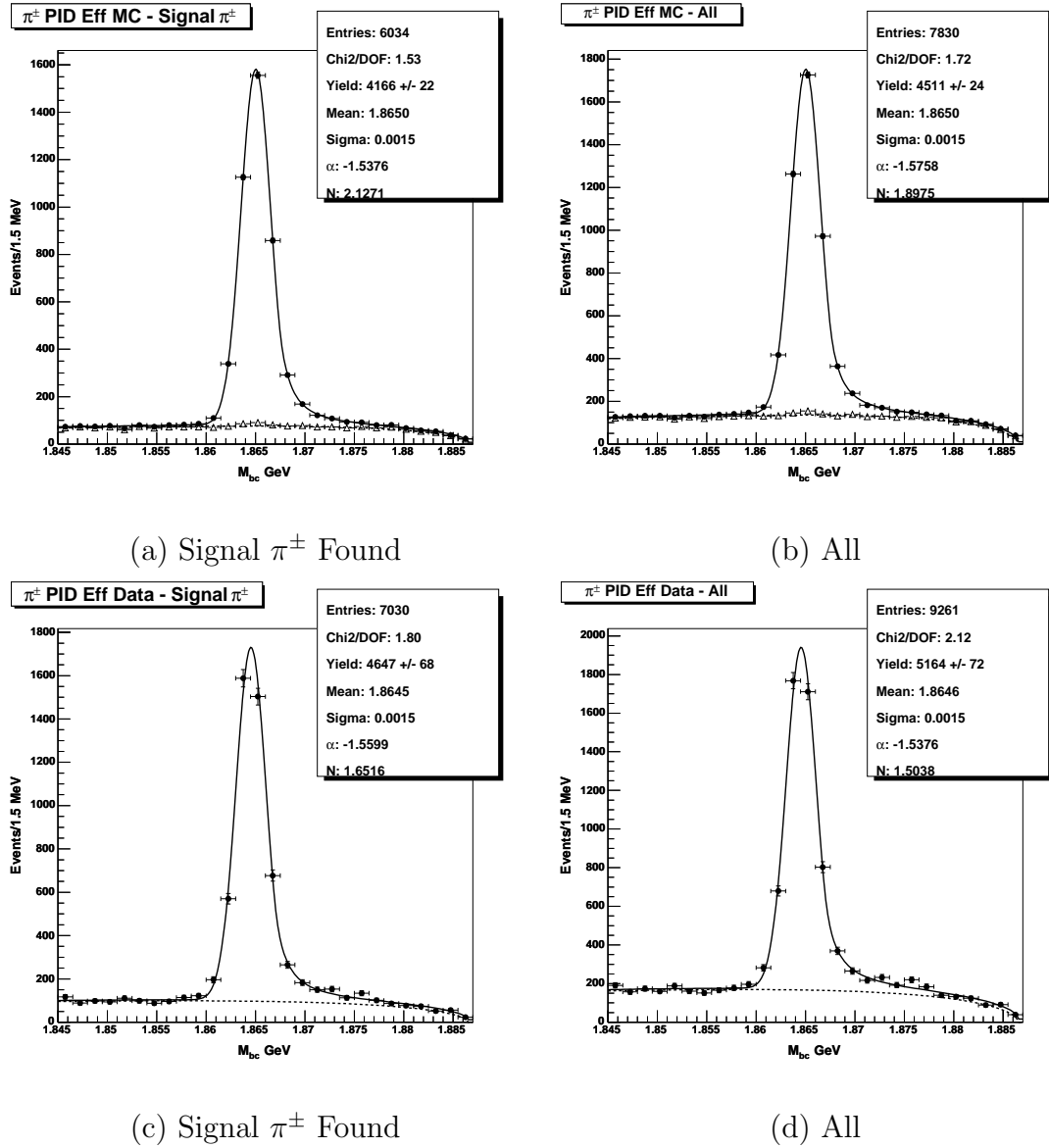


Figure 7.43: Signal π^\pm PID: fits to $D^0 \rightarrow K_S \pi \pi$ M_{bc} distributions for $0.7 \leq p_{\pi^\pm} < 0.8$ GeV/c. In (a) and (b) filled circles show MC histograms and open triangles show MC background histograms. In (c) and (d) filled circles show data histograms. In all cases solid lines show CB line shape fits and dashed lines show Argus background fits.

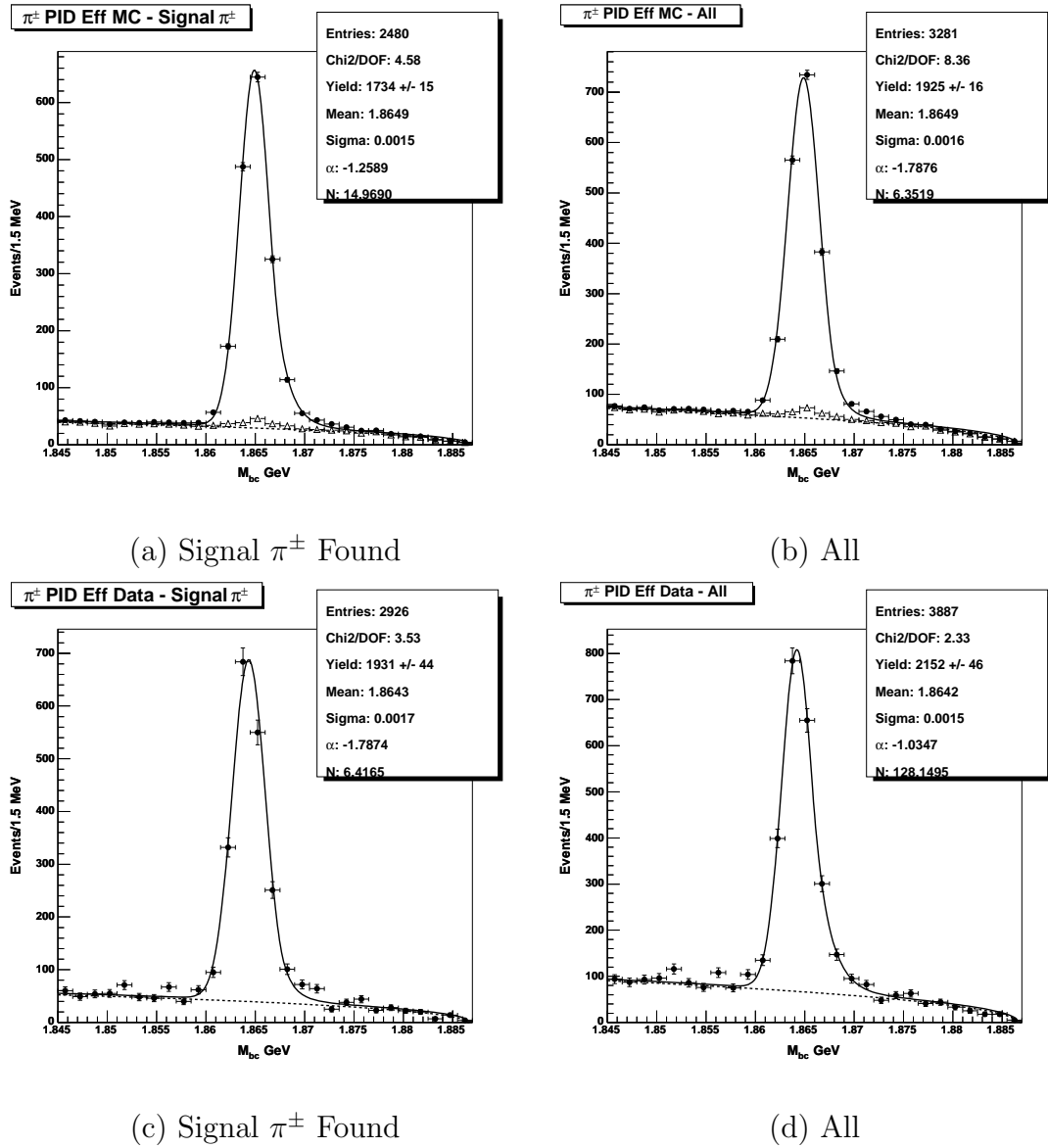


Figure 7.44: Signal π^\pm PID: fits to $D^0 \rightarrow K_S \pi \pi$ M_{bc} distributions for $p_{\pi^\pm} \geq 0.8$ GeV/c. In (a) and (b) filled circles show MC histograms and open triangles show MC background histograms. In (c) and (d) filled circles show data histograms. In all cases solid lines show CB line shape fits and dashed lines show Argus background fits.

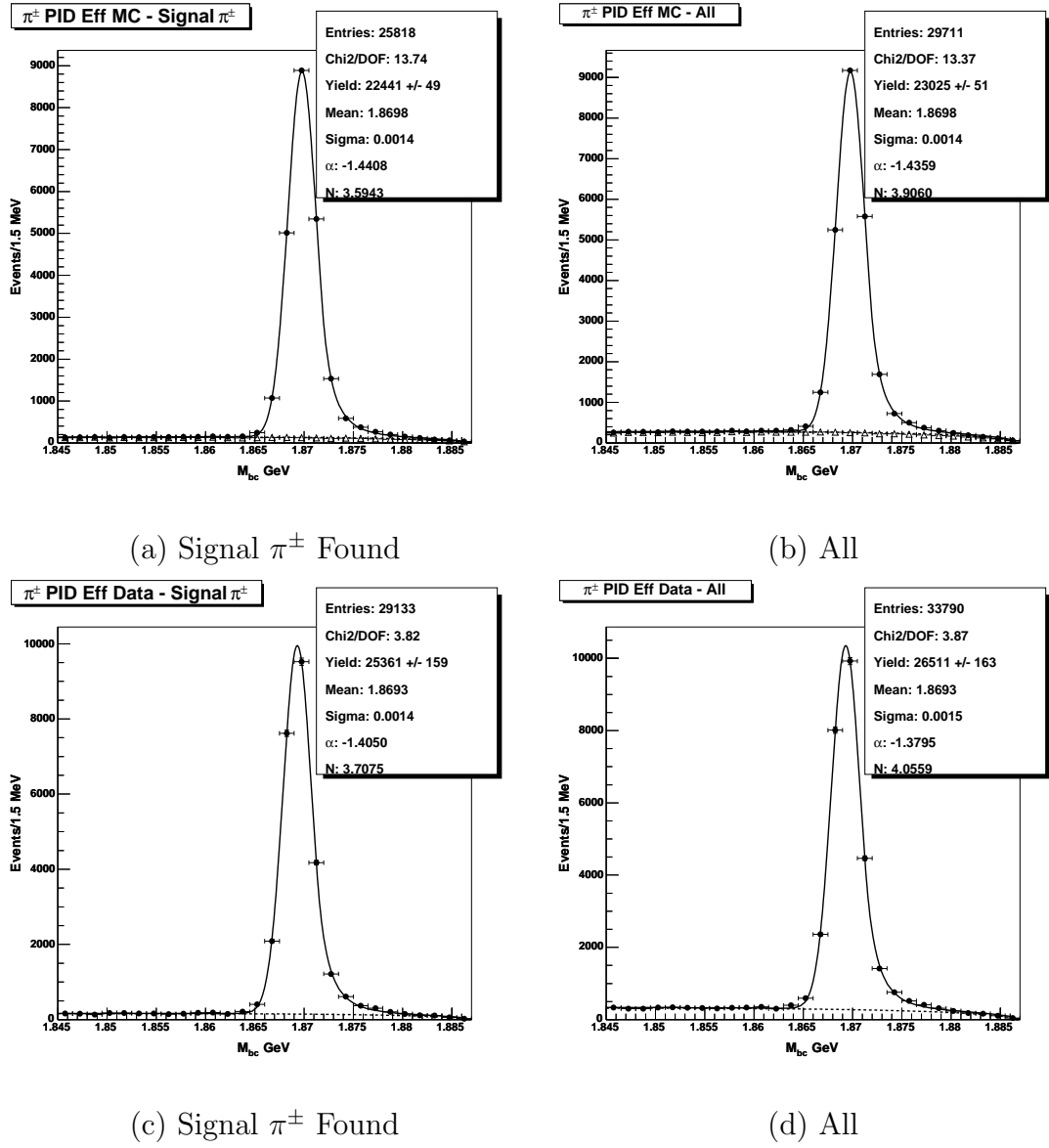


Figure 7.45: Signal π^\pm PID: fits to $D^\pm \rightarrow K\pi\pi$ M_{bc} distributions for $0.0 \leq p_{\pi^\pm} < 0.5$ GeV/c. In (a) and (b) filled circles show MC histograms and open triangles show MC background histograms. In (c) and (d) filled circles show data histograms. In all cases solid lines show CB line shape fits and dashed lines show Argus background fits.

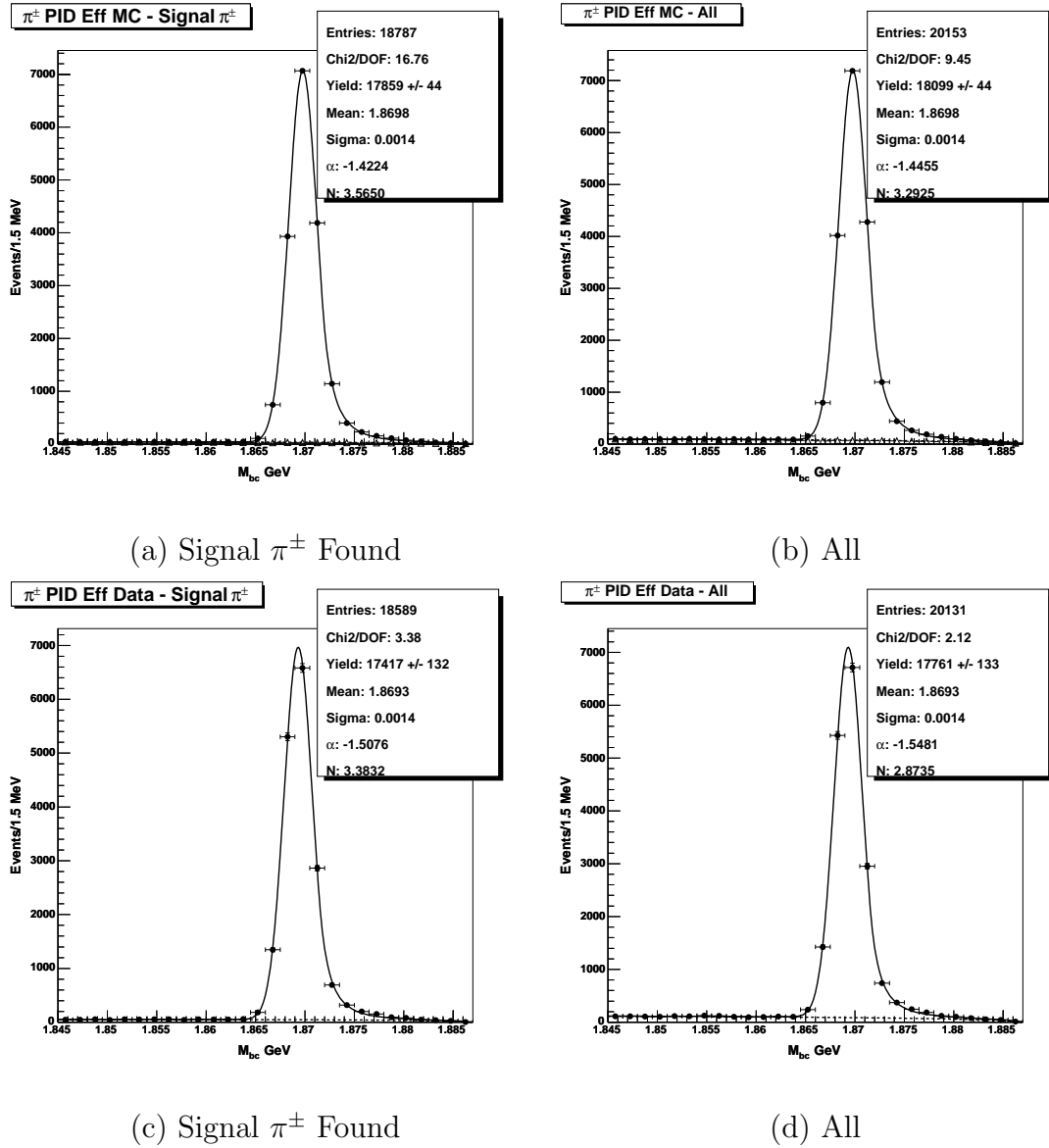


Figure 7.46: Signal π^\pm PID: fits to $D^\pm \rightarrow K\pi\pi$ M_{bc} distributions for $0.5 \leq p_{\pi^\pm} < 0.6$ GeV/c. In (a) and (b) filled circles show MC histograms and open triangles show MC background histograms. In (c) and (d) filled circles show data histograms. In all cases solid lines show CB line shape fits and dashed lines show Argus background fits.

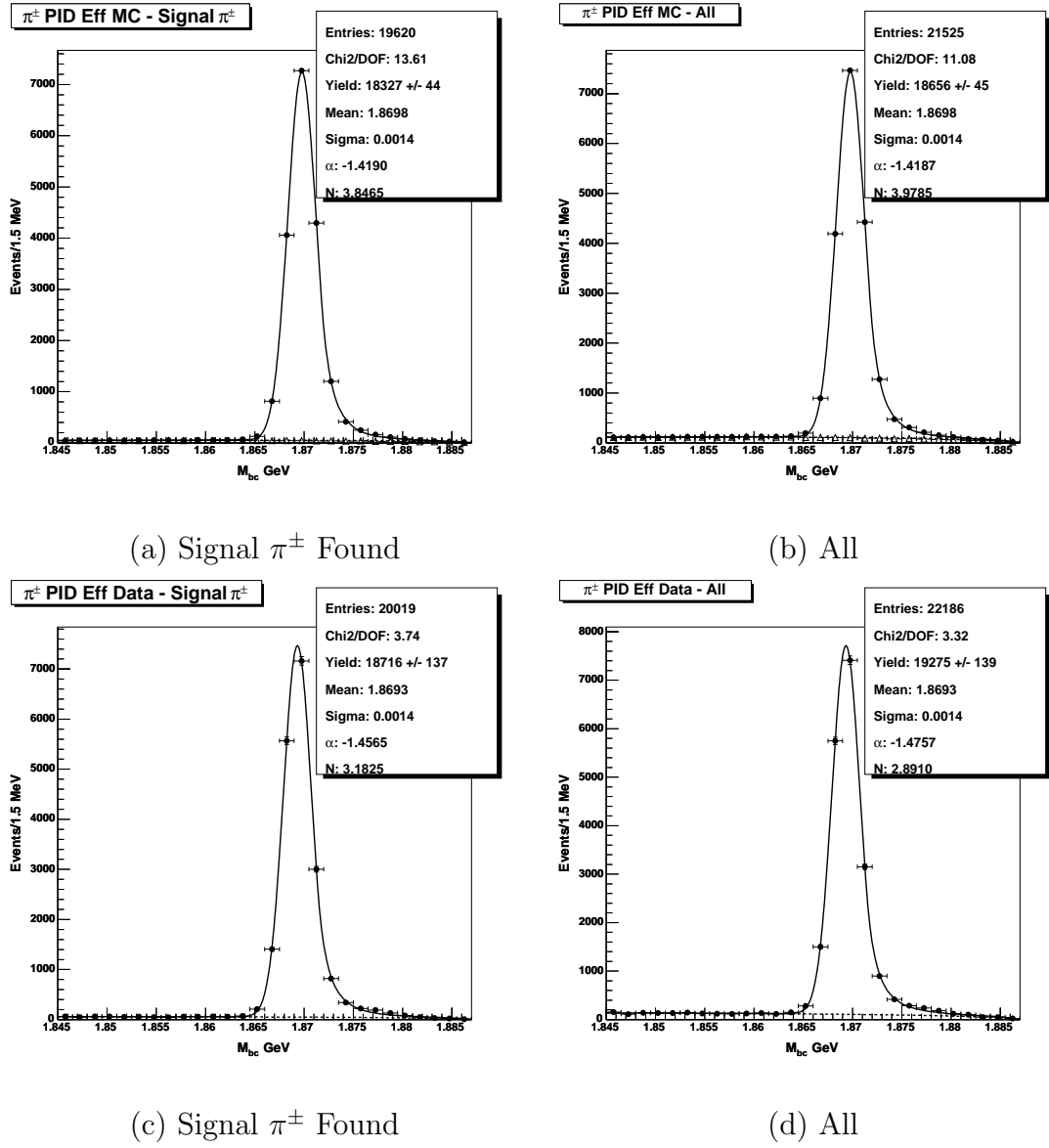


Figure 7.47: Signal π^\pm PID: fits to $D^\pm \rightarrow K\pi\pi$ M_{bc} distributions for $0.6 \leq p_{\pi^\pm} < 0.7$ GeV/c. In (a) and (b) filled circles show MC histograms and open triangles show MC background histograms. In (c) and (d) filled circles show data histograms. In all cases solid lines show CB line shape fits and dashed lines show Argus background fits.

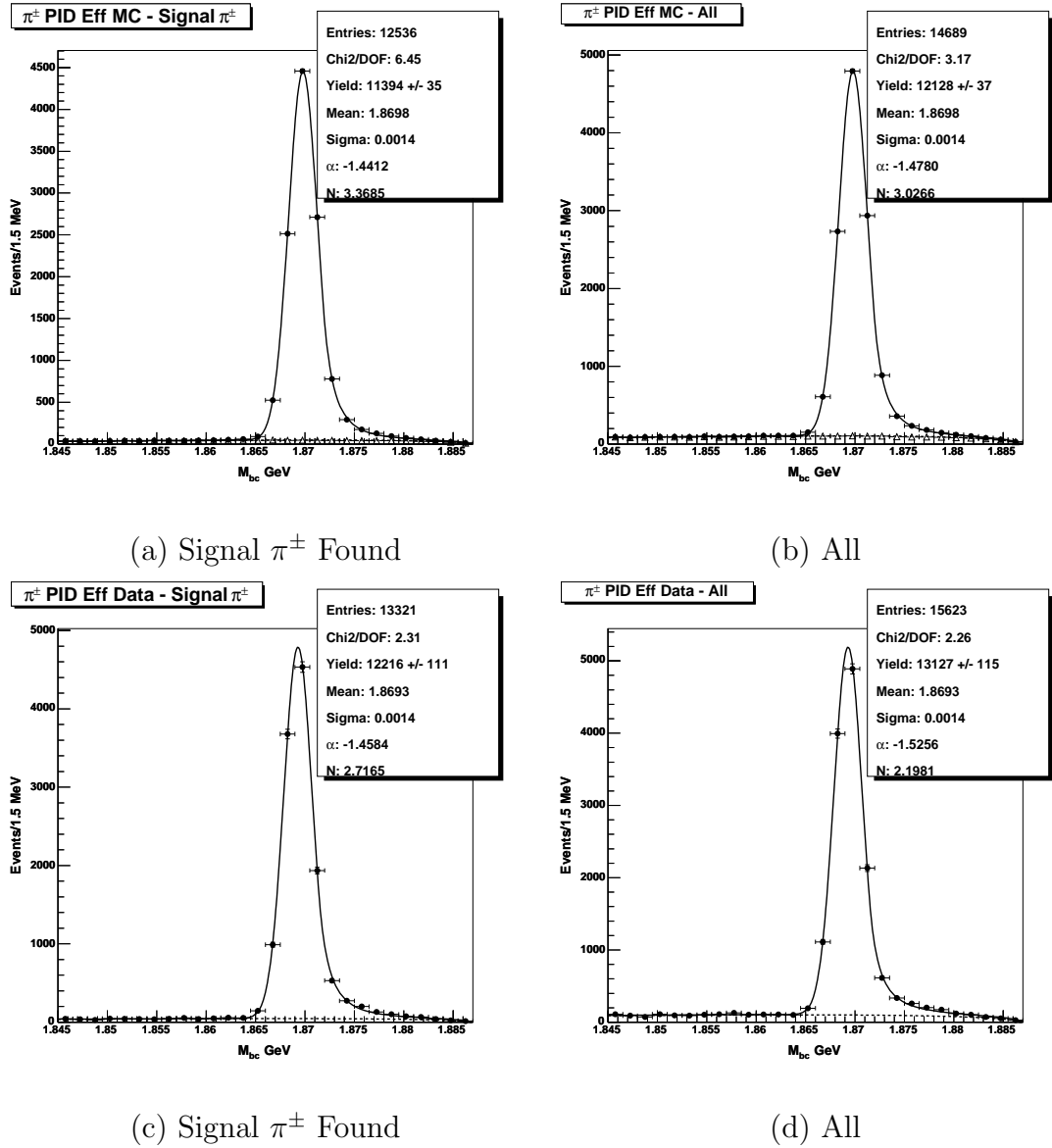


Figure 7.48: Signal π^\pm PID: fits to $D^\pm \rightarrow K\pi\pi$ M_{bc} distributions for $0.7 \leq p_{\pi^\pm} < 0.8$ GeV/c. In (a) and (b) filled circles show MC histograms and open triangles show MC background histograms. In (c) and (d) filled circles show data histograms. In all cases solid lines show CB line shape fits and dashed lines show Argus background fits.

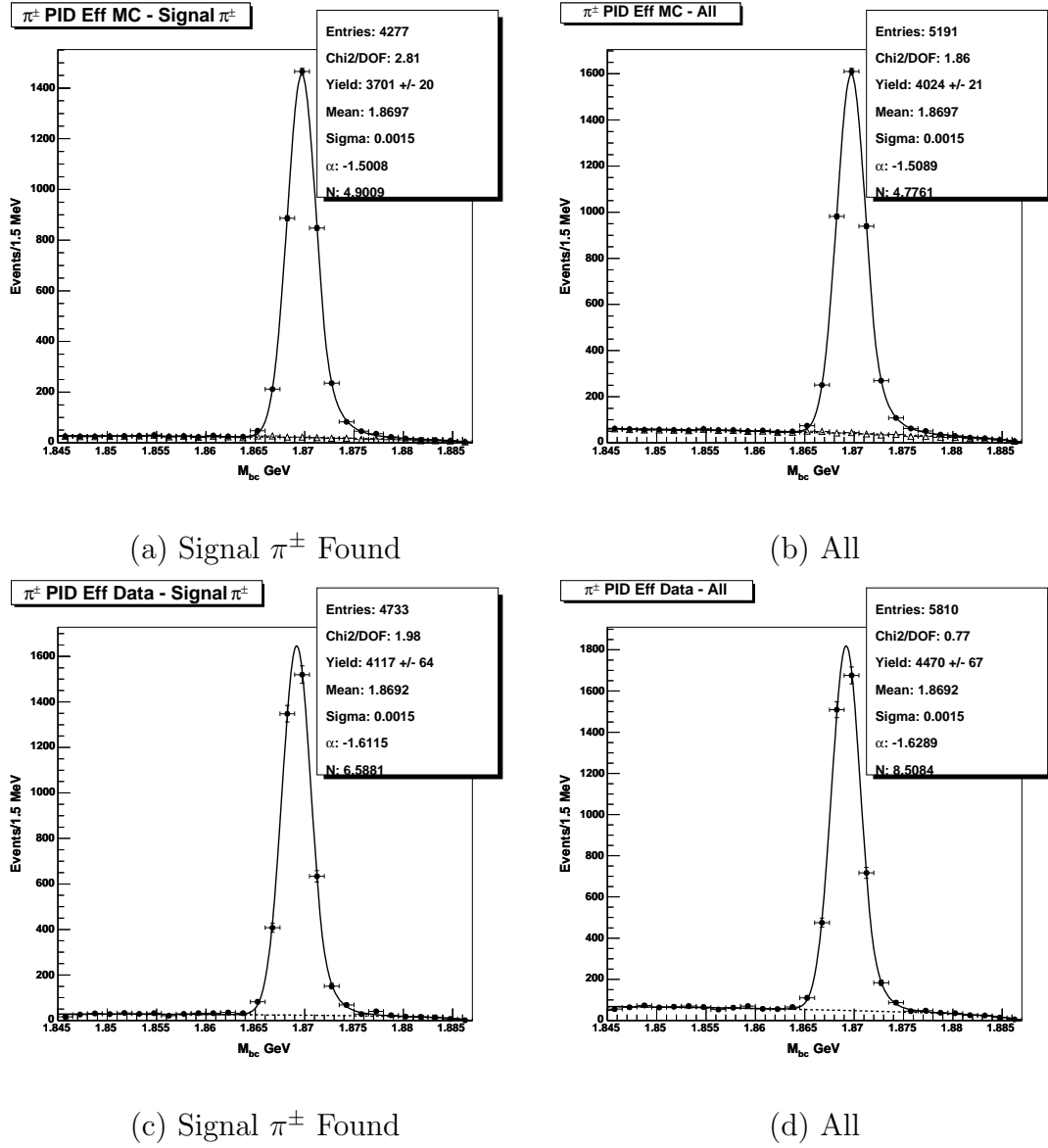


Figure 7.49: Signal π^\pm PID: fits to $D^\pm \rightarrow K\pi\pi$ M_{bc} distributions for $p_{\pi^\pm} \geq 0.8$ GeV/c. In (a) and (b) filled circles show MC histograms and open triangles show MC background histograms. In (c) and (d) filled circles show data histograms. In all cases solid lines show CB line shape fits and dashed lines show Argus background fits.

7.16 Electron ID and Fakes

The procedures used in this analysis to identify electrons have already been discussed in some detail, see Section 5.1.1. In brief, for the MC we use only true electrons with data measured efficiencies and add events with fake electrons to the fit using data. There are two associated systematic uncertainties: the error on the measured electron identification efficiencies and the error on the measured fake rates. To assess these uncertainties we follow the same procedure in each case. Namely, we add the measured one standard deviation errors on the efficiencies or fake rates to their central values and re-fit the data. The resulting deviation from the nominal fit in each case is taken as the systematic error.

7.17 Multiple Electron Veto

The methods of electron identification have been discussed extensively in the previous sections. We now focus on the systematic uncertainty associated with the multiple electron veto, that is how well the number of true electrons per event is modeled in the MC.⁵ To estimate this uncertainty this we follow a similar method to that used in the K_L re-weight systematic. We take events containing a tagged D meson and look for electrons on the other side of the event. The tags used and their quality criteria are the same as in Section 7.5. The same procedure is followed in both data and MC and we compare the resulting number of electrons per event. The MC is normalized absolutely and then the semileptonic events are re-scaled so that the number of data events matches the number of MC events.

⁵We remind the reader that multiple electrons due to the presence of fakes in the MC are handled using a separate procedure that relies on our knowledge of the data measured fake rates.

We do this to compensate for the known discrepancies in semileptonic branching fractions between data and MC.

The resulting electrons per event counts are given in Table 7.11. For the MC we break down the contributions into the three main types of decays that produce the electron: semileptonic decays, photon conversions and fakes. Looking at these results we see that, within error, the MC correctly models the number of electrons per event. Furthermore, we believe that the source of any discrepancy within the error margins is mostly likely to result from the MC modeling of photon conversions. There are several reasons for this deduction.

The number of semileptonic decays results simply from the input branching fractions to the MC and we believe these to be correctly accounted for in our analysis. Likewise the fake electron veto probability in MC is believed to be accurate, being taken from data measured fake rates. Photon conversions on the other hand, which result from material interactions, rely on accurate detector modeling in the MC. Since this is the most likely place for imperfect replication of the data we are left with photon conversions as the best candidate for evaluation of the electron veto systematic. The D^0 results show us that we know the photon conversion rate to within $\sim 8\%$, a value obtained simply from the error margin on the data. For the multiple electron veto systematic error therefore we drop 8% of electrons from photon conversions in the MC, where by drop we mean that the electron does not get called an electron, although the track is still present in the event.

7.18 M_{bc} Smearing

The smearing corrections to the M_{bc} distributions for the $D^0 \rightarrow K^- e^+ \nu$, $D^0 \rightarrow \pi^- e^+ \nu$ and $D^+ \rightarrow \pi^0 e^+ \nu$ signal modes were described in Section 6.2. For the

Table 7.11: Number of electrons per event in data and MC for $D^0\bar{D}^0$ and D^+D^- events. MC is normalized absolutely and then semileptonic events are scaled so that the number of MC events equals the number of data events. The abbreviations used in the MC break down are: PC - photon conversion, SL - semileptonic and FK - fake.

$D^0\bar{D}^0$			
<i>Number of Electrons per Event</i>	<i>1</i>	<i>2</i>	<i>3</i>
<i>Data Event Count Total</i>	18913 ± 138	284 ± 17	3 ± 2
<i>MC Event Count Total</i>	18930 ± 51	268 ± 7	2 ± 1
<i>Break Down of MC Events</i>			
<i>PC Event Count</i>	1819 ± 22	142 ± 6	2 ± 1
<i>SL Event Count</i>	15702 ± 42	63 ± 3	0 ± 0
<i>FK Event Count</i>	0 ± 0	30 ± 2	0 ± 0
<i>PC and SL Event Count</i>	0 ± 0	14 ± 1	0 ± 0
<i>SL and FK Event Count</i>	0 ± 0	26 ± 2	0 ± 0
<i>FK and PC Event Count</i>	0 ± 0	3 ± 1	0 ± 0
D^+D^-			
<i>Number of Electrons per Event</i>	<i>1</i>	<i>2</i>	<i>3</i>
<i>Data Event Count Total</i>	19508 ± 140	141 ± 12	3 ± 2
<i>MC Event Count Total</i>	19517 ± 53	132 ± 5	4 ± 1
<i>Break Down of MC Events</i>			
<i>PC Event Count</i>	626 ± 12	62 ± 3	2 ± 0
<i>SL Event Count</i>	18296 ± 50	71 ± 3	3 ± 1
<i>FK Event Count</i>	0 ± 0	30 ± 2	0 ± 0
<i>PC and SL Event Count</i>	0 ± 0	10 ± 1	0 ± 0
<i>SL and FK Event Count</i>	0 ± 0	26 ± 2	1 ± 0
<i>FK and PC Event Count</i>	0 ± 0	10 ± 1	0 ± 0

systematic uncertainties associated with these smears we fix all the smears to their central values as determined by the fit (given above) and one by one turn the smears up and down by their one standard deviation errors and re-fit. In general the results of smearing up and smearing down are very symmetric about the central value; we take the largest deviation (smear up or smear down) to be the systematic error.

7.19 Final State Radiation

The default final state radiation (FSR) generator in the CLEO MC is PHOTOS [41]. In PHOTOS, generation of FSR is accomplished using a leading-logarithm approximation and in semileptonic decays radiation from the final state pion (or kaon) and electron is treated independently. This treatment should approximate the FSR energy spectrum well, but the angular separation of the photon and electron will require corrections. This is verified by a comparison with the more sophisticated KLOR generator [42], written for the generation of radiative $K^0 \rightarrow \pi^- e^+ \nu$ decays. To correct PHOTOS we modify the KLOR generator to produce radiative D semileptonic decays.⁶ For our nominal results we take the $\cos\theta_{e\gamma}$ and E_γ distributions from the PHOTOS generated radiative events and re-weight them to match the KLOR generated distributions. A comparison of the PHOTOS and KLOR photon energy and angular distributions is shown for each of the signal modes in Figures 7.50 - 7.53. In addition we re-weight the overall number of PHOTOS radiative decays to agree with the radiative branching fractions predicted by KLOR. In all cases KLOR predicts slightly higher radiative branching fractions

⁶This is a simple matter for the D^0 decays, but for the D^+ decays we have to modify the matrix element, switching radiation and interference from the daughter meson to the parent meson.

than PHOTOS, Table 7.12. For the systematic error on FSR production we take the difference between the branching fraction fits for PHOTOS and KLOR. This should be an overestimate of the error, however, this allows us to account for the unknown structure-dependent FSR contributions.

Table 7.12: Predicted fraction of radiative events (with photon energies greater than $\sim 0.9\text{MeV}$) for each signal mode in PHOTOS and KLOR.

<i>Decay Mode</i>	<i>Radiative Fraction</i>	
	PHOTOS	KLOR
$D^0 \rightarrow \pi^- e^+ \nu$	0.183	0.217
$D^0 \rightarrow K^- e^+ \nu$	0.163	0.179
$D^+ \rightarrow \pi^0 e^+ \nu$	0.162	0.184
$D^+ \rightarrow \bar{K}^0 e^+ \nu$	0.154	0.167

7.20 Form Factor Dependence

To determine the dependence of our results on our input form factors,⁷ we re-weight our signal MC with a different form factor model and determine the branching fraction differences. For each of our signal modes the partial width is given by the pseudo-scalar decay rate, Eq. 2.51. Thus to re-shape the q^2 distribution of our MC with input form factor f_{input}^+ , to a new model with form factor f_{model}^+ , without changing the overall branching fraction, we re-weight each signal MC event with weight w , where w is given by

$$w = \frac{|f_{\text{model}}^+(q^2)|^2 \int_0^{q_{\text{max}}^2} p_X^3(q'^2) |f_{\text{input}}^+(q'^2)|^2 dq'^2}{|f_{\text{input}}^+(q^2)|^2 \int_0^{q_{\text{max}}^2} p_X^3(q'^2) |f_{\text{model}}^+(q'^2)|^2 dq'^2}. \quad (7.15)$$

We choose to re-weight our signal MC with the form factor obtained using the ISGW2 model [30], which is known to be inaccurate and also differs significantly

⁷Recall that we use a modified pole (BK) parameterization [29] with values from LQCD calculations [14] as our nominal form factor input.

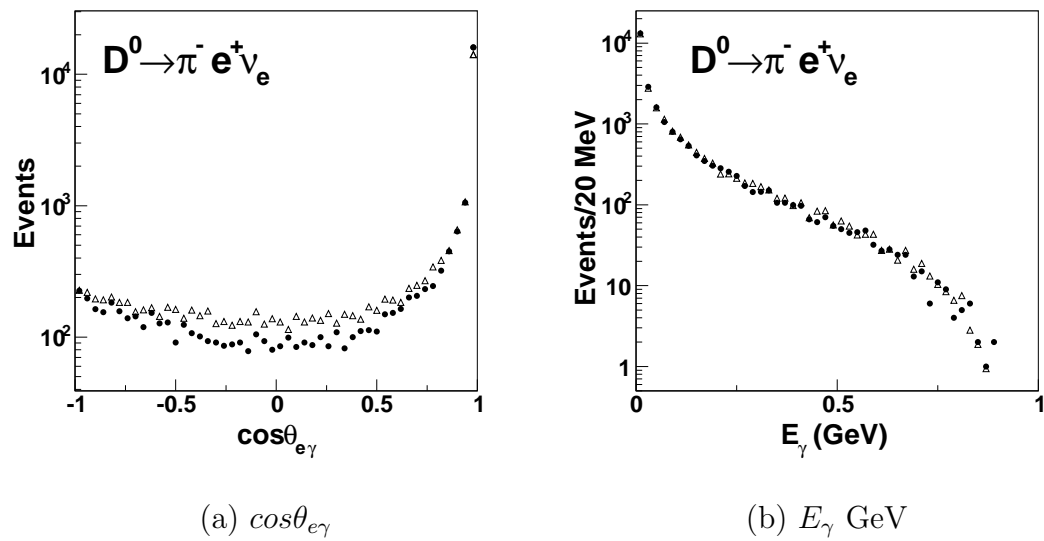


Figure 7.50: Signal $D^0 \rightarrow \pi^- e^+ \nu$ mode comparison of PHOTOS (filled circles) and KLOR (open triangles) generated radiative photon distributions. In (a) we show the comparison for the photon angle to the electron and in (b) we show the comparison of the photon energy distributions.

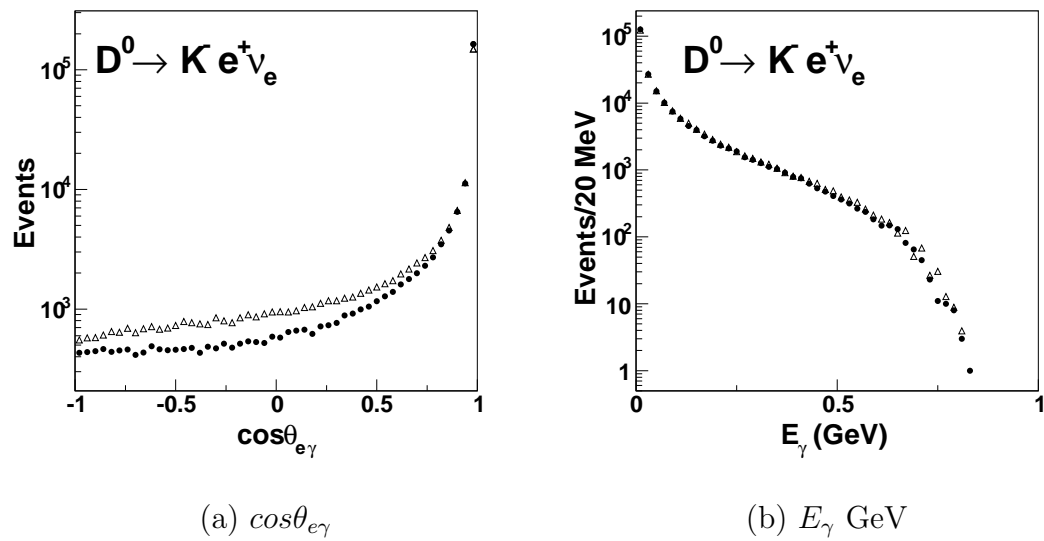


Figure 7.51: Signal $D^0 \rightarrow K^- e^+ \nu$ mode comparison of PHOTOS (filled circles) and KLOR (open triangles) generated radiative photon distributions. In (a) we show the comparison for the photon angle to the electron and in (b) we show the comparison of the photon energy distributions.

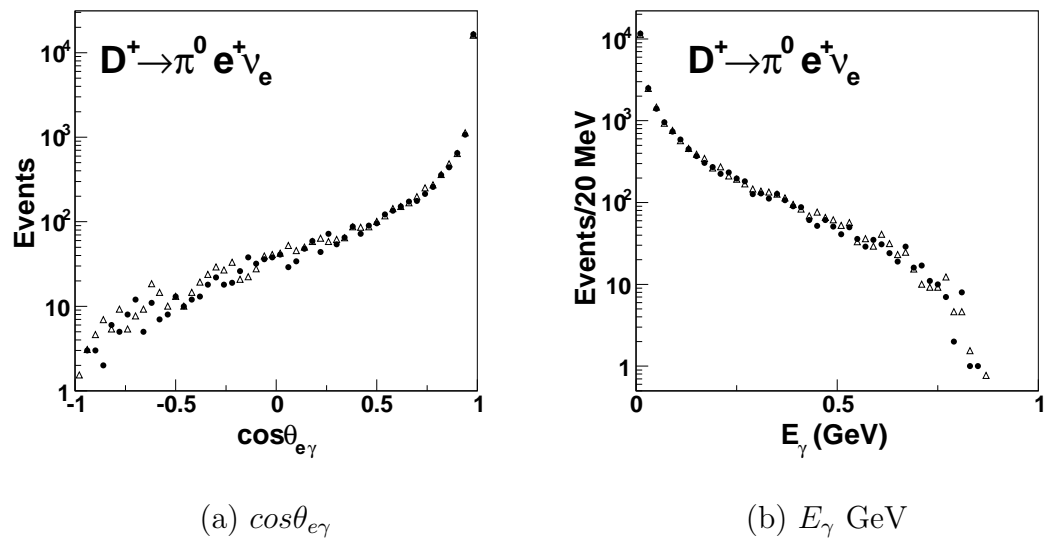


Figure 7.52: Signal $D^+ \rightarrow \pi^0 e^+ \nu$ mode comparison of PHOTOS (filled circles) and KLOR (open triangles) generated radiative photon distributions. In (a) we show the comparison for the photon angle to the electron and in (b) we show the comparison of the photon energy distributions.

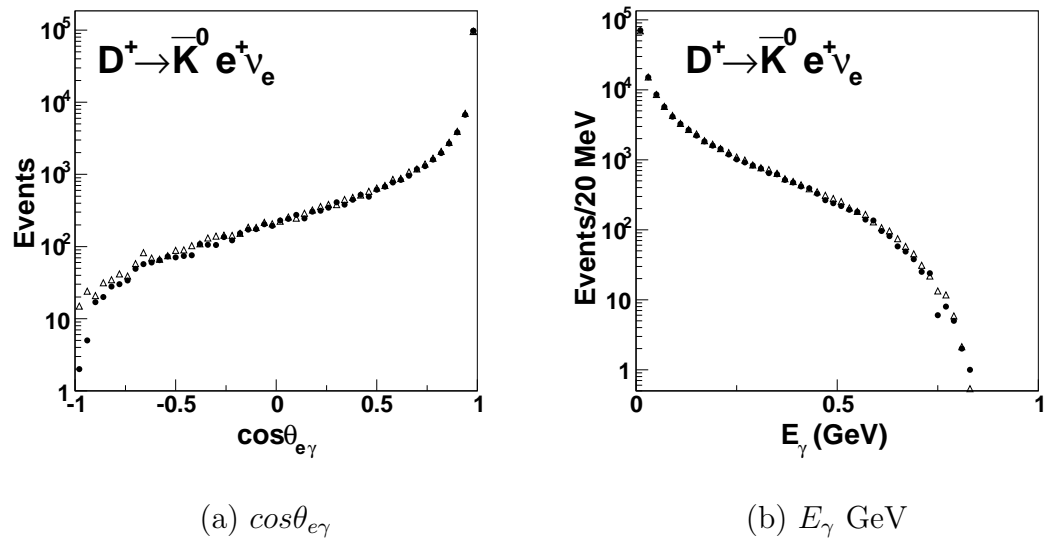


Figure 7.53: Signal $D^+ \rightarrow K_S e^+ \nu$ mode comparison of PHOTOS (filled circles) and KLOR (open triangles) generated radiative photon distributions. In (a) we show the comparison for the photon angle to the electron and in (b) we show the comparison of the photon energy distributions.

from the q^2 spectrum of our nominal signal MC, Fig 7.54. The ISGW2 form factor is given by,

$$f^+(q^2) = \frac{f^+(q_{\max}^2)}{\left(1 + \frac{r^2}{12}(q_{\max}^2 - q^2)\right)^2}, \quad (7.16)$$

where r is a constant determined by the parent and daughter mesons (see [30] for details).

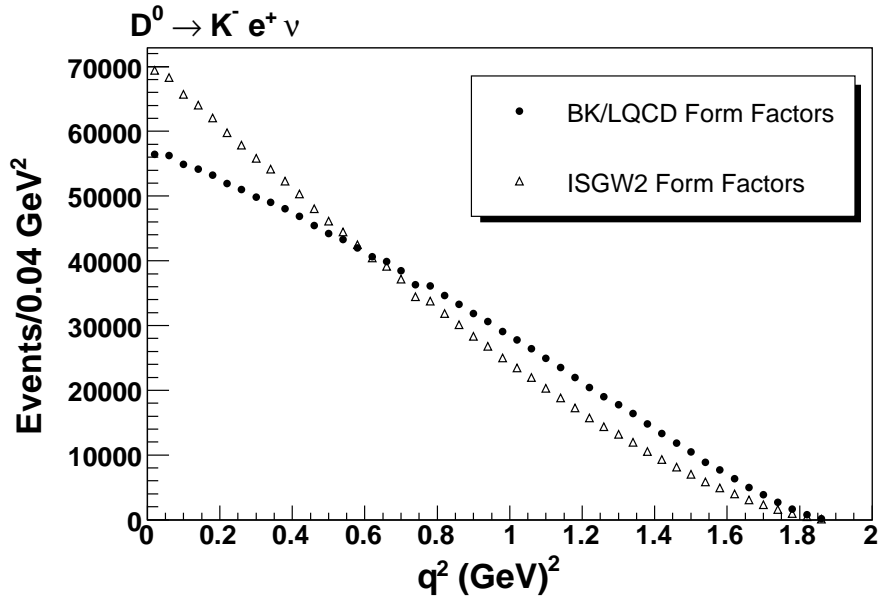


Figure 7.54: The q^2 spectra from $D^0 \rightarrow K^- e^+ \nu$ signal MC generated with ISGW2 form factors (open triangles) and modified pole model (BK) [29] form factors with LQCD calculated parameters [14] (filled circles).

7.21 Systematic Uncertainty Results

Here we list the resulting percent changes in the branching fractions for each of the signal modes and each of the systematic uncertainties described above. These are given for the full range of q^2 bins in Tables 7.13 - 7.16.

Table 7.13: Summary of full and partial branching fraction (\mathcal{B}) systematic errors (%) for the $D^0 \rightarrow \pi^- e^+ \nu$ signal decay mode.

Systematic	$D^0 \rightarrow \pi^- e^+ \nu$ q^2 interval (GeV) ²					$\mathcal{B}_{\text{total}}$
	< 0.4	0.4 – 0.8	0.8 – 1.2	1.2 – 1.6	≥ 1.6	
Hadronic Showers	0.58	0.90	1.92	2.58	0.48	1.17
K_L Showers	0.15	0.13	0.11	0.06	0.60	0.04
K_L Re-weight	0.67	0.66	0.66	0.67	0.65	0.66
Track Eff.	0.60	0.56	0.50	0.63	0.45	0.54
Track Res.	0.00	1.02	0.01	0.46	0.85	0.46
Splitoff Smear	0.58	0.02	0.16	0.04	0.22	0.12
Degrade PID	0.01	0.02	0.08	0.02	0.09	0.04
Shower Res.	0.03	0.09	0.06	0.01	0.11	0.06
Trkman Fakes	0.76	0.72	0.71	0.71	0.72	0.72
π^0 Eff.	0.01	0.01	0.01	0.00	0.03	0.00
K_S Eff.	0.01	0.01	0.02	0.04	0.08	0.03
π^- PID	0.44	0.41	0.39	0.39	0.40	0.41
K^- PID	0.05	0.02	0.02	0.01	0.02	0.03
e^+ PID	0.76	0.40	0.75	0.36	0.44	0.56
e^+ Fakes	2.50	0.45	0.01	0.05	0.92	0.88
π^0 Re-weight	0.01	0.02	0.03	0.01	0.06	0.03
π^- Re-weight	0.07	0.42	0.44	0.10	1.96	0.24
K^- Fakes	0.67	1.01	0.93	0.35	0.08	0.58
π^- Smear	0.93	1.06	0.85	0.83	1.05	0.95
K^- Smear	0.07	0.04	0.02	0.01	0.01	0.03
π^0 Smear	0.01	0.02	0.00	0.01	0.13	0.02
e^+ Veto	0.05	0.04	0.01	0.14	0.01	0.00
FSR	0.85	1.53	0.97	0.91	0.75	0.99
Form Factor Dep.	0.50	0.01	0.09	0.43	1.55	0.19
Number $D\bar{D}$	1.26	1.26	1.26	1.26	1.26	1.26
Total	3.61	3.14	3.15	3.46	3.59	2.83

Table 7.14: Summary of full and partial branching fraction (\mathcal{B}) systematic errors (%) for the $D^0 \rightarrow K^- e^+ \nu$ signal decay mode.

Systematic	$D^0 \rightarrow K^- e^+ \nu$ q^2 interval (GeV) ²					$\mathcal{B}_{\text{total}}$
	< 0.4	0.4 – 0.8	0.8 – 1.2	1.2 – 1.6	≥ 1.6	
Hadronic Showers	0.89	1.54	1.49	2.00	0.67	1.29
K_L Showers	0.01	0.02	0.04	0.05	0.06	0.01
K_L Re-weight	0.66	0.65	0.66	0.67	0.69	0.66
Track Eff.	0.37	0.39	0.44	0.44	0.21	0.39
Track Res.	0.28	0.43	0.50	0.60	0.34	0.39
Splitoff Smear	0.59	0.56	0.48	0.43	0.21	0.54
Degrade PID	0.06	0.04	0.05	0.03	0.04	0.05
Shower Res.	0.00	0.00	0.00	0.00	0.01	0.00
Trkman Fakes	0.72	0.72	0.71	0.71	0.71	0.72
π^0 Eff.	0.00	0.00	0.00	0.00	0.00	0.01
K_S Eff.	0.01	0.00	0.00	0.00	0.07	0.01
π^- PID	0.00	0.00	0.00	0.00	0.00	0.00
K^- PID	0.32	0.30	0.28	0.26	0.26	0.30
e^+ PID	0.65	0.58	0.60	0.52	0.46	0.61
e^+ Fakes	0.57	0.07	0.04	0.01	0.39	0.25
π^0 Re-weight	0.00	0.00	0.01	0.00	0.01	0.00
π^- Re-weight	0.00	0.00	0.00	0.05	0.23	0.01
K^- Fakes	0.00	0.00	0.01	0.01	0.02	0.00
π^- Smear	0.02	0.01	0.01	0.01	0.06	0.01
K^- Smear	0.09	0.08	0.07	0.09	0.16	0.09
π^0 Smear	0.00	0.00	0.00	0.00	0.00	0.00
e^+ Veto	0.08	0.07	0.00	0.02	0.03	0.05
FSR	0.63	0.61	0.56	0.48	0.47	0.59
Form Factor Dep.	0.33	0.11	0.16	0.41	1.29	0.02
Number $D\bar{D}$	1.26	1.26	1.26	1.26	1.26	1.26
Total	2.29	2.52	2.49	2.83	2.37	2.39

Table 7.15: Summary of full and partial branching fraction (\mathcal{B}) systematic errors (%) for the $D^+ \rightarrow \pi^0 e^+ \nu$ signal decay mode.

Systematic	$D^+ \rightarrow \pi^0 e^+ \nu$ q^2 interval (GeV) ²					$\mathcal{B}_{\text{total}}$
	< 0.4	0.4 – 0.8	0.8 – 1.2	1.2 – 1.6	≥ 1.6	
Hadronic Showers	0.62	2.94	2.11	1.30	1.68	1.14
K_L Showers	0.19	0.17	0.08	0.13	0.83	0.03
K_L Re-weight	1.10	1.07	1.07	1.08	1.13	1.09
Track Eff.	0.51	0.37	0.18	0.14	0.13	0.24
Track Res.	1.08	0.05	0.09	0.90	0.13	0.12
Splitoff Smear	1.66	1.08	0.68	1.45	0.81	0.86
Degrade PID	0.09	0.02	0.04	0.07	0.03	0.03
Shower Res.	0.00	0.01	0.18	0.30	0.04	0.08
Trkman Fakes	0.76	0.71	0.69	0.70	0.71	0.71
π^0 Eff.	0.87	0.56	0.77	1.07	1.07	0.85
K_S Eff.	0.02	0.02	0.08	0.11	0.18	0.07
π^- PID	0.17	0.37	0.13	0.24	0.29	0.06
K^- PID	0.17	0.37	0.12	0.24	0.29	0.06
e^+ PID	1.13	0.53	0.33	0.98	0.01	0.62
e^+ Fakes	1.52	0.14	0.29	0.07	0.64	0.44
π^0 Re-weight	0.43	0.81	0.76	0.73	1.87	0.04
π^- Re-weight	0.07	0.02	0.03	0.02	1.46	0.29
K^- Fakes	0.01	0.01	0.04	0.07	0.20	0.05
π^- Smear	0.00	0.00	0.01	0.05	0.29	0.05
K^- Smear	0.00	0.01	0.00	0.00	0.01	0.00
π^0 Smear	2.62	1.27	3.77	1.17	1.97	2.09
e^+ Veto	0.26	0.01	0.20	0.03	0.14	0.07
FSR	0.26	0.48	0.47	0.68	0.65	0.49
Form Factor Dep.	0.56	0.08	0.08	0.76	0.08	0.28
Number $D\bar{D}$	1.34	1.34	1.34	1.34	1.34	1.34
Total	4.49	4.10	4.92	3.66	4.43	3.42

Table 7.16: Summary of full and partial branching fraction (\mathcal{B}) systematic errors (%) for the $D^+ \rightarrow \bar{K}^0 e^+ \nu$ signal decay mode.

Systematic	$D^+ \rightarrow \bar{K}^0 e^+ \nu$ q^2 interval (GeV) ²					$\mathcal{B}_{\text{total}}$
	< 0.4	0.4 – 0.8	0.8 – 1.2	1.2 – 1.6	≥ 1.6	
Hadronic Showers	0.17	0.37	0.21	0.13	1.36	0.18
K_L Showers	0.01	0.06	0.08	0.15	0.46	0.02
K_L Re-weight	1.07	1.07	1.09	1.10	1.09	1.08
Track Eff.	0.62	0.57	0.70	0.66	0.39	0.62
Track Res.	0.43	0.45	0.64	0.49	0.92	0.49
Splitoff Smear	0.81	0.88	0.84	0.99	0.21	0.84
Degrade PID	0.01	0.02	0.00	0.01	0.08	0.01
Shower Res.	0.00	0.02	0.03	0.01	0.09	0.00
Trkman Fakes	0.72	0.70	0.70	0.69	0.70	0.71
π^0 Eff.	0.00	0.01	0.01	0.02	0.09	0.00
K_S Eff.	1.05	1.00	0.94	0.88	0.81	1.00
π^- PID	0.01	0.01	0.00	0.03	0.02	0.00
K^- PID	0.01	0.01	0.00	0.02	0.00	0.00
e^+ PID	0.62	0.65	0.52	0.59	0.76	0.61
e^+ Fakes	0.38	0.03	0.17	0.09	1.00	0.14
π^0 Re-weight	0.02	0.01	0.00	0.11	0.14	0.01
π^- Re-weight	0.02	0.01	0.00	0.19	1.12	0.04
K^- Fakes	0.01	0.01	0.03	0.07	0.16	0.01
π^- Smear	0.01	0.01	0.00	0.04	0.09	0.01
K^- Smear	0.02	0.01	0.00	0.00	0.02	0.01
π^0 Smear	0.01	0.01	0.01	0.05	0.08	0.01
e^+ Veto	0.02	0.09	0.02	0.12	0.30	0.04
FSR	0.25	0.46	0.55	0.64	0.60	0.41
Form Factor Dep.	0.35	0.16	0.28	0.83	1.51	0.06
Number $D\bar{D}$	1.34	1.34	1.34	1.34	1.34	1.34
Total	2.56	2.56	2.59	2.73	3.58	2.53

Chapter 8

Results and Conclusions

In this chapter we give the final results for all branching fractions and branching fraction ratios. In addition, we use these results to extract measurements of the semileptonic form factors and the relevant CKM matrix elements.

8.1 Branching Fraction Results

Combining the results of the fit and the systematic errors gives us the final yield for each mode. From the yield we obtain the branching fraction using

$$\mathcal{B} = \frac{Y}{2N_{D\bar{D}}}, \quad (8.1)$$

where Y is the fit yield (i.e., the efficiency corrected yield) and $N_{D\bar{D}}$ is the number of $D\bar{D}$ pairs of the appropriate charge. We use the CLEO-c measured numbers of $D\bar{D}$ pairs in our data sample [31].¹ For the neutral D signal modes we have

$$N_{D^0\bar{D}^0} = (1.032 \pm 0.013) \times 10^6, \quad (8.2)$$

and for the charged D signal modes we have

$$N_{D^+D^-} = (0.822 \pm 0.011) \times 10^6. \quad (8.3)$$

The resulting fit yields, efficiencies, and branching fractions for each mode, in each q^2 bin, are given in Table 8.1. The total branching fractions for each mode (also

¹In this thesis we use preliminary $N_{D\bar{D}}$ numbers that have been updated from those quoted in the given reference. The updated numbers are based on the same 281 pb⁻¹ of data that has been used for this analysis, and are expected to change very little for the final result.

listed in Table 8.1) are

$$\mathcal{B}(D^0 \rightarrow \pi^- e^+ \nu) = 0.299 \pm 0.011 \pm 0.008 \%, \quad (8.4)$$

$$\mathcal{B}(D^0 \rightarrow K^- e^+ \nu) = 3.55 \pm 0.03 \pm 0.08 \%, \quad (8.5)$$

$$\mathcal{B}(D^+ \rightarrow \pi^0 e^+ \nu) = 0.371 \pm 0.022 \pm 0.013 \%, \quad (8.6)$$

and,

$$\mathcal{B}(D^+ \rightarrow \bar{K}^0 e^+ \nu) = 8.53 \pm 0.13 \pm 0.22 \%. \quad (8.7)$$

A comparison of these results with the recently updated Particle Data Group (PDG) 2006 values [3] and with the results from other measurements is shown in Fig. 8.1.² It is evident that our results are all in good to excellent agreement with the PDG values, while also having significantly improved errors. In addition, our total branching fraction values are generally in good agreement with recent measurements from other experiments and with the CLEO-c results from the complementary D tagging analysis (see Chapter 4).

We also measure the branching fraction and partial width ratios in each q^2 bin, the full results are given in Table 8.2. For all q^2 the branching fraction ratios are found to be,

$$R_0 \equiv \frac{\mathcal{B}(D^0 \rightarrow \pi^- e^+ \nu)}{\mathcal{B}(D^0 \rightarrow K^- e^+ \nu)} = 0.084 \pm 0.003 \pm 0.001 \quad (8.8)$$

and

$$R_+ \equiv \frac{\mathcal{B}(D^+ \rightarrow \pi^0 e^+ \nu)}{\mathcal{B}(D^+ \rightarrow \bar{K}^0 e^+ \nu)} = 0.044 \pm 0.003 \pm 0.001, \quad (8.9)$$

while the partial width ratios, giving the isospin relations, are measured as,

$$I_\pi \equiv \frac{\Gamma(D^0 \rightarrow \pi^- e^+ \nu)}{\Gamma(D^+ \rightarrow \pi^0 e^+ \nu)} = 2.04 \pm 0.14 \pm 0.08 \quad (8.10)$$

²The most recent PDG values cited here have been updated with the first CLEO-c measurements using 56 pb⁻¹ of data.

Table 8.1: Efficiencies (ε), yields and branching fractions (\mathcal{B}) for all q^2 bins and all modes. We note that for the neutral kaon mode, $D^+ \rightarrow \bar{K}^0 e^+ \nu$, the efficiencies and yields are for the reconstructed sub-mode $D^+ \rightarrow K_S(\pi^+ \pi^-) e^+ \nu$, whilst the branching fraction results are for the full mode.

$D^0 \rightarrow \pi^- e^+ \nu$			
q^2 Interval	< 0.4	0.4 – 0.8	0.8 – 1.2
ε (%)	19.4	21.0	22.4
Yield	$1452 \pm 113 \pm 49$	$1208 \pm 102 \pm 35$	$1242 \pm 99 \pm 36$
\mathcal{B} (%)	$0.070 \pm 0.006 \pm 0.003$	$0.059 \pm 0.005 \pm 0.002$	$0.060 \pm 0.005 \pm 0.002$
q^2 Interval	1.2 – 1.6	≥ 1.6	All q^2
ε (%)	22.8	22.4	21.5
Yield	$906 \pm 85 \pm 29$	$1357 \pm 103 \pm 46$	$6165 \pm 228 \pm 157$
\mathcal{B} (%)	$0.044 \pm 0.004 \pm 0.002$	$0.066 \pm 0.005 \pm 0.002$	$0.299 \pm 0.011 \pm 0.008$
$D^0 \rightarrow K^- e^+ \nu$			
q^2 Interval	< 0.4	0.4 – 0.8	0.8 – 1.2
ε (%)	19.2	20.5	20.0
Yield	$29701 \pm 441 \pm 569$	$21600 \pm 377 \pm 473$	$14032 \pm 304 \pm 301$
\mathcal{B} (%)	$1.439 \pm 0.021 \pm 0.033$	$1.047 \pm 0.018 \pm 0.026$	$0.680 \pm 0.015 \pm 0.017$
q^2 Interval	1.2 – 1.6	≥ 1.6	All q^2
ε (%)	18.3	13.9	19.6
Yield	$7001 \pm 225 \pm 178$	$991 \pm 112 \pm 20$	$73325 \pm 676 \pm 1486$
\mathcal{B} (%)	$0.339 \pm 0.011 \pm 0.010$	$0.048 \pm 0.005 \pm 0.001$	$3.553 \pm 0.033 \pm 0.085$
$D^+ \rightarrow \pi^0 e^+ \nu$			
q^2 Interval	< 0.4	0.4 – 0.8	0.8 – 1.2
ε (%)	7.5	8.0	7.9
Yield	$1379 \pm 168 \pm 59$	$1584 \pm 180 \pm 61$	$1012 \pm 154 \pm 48$
\mathcal{B} (%)	$0.084 \pm 0.010 \pm 0.004$	$0.096 \pm 0.011 \pm 0.004$	$0.062 \pm 0.009 \pm 0.003$
q^2 Interval	1.2 – 1.6	≥ 1.6	All q^2
ε (%)	7.2	5.7	7.3
Yield	$1028 \pm 158 \pm 35$	$1102 \pm 174 \pm 47$	$6105 \pm 360 \pm 192$
\mathcal{B} (%)	$0.063 \pm 0.010 \pm 0.002$	$0.067 \pm 0.011 \pm 0.003$	$0.371 \pm 0.022 \pm 0.013$
$D^+ \rightarrow \bar{K}^0 e^+ \nu$			
q^2 Interval	< 0.4	0.4 – 0.8	0.8 – 1.2
ε (%)	11.7	12.3	12.5
Yield	$19480 \pm 466 \pm 418$	$14422 \pm 415 \pm 306$	$9009 \pm 327 \pm 194$
\mathcal{B} (%)	$3.437 \pm 0.082 \pm 0.088$	$2.545 \pm 0.073 \pm 0.065$	$1.590 \pm 0.058 \pm 0.041$
q^2 Interval	1.2 – 1.6	≥ 1.6	All q^2
ε (%)	12.2	12.5	12.1
Yield	$4656 \pm 236 \pm 108$	$789 \pm 104 \pm 26$	$48356 \pm 725 \pm 1013$
\mathcal{B} (%)	$0.822 \pm 0.042 \pm 0.022$	$0.139 \pm 0.018 \pm 0.005$	$8.532 \pm 0.128 \pm 0.216$

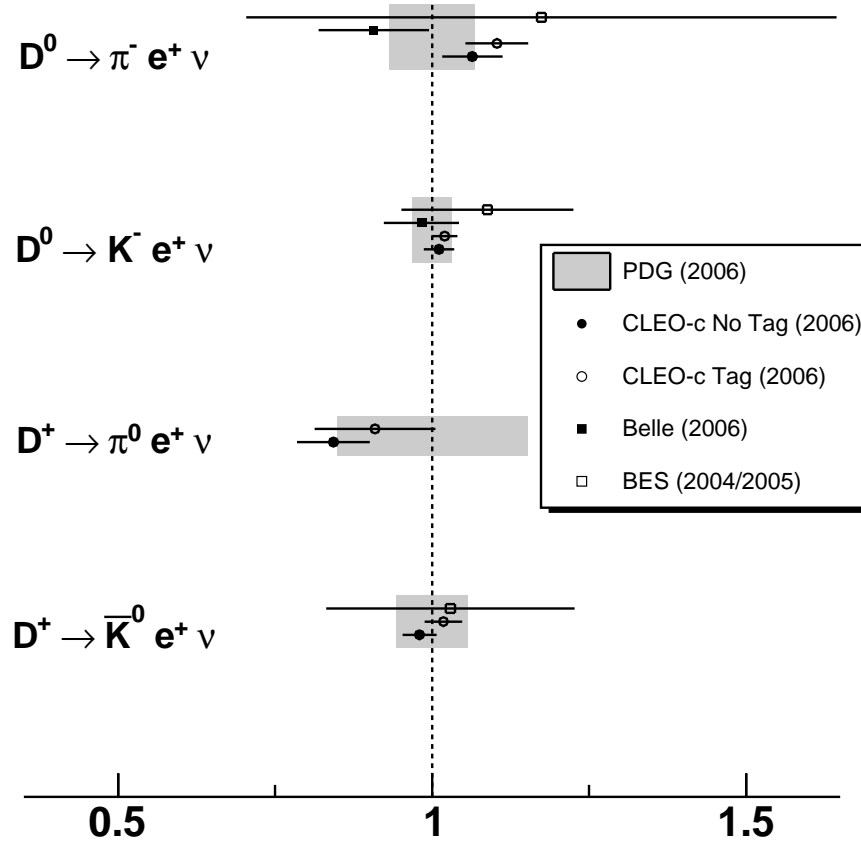


Figure 8.1: Branching fraction measurements from various experiments for our four signal modes. All measurements are normalized to the updated PDG 2006 values [3]. Solid black circles show the results from this analysis (CLEO-c No Tag 2006), open circles show the preliminary 281 pb^{-1} results for the CLEO-c tagged analysis [61] (CLEO-c Tag 2006), solid black squares show the recent Belle results [57] (Belle 2006) and open squares show the BES results [53, 54] (BES 2004/2005).

and

$$I_K \equiv \frac{\Gamma(D^0 \rightarrow K^- e^+ \nu)}{\Gamma(D^+ \rightarrow \bar{K}^0 e^+ \nu)} = 1.06 \pm 0.02 \pm 0.03. \quad (8.11)$$

We find that the partial width ratios obey the expected isospin symmetry relations, $I_\pi = 2$ and $I_K = 1$, within our experimental precision. Our branching fraction ratios are also in good agreement with both other measurements and the updated PDG values, Table 8.3.

Table 8.2: Branching fraction and partial width ratios for all q^2 bins. To calculate the partial width ratios we use the D lifetimes $\tau_{D^0} = (410.3 \pm 1.5) \times 10^{-15} s$ and $\tau_{D^+} = (1040 \pm 7) \times 10^{-15} s$ [2]. R gives the appropriate ratio in each case.

$\mathcal{B}(D^0 \rightarrow \pi^- e^+ \nu) / \mathcal{B}(D^0 \rightarrow K^- e^+ \nu)$			
q^2 Interval	< 0.4	0.4 – 0.8	0.8 – 1.2
R ($\times 10^{-2}$)	$4.89 \pm 0.39 \pm 0.12$	$5.59 \pm 0.48 \pm 0.12$	$8.85 \pm 0.74 \pm 0.15$
q^2 Interval	1.2 – 1.6	≥ 1.6	All q^2
R ($\times 10^{-2}$)	$12.94 \pm 1.29 \pm 0.21$	$137.0 \pm 19.0 \pm 3.3$	$8.41 \pm 0.32 \pm 0.13$
$\mathcal{B}(D^+ \rightarrow \pi^0 e^+ \nu) / \mathcal{B}(D^+ \rightarrow \bar{K}^0 e^+ \nu)$			
q^2 Interval	< 0.4	0.4 – 0.8	0.8 – 1.2
R ($\times 10^{-2}$)	$2.44 \pm 0.30 \pm 0.09$	$3.79 \pm 0.45 \pm 0.13$	$3.87 \pm 0.61 \pm 0.17$
q^2 Interval	1.2 – 1.6	≥ 1.6	All q^2
R ($\times 10^{-2}$)	$7.61 \pm 1.24 \pm 0.25$	$48.14 \pm 10.13 \pm 1.91$	$4.35 \pm 0.27 \pm 0.12$
$\Gamma(D^0 \rightarrow \pi^- e^+ \nu) / \Gamma(D^+ \rightarrow \pi^0 e^+ \nu)$			
q^2 Interval	< 0.4	0.4 – 0.8	0.8 – 1.2
R	$2.125 \pm 0.308 \pm 0.096$	$1.540 \pm 0.219 \pm 0.069$	$2.478 \pm 0.427 \pm 0.131$
q^2 Interval	1.2 – 1.6	≥ 1.6	All q^2
R	$1.779 \pm 0.324 \pm 0.070$	$2.487 \pm 0.455 \pm 0.130$	$2.039 \pm 0.143 \pm 0.081$
$\Gamma(D^0 \rightarrow K^- e^+ \nu) / \Gamma(D^+ \rightarrow \bar{K}^0 e^+ \nu)$			
q^2 Interval	< 0.4	0.4 – 0.8	0.8 – 1.2
R	$1.061 \pm 0.030 \pm 0.032$	$1.043 \pm 0.035 \pm 0.032$	$1.084 \pm 0.046 \pm 0.034$
q^2 Interval	1.2 – 1.6	≥ 1.6	All q^2
R	$1.047 \pm 0.064 \pm 0.038$	$0.874 \pm 0.152 \pm 0.033$	$1.055 \pm 0.019 \pm 0.033$

Table 8.3: Experimental measurements of the branching fraction ratios R_0 and R_+ . In the case where the PDG result is derived from several different measurements, we quote their fit value rather than the average. The CLEO-c No Tag 2006 results are from this analysis.

Measurement	R_0	R_+
PDG 2006 [3]	0.080 ± 0.005	$0.046 \pm 0.014 \pm 0.017$
CLEOIII 2005 [55]	$0.082 \pm 0.006 \pm 0.005$	-
Belle 2006 [57]	$0.081 \pm 0.008 \pm 0.003$	-
CLEO-c No Tag 2006	$0.084 \pm 0.003 \pm 0.001$	$0.044 \pm 0.003 \pm 0.001$

8.2 Form Factors

The relationship between the form factor, $f_+(q^2)$, and the branching fraction for each mode can be derived from the partial decay width, Eq. 2.51. For the total branching fraction the result is

$$\mathcal{B} = \frac{G_F^2 |V_{cq}|^2}{24\pi^3 \Gamma_{\text{total}}} \int_0^{q_{\text{max}}^2} p^3 |f_+(q^2)|^2 dq^2, \quad (8.12)$$

where Γ_{total} is the total decay width of the parent D meson. However, we fit for branching fraction results in five q^2 bins, thus in the i^{th} q^2 bin we have

$$\mathcal{B}_i = \frac{G_F^2 |V_{cq}|^2}{24\pi^3 \Gamma_{\text{total}}} \int_{q_{\text{min}}^2(i)}^{q_{\text{max}}^2(i)} p^3 |f_+(q^2)|^2 dq^2. \quad (8.13)$$

To fit for the form factor therefore we choose a functional form for $f^+(q^2)$ and perform a χ^2 fit to the branching fraction in each q^2 bin, via Eq. 8.13. The χ^2 fit takes into account the correlations between the branching fractions in each q^2 bin as given by the branching fraction fit. We thus minimize the expression

$$\chi^2 = \sum_{ij} (\mathcal{B}_i - y_i) C_{ij}^{-1} (\mathcal{B}_j - y_j), \quad (8.14)$$

where y_i is the fit to the branching fraction in the i^{th} q^2 bin and C_{ij}^{-1} is the inverse of the covariance matrix. The integration in each bin is performed numerically using the trapezoidal rule method.

The systematic errors for the form factor parameters are evaluated using the same method as for the branching fraction analysis, that is we take the resulting branching fractions for each systematic error modification, fit for the form factors and find the difference from the nominal results. In addition, the specific systematic errors evaluated are also the same as in the branching fraction analysis and a full discussion of each source of error may be found in Chapter 7. There is only one small caveat to this claim. For the systematic errors that are found by taking the one sigma ellipse variations giving the largest deviation from the nominal result (π^- PID, K^- PID, π^0 finding and K_S finding), the specific variation can differ between the form factors and the branching fractions. This is simply the difference between variations that make more difference to the shape of the q^2 distribution and those that make more difference to the overall yields.

For the functional form of $f_+(q^2)$ we use the series parameterization as described in the introduction (Section 2.4). For comparative purposes we also provide results based on the two pole parameterizations described in Section 2.4. The parameterizations are fit to our measured rates from the five q^2 regions. For the series parameterization we perform fits using both the first two (Table 8.4) and the first three (Table 8.5) expansion parameters a_k . This tests both our sensitivity to the number of parameters in the expansion and the convergence of the series. In both cases we express our results in terms of the physical observables, the intercept $|V_{cq}|f_+(0)$ and $1 + 1/\beta - \delta$, as well as giving the expansion parameters. For the simple pole parameterization we fit for the intercept and the pole mass m_{pole} , while

for the modified pole parameterization we fit for the intercept and the shape parameter α , which summarizes the effective pole contribution. These results are also given in Table 8.4. Plots of the various fits are shown for each mode in Figs 8.2 - 8.5. In order to elucidate the shape differences between the various parameterizations it is convenient to normalize to the three parameter series result. The plots for all fits and all modes with this normalization are given in Fig 8.6.

Table 8.4: Form factor parameters resulting from two parameter fits to the measured branching fractions, for the three models outlined in the text. In addition, for each set of fit parameters we give the correlation coefficient ρ and the $\chi^2/d.o.f.$ of the fit.

<i>Series Parameterization - Expansion Parameters</i>				
<i>Decay</i>	a_0	a_1	ρ	$\chi^2/d.o.f.$
$\pi^- e^+ \nu$	0.044(2)(1)	-0.174(19)(7)	0.75	1.99/3
$K^- e^+ \nu$	0.0229(2)(3)	-0.047(6)(3)	0.81	3.75/3
$\pi^0 e^+ \nu$	0.046(2)(1)	-0.12(3)(1)	0.73	3.96/3
$\bar{K}^0 e^+ \nu$	0.0218(3)(3)	-0.046(9)(4)	0.80	4.89/3
<i>Series Parameterization - Physical Parameters</i>				
<i>Decay</i>	$ V_{cx} f^+(0)$	$1 + 1/\beta - \delta$	ρ	
$\pi^- e^+ \nu$	0.140(5)(3)	1.27(11)(4)	0.86	
$K^- e^+ \nu$	0.733(6)(8)	0.86(4)(2)	0.83	
$\pi^0 e^+ \nu$	0.146(7)(4)	1.01(16)(5)	0.81	
$\bar{K}^0 e^+ \nu$	0.714(9)(11)	0.87(6)(3)	0.82	
<i>Simple Pole Model</i>				
<i>Decay</i>	$ V_{cx} f^+(0)$	m_{pole}	ρ	$\chi^2/d.o.f.$
$\pi^- e^+ \nu$	0.145(4)(3)	1.87(3)(1)	0.78	3.19/3
$K^- e^+ \nu$	0.734(5)(8)	1.97(3)(2)	0.78	2.69/3
$\pi^0 e^+ \nu$	0.149(6)(4)	1.96(7)(2)	0.68	4.4/3
$\bar{K}^0 e^+ \nu$	0.710(8)(10)	1.96(4)(2)	0.78	4.08/3
<i>Modified Pole Model</i>				
<i>Decay</i>	$ V_{cx} f^+(0)$	α	ρ	$\chi^2/d.o.f.$
$\pi^- e^+ \nu$	0.141(4)(3)	0.37(8)(3)	-0.80	2.08/3
$K^- e^+ \nu$	0.732(6)(8)	0.21(5)(3)	-0.83	4.34/3
$\pi^0 e^+ \nu$	0.147(7)(4)	0.14(16)(5)	-0.79	4.05/3
$\bar{K}^0 e^+ \nu$	0.708(9)(10)	0.22(8)(4)	-0.82	5.26/3

Table 8.5: Three parameter series expansion fit results, where ρ_{ij} is the correlation coefficient for a_i and a_j .

<i>Series Parameterization - Expansion Parameters</i>						
<i>Decay</i>	a_0	a_1	a_2	ρ_{01}	ρ_{02}	ρ_{12}
$\pi^- e^+ \nu_e$	0.044(2)(1)	-0.18(7)(2)	-0.02(35)(12)	0.85	0.74	0.96
$K^- e^+ \nu_e$	0.0234(3)(3)	-0.009(21)(7)	0.52(28)(6)	0.88	0.76	0.96
$\pi^0 e^+ \nu_e$	0.043(2)(1)	-0.23(11)(2)	-0.60(56)(15)	0.84	0.72	0.96
$\bar{K}^0 e^+ \nu_e$	0.0224(4)(3)	0.009(32)(7)	0.76(42)(8)	0.87	0.76	0.96
<i>Series Parameterization - Physical Parameters</i>						
<i>Decay</i>	$ V_{cq} f_+(0)$	$1 + 1/\beta - \delta$	ρ	$\chi^2/d.o.f.$		
$\pi^- e^+ \nu_e$	0.139(7)(3)	1.30(37)(12)	0.87	1.98/2		
$K^- e^+ \nu_e$	0.746(9)(9)	0.62(13)(4)	0.88	0.24/2		
$\pi^0 e^+ \nu_e$	0.138(11)(3)	1.59(60)(12)	0.88	2.81/2		
$\bar{K}^0 e^+ \nu_e$	0.733(14)(11)	0.51(20)(4)	0.87	1.66/2		

For the series expansion, comparison of the two and three parameter fits shows that our kaon data prefers a nonzero quadratic z term. The probability of χ^2 improves from 29% (18%) to 89% (44%) going from two to three terms in the series for the K^- (K^0) fit. The pion measurements currently lack sensitivity to probe this term, and two and three parameter fits yield similar results for the first two parameters. Since a quadratic term appears preferred for the kaons, however, we include that term in our series fits to the pion data to improve the probability that our shape uncertainties bracket the true form factor shape. While the central value for a_2 is an order of magnitude larger than the other terms, we stress that regions of parameter space with a_2 of similar magnitude to a_0 and a_1 fall within the 90% hypercontour for the fit, so no strong statements can be made about the size of a_2 or about the convergence (or potential lack thereof) of the series from these data.

We also observe that our data do not support the physical basis for the pole parameterizations. The poles masses do not agree with the $M_{D_s^*}$ (M_{D^*}) masses

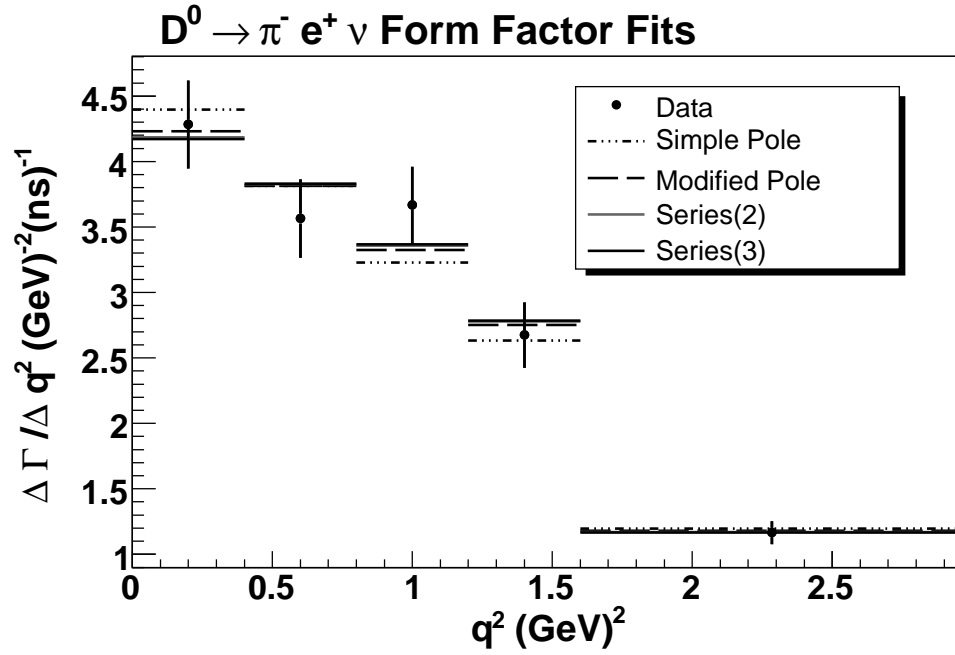


Figure 8.2: Fits of the various form factor models to the measured branching fractions of $D^0 \rightarrow \pi^- e^+ \nu$ in five q^2 bins. The solid line shows the series expansion three parameter fit (Series(3)), the gray line shows the series expansion two parameter fit (Series(2)), the dashed line shows the modified pole model fit and the dash-dot line shows the simple pole model fit.

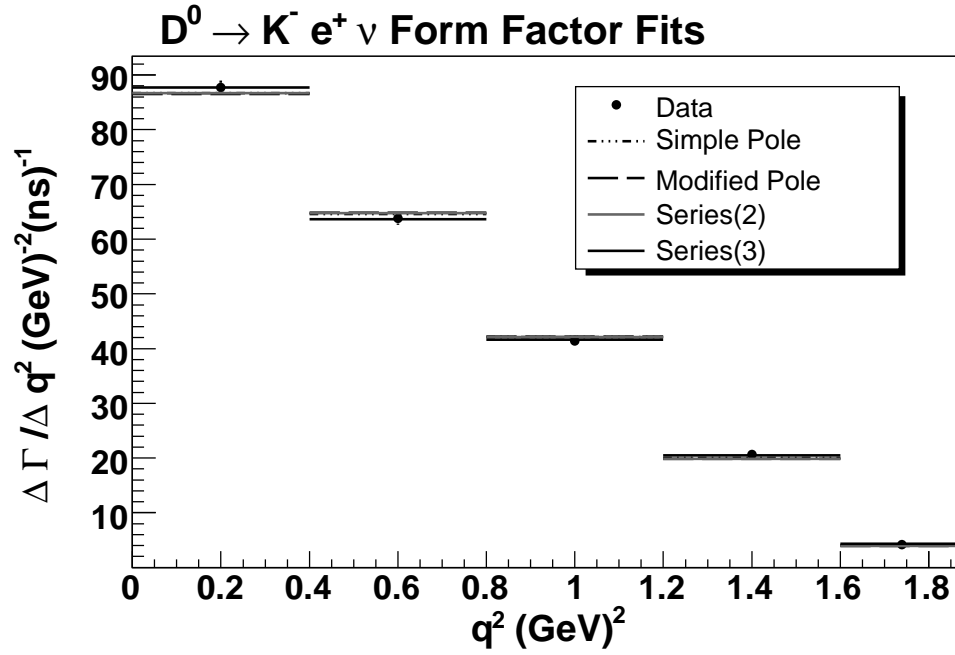


Figure 8.3: Fits of the various form factor models to the measured branching fractions of $D^0 \rightarrow K^- e^+ \nu$ in five q^2 bins. The solid line shows the series expansion three parameter fit (Series(3)), the gray line shows the series expansion two parameter fit (Series(2)), the dashed line shows the modified pole model fit and the dash-dot line shows the simple pole model fit.

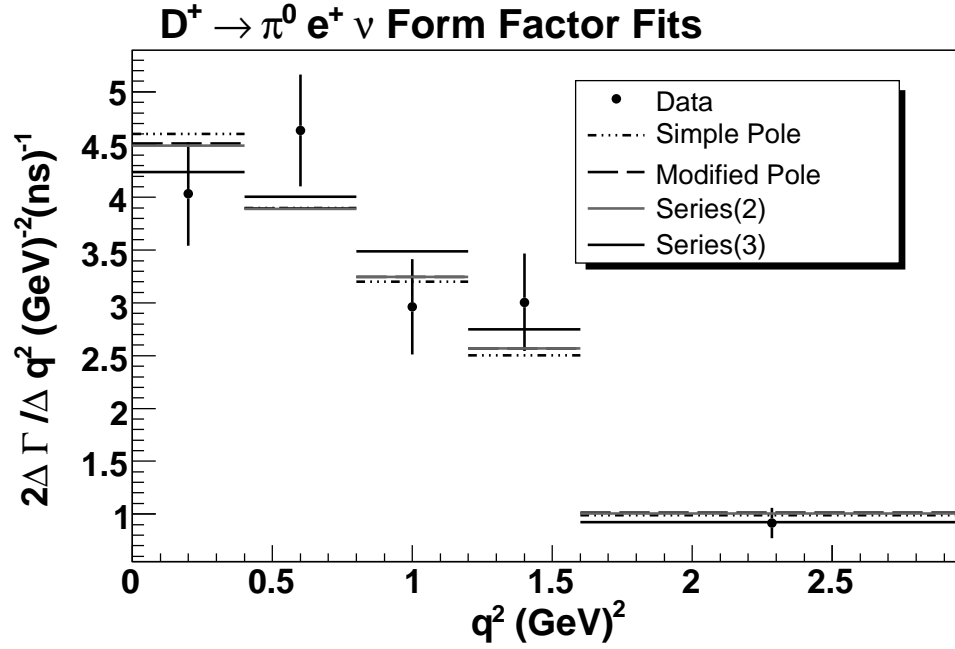


Figure 8.4: Fits of the various form factor models to the measured branching fractions of $D^+ \rightarrow \pi^0 e^+ \nu$ in five q^2 bins. The solid line shows the series expansion three parameter fit (Series(3)), the gray line shows the series expansion two parameter fit (Series(2)), the dashed line shows the modified pole model fit and the dash-dot line shows the simple pole model fit.

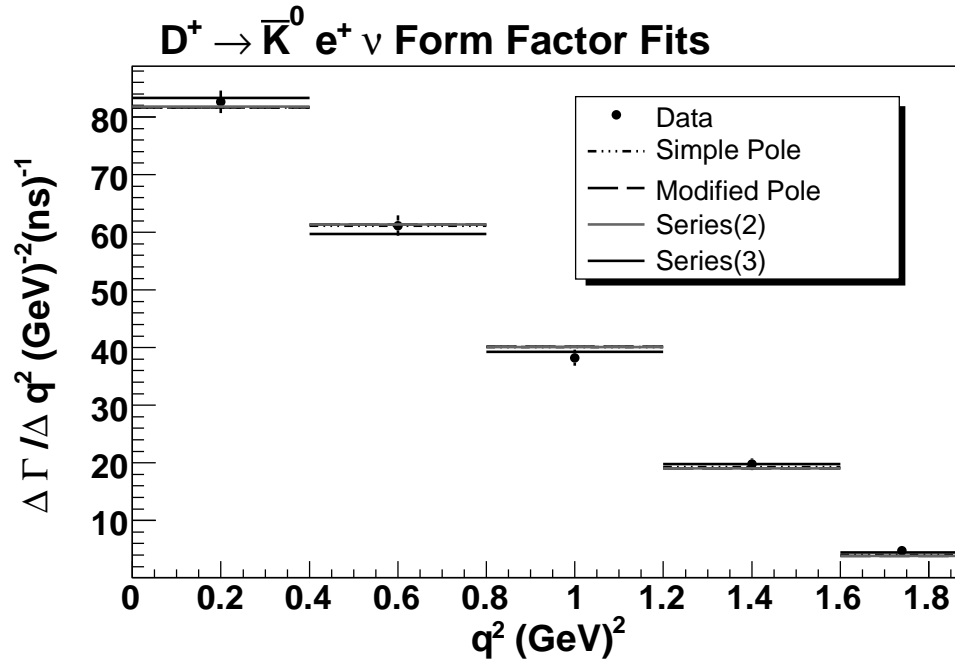


Figure 8.5: Fits of the various form factor models to the measured branching fractions of $D^+ \rightarrow \bar{K}^0 e^+ \nu$ in five q^2 bins. The solid line shows the series expansion three parameter fit (Series(3)), the gray line shows the series expansion two parameter fit (Series(2)), the dashed line shows the modified pole model fit and the dash-dot line shows the simple pole model fit.

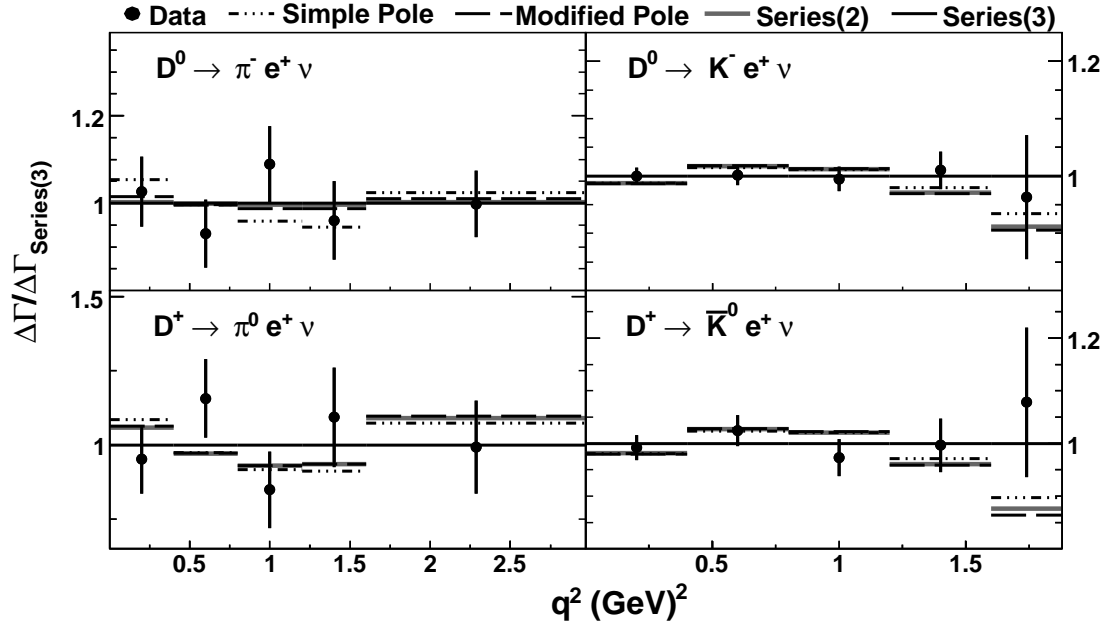


Figure 8.6: Form factor fit comparison for all modes. All data and fits are normalized to the relevant three parameter series fit result. The solid line shows the series expansion three parameter fit (Series(3)), the gray line shows the series expansion two parameter fit (Series(2)), the dashed line shows the modified pole model fit and the dash-dot line shows the simple pole model fit.

expected for the kaon (pion) modes by over three standard deviations for the most precise fits. The $1 + 1/\beta - \delta$ results from the K^- series expansion fit are over three standard deviations from the value of ~ 2 necessary for physical validity of the BK parameterization, while those derived from our α values for the kaon modes are tens of standard deviations away. In addition, a comparison of our results for the shape parameters with those of other experimental measurements can be found in Tables 8.6 and 8.7. With the exception of the Babar preliminary result for $D^0 \rightarrow K^- e^+ \nu$, our results are in very good agreement with previous measurements.

It is also interesting to compare the shape of our q^2 distributions to those predicted using different theoretical methods. To make such a comparison we plot the fraction of events in each q^2 bin. In the i^{th} bin the fraction is given by

$$\frac{N_i}{N_{\text{total}}} = \frac{\int_{q_{\text{min}}^2(i)}^{q_{\text{max}}^2(i)} p^3 |f_+(q^2)|^2 dq^2}{\int_0^{q_{\text{max}}^2} p^3 |f_+(q^2)|^2 dq^2}, \quad (8.15)$$

where N_i is the number of events in bin i and $N_{\text{total}} = \sum N_i$. Taking this ratio ensures that we are completely independent of the normalization, $f_+(0)$, and therefore gives us a pure comparison of the shape parameters. We compare our data results to four different theoretical shape predictions: recent LQCD results [14], a LCSR calculation [17], a constituent quark model (CQM) result [19] and the simple pole model. The predicted shape parameters for each of the models are given in Table 8.8 for the $D \rightarrow K$ decays and Table 8.9 for the $D \rightarrow \pi$ decays. Plots of the data theory comparisons for each mode are shown in Figs 8.7 - 8.10. Our results for the kaon modes disagree with the LQCD prediction by about three standard deviations. The pion modes, with larger errors, are in good agreement.

Table 8.6: Experimental measurements of the $D \rightarrow K$ form factor shape parameters. Here α is the shape parameter for the modified pole model (Eq. 2.72) and m_{pole} is the pole mass of the simple pole model (Eq. 2.71). The first errors are statistical and the second systematic. If only one error is given, it is the combined statistical and systematic error. The CLEO-c tag results are preliminary numbers and the CLEO-c No Tag 2006 results are the ones from this analysis.

<i>Measurement</i>	<i>Shape Parameter</i>	
	α	m_{pole} GeV
E691 1989 [48]	-	$2.1_{-0.2}^{+0.4} \pm 0.2$
CLEO 1991 [49]	-	$2.0_{-0.2-0.2}^{+0.4+0.3}$
MarkIII 1991 [50]	-	$1.8_{-0.2-0.2}^{+0.5+0.3}$
CLEOII 1993 [51]	-	$2.00 \pm 0.12 \pm 0.18$
E687 1995 [52]	-	$1.87_{-0.08-0.06}^{+0.11+0.07}$
CLEOIII 2005 [55]	$0.36 \pm 0.10_{-0.07}^{+0.03}$	$1.89 \pm 0.05_{-0.02}^{+0.04}$
FOCUS 2005 [56]	$0.28 \pm 0.08 \pm 0.07$	$1.93 \pm 0.05 \pm 0.03$
Belle 2006 [57]	$0.40 \pm 0.12 \pm 0.09$	-
Babar 2006 [58]	$0.43 \pm 0.03 \pm 0.04$	$1.854 \pm 0.016 \pm 0.020$
CLEO-c Tag 2006 D^0 [61]	0.26 ± 0.06	1.94 ± 0.04
CLEO-c Tag 2006 D^+ [61]	0.13 ± 0.10	2.02 ± 0.06
CLEO-c No Tag 2006 D^0	$0.21 \pm 0.05 \pm 0.03$	$1.97 \pm 0.03 \pm 0.02$
CLEO-c No Tag 2006 D^+	$0.22 \pm 0.08 \pm 0.04$	$1.96 \pm 0.04 \pm 0.02$

Table 8.7: Experimental measurements of the $D \rightarrow \pi$ form factor shape parameters. Here α is the shape parameter for the modified pole model (Eq. 2.72) and m_{pole} is the pole mass of the simple pole model (Eq. 2.71). The first errors are statistical and the second systematic. If only one error is given, it is the combined statistical and systematic error. The CLEO-c tag results are preliminary numbers and the CLEO-c No Tag 2006 results are the ones from this analysis.

<i>Measurement</i>	<i>Shape Parameter</i>	
	α	m_{pole} GeV
CLEOIII 2005 [55]	$0.37^{+0.20}_{-0.31} \pm 0.15$	$1.86^{+0.10+0.07}_{-0.06-0.03}$
FOCUS 2005 [56]	-	$1.91^{+0.30}_{-0.15} \pm 0.07$
Belle 2006 [57]	$0.03 \pm 0.27 \pm 0.13$	-
CLEO-c Tag 2006 D^0 [61]	0.20 ± 0.11	1.94 ± 0.04
CLEO-c Tag 2006 D^+ [61]	0.04 ± 0.21	1.99 ± 0.10
CLEO-c No Tag 2006 D^0	$0.37 \pm 0.08 \pm 0.03$	$1.87 \pm 0.03 \pm 0.01$
CLEO-c No Tag 2006 D^+	$0.14 \pm 0.16 \pm 0.05$	$1.96 \pm 0.07 \pm 0.02$

Table 8.8: $D \rightarrow K$ form factor shape parameters from four different theoretical predictions. Here α is the shape parameter for the modified pole model (Eq. 2.72) and m_{pole} is the pole mass of the simple pole model (Eq. 2.71). For the LQCD results we have combined the statistical and systematic uncertainties.

<i>Form Factor Calculation</i>	<i>Shape Parameter</i>	
	α	m_{pole} GeV
Simple Pole	-	2.112
LQCD [14]	0.50 ± 0.06	-
LCSR [17]	$-0.07^{+0.15}_{-0.07}$	-
CQM [19]	0.24	-

Table 8.9: $D \rightarrow \pi$ form factor shape parameters from four different theoretical predictions. Here α is the shape parameter for the modified pole model (Eq. 2.72) and m_{pole} is the pole mass of the simple pole model (Eq. 2.71). For the LQCD results we have combined the statistical and systematic uncertainties.

<i>Form Factor Calculation</i>	<i>Shape Parameter</i>	
	α	m_{pole} GeV
Simple Pole	-	2.01
LQCD [14]	0.44 ± 0.06	-
LCSR [17]	$0.01^{+0.11}_{-0.07}$	-
CQM [19]	0.30	-

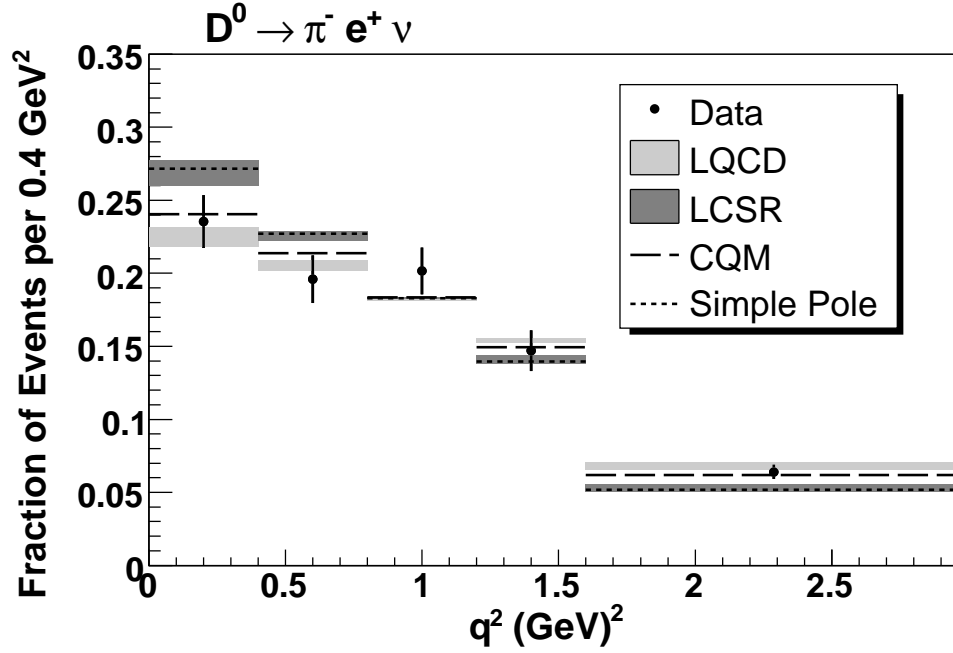


Figure 8.7: Fraction of events in each q^2 bin for the decay mode $D^0 \rightarrow \pi^- e^+ \nu$. The event fraction in the highest q^2 bin is scaled to the same q^2 range (0.4 GeV^2) as the other four bins. We compare our data results with four theoretical predictions: LQCD [14], LCSR [17], CQM [19] and the simple pole model. The data errors represent combined statistical and systematic uncertainties.

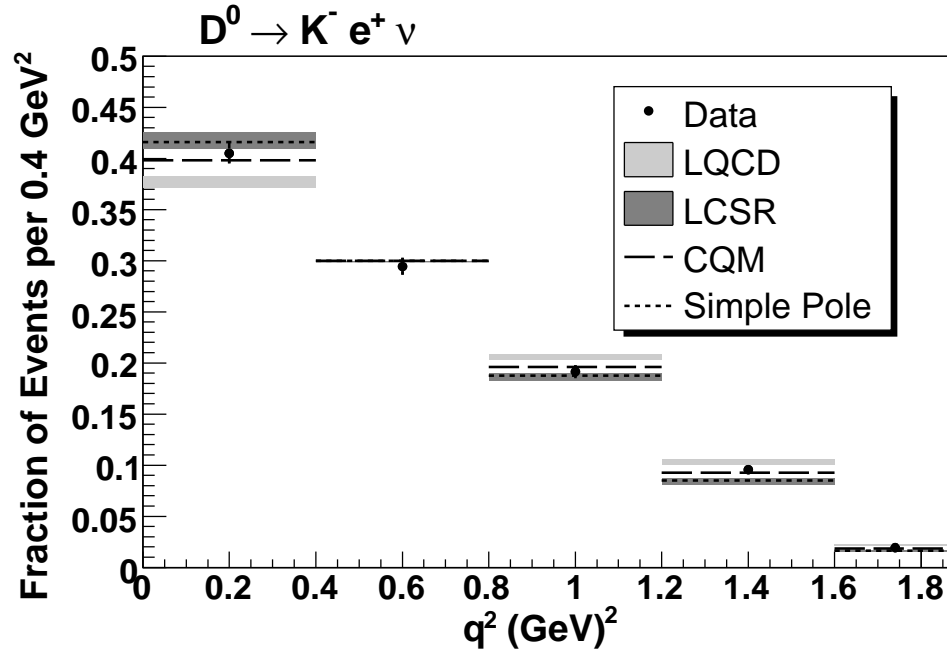


Figure 8.8: Fraction of events in each q^2 bin for the decay mode $D^0 \rightarrow K^- e^+ \nu$. The event fraction in the highest q^2 bin is scaled to the same q^2 range (0.4 GeV^2) as the other four bins. We compare our data results with four theoretical predictions: LQCD [14], LCSR [17], CQM [19] and the simple pole model. The data errors represent combined statistical and systematic uncertainties.

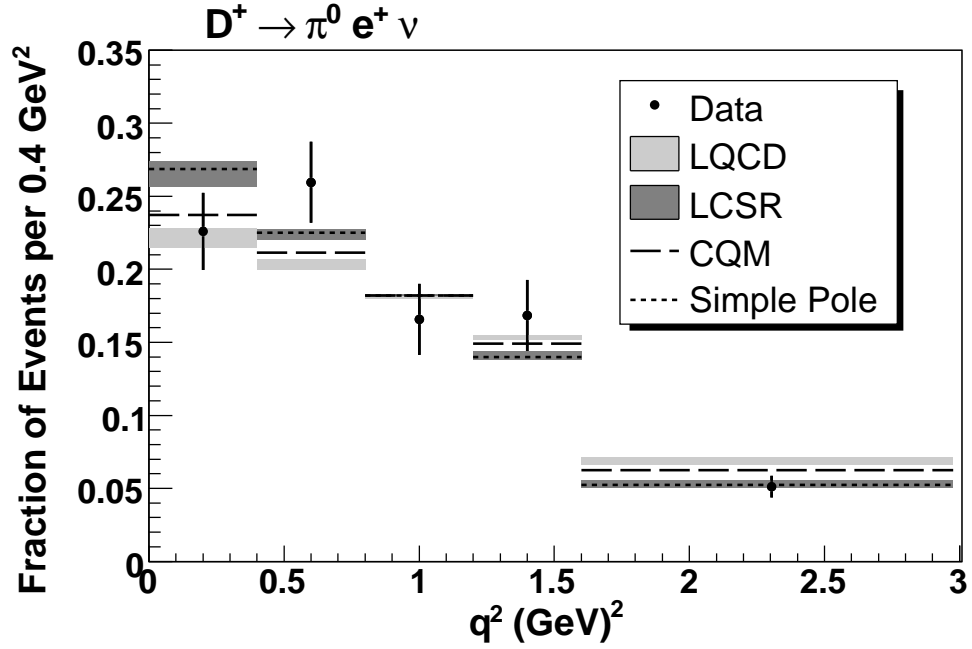


Figure 8.9: Fraction of events in each q^2 bin for the decay mode $D^+ \rightarrow \pi^0 e^+ \nu$. The event fraction in the highest q^2 bin is scaled to the same q^2 range (0.4 GeV^2) as the other four bins. We compare our data results with four theoretical predictions: LQCD [14], LCSR [17], CQM [19] and the simple pole model. The data errors represent combined statistical and systematic uncertainties.

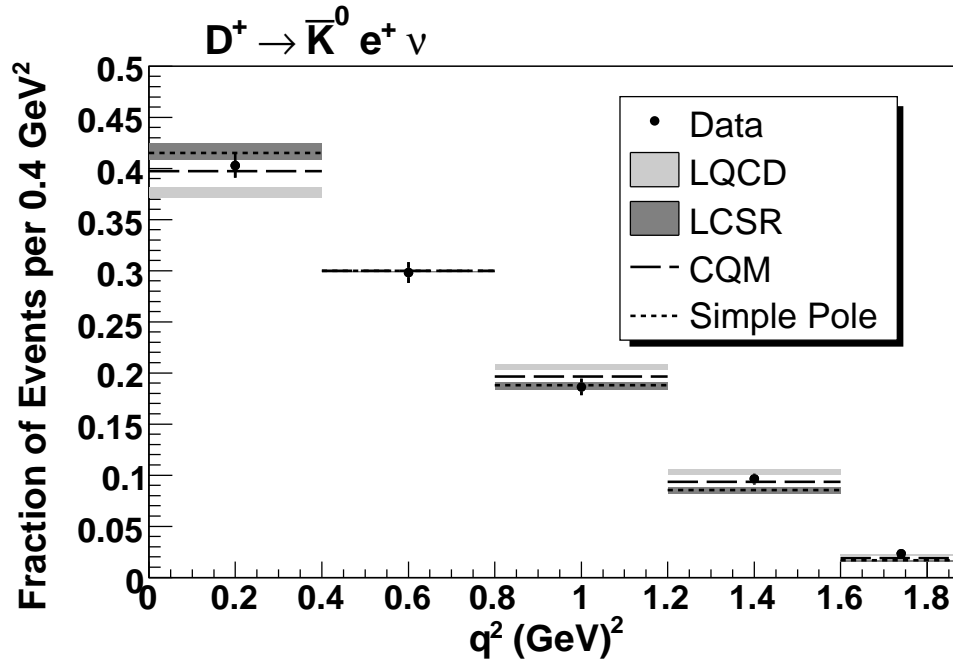


Figure 8.10: Fraction of events in each q^2 bin for the decay mode $D^+ \rightarrow \bar{K}^0 e^+ \nu$. The event fraction in the highest q^2 bin is scaled to the same q^2 range (0.4 GeV^2) as the other four bins. We compare our data results with four theoretical predictions: LQCD [14], LCSR [17], CQM [19] and the simple pole model. The data errors represent combined statistical and systematic uncertainties.

8.3 CKM Matrix Elements: V_{cs} and V_{cd}

We extract $|V_{cd}|$ and $|V_{cs}|$ by combining our $|V_{cq}|f_+(0)$ results from the three parameter series expansion fit with the unquenched LQCD results $f_+(0)^{(D^0 \rightarrow \pi^+)} = 0.64(3)(6)$ and $f_+(0)^{(D^0 \rightarrow K^+)} = 0.73(3)(7)$ [14]. For the D^0 signal decay modes we obtain

$$|V_{cs}| = 1.02 \pm 0.01 \pm 0.01 \pm 0.11 \quad (8.16)$$

and

$$|V_{cd}| = 0.218 \pm 0.011 \pm 0.005 \pm 0.023, \quad (8.17)$$

where the errors are statistical, systematic and theoretical respectively. For the D^+ signal decay modes we obtain

$$|V_{cs}| = 1.00 \pm 0.02 \pm 0.01 \pm 0.10 \quad (8.18)$$

and

$$|V_{cd}| = 0.216 \pm 0.017 \pm 0.005 \pm 0.023, \quad (8.19)$$

with the errors as for the D^0 modes. Averaging the D^0 and D^+ results (taking into account correlated and uncorrelated systematic uncertainties) we find

$$|V_{cs}| = 1.01 \pm 0.01 \pm 0.01 \pm 0.11. \quad (8.20)$$

and

$$|V_{cd}| = 0.217 \pm 0.010 \pm 0.004 \pm 0.023 \quad (8.21)$$

The uncertainties are dominated by the discretization uncertainty in the LQCD charm quark action, which should be improved in the near future.³

³Here we refer specifically to the charm quark action used by the FNAL LQCD group [14]. Other calculations, which should be available in the near future, e.g., those of the UKQCD group will not suffer from this problem.

8.4 Conclusion

We have studied the four semileptonic charm decays $D^0 \rightarrow \pi^- e^+ \nu$, $D^0 \rightarrow K^- e^+ \nu$, $D^+ \rightarrow \pi^0 e^+ \nu$, and $D^+ \rightarrow \bar{K}^0 e^+ \nu$. These modes result from the decay of the heavy charm quark to the lighter strange and down quarks and our measurements provide information about their form factors and normalizations. For each mode we have measured branching fractions and the appropriate branching fraction and partial width ratios in five q^2 ranges. For the total branching fractions we find $\mathcal{B}(D^0 \rightarrow \pi^- e^+ \nu) = 0.299 \pm 0.011 \pm 0.008 \%$, $\mathcal{B}(D^0 \rightarrow K^- e^+ \nu) = 3.55 \pm 0.03 \pm 0.08 \%$, $\mathcal{B}(D^+ \rightarrow \pi^0 e^+ \nu) = 0.371 \pm 0.022 \pm 0.013 \%$, and $\mathcal{B}(D^+ \rightarrow \bar{K}^0 e^+ \nu) = 8.53 \pm 0.13 \pm 0.22 \%$. While for the ratios we measure $R_0 = 0.084 \pm 0.003 \pm 0.001$, $R_+ = 0.044 \pm 0.003 \pm 0.001$, $I_\pi = 2.04 \pm 0.14 \pm 0.08$, and $I_K = 1.06 \pm 0.02 \pm 0.03$. Our results are based on total raw yields of 1325 ± 49 $D^0 \rightarrow \pi^- e^+ \nu$ events, 14352 ± 132 $D^0 \rightarrow K^- e^+ \nu$ events, 446 ± 26 $D^+ \rightarrow \pi^0 e^+ \nu$ events, and 5844 ± 88 $D^+ \rightarrow K_S e^+ \nu$ events, where the errors are statistical only. These measurements are about factor of two more precise than the previous CLEOIII measurements [55] and are comparable in accuracy to the CLEO-c tagged D measurements.⁴ They are all in good agreement with the updated PDG 2006 values [3].

In addition, our extraction of the branching fractions in five q^2 ranges allows us to study the properties of the q^2 spectrum for each decay mode. In particular, we have fit our results with three different parameterizations of the form factor: the series parameterization, as well as the simple and modified pole parameterizations for comparative purposes. For the Cabibbo favored modes we find that we are

⁴For all modes we have better or comparable statistical errors and slightly higher systematic errors than in the tagged analysis. We expect our systematic errors to be higher due to the neutrino reconstruction and our reliance on the measured number of $D\bar{D}$ pairs in our data sample.

sensitive to the first three parameters in the series expansion. The accuracy of our results also allows for an informative comparison of the shape of our spectra with various theoretically predicted shapes. Such a comparison gives us an idea of how well these methods can model form factors for the semileptonic B decays, which are important for measuring the small CKM matrix element $|V_{ub}|$.

Finally, using our results in combination with recent unquenched LQCD calculations, we have made the most precise CKM determinations from D semileptonic decays to date. We find $|V_{cd}| = 0.217 \pm 0.010 \pm 0.004 \pm 0.023$ and $|V_{cs}| = 1.01 \pm 0.01 \pm 0.01 \pm 0.11$: results that agree very well with neutrino based determinations of $|V_{cd}|$ and charmed tagged W decay measurements of $|V_{cs}|$ [2]. Overall, these measurements represent a marked improvement in our knowledge concerning D semileptonic decay.

BIBLIOGRAPHY

- [1] R. Barate *et al.*, Phys. Lett. B **565** 61 (2003)
- [2] S. Eidelman *et al.*, Phys. Lett. B **592**, 1 (2004).
- [3] W.-M. Yao *et al.*, J. Phys. G **33**, 1 (2006).
- [4] M. C. Gonzalez-Garcia and Y. Nir, Rev. Mod. Phys. **75** 345 (2003)
- [5] V. I. Borodulin, R. N. Rogalyov and S. R. Slabospitsky, Compendium of Relations (CORE), hep-ph/9507456 (1995).
- [6] M. E. Peskin and D. V. Shroeder, An Introduction to Quantum Field Theory, Addison-Wesley (1995).
- [7] M. Battaglia *et al.*, Proceedings of the First Workshop on the CKM Unitarity Triangle, CERN 13-16 February 2002, hep-ph/0304132 (2003).
- [8] K. HagiWara *et al.*, Phys. Rev. D **66**, 010001 (2002)
- [9] M. Kobayashi and T. Maskawa, Prog. Theor. Phys. **49**, 652 (1973).
- [10] L. Wolfenstein, Phys. Rev. Lett. **51**, 1945 (1983).
- [11] C. Jarlskog, CP Violation, World Scientific, Singapore (1989)
- [12] CKM Fitter Group (J. Charles *et al.*), Eur. Phys. J. C **51** 1 (2005)
- [13] J. D. Richman and P. R. Burchat, Rev. Mod. Phys. **67**, 893 (1995)
- [14] C. Aubin *et al.*, Phys. Rev. Lett. **94**, 001601 (2005).
- [15] P. Ball and R. Zwicky, Phys. Rev. D **71**, 014015 (2005)
- [16] Y. L. Wu, M. Zhong and Y. B. Zuo, hep-ph/0604007
- [17] A. Khodjamirian *et al.*, Phys. Rev. D **62**, 014002 (2000)
- [18] W. Y. Wang, Y. L. Wu and M. Zhong, Phys. Rev. D **67**, 014024 (2003)
- [19] D. Melikhov and B. Stech, Phys. Rev. D **62**, 014006 (2000)
- [20] P. Lepage, Proceedings of HUGS 98, Edited by J.L. Goity, World Scientific (2000), hep-lat/0506036.
- [21] R. Gupta, hep-lat/9807028.
- [22] G. Münster and M. Walzl, hep-lat/0012005.
- [23] J.M. Flynn and C.T. Sachrajda, hep-lat/9710057.

- [24] E. Gulez *et al.*, Phys. Rev. D **73**, 074502 (2006).
- [25] MILC Collaboration, C. Bernard *et al.*, Phys. Rev. D **64** 054506 (2001).
- [26] MILC Collaboration, C. Aubin *et al.*, Phys. Rev. D **70** 094505 (2004).
- [27] C. Davies *et al.*, Phys. Rev. Lett. **92**, 022001 (2004).
- [28] S. Mehrabyan and B. Heltsley *et al.*, CBX 05-10.
- [29] D. Becirevic and A. B. Kaidelov, Phys. Lett. B **478**, 417 (2000).
- [30] D. Scora and N. Isgur, Phys. Rev. D **52**, 2783 (1995).
- [31] Q. He *et al.*, Phys. Rev. Lett. **95**, 121801 (2005).
- [32] L. Fields, CBX 04-37.
- [33] P. Avery, CBX 92-39.
- [34] R. Barlow and C. Beeston, Comput. Phys. Commun. **77**, 219 (1993).
- [35] N. Adam and L. Gibbons, CBX 05-59.
- [36] B. Heltsley and S. Li CBX 01-62.
- [37] D. Cassel *et al.*, CBX 05-07.
- [38] I. C. Brock and R. A. Briere, CBX 05-43.
- [39] H. Muramatsu and T. Skwarnicki, CBX 04-24.
- [40] S. Stroiney and A. Ryd, CBX 06-XX.
- [41] E. Barberio and Z. Was, Comput. Phys. Commun. **79**, 291 (1994).
- [42] T. C. Andre, hep-ph/0406006 and T. Alexopoulos *et al.*, Phys. Rev. D **71**, 012001 (2005)
- [43] C. Glenn Boyd, B. Grinstein and R. F. Lebed, Phys. Rev. Lett. **74**, 4603 (1995), hep-ph/9412324.
- [44] C. Glenn Boyd, and M. J. Savage, Phys. Rev. D **56**, 303 (1997), hep-ph/9702300.
- [45] M. C. Arnesen, B. Grinstein, I. Z. Rothstein and I. W. Stewart, Phys. Rev. Lett. **95**, 071802 (2005)
- [46] T. Becher and R. J. Hill, Phys. Lett. B **633**, 61 (2006), hep-ph/0509090.

- [47] R. J. Hill, Flavor Physics and CP Violation Conference, Vancouver (2006), hep-ph/0606023.
- [48] E691 Collaboration, J. C. Anjos *et al.*, Phys. Rev. Lett. **62**, 1587 (1989).
- [49] CLEO Collaboration, G. Crawford *et al.*, Phys. Rev. D **44**, 3394 (1991).
- [50] MarkIII Collaboration, A. Bai *et al.*, Phys. Rev. Lett. **66**, 1011 (1991).
- [51] CLEO Collaboration, A. Bean *et al.*, Phys. Lett. B **317**, 647 (1993).
- [52] E687 Collaboration, P. L. Frabetti *et al.*, Phys. Lett. B **364**, 127 (1995).
- [53] BES Collaboration, M. Ablikim *et al.*, Phys. Lett. B **597**, 39 (2004.)
- [54] BES Collaboration, M. Ablikim *et al.*, Phys. Lett. B **608**, 24 (2005.)
- [55] CLEO Collaboration, G. S. Huang *et al.*, Phys. Rev. Lett. **94**, 011802 (2005).
- [56] FOCUS Collaboration, J. M. Link *et al.*, Phys. Lett. B **607**, 233 (2005).
- [57] Belle Collaboration, L. Widhalm *et al.*, hep-ex/0604049.
- [58] Babar Collaboration, C. Bozzi, The XL Recontres de Moriond, La Thuile, Italy (2006) and hep-ex/0607077.
- [59] CLEO Collaboration, G. S. Huang *et al.*, Phys. Rev. Lett. **95**, 181801 (2005).
- [60] CLEO Collaboration, T. E. Coan *et al.*, Phys. Rev. Lett. **95**, 181802 (2005).
- [61] CLEO Collaboration, Y. Gao, International Conference on High Energy Physics, Moscow (2006).